Università Campus Bio-Medico di Roma

Corso di dottorato di ricerca in Scienze e Ingegneria per l'Uomo e l'Ambiente
Science and Engineering for Humans and the Environment
XXXIII ciclo a.a. 2017-2018

Biophysical modeling of *Caenorhabditis elegans* nervous system: from single cells up to neuronal networks

Martina Nicoletti

<div style="display:flex">

Coordinatore
Prof. Giulio Iannello

Tutore
Prof. Simonetta Filippi
Dott. Letizia Chiodo
Dott. Viola Folli

</div>

9 Aprile 2021

To my granmothers,
Elena and Rosina

ii

Abstract

Caenorhabditis elegans is a small free-living nematode whose anatomical simplicity, reduced size and, ease of genetic manipulation has made it a powerful model organism for different research studies, including neuroscience. The *C. elegans* nervous system, made up of only 302 neurons, was the first to be fully characterized in neurons number and connections. Unraveling the working principles of neuronal networks requires the knowledge of single neurons functioning, which is normally achieved through electrophysiology experiments. In *C. elegans* neurons, these experiments are particularly challenging due to the small size of neurons and difficulties in preserving the worm life and cell functionality after dissection. However, in the last few years, many efforts have been made to increase the number of characterized neurons. The increased amount of available electrophysiology data for *C. elegans* neurons has paved the way for extensive biophysical modeling of the nematode nervous system. This work aims at developing a comprehensive biophysical description of *C.elegans* neuronal dynamics, starting from the models of the single ionic currents. A biophysically accurate description of the neuronal dynamics is particularly important in a context where experimental informations are incomplete or missing since it could help to elucidate the molecular mechanisms at the basis of signal generation, integration and transmission.

The models of single neurons here presented rely on a classical Hodgkin-Huxley description adapted to describe the single ionic currents recorded in *C. elegans* neurons. According to gene expression profiles and available experimental data, these models are combined to reproduce voltage-clamp experiments on four representative *C. elegans* neurons: AWC^{ON}, AIY, RIM, and RMD neurons. Moreover, a detailed analysis of the contribution of each ionic current to the whole-neuron dynamics is conducted by simulating the responses of *in silico* knockout neurons, where the contribution of one channel is suppressed, leaving unchanged the others. The modelling work allows, among the other results, to establish the central role of T-type calcium channels in the bistable behaviour of RMD neurons. Moreover, the electrical model of the AWC^{ON} neuron is merged with a detailed model of the olfactory response developed by Usuyama et al. [1] to obtain a unified description of the electro-chemical processes at the basis of AWC^{ON}-mediated olfaction. A further refinement through genetic algorithm optimization of the electrical model of AWC^{ON} highlighted a previously unreported putative bistable behaviour that is investigated through *in silico* knockout simulations. Finally, single-neurons models are used to build a biophysical model of a minimal circuit.

In conclusion, this work provides a useful platform for the biophysical study of *C. elegans* nervous system, which could help to elucidate the molecular mechanisms at the basis of neuronal signalling and sensory processing, and could be applied to the study of complex neuronal functions such as sensory processing and motor control.

Contents

CONTENTS

CONTENTS

List of Figures

ix

LIST OF FIGURES

List of Tables

xiii

Introduction

Caenorhabditis elegans is a free-living nematode discovered in 1900 [2]. Thanks to its anatomical simplicity, optical transparency, reduced size ($\sim$1 mm long), and ease of genetic manipulation, it has been established as a powerful tool for biology and neuroscience studies. *C.elegans* is the first multicellular organism whose genome has been completely sequenced [3]. Many works have demonstrated that the 60%-80% of the human genes have an ortholog in the nematode genome [3, 4, 5, 6, 7], with a high degree of sequence similarities, resulting in similar protein functions and conserved signalling pathways [8, 9, 10]. These similarities make the nematode an excellent model for *in vivo* studies of human diseases and for drug discovery [8, 9, 10, 11]. Moreover, its nervous system has been fully reconstructed in terms of neurons number and connections [12], constituting an ideal framework for neuroscience studies. Despite its simplicity, it is complex enough to generate and control complex neuronal functions such as those related to sensory perception, signal integration, and motor control, and thereby it can be used a platform to study complex behaviours in a simple, but realistic framework.

A vast literature exists on the *C. elegans* nervous system, with many works dedicated to unravel the working principles neuronal circuits in the nematode, e.g. [13, 14, 15, 16, 17]. However, unravelling the working principles of a nervous system requires also the knowledge of single neurons functioning, which is normally achieved through electrophysiology experiments. In the case of *C. elegans* neurons, these experiments are particularly challenging due to the small size of neurons and difficulties in preserving the worm life and cell functionality after dissection. For these reasons, the electrophysiological characterization of the nematode neurons is still incomplete. Despite these difficulties, in the last few years many efforts have been made to increase the number of characterized neurons (e.g. [18, 19, 20, 21, 21, 22, 23, 24, 25]). The increasing amount of electrophysiology data for *C. elegans* neurons has paved the way for extensive biophysical modelling of the nematode nervous system.

Many computational works have successfully attempted to describe at various scales with mathematical models the nematode nervous system behaviour. Most of these works are dedicated to the study of the entire nervous system or to small sub-circuits regulating specific behaviours [26, 27, 28, 29, 30, 31, 32, 33, 34]; while few works are dedicated to single-cell studies, especially for what concerns the calcium dynamics [1, 21, 35, 36]. However, in most of these models, the electrical dynamics of single neurons is treated in a simplified way that does not allow the investigation of the mechanisms at the basis of neuronal responses. To date, there is no report of a comprehensive biophysical modelling of *C. elegans* neurons based on single ionic currents.

In this study, a framework for extensive modelling of the *C. elegans* nervous system, from the single ionic currents up to the network scale, is developed, based on available experimental data. The models of 15 ionic currents have been developed and combined together based on gene expression profiles derived from literature and from the Wormbase [5] and the CeNGEN databases [37] to reproduce the observed dynamics of four of the most studied *C. elegans* neurons: the AWC$^{\text{ON}}$ sensory neurons [38], the AIY and RIM

interneurons (M Nicoletti et al., to be published), and the RMD motor neurons [38, 39]. In the case of AWC^{ON} neurons, the detailed model of the electrical responses, has also been coupled to a detailed model of the intracellular calcium dynamics in the olfactory process to obtain a biophysically accurate description of the AWC^{ON} chemosensory responses [40]. The computational results obtained from the electrical model of AWC^{ON} neurons highlighted a previously unobserved putative bistable behaviour of the sensory neuron that has been further elucidated through calcium imaging experiments [41]. Notably, the putative bistability has also been observed *in vivo* under particular experimental conditions in which the neurons are mechanically stimulated [41]. Finally, the single-neuron models have been coupled with chemical ad electrical synapses to recreate a minimal circuit.

The work is organized in an Introduction section, seven chapters, and Conclusions; where the *C. elegans* nervous system biology, the computational and experimental methods, and the models of single ionic current, single neuronal cells, and of a minimal circuit are described.

The first chapter is dedicated to the review of the *C. elegans* nervous system functioning principles. The first two sections (Section 1.1 and 1.2) describe the nematode potential as a model organism and give the basilar notions about its anatomical features. In Section 1.3 an overview of the *C. elegans* nervous system is given, including the neuron classification criteria and detailed description of the biological role of the neurons modelled in this study. Section 1.4 is dedicated to reviewing the biophysical principles of the neurons' functioning, with particular attention to the electrical signal generation in neurons and to the olfactory stimuli transduction in AWC^{ON} neurons. In Section 1.5, a complete and detailed description of the physiological role of the modelled channels is also given with respect to their mammalian counterparts. Finally, a brief resume of the state of the art in *C. elegans* nervous system modelling is given in Section 1.6.

The second chapter is focused on the theoretical and computational methods used in this work. In the fist part (Section 2.1), the theoretical basis of the models used in this study are described, including the equivalence between the cells and the electrical circuit, the generalization of the Hodgkin-Huxley model to the *C. elegans* case, and the three intracellular calcium models used in the work (Section 2.1.3). Also, the single-cell and the network models are described. The second part of the chapter is dedicated to the description of the computational tools (Section 2.2) used to develop the models, i.e., XPPAUT, NEURON, and Python libraries for parameter optimization, and to description of models implementation (Section 2.3). Appendices A and B report the full list mode single-current model equations and parameters, respectively. Moreover, given the increasing interest in evolutionary computing-based optimization strategies, a description of their working principles is reported in Appendix C.

Chapter 3 is dedicated to the description of the experimental methods (Section 3.1) and results (Section 3.2) that have been used in this work. The contribution of the candidate

to the experimental work is explicitly stated in the chapter (mainly data analysis and data interpretation). Calcium imaging experiments preparation and data acquisition have been performed at the CLNS@Sapienza in the framework od an active research collaboration between UCBM ans CLNS. Despite no patch-clamp recordings have been directly performed in this work, an overview of its working principles is given, due to the fundamental role of patch-clamp results as reference data to develop the biophysical models here presented.

In Chapter 4, the models of the 17 ionic currents developed in this work are described. Three main classes of channels involved in the nematode neuronal dynamics have been described with a Hodgkin-Huxley formulation of the ionic currents: voltage-gated potassium channels, voltage-gated calcium channels, and calcium-regulated potassium channels. For each ionic channel, the curves for activation and inactivation variables and time constants are reported together with the simulated currents reproducing the experimental recording for *C. elegans* neurons. These models constitute a "database" from which the ingredients for single neurons modelling have been taken, and therefore, they have a key importance for the rest of the study.

The fifth chapter is entirely dedicated to the biophysical modelling of AWC^{ON} neurons. The chapter is divided into four main sections. In Section 5.1, the first electrical model of AWC^{ON} neurons is presented. The model correctly reproduces the experimental whole-cell recordings [19]. The *in silico* knockout analysis, allowed the dissection of the role of single ionic currents in the whole-neurons dynamics, highlighting the key role of the calcium currents EGL19 and UNC2 and the potassium currents carried by SHL1 and EGL2 currents. Thus the detailed electrical model is then coupled with a refined model of the chemical response of AWC^{ON} neurons developed by Usuyama et al. [1], to obtain a comprehensive description of the neuron responses to chemical stimuli (Section 5.2) [40]. The responses have been analysed in a wide range of odour concentrations and exposure times. The model correctly reproduces the available experimental data [13, 42] for different odor concentrations and exposure times. Section 5.3 is dedicated to a refinement of the electrical model of the AWC^{ON} neurons through a genetic-algorithm based optimization routine. Strikingly, in the new model, the neuron shows two stable resting states and can switch between them when a depolarizing stimulus is applied. This particular behaviour,previously unreported, is defined throughout the work as "putative bistable" or "bistable", and has been analysed through *in silico* knockouts (Section 5.3.2) and bifurcation analysis (Section 5.3.3) to identify the set of ionic currents that are responsible for the bistable behaviour. In the last section of the Chapter (Section 5.4) preliminary experimental data showing a previously unreported AWC^{ON} ability to sense mechanical stimuli are presented and discussed [41].

In Chapter 6, the model of three neurons, representative of the interneurons and the motorneurons classes, are presented. The AIY interneuron model (Section 6.1) has been based on published whole-cell recordings [21], and optimized through a genetic

algorithm routine. The simulated whole cell voltage and current clamp correctly reproduce the observed behaviour, and the *in silico* knockout analysis is used to dissect the putative role of outward rectifier potassium channels in the overall neuron dynamics. The model of RIM interneuron (Section 6.2) reproduces the experimental voltage-clamp recording [21], while it shows some discrepancies with the current-clamp recordings that have been investigated with *in silico* knockout and conductance analyses. In the last section (Section 6.3), the model of RMD motor neurons is presented. It correctly reproduces the known bistable behaviour of the RMD neurons and the bistability analysis here presented (Section 6.3.3) suggests the involvement of T-type calcium currents and leak current in shaping the bistability. Interestingly, the bistability analysis highlighted the existence of periodic and spiking solutions very similar to that recently observed in AWA neurons [21].

In Chapter 7, the model of a minimal sensing circuit is developed. As starting unit, the connection between AWC^{ON} and AIY is modelled through a standard model [43] of graded synaptic connection, and the responses of the two neurons have been analysed (Section 7.1). The model correctly reproduces the inhibitory connection between AWC^{ON} neurons, but for what concerns the intracellular calcium dynamics, it fails to reproduce the large calcium excursions observed in AIY interneurons [44, 45]. The same consideration holds for the electrical coupling between AIY and RIM interneurons and between RIM and RMD motor neurons that is realised through gap junction connections (Section 7.2). These results suggest that further work is needed to characterize and to model the intracellular calcium in *C. elegans* interneurons, as well as the chemical and electrical synapses.

Finally, some conclusions and future perspectives are reported.

Overall, this Ph.D. thesis work aims at establishing a solid basis to develop biophysical models of single-cells and circuits for the nematode *C. elegans*, treating at high level the description the various ionic currents involved in the nematode neuronal dynamics.

Chapter 1

The nervous system of the nematode *Caenorhabditis elegans*

1

In this chapter, introductory notions about *C. elegans* biology are given. Sections 1.2, 1.3 and 1.4 briefly describe *C. elegans'* anatomy, life-cycle, and nervous system. Sections 1.4 and 1.5 are dedicated to the description of ionic channels involved in the nematode neuronal dynamics. Finally, section 1.6 describes the intracellular processes at the basis of AWC^{ON} olfaction. But, first of all, a brief overview of *C. elegans* poential as model organism is given.

1.1   The *C.elegans* as model organism.

Caenorhabditis elegans is a free-living nematode discovered by the French zoologist Émile Maupas in 1900 in the surroundings of Algiers [2]. *C. elegans* was initially classified as soil nematode, but many studies confirmed it as a colonizer of microbe-rich environments, especially rotting plant materials, sharing the natural habitat with two other well-known model organisms: the *Drosophila melanogaster* and the *Saccharomyces cervisiae* [46]. *C. elegans* belongs to the *Caenorhabditis* genus, which includes over 50 putative species of nematodes found worldwide [46, 47]. The favourable anatomical and genetic characteristics have elected *C. elgans* as an excellent model organism for biological studies since the 60s when Sidney Brenner proposed this small transparent nematode as a tool for the study of developmental biology [7]. *C. elegans* has a short life cycle (3 days at 25°C between the larval and the adult stages, and 2-3 weeks of life in the adulthood) and can be easily grown and maintained in the laboratory. Adult worms are transparent and have an invariant number of somatic cells (959 in the hermaphrodite and 1031 in the male), whose fate have been followed from the fertilization to death, allowing the determination of the complete cell lineage [48, 49, 50]. The genome of *C.elegans* is the first genome of a multicellular organism to be entirely sequenced [3]. It contains ∼19000 genes, and at least the 38% of them is predicted to have orthologs in the human genome. Many works have demonstrated that 60%-80% of human genes have an ortholog in the nematode genome [3, 4, 5, 6, 7], with a high degree of sequence similarities, resulting in similar protein functions and conserved signaling pathways [8, 9, 10]. Moreover, 40% of the genes related to human diseases have a clear ortholog in *C.elegans*, establishing the nematode as an excellent model organism for the study of human genetic and age-related diseases, such as Alzheimer's, Parkinson's, and Huntington's diseases, and drug screening [8, 9, 10, 11, 51]. Moreover, *C.elegans* is the first organism whose connectome has been fully reconstructed from electron micrograph images [12]. The connectome is a map describing the connections among the neurons, and it constitutes an essential instrument and a starting point for studies devoted to understand the origin of the surprisingly rich repertoire of complex neuronal behaviours, arising from a nervous system with only 302 neurons. This compactness combined with conserved biophysical properties have made the *C.elegans* nervous system an excellent framework to unveil the working principles of large and complex neuronal circuits in the human brain.

1.2   *C. elegans* anatomy and life cycle

C. elegans is a nematode belonging to the *Caenorhabditis* genus. It has a transparent cylindrical body with tapered endings (Fig. 1.1 A). Adult worms are about 1 mm long and 80 μm thick. As in other nematodes, the body is composed of two concentric tubes separated by the pseudocoelom, a fluid-filled cavity, in which the digestive and reproductive systems are embedded [52] (Fig. 1.1 B-C). The fluid inside the pseudocoelom cavity is essential for tissue lubrification and provides the turgor pressure necessary to maintain the body shape [52]

The sinusoidal motion of the nematode is coordinated through alternating contractions and relaxations of ventral and dorsal muscles: when dorsal muscles are contracted, the ventral are relaxed and vice versa [52]. Other components of the outer tube are the nervous system, the gonads, and the excretory/secretory system [52](Fig. 1.1 B-C). In contrast, the pharyngeal muscle, the intestine and the autonomous nervous system are part of the inner tube [52].
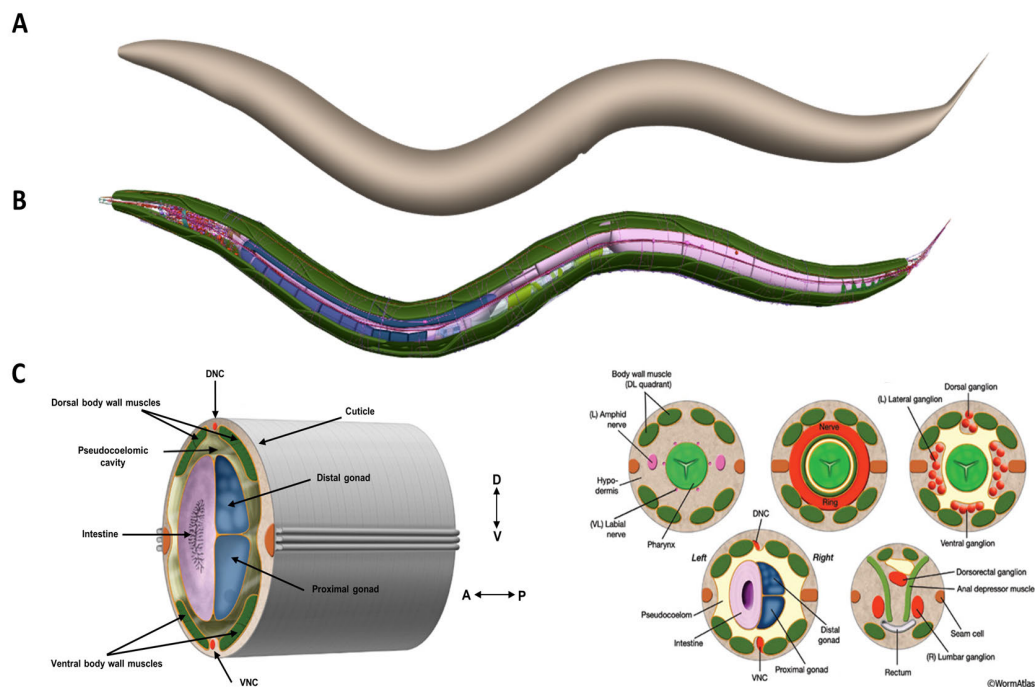
Figure 1.1: *C. elegans anatomy* **A). Sketch of the adult *C. elegans* hermaphrodite** The image was generated using the OpenWorm browser (`http://browser.openworm.org/`). **B). Sketch of the *C. elegans* hermaphrodite interior**. The image was generated using the OpenWorm browser (`http://browser.openworm.org/`). **C). Detailed view of *C. elegans* interior**. The image shows a section of the nematode interior composed of two concentric tubes. The outer tube contains the dorsal and ventral muscles as well as dorsal and ventral nerve cords (DNC and VNC respectively). The inner tube contains the pharinx, intestine, reproductive system and the antonomous nervous system. (Images are adapted from Wormatlas [53])

C. elegans exists in two sexual forms: hermaphrodites and males. Hermaphrodites are self-fertilizing females that can produce a little amount of sperm used for internal fertilization [54], although when possible, they preferentially mate with males and produce a more numerous progeny. Males arise from rare spontaneous mutations of the X chromosome and typically represent the 0.1-0.2% of the progeny [55]. Despite the similar shape and some common anatomical features, the two sexes display a marked sexual dimorphism, manifested in the number of somatic cells, anatomical structures, and sex-specific behaviours. Somatic cells are 1031 in the male and 959 in the hermaphrodite. The 30% of nuclei of the somatic cells in the hermaphrodite are sexually specialized, and this percentage increases up to 40% in the male [54].

The *C. elegans* life cycle is similar to that of other nematode species. It comprises six stages: the embryonic stage, the four larval stages L1-L4 and adulthood (Fig. 1.2 B) [53]. The life cycle is short and temperature-dependent: it lasts 3 days at 25°C from egg-laying to adult stage and shortens at increasing temperatures [56]. Once adulthood is reached, the worm survives 2-3 weeks. If during the development the L2 larva experiences adverse environmental conditions, such as low temperature, limited food availability, or overcrowding, it enters the "dauer" stage. Dauer larvae are incredibly resistant to stress conditions and could survive in this "non-aging" stage even for several months without food. When new favourable conditions are encountered, the animal exits from the dauer stage, and re-enters in the life cycle at the L4 stage and completes the development [7].

1.3 *C. elegans* nervous system

The *C. elegans* nervous system constitutes an ideal framework for neuroscience studies, thanks to its compactness and the conserved mechanisms. The nematode nervous system has been completely reconstructed from electron micrograph studies [12]. It can be divided into two independent units: the somatic nervous system and the pharyngeal nervous system. The pharyngeal nervous system is composed of 20 neurons that are distributed along the pharyngeal muscles and directly attached to their target muscles [58]. In contrast, the neurons of the somatic nervous system lie in the basal lamina that separates the hypodermis and the body wall muscles and communicate with the pharyngeal neurons through a single pair of interneurons: the RIP interneurons [58]. The two sexes exhibit sex-related differences in the nervous system. The most evident difference is in the number of neurons: the hermaphrodite has 302 neurons, while the male possesses 385 neurons, 81 of which are male-specific that specifically regulate mating behaviours, such as the hermaphrodite contact, vulval location, and insemination [59] (Fig. 1.3 A-B). However, there are also sex-related gene expression and synaptic strength differences [54, 60]

1.3.1 Neurons in *C. elegans*

Several criteria are used to classify the neurons based on molecular profiles, morphological features, and functionality. The first obvious classification of the *C. elegans* neurons

1.3. *C. ELEGANS* NERVOUS SYSTEM
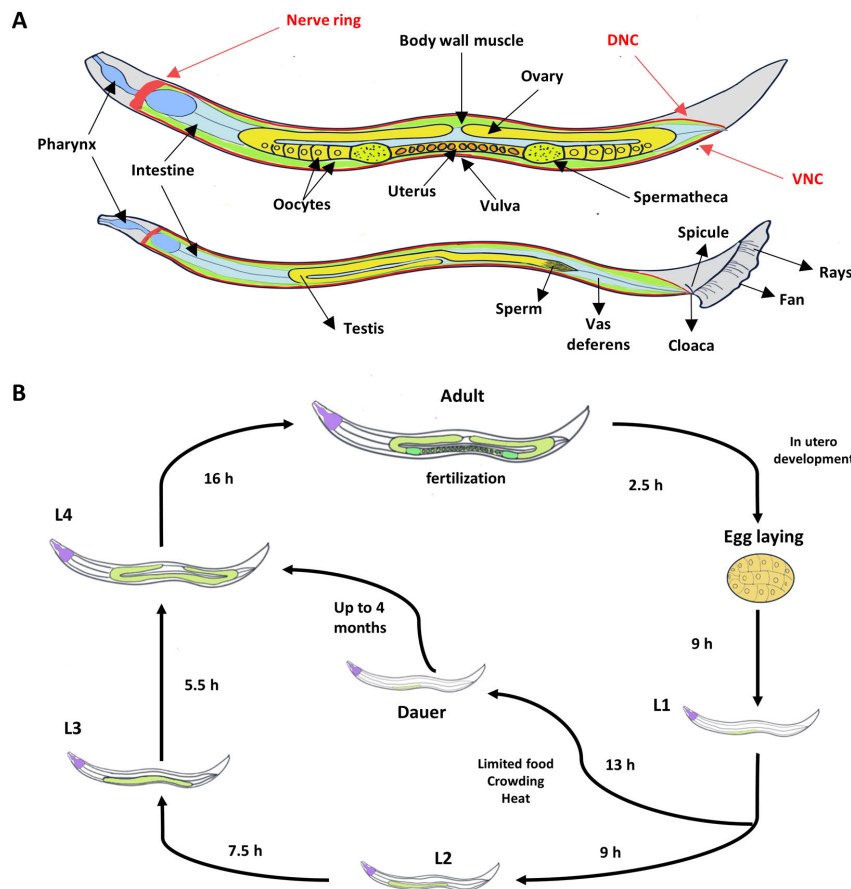
Figure 1.2: **A). Hermaphrodite and male anatomical characteristics**. Hermaphrodites (top panel) are about 1 mm long and 80 μm thick. They have two functionally independent U-shaped gonads. Each gonad is composed by an ovary, an oviduct and a sphermatheca. The ovary is located in the distal part to the vulva; while the oviduct and the spermatheca are located in the proximal part and connected to a common uterus centred around the vulva [57]. Males (bottom panel) are 30% shorter and thinner than hermaphrodites. They are equipped with a single U-shaped gonad. and peculiar tail with specialized sensory neurons and copulatory structures to enable the hermaphrodite vulva localization [54]. **B). *C. elegans* life cycle.** Hermaphrodite life cycle from the embryonic to the adult stage.

is based on their functionality.

- Sensory neurons: they receive informations from the external environment, such as chemical, mechanical, light, and other stimuli.

- Interneurons: they receive signals from presynaptic neurons and process them before sending to other neurons.
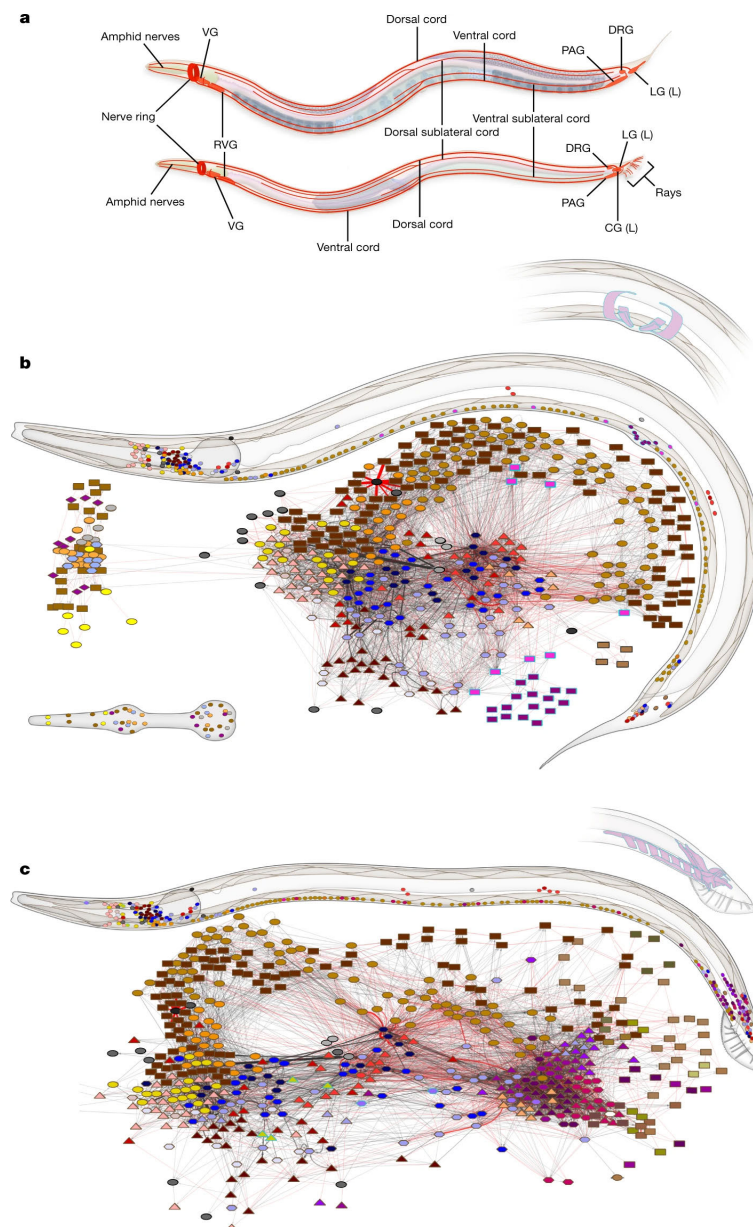
Figure 1.3: **Hermaphrodite and male connectome**. Reprinted by permission from [RightsLink®]: [Nature/Springer/Palgrave] [Nature] [Whole-animal connectomes of both *Caenorhabditis elegans* sexes, Steven J. Cook et al] [4970620508627] (2019)

- Motor neurons: they innervate muscles and regulate their contractile activity.

- Polymodal neurons: that perform more than one of the functions mentioned above, or, in the case of sensory neurons, they are capable of detecting different types of

1.3. *C. ELEGANS* NERVOUS SYSTEM

Superclass	Number of classes	Characteristics
Unpaired	26 classes (26 neurons): ALA, AQR, AVG, AVL, AVM, DVA DVB, DVC, PDA, PDB, PQR, PVM, PVR, PVT, RID, RIH, RIR, RIS, I3, I4, I5, I6, M1,M4, M5, MI	Each class has a single member.
Bilaterally symmetric	70 classes (140 neurons) AIA, AIB, AIY, AIZ, AWA, AWC, and others.	All neurons, except AWC and ASE, show left-right assymmetry in gene expression and function.
3-fold symmetry	1 class SAB neurons	The class has 3 members with a radial symmetry.
4-fold symmetry	10 classes (40 neurons): CEP, OLQ, RME, SAA, SIA, SIB, SMB, URA, URY.	Each class is composed of 4 radially symmetric neurons: 2 sub-dorsal and 2 sub-ventral neurons. The two pairs differ in gene expression and synaptic connectivity.
6-fold symmetry	3 classes IL1, IL2, RMD	Each class has three pairs of neurons: dorsal, ventral, left and right
VNC motor neurons	8 classes (66 neurons) DA (9 neurons), DB (7 neurons), DD (6 neurons), VA (12 neurons), VB (11 neurons), VC (6 neurons), VD (13 neurons), AS (11 neurons)	Some classes display molecular or synaptic connectivity differences

Table 1.1: *C. elegans* **neurons classification**. Six classes superclasses of neurons divided on the basis of number of neurons per class. (Adapted from [63]).

cues [17, 61, 62].

Another criterion for classification is based on morphological features and synaptic connectivity. According to this criterion, 118 classes of neurons have been identified [12]. The number of members per class varies among the classes, e.g., some classes have only one member, while others can contain up to 13 members [12]. Neurons inside the same class are morphologically similar, and, except for the single neuron classes, they are symmetrically arranged. The number of members per class can be used as a criterion to simplify the classification, allowing the definition of 6 superclasses that also reflect their symmetric arrangement [63]. The classification of the neurons based on this criterion is summarized in Table 1.1.

Most of the *C. elegans* neurons have a simple unipolar or bipolar structure, with somata clustered in the ganglia of the head and tail (Fig. 1.4 A). Some neurons are equipped with

a unique process, a dendrite or an axon, and perform purely sensory or synaptic output functions, respectively. Other neurons are capable of processing both input and output informations and possess both axons and dendrites [58]. In addition to the simple basilar architecture, some neurons have evolved with specialized structures that enable the fulfilment of specific functions. For example, sensory neurons detecting chemical, light touch, and nose harsh touch stimuli display ciliated dendritic endings where specific receptors are localized. In contrast, body harsh touch neurons are equipped with a complex dendritic arborization that innervates the entire body of the worm (Fig. 1.4 B-C). *C. elegans* neurons cell bodies and processes are very small compared to the vertebrate ones: the typical soma diameter is less than 5 μm, and the processes are 100-200 nm thin. In the following are briefly described the main functional classes of the nematode neurons, with particular attention devoted to the neurons modelled in this work.
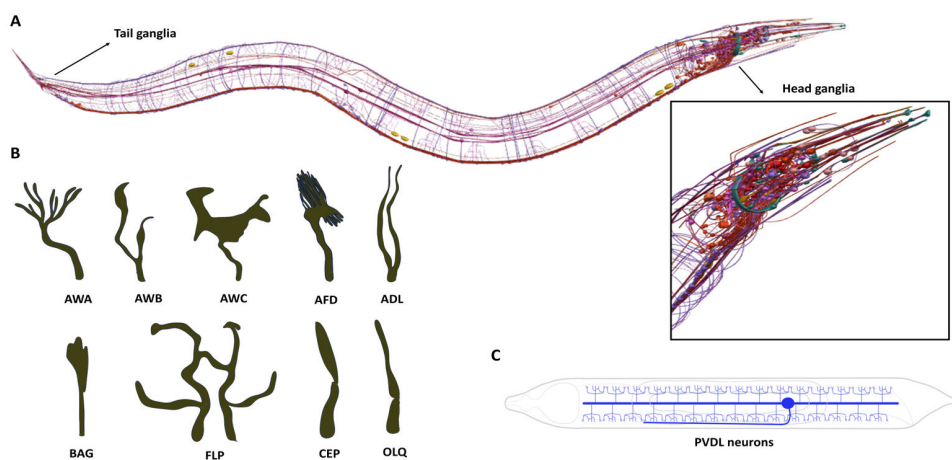
Figure 1.4: ***C. elegans* neurons antomical features. A) Representation of the *C. elegans* neurons in the worm**. The image is generated using the Openworm browser (`http://browser.openworm.org/`). The insert show an enlargement of head ganglia, where most of the neuronal cell bodies are localized. **B). Ciliary structures examples**. Schematic representation of the ciliary structure of some sensory neurons (Adapted from [64]).**C). Schematic representation of PVDL neurons**. PVD are sensory neurons whose function is the detection of noxious mechanical stimuli in the body. They envelope the body with a series of thin dendritic processes that are essential for harsh touch sensation [65].

Sensory neurons

C. elegans survival depends on its ability to detect a wide variety of environmental cues. The worm is equipped with a set of 70 sensory neurons, whose morphology (Fig. 1.4 B) and molecular characteristics are specialized to enable the perception of mechanical stimuli, temperature variations, oxygen levels, ambient osmolarity, pH, light, and both water-soluble and volatile chemicals. The majority of sensory neurons, 52 of 70, have evolved with ciliated endings grouped in sensory organs called sensilia. Only oxygen and

mechanical stimuli detection is performed by isolated neurons.

Mechanosensation and proprioception. Mechanosensation is one of the most important sensory functions in *C. elegans*. Adult hermaphrodites have 45 putative mechanoreceptor neurons, and males have additional 42 neurons involved in sex-specific functions [66]. The different morphological and molecular characteristics of the touch receptor neurons enable the worm to sense a wide range of mechanical stimuli, including gentle and harsh touch along the body and genetle tough to the nose [66]. Touch sensation is mediated by 20 classes of neurons, among which 4 are specific for low-threshold mechanical stimuli (gentle-touch), and the other 16 are required for the response to high-threshold mechanical stimuli (harsh touch) [58].
Another sensory function strictly related to mechanosensation is proprioception. Proprioception consists in the capability of an individual to perceive its position and self-movement in the environment. In the worm, proprioception is coordinated by mechanosensory neurons that innervate the central and the posterior parts of the body (DVA, PVD and B class motor neurons) and the head (SMD neurons) [66].

Nociception Nociception consists in the ability to perceive noxious stimuli that could jeopardize the integrity and the survival of the animal. Noxious stimuli come up in different forms, such as acidic pH, extreme heat or cold, toxic chemicals, or painful mechanical stimuli [64]. In the worm, mechanical nociception is mediated by the harsh-touch receptors that detect intense mechanicals stimuli. The most important *C. elegans* nociceptors are the ASH neurons that are responsible for the sensation of a wide variety of noxious stimuli, including nose harsh-touch, high concentration of salts or sugars, acidic pH, quinine, and other bitter compounds, heavy metals, and aversive odors such as 2octanone, octanol, and benzaldehyde. ASH neurons are amphid sensory neurons, whose cilia belong to the amphid sensilia and are exposed to the external environment. Interestingly, all the ASH sensory functions rely on the same molecular players: the homologues of the human TRPV channels, OSM-9, OCR-2, and OCR-4 [67, 68, 69]. These channels are also involved in thermal avoidance that is mediated by AFD neurons [70]

Thermosensation Thermosensation is another important sensory function in *C. elegans*. The worm is extremely sensitive to unfavorable temperatures, for example, high temperatures are among the environmental conditions that can induce dauer state entry. *C. elegans* usually lives in a restricted range of temperature, between 12° C and 25° C, and tends to migrate to its cultivation temperature and to escape from temperatures at which it is starved [71, 72]. Moreover, the worm is an extremely sensitive to temperature variations, being able to detect changes of 0.01° C [73]. The main thermosensors neurons are AFD neurons, a pair of bilaterally symmetric ciliated neurons of the amphid (Fig. 1.4 A). In addition to AFD neurons, also AWC and ASI neurons display thermosensory ability and support the normal functioning of AFD [58]. Noxious thermosensation is performed by AFD, FLP and PHC neurons, while acute cold is sensed by PVD neurons [58].

Electromagnetic field sensation   The worm can detect electric and magnetic fields that permeate the surrounding environment. Galvanotaxis is mainly performed by ASJ neurons [74, 75]. In addition to ASJ, other sensory neurons such as AWC, AWB, ASK and ASH display weak responses to electric fields [74, 75]. Magnetic fields are detected by the ADF thermosensory neurons [76]. Finally, the worm is sensitive also to UV and visible light. *C. elegans* light sensation is still poorly explored; however, it has been demonstrated that UV induces avoidance behaviour mediated by the ASJ and ASH neurons through the homologous of insect taste receptor LITE-1 [77, 78].

Oxygen and CO_2 sensation   *C.elegans* can detect in the environment levels of oxygen and carbon dioxide associated with the food abundance. Also, the oxygen diffusing through the pseudocoelem fluid is essential for metabolism maintenance. Oxygen detection rely on many unpaired sensory neurons distributed throughout the body, such as URX, PQR, AQR, SDQ, BDU, ALN, PLN, ASH, and ADF neurons [79, 80, 81, 82]. Carbon dioxide levels are detected by AFD, BAG and ASE neurons [80].

Chemosensation   Chemosensation is one of the most important and complex functions for a *C. elegans* life. In *C. elegans*, chemosensation is performed by 32 sensory neurons divided into 14 classes, most of which (11 classes) are found in the amphid sensilia [71, 83]. The chemosensory neurons detect both volatile and water-soluble chemicals such as alcohols, aldehydes, ketones, esters, pyrazines, thiazoles, and aromatic compounds. Water-soluble odorants are mainly detected by ASE neurons, with minor contributions from ADF, ASG, ASI, ASJ, ADL and ASK neurons [71, 83]. Volatile chemotaxis is mediated by three pairs of neurons located in the amphid: AWA, AWB, and AWC. AWA and AWC mediate the chemotaxis of attractive odorants, while AWB is specialized for detecting aversive chemicals. The three neurons possess winged cilia surrounded by the amphid sheath cell (Fig. 1.4 B). Among chemosensory neurons, a key role is played by AWC neurons, which are modelled ad discussed in this thesis work.

AWC neurons. AWC neurons amphid sensory neurons whose primary function is the detection of attractive volatile odorants. In addition to that, AWC neurons are also involved in thermosensation [19, 84], electrosensory navigation [74], and sexual attraction in males [85]. In contrast to AWA and AWB that show left-right symmetry in gene expression, AWC neurons are characterized by a stochastic left-right asymmetry that results in distinct functionalities of the two neurons [86, 87]. The asymmetrically expressed genes encode for a particular class of receptors, the G-protein coupled receptors (GPCRs). GPCRs are essential for *C. elegans* nervous system functioning, being involved in chemotaxis, aerotaxis, locomotion, reproduction, and many other signalling pathways among neurons [88, 89]. Many works have reported that the left-right asymmetry is determined by the expression of two genes, *str-2* and *srx-3* [**?** **?**]. The *str-2* receptor is expressed in the AWC^{ON} neuron that is specialized for the detection of butanone, while AWC^{OFF} expresses the *srx-3* receptor and senses 2,3-pentanedione. However, a recent work by Vidal et al. identified six other GPCRs that are asymmetrically expressed in AWC, suggesting that the left-right asymmetry is a more complex

phenomenon than previously believed [90]. Both AWC neurons show an ODOR-OFF response, i.e., the neurons inactivate in the presence of attractive volatile odorants, such as benzaldehyde and isoamyl alcohol, and activate when the odour is removed. AWC neurons are particularly important for local search behaviour. Their robust graded activity is essential to regulate reversals and to correct erroneous turns promoted by the pulsatile activity of AWA neurons [91]. AWCs form excitatory and inhibitory synapses with various interneurons, including AIY, AIA, AIB, and AVA. AIY and AIB interneurons are regulated oppositely by AWC and generate a coordinated behavioural response to chemical stimulation [13]. AWC neurons inhibit AIY interneurons through the glutamate chloride channel GLC-3, while they activate AIB neurons *via* AMPA-type glutamate receptors [13, 92]. AIY and AIB interneurons are crucial for regulating the local search behaviour, being responsible for the suppression and the enhancement of turns [13, 93]. GLC-3 channels also mediate the inhibitory synapse between AWC and AIA, that is further modulated by the neuropeptide NLP-1 [94]. NPL-1 knockout worms exhibit a high turning rate as well as defective odor-adaption, indicating that NLP-1 signalling regulates both the local search and the adaption behaviour [94]. The adaption behaviour is also mediated by the INS-1 peptide released by AIA neurons that provides a feedback signal for AWC neurons [94]. The modelling and analysis of AWC are reported in Chapter 5, while its role in the circuit is described in Chapter 7.

Interneurons

Interneurons represent the most numerous class of neurons in *C. elegans* and play a key role in information processing and integration. Interneurons receive input signals from their presynaptic neurons and process them before transmitting it to other neurons. Interneurons can receive information from sensory, motor, and even from other interneurons. In this work, two interneurons, AIY, and RIM are modelled; both are crucial for information processing in the olfactory circuit. In the following their specific functions in the nematode nervous system are described in detail.

AIY neurons. AIY belongs to the first layer of amphid interneurons and receives synaptic inputs from many amphid sensory neurons, including olfactory, gustatory, and thermosensory neurons, and conveys them to other interneurons. Laser ablation of AIY interneurons induces cryophilic behaviour, indicating their involvement in the regulations of the thermophilic behaviour [95]. Moreover, they are critical for regulating food- and odor-evoked behaviours, receiving inputs from AWC neurons, and functioning in concert with AIB interneurons to regulate turns and reversals [13, 93]. AIY neurons play a critical role in locomotion regulation. Their ablation or *ttx-3* gene mutations induce a hyper-reversal phenotype characterized by enhanced reversals and turns, disruption of dispersal, and shortened forward movements [96]. They are also involved in life span regulation and response to starvation. Also, AIY functions in opposition to AIB and inhibits the starvation promoted by AIB. AIY ablation shortens the life span of wild-type and *daf-2* mutants [97]. Also, longevity is regulated in a temperature-independent manner by *ttx-3* and *ceh-10* genes, which are essential for AIY functioning [97]. Furthermore, AIY is involved in temperature-dependent regulation of life-span through FLP-6

and DAF-9, and INS-7 signaling [98].

RIM neurons. RIM neurons belong to the second layer interneurons, a set of interneurons whose function is to collect information about the external environment and internal animal state and process them to regulate the locomotion behaviour. In particular, RIM are inter/motor neurons that downstream many interneurons and send informations to head motor neurons and neck muscles [12]. They are particularly important in the inhibition of reversal behaviour. Indeed, RIM-ablated animals display an increased reversal frequency, while ablation of the other second-layer interneurons RIA and RIB do not significantly affect the reversal behaviour [99]. RIM neurons are thought to act in a circuit in parallel to command interneurons (AVA/AVD/AVE) to suppress reversals during the forward movement [99]. RIM neurons receive informations from many interneurons, most of which form with RIM sparse synaptic connections [99]. Among the few first-layer interneurons that upstream RIM and form dense synaptic connections with it, there are the AIB interneurons that promote reversals by inhibiting RIM [99]. RIM interneurons are connected through gap junctions to AVA, so that AVA activation induces RIM activation [100]. RIM, AVA, and AIB neurons are part of the olfactory network that downstream AWC, and their collective activity is essential to induce variability in the AIB response to odours [100]. Moreover, RIM neurons form synaptic connections, mediated by the tyramine-gated chloride channel LGC-55, with AVB command interneurons, and with motor neurons of the head movement circuit (RMD, and SMD). RIM ablated animals, as well as LGC-55 mutants also show suppressed head movements in response to anterior touch [101, 102].

Motor neurons

The nematode possesses 113 motor neurons, among which 75 innervate 16 neck and 63 body-wall muscles, belonging to eight different classes (AS, DA, DB, DD, VA, VB, VC, VD). According to their molecular characteristics, motor neurons controlling the body movement are divided into four classes: A, B, C and D. A-class (AS, DA, and VA) motor neurons are cholinergic excitatory neurons that control body bending and dorso-ventral sinusoidal movement, by generating intrinsic oscillatory activity [103, 104]. B-class motor neurons are cholinergic neurons whose oscillatory activity is strictly related to gap junction connections with premotor interneurons [104]. They function in proprioception by sensing the bending of the anterior segments of the body [105], and are essential for L1 larvae forward locomotion [106, 107] C-class (VC) motor neurons are mainly involved in the regulation of vulval muscle activity. They form synapses with serotoninergic HSN neurons and vulval muscles, so that their release of acetylcholine inhibits the egg-laying activity [108]. Finally, D-class motor neurons are inhibitory GABA-ergic neurons that control the sinusoidal movement by forming synaptic connections with ventral and dorsal body-wall muscles [109]. In contrast to the body that can only perform dorso-ventral flexures, the head can also make lateral movements, thanks to specialized muscles and motor neurons. Head and neck muscles activity is coordinated by 11 motor neuron classes: RMD, SMB, URA, RIM, RMF, RMG, RMH, RIV, RMH, IL1, SMD. [110]. Among motor neurons, the RMD class has been selected for this study because of its

importance in regulating the worm foraging behaviour and because RMD neurons are among the few motor neurons that have been characterized with electrophysiology experiments [20].

RMD neurons. RMD neurons are six-fold symmetric neurons that regulate the foraging behaviour by innervating head and neck muscles via neuromuscular junctions in the nerve ring. RMD neurons regulate spontaneous foraging movements, as well as head withdrawal reflex [111]. Foraging behaviour is characterized by rapid and continuous side-to-side movements of the head, while head withdrawal reflex consists of an aversive response to light nose touch that interrupts the normal foraging movements [111]. Both behaviours are initiated by the mechanosensory neurons OLQ and IL1 that synapse on RMD [112]. The synapses of OLQ and IL1 on RMD are glutamatergic and rely on the GLR-1 receptor [112, 113]. Also, RMD neurons are synaptic targets of RIM interneurons through the tyramine-gated chloride channels LGC-55 and of other command interneurons such as RIA [114]. RMD neurons have also been suggested to have a regulatory action on the turning frequency, based on the thermal information received from the glutamate-mediated communication with RIA neurons [114].

1.4   Biophysical basis of neurons functioning

In this section, the fundamental principles of cellular functioning are described. The molecular mechanisms behind the generation of characteristic neuronal electrical responses, as well as those at the basis of sensory information processing are reviewed with particular attention to the *C. elegans* case. Concerning the sensory information processing, due to the vastness, richness and, complexity of the argument, the description will be restricted to the case of the AWC *C. elegans* neurons here studied.

1.4.1   Cell membrane and ion channels

Neurons are special cells that evolved to communicate precisely and rapidly with other cells thanks to their ability to generate electrical signals. This ability is derived from the peculiar properties of the neuronal cell membrane. More in general, the biophysical properties of a cell, i.e., its capability to perform specific functions and communicate with other cells, are related to the peculiar composition of its membrane [115]. The cell membrane is an essential component of a cell, acting as a barrier that protects the interior of the cell from the external environment but allowing at the same time the exchange of essential nutrients and the excretion of metabolic waste products [115]. Also, the cell membrane is critical for preserving the proper solute concentrations in intracellular and extracellular media. The main component of the cell membrane is a lipid bilayer that forms a fluid substrate in which other membrane components are embedded. Membrane lipids are amphiphilic phospholipids with and hydrophilic head and hydrophobic tail [115] (Fig. 1.5).

The barrier function exerted by the cell membrane causes charged ions accumulation on both sides of the membrane and favours the establishment of an electrochemical
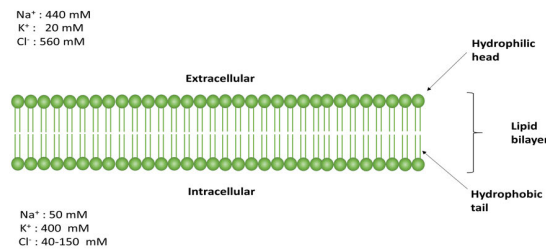
Figure 1.5: **Lipid bilayer**. Structural organization of the cell membrane. The membrane is composed of two layers of phospholipids that arrange exposing the polar (hydrophilic) heads to the exterior and the hydrophobic tails to the interior [115]. Extracellular and intracellular media are characterized by different ion concentrations. Here are reported the concentrations of K^+. Na^+, and Cl^- in the squid giant axon [116]

gradient. The "membrane potential" is the electrical potential that arises from different charge distributions on the two sides of the membrane, and is a key regulator of many cellular functions, especially in the case of neurons. The physical origin of the membrane potential (also called "transmembrane potential") and its importance for neurons will be extensively discussed in Section 1.4 and Chapter 2, Section 2.1.1

The exchange through the membrane of a rich variety of ions and molecules is achieved by two classes of proteins: the carrier proteins and the ion channels. The first are specialized proteins that aid the movement of ions and molecules against the concentration gradient using energy provided by the cell metabolism, e.g., ATP hydrolysis. This mechanism of transport is usually referred as "active transport" to indicate that it is energetically expensive for the cell. Ion channels are a class of membrane proteins that allow small water-soluble molecules to cross the membrane by diffusing across an aqueous pore. The transport through ion channels is also called "passive transport" to emphasize that is does not require an additional energy source provided by the cell [115, 117].

Ion channels are critical for the control of membrane permeability to ions and molecules, and thereby they guarantee the functional integrity of the cell. Alterations of their functions cause several pathologies, such as cystic fibrosis, Dravet syndrome, Charcot-Marie-Tooth disease, different forms of episodic ataxia and epilepsy, and many other genetic diseases usually called "channelopathies" [118]. Living organisms have evolved with an impressively reach repertoire of ion channels that differ in ion selectivity and gating mechanisms. Ion channels are not continuously open, but they open or close through conformational changes induced by the gating mechanism. Based on the gating mechanism, ion channels can be divided into three main classes [117]:

- *Voltage-gated channels*. Voltage-gated channels are sensitive to transmembrane potential that is established by charge unbalance between the two sides of the membrane. These channels possess a specialized region, the "voltage sensor", that

changes its position within the protein in response to membrane voltage changes, allowing the pore opening or closing [117]. Voltage-gated channels are particularly important for neuronal cells [117]. Indeed their ability to fire action potentials is critically determined by the peculiar set of voltage-gated K^+ and Na^+ channels expressed in their membranes (Fig 1.6 A).

- *Ligand-gated channels.* Ligand-gated channels change their conformation as a consequence of the binding of specific molecules, the ligands, to dedicated sites in the protein. The most common ligands are hormones, neurotransmitters, calcium ions, and many other intracellular and extracellular compounds (Fig. 1.6 B).

- *Mechanically-gated channels.* Mechanically-gated channels are a class of ion channels that groups different categories of channels sharing the common ability to open in response to force application [117]. The force gating relies on two main mechanisms, the force-from-lipid and the force-from-tether mechanism. Channels gated with the force-from-lipid mechanism change their conformation in response to the membrane tension and curvature and do not need additional proteins that link the channel to the membrane, as happens in the case of force-from-tether model [119] (Fig. 1.6 C).

Given their relevance for this study, a dedicated section (Section 1.5) will be entirely reserved for the description of the nematode ionic channels. In particular, their physiological role and their contribution to the *C. elegans* neuronal dynamics will be extensively reviewed.

1.4.2 Physiological basis of neurons excitability

Neurons are the core units of the nervous system. They play a key role in organisms' life, being responsible for collecting and processing a wide variety of informations from the environment to originate behavioural responses. This ability is conferred to the neurons by a combination of specialized morphological features and physiological properties. The morphological features and their relevance for the *C. elegans* neurons case have already been reviewed in Section 1.3. In the following, the discussion will be focused on the physiological characteristics that enable neurons to generate electrical signals. Neurons are classified as excitable cells that generate electrical signals in response to different kind of stimuli such as sensory receptors activation or synaptic inputs from other neurons. These signals are called "action potentials" (APs) and represent the quantum of information in the nervous system. Action potentials arise thanks to a peculiar combination of voltage-gated ionic channels expressed on the neurons' membrane and cannot be explained with static membrane properties.

In mammalian neurons, action potentials are originated from a combination of voltage-gated sodium and potassium channels, whose opening and closing in response to membrane voltage changes shape the electrical responses of the neurons (Fig. 1.7) [117]. Upon stimulus application, the membrane potential rises, reaching the activation threshold.
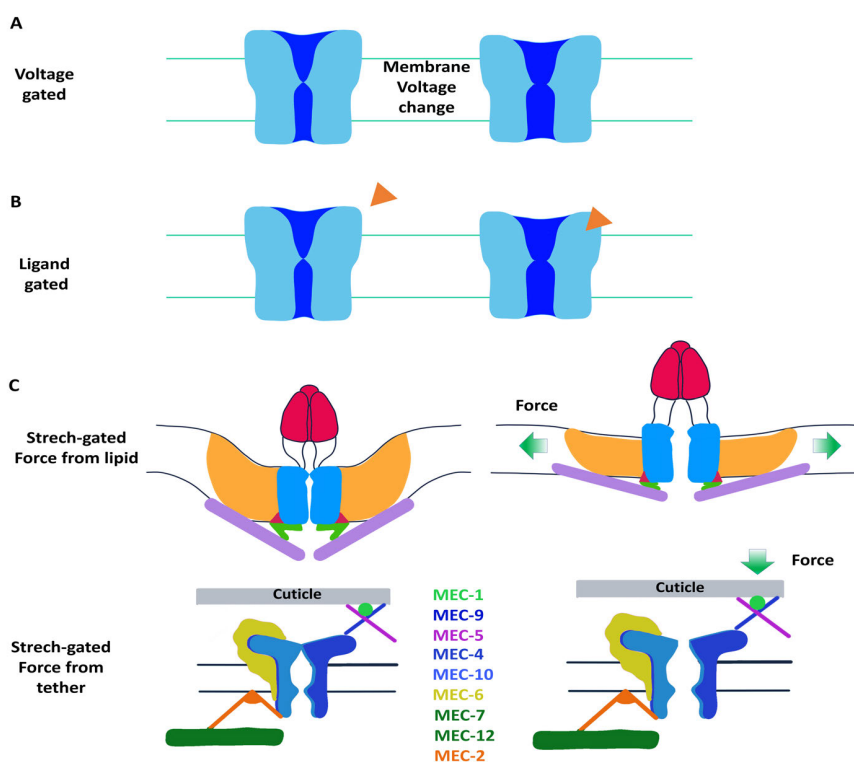
Figure 1.6: **Ion channel gating mechanism**. **A) Voltage-gated channels**. Voltage-gated channels open in response to changes in the membrane voltage (adapted from [117]). **B) Ligand-gated channels.** Ligand binding to a specific site induces conformational changes and thereby the opening of the channel (adapted from [117]). **C) Mechano-gated ion channels**. Mechano-gated ion channels can sense mechanical stimuli acting on the membrane through two main mechanisms: the force-from-lipid and the force from tether. In the force from lipid model the channel changes its conformation in response to the tangential force applied to the lipid bilayer. In the panel, is sketched the activation mechanism of mouse Piezo-1, a class o stretch-gated channels expressed in many living organisms, including *C. elegans* (adapted from [120]). Other mechano-gated channels, such as the DEG/ENaC channels, need tether proteins that deliver mechanical stimulus to the channel. DEG/ENaC channels assemble in large complexes with other proteins. In the panel, is sketched the complex formed by the *C. elegans* MEC proteins (adapted from [121]). MEC-4 and MEC-10 are the pore forming subunits that assemble in trimers and aggregate with other proteins (MEC-1,2,5,6,7,9,12) [122, 123, 124, 125, 126]. MEC-2 links the channel conformational changes to the α-tubulin filaments (MEC-7 and MEC-12) of the intracellular matrix [127]. Also, the complex is directly connected to the cuticle through the extracellular matrix components (MEC-1, MEC-9 and MEC-5) [125, 126].

At this point, membrane potential shoots up (depolarization) due to the collective activation of voltage-gated sodium channels, until it reaches the sodium reversal potential (sees Chapter 2). Then a concerted inactivation of Na^+ channels and activation of potassium channels allow the decrease of the potential (repolarization) to values below the

resting state (hyperpolarization) in correspondence of which potassium channels close. The resting value of the potential is then restored by potassium ions diffusion inside the cells. The period in which the membrane potential is under the resting level is usually called "refractory period". Action potentials are all-or-none events that start only if the activation threshold is reached and show the same shape independently from the stimulus intensity and duration, that are instead encoded by the specific firing patterns [117].
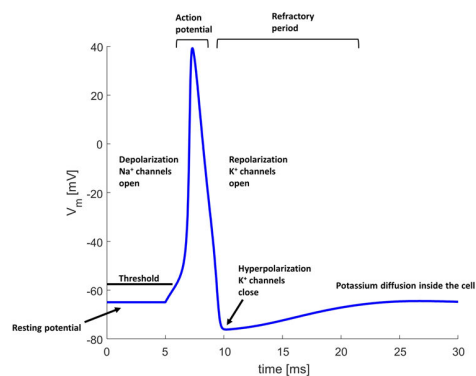
Figure 1.7: **Action potential in mammalian neurons**

C. elegans neurons do not express the traditional Na^+ channels so important for APs generation in vertebrate neurons [128]. However, they are able to fire action potentials exploiting voltage-gated calcium channels instead of sodium ones [21]. It has to be noted that not all *C. elegans* neurons fire action potentials. The nematode neurons have been shown to display different kinds of electrical activity mediated by voltage-gated potassium and calcium channels, including action (AWA), plateau, potentials (ASER, AIA, AFD), and bistable behaviours [18, 20, 21]. Fig. 1.8 reports the current clamp recordings performed on different classes of *C. elegans* neurons. Notably, the striking differences on single neuron dynamics can be observed in sensory neurons (ASER, AWA, and AFD), suggesting that their responses are differentiated non only by the expression of specific sensory receptors but also in the intrinsic electrical properties. Also, interneurons display different behaviour related to their role in information processing. AIA neurons show threshold responses triggered by depolarizing stimuli sent by AWA neurons through gap junction connections [25], while AIY and RIM interneurons seem to activate more with hyperpolarizing than with depolarizing stimuli [21]. In this work, RMD, AIY, and RIM will be modelled (see Chapter 6), taking into account the specific ion channels that generate the observed responses. A detailed analysis will be performed to dissect the role of different ionic currents in the overall dynamics with particular attention to peculiar bistable behaviour displayed by RMD.
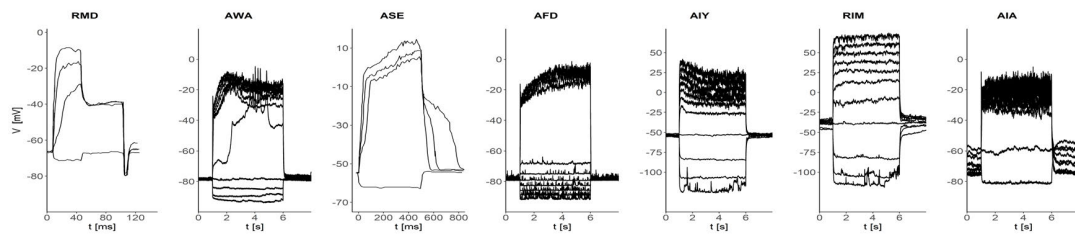
Figure 1.8: **Electrical responses of *C. elegans* neurons**. Despite the lack of voltage-gated sodium channels, the nematode neurons display a rich variety of behaviours, including bistable plateaus (RMD), action potential firing (AWA), active threshold responses (AFD, ASER, and AIA). RIM and AIY neurons rely more on potassium channels, as will be shown in Chapter 6, and are classified as outward rectifier and transient outward recifier based on their electrophysiological properties [21]. Experimental data points are obtained from the following sources: RMD from [20], AWA, AIY, RIM, and AFD from the [21], AIA from [25], and ASER from [18].

1.4.3 Sensory processing: the example of AWC neurons

Sensory stimuli transduction is the result of a complex cascade of biochemical reactions initiated by the activation of sensory receptors. Living organisms have evolved with a wide variety of sensory receptors, among which an important class is constituted by the G protein-coupled-receptors (GPCRs). AWC-mediated chemosensation relies on a combination of more than twenty GPCRs expressed in the cilia of the neurons [83]. This set of receptors enables the neurons to detect a wide variety of attractive volatile compounds, including butanone, isoamyl alcohol, 2,3-pentanedione and, benzaldehyde [71, 83]. Among the expressed GPCRs, there are *str-2*, *srx-3*, and six other receptors that determine the left-right asymmetry of the two neurons. Despite the different functions, both neurons rely on the same transduction pathway based on cGMP, that shares many similarities with mammalian phototransduction in cones and rods [83]. The neurons activate upon odour removal, originating the so-called ODOR-OFF responses. The activation of the receptor initiates a cascade of processes that finally result in an inhibition of the neuron (Fig. 1.9). The odorant binding to the GPCR causes the dissociation of the G-protein complex into G_α and $G_{\beta,\gamma}$ subunits. The *C. elegans* genome possesses 20 genes encoding for α subunits, 2 for β subunits, and 2 for γ subunits, in addition to fourteen G_i-like *gpa* genes [83]. ODR-3 is one of the most important G_α subunits in chemosensory and nociceptive neurons [83]. ODR-3 mutants show impaired chemosensation and abnormal cilia morphology [133]. In AWC ODR-3 regulates the activity of the receptors guanylate cyclase ODR-1 and DAF-11 [134]. ODR-1 and DAF-11 function in heterodimers to downstream the G-protein activity converting GTP into cGMP, similarly to guanylate cyclase in mammalian rods and cones [83]. The cGMP produced by guanylate cyclase regulated the activity of cyclic-nucleotide-gated channels (CNG), encoded in the nematode by the *tax-2* and *tax-4* genes. *tax-2* and *tax-4* genes are expressed in many sensory neurons and localize in the cilia [83]. When heterologously expressed, they form heteromeric channels that display a high sensitivity to cGMP and cAMP [135]. Membrane potential depolarization promote the opening

Figure 1.9: **Biochemical reactions in the AWC olfactory process**. AWC neurons express more than twenty GPCRs and different G-proteins that can mediate the detection of different odorants. Receptor guanylate cyclase are encoded by *daf-11* and *odr-1* [129, 130]. cGMP-gated channels are encoded by the *tax-2* and *tax-4* genes [131, 132]. Hyperpolarization or depolarization induced by the closing or opening of CNG channels regulates the activity of voltage-gated calcium channels.

of VGCC that allow a further increase of intracellular calcium until their inactivation threshold is reached.

In summary, odorant binding to GPCRs leads to the dissociation of the G-protein complex. The G_α subunit ODR-3 inhibits the guanylate cyclase activity, thereby causing a decrease of cGMP in the cell. The reduction of cGMP leads to a closure of CNG channels and, in turn, of VGCC, with a consequent hyperpolarization of the cell. Conversely, when the odour is removed, the inhibition of the guanylate cyclase is released, and the opening of CGN channels and VGCCs activate. The combination of these two opposite processes gives rise to the characteristic ODOR-OFF response of the neuron.

1.5 Ionic channels in *C. elegans* neurons

In this work, voltage-gated potassium and calcium channels, as well as some ligand-gated channels will be modelled. The model of single ionic channels are discussed in detail in Chapter 4, while in the following, their physiological role in *C. elegans* is reviewed. The complete list of modelled channels is reported in Table 1.2. Most of the modelled channels belong to the class of potassium channels, which includes both voltage-gated (KV), voltage/ligand-gated, and ligand-gated ion channels. In addition to potassium channels, also voltage-gated calcium channels and passive sodium channels have been studied. All these channels have been selected because they are of capital importance

for the nematode nervous system functioning, being responsible for the generation of active neuronal responses in neurons and muscles [18, 21, 22, 23, 136, 137].

1.5.1 Potassium channels

Potassium channels represent one of the widest and heterogeneous families of ion channels. They are expressed both in excitable and non-excitable tissues and perform many different functions, such as immune response modulation, intestinal function control, neuronal excitability regulation, and resting potential control [162]. This number of functionalities is reflected by a high differentiation level of single-channel properties.
The *C.elegans* genome contains 72 genes encoding for potassium channels that are expressed in all cell types [128, 136, 162]. Based on the structural criterion of transmembrane (TM) domains number, *C.elegans* potassium channels can be divided into three classes: 2TM, 4TM and 6TM [162]. Channels of the 2TM and 6TM classes are highly conserved among different species, having orthologues in both human and *Drosophila*, while 4TM channels are encoded by rapidly evolving genes unique to *C.elegans* [136]. The 2TM class includes channels with the same subunit structure as vertebrate inward rectifier channels [162] encoded by the three genes *nIRK1-3*. The 4TM channels, usually known as TWK-channels, constitute the widest family, as 46 out of 72 genes encode for such channel typology. However, their specific expression and role in the nematode neurons are still largely unexplored. The 6TM class contains six conserved gene families: voltage-gated, *Kcqt*, *Eag*, big conductance (*Slo* or *Bk*), cyclic-nucleotide-gated (CNG), and small conductance (*Sk*). The majority of the 6TM class channels are voltage-gated channels regulating neurons and muscles electrical activity, determining the membrane resting potential [23], shaping the action potentials, and regulating the firing rate in muscles [137, 163]. In this work, all the potassium channels of the 6TM class (except CNG, *Shab*) are modelled. In addition to 6TM channels models, the model for IRK channels of the 2TM family is developed. 4TM channels are excluded from the modelling due to their secondary role in the neuronal electrical activity and with a consequent lack of experimental data. The models of potassium channels are described in Chapter 4. In the following, their biological functions are reviewed, with particular attention to their role in the nematode neuronal dynamics.

2TM channels

Concerning the 2T class of ion channels, only the IRK channels have been selected for modelling in this work.

IRK-1/3. Inward rectifier channels (IRK or Kir) are a class of voltage-gated K^+ channels that show anomalous rectifier properties [164]. Indeed, in contrast to the majority of potassium channels, they preferentially conduct an inward instead of an outward current [164, 165]. IRK channels are expressed in different cells and organs, including heart, blood vessels, and skeletal muscles [164]. In the brain, they are widely expressed in somata and dendrites of different classes of neurons, and also in glial cells [166] Due to their peculiar characteristics, they play a critical role in the regulation of resting

Table 1.2: **List of modelled ion channels.** The table reports the list of modelled ion channels (second column), grouped based on their ion selectivity (first column). The channels are also classified based on the vertebrate (third column) and *C. elegans* (fourth column) gene family. The fifth column reports the reference to experimental data used for modelling and the organism on which the recordings have been performed. The symbols indicate the specific recording conditions, i.e., • on dissected worm cultured myocytes [138], body wall muscles [139] or pharynx [140], ∗ , ∘ and ◇ respectively on *Xenopus* oocytes, HEK cells, and CHO cells expressing the desired genes. In the following and throughout the work, the genes encoding for the modelled channels and the corresponding channel proteins are reported in italic and capital letters, respectively (e.g., *egl-19* genes encode for EGL-19 channels). Further, the current associated with a specific class of channels is indicated with the channel protein name, omitting the dash between the gene family name and the number (e.g., EGL19 are the currents carried by EGL-19 channels). When two or more genes encode for a channel type, the corresponding currents are named with the gene family name in capital letters (e.g., *kcnl-1/4*, KCNL).

Ion	Channel type	Vertebrate gene family	C. elegans gene	Experimental data
K⁺	Kv1,*shaker*	*kcna*	*shk-1*	[138]: *C.elegans*• [141]: *Human*∗
	Kv2		*exp-2*	[142]: *C.elegans*◇
	Kv3,*shaw*	*kcnc*	*egl-36*	[143]: *C.elegans*∗
	Kv4,*shal*	*kcnd*	*shl-1*	[138]: *C.elegans*•
	Kvs-1		*kvs-1*	[144]: *C.elegans*◇
	Kv7	*kcnq*	*kqt-3*	[145]: *C.elegans*∗
	Kv10, *eag* Kv11, *erg*	*kcnh* *kcnh*	*egl-2* *unc-103*	[146]: *C.elegans*∗ [147]: *Human*∘ [148]: *Drosophila*∗
	Kir	*kcnj*	*irk1-3*	[149]: *C.elegans*∗ [150]: *Rat* [151]: *Aplysia californica*
	KCa1.1, BK	*slo1*	*slo-1*	[152]: *C.elegans*∗
	BK	*slo2, slack*	*slo-2*	[153]: *C.elegans*∗
	KCa2, SK	*kcnn*	*kcnl-1/4*	[154] *No published patch clamp data*
Ca²⁺	CaV1, L-type	*cacna*	*egl-19*	[139, 140]: *C.elegans*•
	CaV2, P/Q-type	*canca*	*unc-2*	[155]: *Rat*∘ [156]: *Rat* [157]: *Mammalian*∘
	CaV3, T-type	*canca*	*cca-1*	[158]: *Drosophila*∗
Na⁺	NALCN	*nalcn*	*nca-1/2*	[159, 160, 161] *No published patch clamp data*
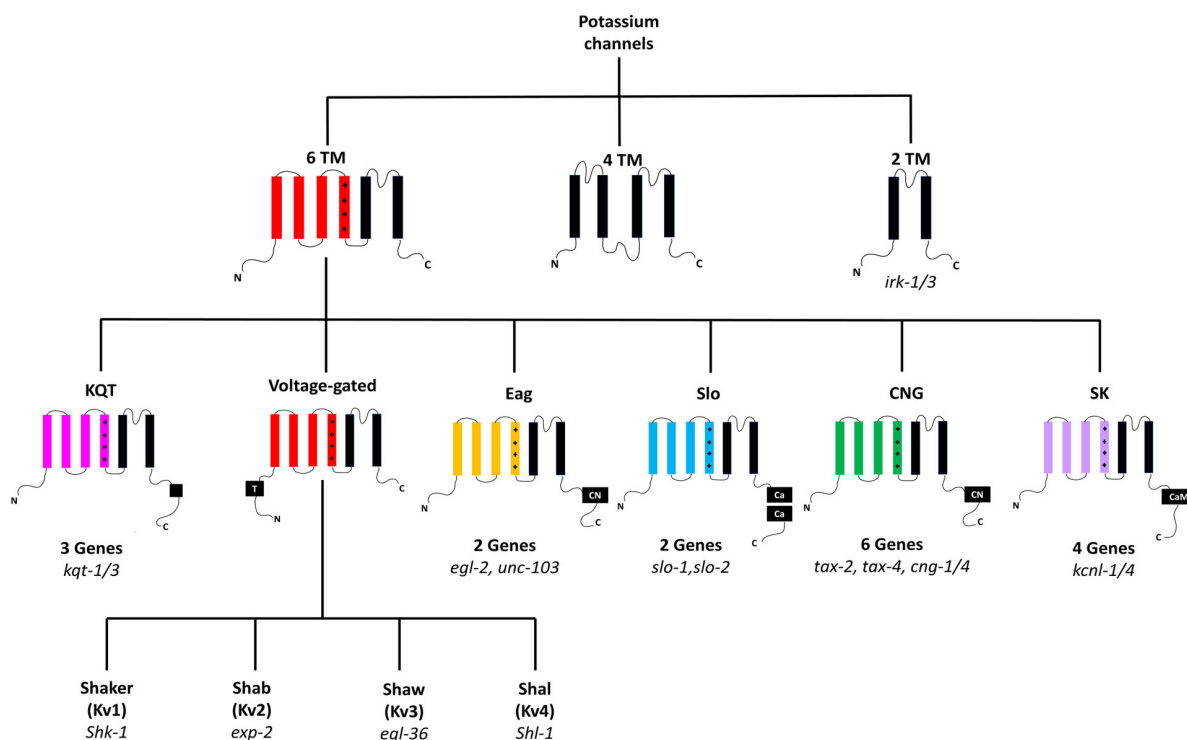
Figure 1.10: **Classification of potassium channels**. Three families are defined according to the structural criterion of transmembrane domains: 2TM, 4TM, and 6TM. The 6TM family contains the voltage-gated channels involved in the generation of active neuronal responses in the nematode. (Adapted from [162])

potential and action potential duration in excitable cells [164]. In *C. elegans*, irk channels are encoded by the genes *irk-1/3*. IRK-1 mediate the inhibition of serotoninergic hermaphrodite-specific neuron (HSN neurons), being regulated by the G_o coupled receptor EGL-6 [149]. IRK-2 and IRK-3 channels are expressed in head neurons, however their specific function in the nematode nervous system is still poorly unexplored [128].

6TM channels

The list of modelled 6TM potassium channels includes SHK-1, EXP-2, SHL-1, KVS-1, UNC-103, KQT-1, KQT-3, EGL-2 EGL-36, SLO-1, SLO-2, and KCNL-1/4.

SHK-1 (KV1) channels.

The *shk-1* gene encodes for Kv1.1 (*Shaker*) potassium channels in *C.elegans*, and it is expressed in body wall, vulval and diagonal muscles and in motor, inter, and some sensory neurons [21, 23, 137, 138]. In mammals, *Shaker* channels (Kv1.1-1.8) are expressed in a large variety of cell types. Kv1 channels have been shown to regulate the excitability of sensory neurons in rats [167], and deletions or mutations of the subtype Kv1.1

were associated with ataxia and epilepsy in mice and humans [168, 169]. Moreover, in humans Kv1.1 currents have been suggested to be involved in atrial depolarization, and alterations in Kv1.1 expression are supposed to contribute to atrial fibrillation susceptibility [170]. In *C. elegans*, patch-clamp experiments on body wall muscles, performed in combination with genetic deletion, showed that the role of Kv1.1 in repolarization is conserved [163]. *shk-1* knockout worms show increased spike amplitude, duration, and decay [137]. Similar effects have also been observed in the AWA neurons of *shk-1* mutants [21].

EXP-2 (KV2) channels. EXP-2 channels are a class of voltage-gated potassium channels with electrophysiological properties similar to human *ether-a-go-go* (hERG) channels. Despite the shared inward-rectifier properties, EXP-2 and hERG channels are structurally dissimilar [142]. *Exp-2* is strongly expressed in pharyngeal, intestinal, and less in egg-laying muscles [142]. Also, *exp-2* is found in sensory neurons of the amphid, indicating their possible contribution in tuning sensory neurons excitability [142]. When heterologously expressed in *Xenopus oocytes*, EXP-2 channels give rise to inward rectifier currents promoted by ultrafast inactivation [171]. In muscles, EXP-2 channels regulate the shape and duration of the action potentials [142, 172]. *exp-2* loss-of-function mutants show broadened pharyngeal action potentials (APs) and decreased pharyngeal pumping rate [142, 171]. In contrast, gain-of-function mutations shorten the APs and increase the pumping rate [171]. Similarly to other Kv channels, EXP-2 assembles with additional subunits, like the MPS-4 subunits, the homologue of mammalian KCNE proteins. MPS-4 deletion slows down both the upstroke and repolarization phase of the action potential, indicating that its co-expression with EXP-2 is essential for the normal pharyngeal function [172].

EGL-36 (KV3) channels. Kv3 currents have been shown to contribute to excitability, firing frequency, and neurotransmitter release in mammalian neurons. The Kv3.1, Kv3.2, Kv3.3, Kv3.4 subclasses of Kv3 potassium channels, expressed in mammals, are characterized by different activation and inactivation properties [173, 174]. In *C.elegans*, *egl-36* gene encodes for Kv3 channels, which are expressed in body wall, vulval and diagonal muscles, and in sensory motor, and interneurons. *Shaw* currents were proven to have a role in egg-laying and defecation by investigation of deficient mutants [143, 175].

SHL-1 (KV4) channels. *Shal* (Kv4) channels are among the most structurally and functionally conserved channel types between different animal species. Kv4 channels play a key role in regulating the cellular excitability by contributing to the repolarization phase of the action potential and regulating the interspike intervals through the generation of fast transient outward currents, usually known as A-type currents [176]. *C.elegans Shal* channels α-subunit is encoded by the *shl-1* gene. The analysis of the tissue expression pattern showed that SHL-1 channels are expressed in body wall muscle, vulval muscle, pharynx, male-specific diagonal muscles, intestine, and different classes of neurons [138]. The broad expression in different cell types suggests that these channels participate in the generation of different behaviors such as the response to aldicarb or mating efficiency in males [138].

KQT (KV7) channels. *Kcnq* genes in mammals encode different types of Kv7 potassium channels, driving slow voltage-activated currents. These currents are commonly known as M-type currents because of their modulation through muscarinic receptors [177]. KCNQ channels have been shown to regulate sustained firing, excitability, and spike suppression in neurons [178, 179] and uterine smooth muscle cells [180]. The Kv7.1 subtype, encoded by *kcnq-1* gene, has a significant role in shaping cardiac action potentials. Mutations in this gene are linked to long QT syndrome (similarly to *hErg*) and cardiac arrhythmias [181, 182].

In *C.elegans*, KCNQ-like channels are encoded by three genes: *kqt-1, kqt-2*, and *kqt-3* [145]. KQT channels are expressed in pharyngeal muscles, mechano- and chemosensory neurons, and intestinal cells [145, 183, 184], where they solve physiological functions similar to that of mammalian KCNQs [145]. In particular, KQT-1 currents in the pharyngeal muscle have a similar role of slowly activating delayed rectifier potassium channels (I_{Ks}) of the cardiac muscle [145]. KQT-2 channels control calcium influx into intestinal cells [184] and cold acclimation [183]. The *kqt-3* gene encodes for KCNQ-1 like currents found in mechano- and chemo-sensory neurons [145]. Furthermore, similarly to their mammalian counterparts, both KQT-1 and KQT-3 currents are suppressed by oxotremorine, an agonist of the M1 muscarinic receptor, whose effect is more pronounced on KQT-1 than on KQT-3 currents [145].

Eag-like channels. Ether-à-go-go (*Eag*) potassium channels are a family of voltage-gated channels found in brain, heart, and cancer cells [185]. They control the repolarization of cardiac action potentials [186], cancer cell proliferation [187], spiking frequency adaption, and the stabilization of the resting potential [185, 188]. Mutations in these channels have been linked to cardiac and neurological disorders such as the long QT [189], the Zimmermann-Laband [190] and, the Temple-Baraitser [191] syndromes. Mammalian *eag* channels are divided into three subfamilies: *Eag*, *Elk*, and *Erg* [192]. *C. elegans* possesses orthologues only of *Erg* and *Eag* channels, encoded by the genes *unc-103* and *egl-2* respectively [162].

Unlike *Erg* channels, which show inactivation and inwardly rectifying properties, *Eag* channels (Kv10) are non-inactivating and outwardly rectifying [185]. Eag channels are expressed in many brain regions, including the olfactory bulb, cerebral cortex, and hyppocampus [185]. In rats, they modulate Ca^{2+} influx and neurotransmitter release at presynaptic terminals [193]. Also, there are evidences that *Eag* channels are implicated in odorant signal transduction in *Drosophila* [194]. In *C. elegans*, eag channels are encoded by the *egl-2* gene [146]. EGL-2 potassium channels are widely expressed in muscles and neurons, where they are involved in muscles contraction and sensory neurons chemotaxis, as shown by studies on defective mutants [146].

Mammalian *Erg* channels (Kv11) stabilize the resting potential and regulate the excitability by generating a small and persistent current near the resting potential [185]. They also contribute to frequency adaption in vestibular [195] and auditory neurons [196], and Purkinje cells [188]. Furthermore, Erg currents are inhibited by TRH and mGlu receptors that usually couple with G proteins of the $G_{q/11}$ family [197]. In *C.elegans* *Erg*-like channels are encoded by the *unc-103* gene [162]. UNC-103 channels are ex-

pressed in sensory, inter, and motor neurons in the head and the tail region [198]. In particular, they are essential for regulating the contraction of sex muscle in the male during mating [198]. Null and loss-of-function mutants show abnormal spontaneous spicule protractions in absence of sexual stimulus, suggesting that UNC-103 retain spicule muscles from contracting [198]. Furthermore, it has been suggested that UNC-103 regulate enteric muscles activity being activated by the *unc-43* Calcium/Calmodulin-dependent serine/threonine Kinase type II (CaMKII) [199].

KVS-1 channels. KVS-1 channels are a class of ion channels unique to *C. elegans*. *kvs-1* sequence shows similarity with both *Shab* and *Shal*, and it was suggested to be a mosaic of these two families [200]. KVS-1 originate rapidly activating and inactivating in muscles and neurons, where they are widely expressed [144, 200, 201]. Furthermore, they have been found to form complexes with Mink related proteins homologues and inactivation of such complexes impairs chemotaxis, mechanosensing and locomotion [200, 201].

Calcium regulated potassium channels. Among 6TM potassium channels, a special class is the family of calcium-regulated potassium channels, whose kinetic properties are dependent on the intracellular calcium concentration. These channels are widely expressed in the nervous system where they play a key role in regulating neuronal activity by providing a connection between the processes that cause intracellular calcium concentration changes and those that are strictly related to membrane excitability. They can be divided into three classes according to the value of single channel conductance: big ($\sim$ 100 pS), intermediate($\sim$ 50 pS), and small conductance ($\sim$ 10 pS). Only BK and SK channels are discussed, in the present work, because the nematode does not express intermediate conductance channels.

SLO1 and SLO2 channels. Big conductance potassium channels (BK) are a class of voltage-gated channels that are additionally regulated by intracellular calcium concentration ($[Ca^{2+}]_i$). In mammals, BK channels are expressed mainly in axons and presynaptic terminals in the central nervous system. BK channels play a key role as regulators of neuronal excitability; indeed, they contribute to the repolarization and fast afterhyperpolarization phase of the action potential. Thanks to their sensitivity to calcium, they provide an important negative feedback for calcium entry, and they contribute to neurotransmitter release in some neurons [23, 152, 202, 203]. BK channels are almost closed at rest, and the calcium concentration required to activate them can be reached only in the proximity of a voltage-activated calcium channel [204]. Therefore, BK channels are usually strictly coupled with one or more voltage-gated calcium channels (VGCCs or CaVs) and localized within a nanodomain ($r \sim$ 10 nm) around the calcium channel. When the coupled VGCC activates, the rise of the intracellular calcium causes a shift towards more negative potentials of the BK channels activation curve, thereby permitting its activation in physiological conditions. *C.elegans* genome possesses two genes encoding for BK channels, *slo-1* and *slo-2*. The two channels show an overlapping expression pattern in muscles and neurons, where they colocalize with EGL-19 and UNC-2 VGGCs. SLO-2 channels are known to play an important role in the definition of resting membrane potential in muscles and motor neurons, and they con-

25

tribute together with *slo-1* channels to neurotransmitter release processes [23, 137, 152]. Furthermore, both SLO-1 and SLO-2 were found to participate in the AWC neurons asymmetric differentiation process by inhibiting the calcium signaling pathways that control the process [205]. Despite the overlapping expression and similar functions, they exhibit some differences in their kinetics of activation: SLO-2 shows a less strong voltage dependence and an additional regulation by intracellular chloride concentration, with respect to SLO-1 [23, 206]. **KCNL** SK channels are calcium-gated potassium channels characterized by small single-channel conductance (10 pS) [204]. Despite the structural similarity with Kv channels, SK channels are voltage-independent: their activation and inactivation are modulated by intracellular calcium transients induced by many different sources such as voltage-gated channels, L,T, and P/Q type, SERCA, NMDA, and acetylcholine receptors [204]. Furthermore, in contrast with BK channels that are strictly coupled with voltage-gated calcium channels, SK channel activation is affected by multiple calcium sources located inside a microdomain (of radius $\sim 100\mu$m) surrounding the SK channel [204]. SK channels are expressed in many regions of the nervous system, and, due to their fast calcium-induced activation, they exert a fast control on intrinsic excitability and synaptic transmission, as well as on long-term changes that affect learning and memory [154, 207]. In *C.elegans* genome, SK channels are encoded by *kcnl-1 to -4* genes that are expressed in many different classes of neurons. In particular, *kcnl-2* channels were found to show a high degree of structural similarity with the mammalian *kcnn* homologues and to take part in the egg-laying rate regulation [154].

To resume, comparing the two type of channels, some important difference exists between BK and SK channels: the former are modulated both by membrane voltage and intracellular calcium concentration, while the latter are voltage-independent and thus modulated solely by calcium [204]. However, BK and SK channels differ also in their sensitivity to intracellular calcium changes. SK channels are usually active at physiological calcium concentrations and very sensitive to small changes caused by a variety of sources such as VGCCs, $Na^+ - Ca^+$ exchangers, and Ca^{2+}-ATPases. While BK channels are usually activated at calcium concentrations so high that could be reached only in the proximity of voltage-gated calcium channels with which they usually colocalize in nanosized domains [204]. All these aspects are reflected in the details of the modelling presented in Chapter 2 and Chapter 4

1.5.2   Calcium channels

Ca^{2+} plays a crucial role in regulating a wide variety of signalling, control and sensory transduction processes in cells. Calcium signalling, *via* concentration changes, is particularly important in neurons, where it regulates cellular excitability and synaptic transmission [208, 209]. Cells regulate calcium levels through a complex interplay of molecules and channels, among which there are voltage-gated calcium channels. According to their peculiar properties, voltage-gated calcium channels can be classified as T-type, L-type, and RNPQ-type. Mammals genome possesses 10 genes encoding for the α_1 subunits of these channels: four genes (*CaV1.1-4*) for L-type, three (*CaV3.1-3*) for T-type and three for non-L-type channels (*CaV2.1* for P/Q-type, *CaV2.2* for N-type,

CaV2.3 for R-type) [209]. In contrast, *C.elegans* only has three genes encoding for L, T, and P/Q-type channels α_1 subunit: *egl-19*, *cca-1*, and *unc-2*, respectively [128]. Moreover, the activity of these channels is modulated by the $\alpha_2\delta$ subunits *unc-36* and *tag-180*, and by the β subunits, encoded by *ccb-1* and *ccb-2* [128]. *C.elegans* expresses NCALN channels homologues, encoded by *nca-1* and *nca-2* genes [128]. Voltage-gated calcium channels are essential for *C.elegans* neuronal activity because the nematode lacks the usual Na^+ channels that generate action potentials in vertebrates. L, T, and P/Q-type channels are found in both *C.elegans* neurons and muscles, where they play a key role in generating active neuronal responses, giving rise to calcium-driven action, graded, and plateau potentials [18, 20, 21, 22, 210].

EGL19. L-type channels represent a class of high voltage activated (HVA) calcium channels found in muscles and neurons (soma and dendrites). Vertebrate L-type channels are characterized by a high-voltage activation threshold with slow inactivation kinetics. Such characteristics confer to these channels the ability to generate persistent inward currents that have been associated with plateau potentials vertebrate motoneurons [211]. In *C. elegans*, *egl-19* is the only gene encoding for L-Type channels α_1 subunit. EGL-19 channels are found in the nematode neurons and muscles, where, similarly to their mammalian counterpart, they play a key role in the regulation of the width and decay time of plateau potentials and calcium-driven action potentials [20, 21, 137]. It has been shown that *C.elegans* EGL-19 channels show biophysical characteristics very similar to their vertebrate homologues, but with faster activation and inactivation kinetics [139]. Furthermore, as expected for L-type of currents, *C.elegans egl-19* currents are blocked by Cd^+, and sensitive to dihydropyridines (DHPs) [137, 139]. Normally *egl-19* α_1 subunits are coupled with one of the two $\alpha_2\delta$ subunits *unc-36* and *tag180*, that influence channel kinetic properties by shifting the activation curve to more hyperpolarized potentials and decreasing activation time constants [212].

UNC2 channels. P/Q-type channels are a class of voltage-gated calcium channels expressed in the mammalian central and peripheral nervous system. In humans, P/Q-type channels are encoded by the *cacna1a* gene, and they localize at the synaptic sites, where they play an important role in neurotransmitter release regulation. Mutations in the gene *cacna1a* have been connected with different pathologies such as familial hemiplegic migraine, episodic ataxia type2, and spinocerebellar ataxia type6 [213]. In *C. elegans*, the *unc-2* gene encodes for the unique P/Q-type α_1 subunit. UNC-2 channels localize at presynaptic active zones in motor and sensory neurons [155]. The synaptic localization of UNC-2 channels is mediated by the protein *calf-1* and the $\alpha_2\delta$ subunit *unc-36* [214], that also affect the channel properties accelerating activation and inactivation kinetics and shifting the activation curve towards more hyperpolarized potentials [215]. UNC-2 channels are involved in many physiological and behavioural processes. Indeed *unc-2* mutants exhibit defective locomotions and egg-laying, decreased number of spikes-per-train in body wall muscles and impaired neurotransmitter release [137, 155]. Furthermore these channels, together with EGL-19, are reported to be key regulators of the asymmetric AWC neurons differentiation [205, 216].

CCA1 channels. T-type are among the most ancient and conserved calcium chan-

nels [217, 218]. In vertebrates, T-type channels are not only involved in the regulation of neuronal and muscular excitability, but also in cell development and proliferation [217]. T-type channels exhibit fast activation and inactivation kinetics with a strong voltage dependence. They activate at more hyperpolarized potentials than P/Q and L-type channels, playing a key role in modulating shape and frequency of action potentials in neurons and muscles [137, 217]. Another relevant property of Cav3 channels consists in the overlap of the activation and inactivation curves, which give rise to a small, but continuous, calcium influx through few open channels near the rest. This calcium influx is known as "window current" and it has been shown to play an important role in regulating intracellular calcium near rest, and, thereby, in controlling cell growth and proliferation [217, 218], as well as in the determination of firing modes in neurons [217, 219, 220]. In mammals genome, there are three α_1 subunits for T-type calcium channels [209]. In contrast with mammals, in the *C.elegans* genome there is only one gene, *cca-1*, encoding for α_1 subunit of T-type calcium channels [128] CCA-1 channels are expressed both in muscles and neurons, where they regulate cellular excitability and the shape of action potentials [140, 221]. In *C.elegans* pharynx, CCA-1 channels are localized at the neuromuscular junctions where they activate thanks to the small calcium influx through the *eat-2* non-alpha nicotinic receptor, stimulated in turn, by the MC motor neuron [221]. Their activation promotes muscular contractions and initiation of pharyngeal action potentials by boosting the membrane potential to the EGL-19 activation threshold [221]. In *cca-1* mutants, body wall muscles action potentials show increased width, lower amplitude, and higher frequency than wild-type worms [137]. T-type channels are also reported to be important regulators of serotonin neurons responsible of female reproductive behavior [222].

1.5.3 NCA sodium leak channels

C.elegans genome does not posses any gene encoding for voltage-gated sodium channels. However, two genes were found to encode for sodium leak channels: *nca-1* and *nca-2*. These channels are the homologues of the mammalian *ncaln* channels. Mammalian *ncaln* are expressed in heart, adrenal gland, thyroid gland, lymph nodes, and in the central nervous system, where they act as regulators of resting membrane potential and excitability, influencing the sodium permeability of the membrane. Usually, *ncaln* channels are found in complexes with GPCRs and the proteins *unc-80* and *unc-79*, that regulate the channel activity and localization [161, 223, 224, 225]. The *C.elegans* homologues *nca-1* and *nca-2* are expressed in synaptic regions, where they form, as the mammalian counterpart, complexes with *unc-80* and GPCRs [161, 223]. This coupling confers to *nca* channels an important role in regulating synaptic transmission and neuronal resting potential [226]. *nca* mutants worms exhibit defective locomotion with loss of forward and backward movements [159], a hypersensitivity to volatile anesthetics (halothane) and a decreased sensitivity to ethanol [223].

1.6 State of the art in *C. elegans* nervous system modelling

As already said, the *C. elegans* nervous system constitutes an appealing model system for computational neuroscience. In the last years, many efforts have been dedicated to model the nematode neurons dynamics both at the single-cell and at the network state. In this section, the main computational approaches in modelling the nematode nervous system and the main results are reviewed.

Concerning the network models, many works (e.g. [26, 27, 28, 29, 30, 31, 32, 33, 34] are based on dynamic network simulations in which single neurons are modelled as passive isopotential compartments, whose voltage dynamics is regulated by a first order differential equation:

$$C_m \frac{dV(t)}{dt} = g_{LEAK} \cdot (V_{LEAK} - V) + \sum I_{SYN} + I_{EXT}, \qquad (1.1)$$

where C_m is the membrane capacitance, $V(t)$ is the membrane potential, g_{LEAK} is the leakage conductance, I_{syn} is the total synaptic current, and I_{EXT} is the external stimulus applied. The total synaptic current is given by the sum of the currents from chemical and electrical synapses. Electrical synapses are described in the simplest way as ohmic resistors, whose current depends on the presynaptic, V_{pre}, and postsynaptic, V_{post}, potential

$$I_{gap} = g_{gap} \cdot (V_{pre} - V_{post}). \qquad (1.2)$$

Chemical synapses are modelled in different ways, but in any case, they are exponentially dependent on the presynaptic potential as suggested by experimental works on the *Ascaris suum*, a nematode very similar to *C. elegans* [227].
The models based on this approach have a wide range of applicability and can be easily used to model different circuits [26, 27, 28, 29, 30, 31, 32], as well as the entire nervous system [33, 34]. However, their main limitation is that they do not account for the different electrophysiological properties of single neurons that display different behaviours, ranging from passive to spiking and plateau potentials (Fig. 1.8).

Other works have addressed the single-cell modelling, most of the times with a special focus on intracellular calcium dynamics [1, 35, 36]. These model are very effective in describing the physiological processes at the basis of sensory transduction, but as in case of the network models they treat the electrical dynamics of the neurons in a simplified way by considering only the steady-state value of the membrane potential [1], or assuming graded responses [36], or even disregarding its contribution [35].

In past decades many experimental works have uncovered the richness of *C. elegans* neuronal responses (e.g. [18, 19, 20, 21, 21, 22, 23, 24, 25]) that are not captured by the models described above. Another class of models, developed by Hodgkin and Huxley [228], has been widely and successfully used by neuroscientists to reproduce the

dynamics of single neurons, taking into account also their physiological origin (i.e., the ionic currents that shape the responses). The Hodgkin-Huxley models have been recently successfully applied to the *C. elegans* AWA neurons [21], demonstrating their potential for *C. elegans* nervous system modelling.

In this work, the Hodgkin-Huxley model is used to reproduce a set of 17 ionic currents involved in the nematode neurons dynamics, to be combined, based on gene expression profiles, to reproduce *in silico* the responses of *C. elegans* neurons. A detailed description of the theoretical basis of the Hodgkin-Huxley model is given in Chapter 2 (Section 2.1.2) while the models of the currents developed in this work are reported in Chapter 4.

Chapter 2

Theoretical and computational methods.

31

This chapter describes the computational and theoretical methods applied in this work. In the first section, the theoretical basis of the models are reviewed, including the Hodgkin-Huxley model, and different formulations of the intracellular calcium dynamics model are presented. The second section is dedicated to the computational tools and the optimization algorithms applied in model implementation and optimization and in the analysis of experimental data and simulation results. In the third section, the details of model implementation from the single currents up to the network scale are discussed.

2.1 Theoretical basis of neurons modelling

In this section the fundamental theoretical basis of the models used in this thesis work are reviewed. In particular, the electrical properties and their mathematical description through the Hodgkin-Huxley models is described with a particular attention to the *C. elegans* case. In the same way, the models of intracellular calcium, synaptic channels, and biophysical network models used in this work are described.

2.1.1 Electrical properties of the cell

Biological membranes are usually less than 10 nm thick. The phospholipid bilayer acts as a barrier for the movement of charged particles, causing charge accumulation on both sides of the membrane. The intracellular and extracellular media are ion rich conductive environments behaving as conductors. As a consequence, the membrane can be described as an insulator between two conductors, that is a capacitor. The membrane capacitance is proportional to the cell area so that a large surface accumulates more charge than a small one, and it is inversely proportional to membrane thickness [229]. The insulation provided by the membrane is not complete since ion channels and transporters allow ions to flow through the membrane. Each ion channel can be described as a conductor in series with a battery that represents the reversal potential for the specific ionic current. Since ion channels are not continuously open, but they open or close based on their gating mechanism, their associated conductance is not constant over time, but it changes according to the state of the channel. All channels are sensitive to the membrane potential difference existing between the two sides of the membrane and thereby are modelled as connected in parallel between them and in parallel with the membrane capacitance (Fig. 2.1).

Therefore, each cell derives its electrical properties mostly from the composition of the lipid bilayer and from the ion channels expressed on its surface. Different ions species populate the intracellular and the extracellular media. These ions accumulate on both sides of the membrane and generate an electrochemical gradient. The "membrane potential" is the electrical potential arising from different charge distributions on the two sides of the membrane.

The resting potential of a biological cell can be calculated by means of the Goldman-Hodgkin-Katz (GHK) equation for the membrane potential, in the approximation of constant electric field. In the following, the subscripts i and e indicate the intracellular
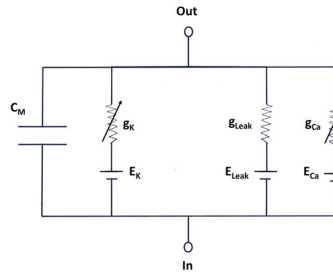
Figure 2.1: **Equivalent electrical circuit for *C. elegans* neurons**. The figure show the representation of a *C. elegans* neuronal cell. It includes the contribution of voltage-gated calcium and potassium channels as well as the leak current contribution.

and extracellular quantities, respectively. Each of the ionic species that contribute to cell electrical activity gives rise to flow of ions across the membrane. This flow from one side of the membrane to the other is driven by both concentration gradients and electric fields. Electric field-driven flows can be expressed with the Planck's equation:

$$J = -u\frac{|z|}{z}c\nabla\phi, \tag{2.1}$$

where u is the mobility of the ion, i.e. its velocity in a constant electric field, z is the valence of the ion, c is the concentration of the considered ionic species (ψ), and ϕ is the electrical potential (and thus $(-\nabla\phi)$ is the electric field). The relation between the mobility of the ion and the Fick's diffusion coefficient has been derived by Einstein:

$$D = \frac{uRT}{|z|F}, \tag{2.2}$$

where R is the gas constant, T is the absolute temperature, and F is the Faraday constant. Combining the flow driven by the electric with the diffusion-driven one, the Nernst Planck Electrodiffusion equation is obtained:

$$J = -D\left(\nabla C + \frac{zF}{RT}c\nabla\phi\right), \tag{2.3}$$

that in one dimension becomes:

$$J = -D\left(\frac{dc}{dx}C + \frac{zF}{RT}c\frac{d\phi}{dx}\right) \tag{2.4}$$

The Nernst equation that gives the equilibrium potential for the x-th ion species can be derived by solving Eq. 2.4 by imposing the zero flux condition, so that:

$$-D\left(\frac{dc}{dx} + \frac{zF}{RT}c\frac{d\phi}{dt}\right) = 0 \longrightarrow \frac{dc}{dx} + \frac{zF}{RT}c\frac{d\phi}{dt} = 0 \tag{2.5}$$

The solution Eq. 2.5 in a semipermeable membrane of thickness L is

$$ln(c)|_{c_e}^{c_i} = \frac{zF}{RT}(\phi_i - \phi_e),$$

(2.6)

that gives:

$$V = \phi_i - \phi_e = \frac{RT}{zF}ln\left(\frac{c_e}{c_i}\right).$$

(2.7)

Eq. 2.7 is the Nernst equation that gives the equilibrium potential of a single ionic species in a semipermeable membrane. However, in a biological cell, many different ion species accumulate in the intracellular and extracellular media, and their flow is regulated by their own current-voltage relation. Generally, there is no value of the potential for which these currents are all null. However, a value of the potential exists, for which the net ionic current in the cell is zero. This potential is called " resting potential", and depends on the intracellular and extracellular concentrations of all the different ion species found on both sides of the membrane. The relation between these concentrations and the resting potential of the cell is described by the Goldman-Hodgkin-Katz (GHK) equation for the voltage. The GHK equation could be derived by solving the Nernst-Plack electrodiffusion equation (Eq. 2.4) for a semipermeable membrane of thickness L, in the approximation of constant electric field. If the electric field is constant through the membrane, then $\partial\phi/\partial x = -V/L$. Also, in stationary conditions and with no production of ions, the flux is constant, so that the Nernst Planck equation becomes an ordinary differential equation

$$\frac{dc}{dx} - \frac{zFV}{RTL}c + \frac{J}{D} = 0.$$

(2.8)

Using as boundary condition $c(0) = c_i$, the solution of the equation is:

$$c(x)e^{\frac{-zVFx}{RTL}} = \frac{JRTL}{DzVF}\left[e^{\frac{zVFx}{RTL}} - 1\right] + c_i$$

(2.9)

The other boundary condition $c(L) = c - e$ is satisfied when:

$$J = \frac{D}{L}\frac{zFV}{RT}\frac{c_i - c_e e^{\frac{-zFV}{RT}}}{1 - e^{\frac{-zFV}{RT}}}$$

(2.10)

J represents a flux density that is usually expressed in moles per area per unit of time. This flux density can be converted into a current density by multiplying J for zF, so that the classical Goldman-Hodgkin-Katz equation for the current can be obtained.

$$I_x = \frac{D}{L}\frac{z^2F^2}{RT}V\frac{c_i - c_e e^{\frac{-zFV}{RT}}}{1 - e^{\frac{-zFV}{RT}}}$$

(2.11)

Eq. 2.11 represents the ionic current associate with a flow of a specific ion species. The ratio between the diffusion coefficient and the membrane thickness is usually referred as "permeability" of the membrane, and indicated as P_x. The GHK current equation 2.11 can be easily generalized to include the contribution of the other ions that accumulate

on both sides of the membrane, so that the net ionic current for a collection of ions with valence z is:

$$I_{ion} = \sum_x P_x \frac{c_i^x - c_e^x e^{\frac{-zFV}{RT}}}{1 - e^{\frac{-zFV}{RT}}}. \tag{2.12}$$

Imposing now the zero current condition and solving with respect to the voltage, the following expression for the membrane equilibrium potential can be obtained:

$$V = \frac{-RT}{F} ln \left[\frac{\sum_{z=1,x} P_x c_i^x + \sum_{z=-1,x} P_x c_e^x}{\sum_{z=-1,x} P_x c_i^x + \sum_{z=1,x} P_x c_e^x} \right] \tag{2.13}$$

Eq. 2.13 gives the equilibrium potential for a membrane semipermeable to both cations and anions.

2.1.2 Hodgkin-Huxley model: application to *C.elegans* single ionic currents

In the following, the theoretical basis of the Hodgkin-Huxley model [228] are reviewed, and its generalization to *C. elegans* case is discussed.

Standard ion currents Hodgkin-Huxley model

The biophysical models here presented are based on a Hodgkin-Huxley-type description of ionic currents and membrane voltage dynamics. The Hodgkin-Huxley model is a widely applied formalism that allows a quantitative description of the electrical dynamics in both excitable and non-excitable cells. The model was developed in 1952 by the physiologists Alan Lloyd Hodgkin and Andrew Huxley to describe the action potential generation in giant squid axon [228]. Its great potential resides in the fact that, although specifically developed for squid, it can be easily generalized to nearly all classes of ion channels, whose electrophysiological properties have been experimentally characterized. The basic idea behind the Hodgkin-Huxley model is that the physiological properties of neurons can be quantitatively reproduced by solving the equations that govern the dynamics of the equivalent electrical circuit (Fig. 2.1).

$$C\frac{dV(t)}{dt} = -(I_{ext}(t) + I_{ion}(V,t)) \tag{2.14}$$

where I_{ext} is the externally applied current to the neurons and represents the analogous of the stimulus applied to the neuron during patch-clamp experiments performed in the current-clamp mode (see Chapter 3, Section 3.2). In Eq. 2.14, I_{ion} contains all the significant ionic currents included in the model of the considered neurons. For each modelled neuron the set of ionic currents to be included in the model is here chosen according to the gene expression profiles extracted from the Wormbase[1] [5] and CeNGEN[2] [37] databases

---

[1]`https://wormbase.org`
[2]`https://cengen.shinyapps.io/SCeNGEA`

and literature reporting expression patterns of the specific genes (see Table 1.2). In particular, among all the voltage-gated, ligand-gated, voltage/ligand-gated potassium and calcium channels, as well as other specific and aspecific leakage channels, expressed channels in *C. elegans*, 17 channels have here been selected for modelling based on their importance for *C. elegans* neuronal activity.

The majority of currents included in the model (voltage-gated potassium and calcium channels) can be described within the standard mathematical formulation of the Hodgkin Huxley model, in which the channel gating by voltage is described through a time dependent conductance $G_x(V, t)$ (Eq. 2.15). The ionic current generated by a specific class of ion channels is therefore given by Eq. 2.15.

$$
\begin{aligned}
I_x(t, V) &= G_x(t, V)(V - V_x) = \bar{g}_x m_x^p(t, V) h_x^q(t, V)(V - V_x) \qquad (2.15) \\
\bar{g}_x &= N_x \gamma_x \qquad (2.16)
\end{aligned}
$$

where x denotes an arbitrary ionic species, V_x represents the reversal potential for the current carried by the ion x. The conductance $G_x(t)$ can be written as a function of the maximal conductance $\bar{g}_x$ (Eq. 2.16), given by single-channel conductance γ_x multiplied by the total number, N_x, of channels expressed in the cell, and of two variables m and h that represent the voltage-dependence of the gating. m and h are called activation and inactivation variables, respectively, and account for the gating mediated by two processes with opposite voltage-dependence. The probability of a channel to be open or closed is given m^p or h^q respectively, with p and q integers representing the number of subunits to be activated or inactivated. Activation and inactivation variables dynamics follows the first-order equations:

$$
\frac{dm_x(t, V)}{dt} = \frac{m_{x,\infty}(V) - m_x}{\tau_{m_x}(V)} \qquad (2.17)
$$

$$
\frac{dh_x(t, V)}{dt} = \frac{h_{x,\infty}(V) - h_x}{\tau_{h_x}(V)} \qquad (2.18)
$$

where $m_{x,\infty}(V)$ $(h_{x,\infty}(V))$ denotes the steady-state activation (inactivation) function, and $\tau_{m_x}(V)$ $(\tau_{h_x}(V))$ represents the activation (inactivation) voltage-dependent time constant. The voltage-dependence of gating variables and time constants are modelled with the following Boltzmann-like functions:

$$
m_{x,\infty}(V) = \frac{1}{1 - e^{\frac{-(V - V_{0.5}^a)}{k_a}}} \qquad (2.19)
$$

$$
h_{x,\infty}(V) = \frac{1}{1 + e^{\frac{(V - V_{0.5}^i)}{k_i}}} \qquad (2.20)
$$

$$
\tau_{m_x}(V) = \tau_{h_x}(V) = \frac{a}{1 + e^{\frac{(V - b)}{c}}} + d \,. \qquad (2.21)
$$

In Eqs. 4.1-2.20, $V_{0.5}^{a,i}$ represents the membrane voltage at which half of the channels are activated $(V_{0.5}^a)$ or inactivated $(V_{0.5}^i)$, $k_{a,i}$ is the slope factor that regulates the rapidity

with which the fraction of activated/inactivated channels changes. In Eq. 2.21 a, b, c, and d are numerical parameters that regulated the dependence of activation/inactivation time constants from the membrane voltage. All the above mentioned parameters can be derived by fitting experimental data for the specific current.

Eqs. 2.15-2.21 represent the standard formulation for single-current modelling. The different channels species differ in the peculiar values of half activation, inactivation, and time constants. The currents modelled within this formalism can be classified as inactivating or non-inactivating. Inactivating currents display both activation and inactivation and give rise to transient currents characterized by an initial peak followed by a decrease to a plateau level. Non-inactivating channels give rise to sustained currents that extinguish only with the intervention of other mechanisms that change the membrane potential, e.g., the opening and closing of other channels. The specific activation and inactivation characteristics of the single currents modelled in this work are discussed in detail for each channel species in Chapter 3. The study of currents regulated by both ligands and voltage requires more refined models and more complex fitting functions than the standard model above discussed. In the following, the model of calcium/voltage-regulated channels is described.

Calcium-regulated potassium channels

Calcium-regulated potassium channels represent a class of ion channels, whose electrophysiological properties are modulated in different ways by intracellular calcium levels. In the following paragraphs, the models of small and big conductance potassium channels are discussed. Two modelling strategies have been developed to adequately describe their different regulation by intracellular calcium.

SK channels modeling   SK channels are uniquely regulated by the intracellular calcium concentration in a micrometric domain around the channel itself [207]. Their modulation by calcium can be formalized in a Hodgkin-Huxley like formulation by writing the activation variable as a Hill function of the intracellular calcium concentration.

$$m_{\mathrm{KCNL},\infty}(Ca) = \frac{\mathrm{Ca}}{K_{\mathrm{Ca}} + \mathrm{Ca}}, \qquad (2.22)$$

where K_{Ca} is the dissociation constant, that in present work is equal to $0.33\,\mu\mathrm{M}$ [230, 231], and the Hill coefficient is assumed equal to 1 according to [232].

Thus the KCNL current can be written in Hodgkin-Huxley form as in Eq. 4.28

$$I_{\mathrm{KCNL}}(t, Ca) = \bar{g}_{\mathrm{KCNL}} \cdot m_{\mathrm{KCNL}}(t, Ca) \cdot (V - V_K). \qquad (2.23)$$

BK channels modelling

Similar to mammalian BK channels, the *C. elegans* SLO-1 and SLO-2 channels are co-regulated both by voltage and intracellular calcium concentration. Also, SLO-2 channels exhibit an additional modulation by intracellular chloride [23, 206]. Due to the lack

of experimental data to fully characterize such chloride dependence, the model here presented only accounts for their calcium and voltage regulation. In any case, BK channels require a more complex modelling than SK. The nematode BK channels are here described according to the Montefusco et. al [233] model applied to the experimental data available for $C.elegans$ [152, 153]. For the sake of clarity, in the following, the main equations of the model are reported and discussed.

The BK channel open probability with its double dependence from voltage and calcium is governed by Eq. 2.24.

$$\frac{dm_{\mathrm{BKs}}(t, V, \mathrm{Ca})}{dt} = \frac{m_{\mathrm{BKs},\infty}(V, \mathrm{Ca}) - m_{\mathrm{BKs}}}{\tau_{m_{\mathrm{BKs}}}(V, \mathrm{Ca})}, \tag{2.24}$$

where $m_{\mathrm{BKs},\infty}$, $\tau_{m_{\mathrm{BKs}}}$ are the steady-state activation variable and the relative time constant. $m^{\infty}_{sc,BK}$ obeys a standard Boltzmann function (Eq. 2.25), in which the half activation voltage and the slope are functions of the eight parameters w_0^+, w_0^-, w_{yx}, w_{xy}, n_{yx}, n_{xy}, K_{yx}, an (d K_{xy} and of the intracellular calcium concentration, as stated by Eqs. 2.25-2.28. The activation time constant ($\tau_{m_{\mathrm{BKs}}}$) can be expressed as a function of the same eight parameters according to Eq. 2.28

$$m^{\infty}_{sc,BK,j} = \frac{1}{1+e^{-\frac{V-V_a^{0.5}}{k_a}}} \tag{2.25}$$

$$V_a^{0.5} = k_a \cdot \left[log\left(\frac{w_0^-}{w_0^+}\right) + log\left(1+\left(\frac{K_{xy}}{\mathrm{Ca}}\right)^{n_{xy}}\right) - log\left(1+\left(\frac{\mathrm{Ca}}{K_{yx}}\right)^{n_{yx}}\right) \right] \tag{2.26}$$

$$k_a = \frac{1}{w_{yx}-w_{xy}} \tag{2.27}$$

$$\tau_{m,sc,BK} = \frac{e^{w_{xy}V}}{w_0^+}\left(1+\left(\frac{K_{xy}}{\mathrm{Ca}}\right)^{n_{xy}}\right)\frac{1}{1+e^{-\frac{V-V_a^{0.5}}{k_a}}} \tag{2.28}$$

The eight parameters regulating the voltage and calcium dependence of BK channels can be defined starting from the single BK channel dynamics. The open probability of a BK channel, p_y, follows a first order differential equation:

$$\frac{dp_y(t)}{dt} = -k^-(V, \mathrm{Ca})p_y + k^+(V, \mathrm{Ca})(1 - p_y) \tag{2.29}$$

where $k^-(V, \mathrm{Ca})$ and $k^+(V, \mathrm{Ca})$ are the voltage and calcium-dependent rate constants that regulate the transition of the channel in the open state (y). Their modulation by voltage and calcium has been modelled by Montefusco et al. [233], according to Eqs. 2.30-2.31, which assume that the calcium and voltage regulations are independent from each other.

$$k^- = w^-(V) \cdot f^-(\mathrm{Ca}) \tag{2.30}$$

$$k^+ = w^+(V) \cdot f^+(\mathrm{Ca}) \tag{2.31}$$

$w^+(V)$ and $w^-(V)$ describe the voltage regulation on the transitions between closed (x) and open state (y), and between open and closed state, respectively. $f^+(\mathrm{Ca})$ and

$f^-(\text{Ca})$ are the corresponding of $w^+(V)$ and $w^-(V)$ for the calcium modulation. These four rate constants could be modelled as functions of eight parameters that describe the exponential dependence on voltage of $w^+(V)$ and $w^-(V)$ (w_0^-, w_0^+, w_{xy}, and w_{yx}), and the sigmoidal dependence on calcium of $f^+(\text{Ca})$ and $f^-(\text{Ca})$ (n_{xy}, n_{yx}, K_{xy}, and K_{yx}).

$$
\begin{aligned}
w^-(V) &= w_0^- \cdot e^{-w_{yx}V} & (2.32)\\
w^+(V) &= w_0^+ \cdot e^{-w_{xy}V} & (2.33)\\
f^-(Ca) &= \frac{1}{1+\left(\frac{\text{Ca}}{K_{yx}}\right)^{n_{yx}}} & (2.34)\\
f^+(Ca) &= \frac{1}{1+\left(\frac{K_{xy}}{\text{Ca}}\right)^{n_{xy}}} & (2.35)
\end{aligned}
$$

The final expressions for the steady-state activation variable and time constants, i.e., Eqs. 2.25 and 2.28, can be derived from Eqs. 2.30-2.35 taking into account that:

$$
p_y = \frac{k^+}{k^+ + k^-} = \frac{1}{1 + exp\left[\frac{V - V_a^{0.5}}{k_a}\right]} \tag{2.36}
$$

$$
\tau_y = \tau_{m,sc,BK} = \frac{1}{k^+ + k^-} \tag{2.37}
$$

Since BK channels are strictly coupled with CaV1 and CaV2 channels, it is not surprising that their activation is dependent on the CaV channels state. In particular, when the CaV channel is closed, the opening probability for the corresponding BK channel is almost zero since the calcium concentration inside the CaV surrounding nanodomain is too low to induce a robust activation. The coupling between BK and CaV channel is modelled according to [233]. Eqs. 2.38-2.39 report the expressions for opening probability and activation time constants of the BK-CaV complex, in the case of 1:1 stoichiometry. It is in principle possible to include more than one calcium channel in the complex, however, in absence of enough data on BK-CaV channels clustering in *C. elegans*, the simple formulation of 1:1 stoichiometry has been preferred.

$$
m_{BK,\infty} = \frac{m_{CaV}k_o^+(\alpha + \beta + k_c^-)}{(k_o^+ + K_o^-)(k_c^- + \alpha) + \beta k_c^-} \tag{2.38}
$$

$$
\tau_{m,BK} = \frac{\alpha + \beta + k_c^-}{(k_o^+ + K_o^-)(k_c^- + \alpha) + \beta k_c^-} \tag{2.39}
$$

where m_{CaV} is the activation variable of the voltage-gated Ca^{2+} channel, whereas $\alpha = \frac{m_{\infty,CaV}}{\tau_{m,CaV}}$, $\beta = \tau_{m,CaV}^{-1} - \alpha$, and k_o^+ k_o^-, and k_c^- are calculated according to Eqs.126 2.30 to 2.31 for the closed, subscript c, and the open, subscript o, state of the CaV channel. The intracellular calcium concentration inside the nanodomain containing BK and CaV channels is calculated as described in the subsection 2.1.3.

2.1.3   Intracellular calcium modelling

Intracellular calcium dynamics is extremely important for the nematode neurons. Indeed, calcium channels are the main responsible for active neuronal responses in the

worm, e.g., action and plateau potentials [18, 20, 21, 22]. Also, the dynamics of calcium is critical in the transduction of sensorial stimuli, such as olfactory, mechanical, and thermal stimuli [1, 36?]. Moreover, as discussed above, intracellular calcium modulates the activity of BK and SK channels, so that the proper description of their gating requires a specific description of the intracellular calcium dynamics at the nano and micro scales. In the following paragraphs, the intracellular calcium models are described that have been applied in this work to describe the BK and SK channels calcium modulation and the olfactory stimuli processing in the AWC neurons.

Intracellular calcium model in BK channels

In the case of BK channels, the regulation by the calcium acts at the nanoscale. BK channels are co-localized with CaV in clusters within nanometric distances [204]. In the existing models [233], the intracellular calcium concentration ($[Ca^{2+}]_i$) is described inside a spherical domain ($r \sim 10$ nm) centred on the CaV, using reaction diffusion equations in the steady-state excess buffer approximation (EBA) described in [233, 234, 235]. In these conditions, the $[Ca_{2+}]_i$ concentration in the proximity of an open CaV channel is given by Eq. 2.40.

$$[\text{Ca}^{2+}]_i^{open} = \frac{i_{\text{Ca}}}{8\pi r D_{Ca} F} e^{\left[\frac{-r}{\sqrt{\frac{D_{Ca}}{k_B^+ [B]_{total}}}}\right]}, \tag{2.40}$$

$$i_{\text{Ca}} = g_{sc} \cdot (V - V_{\text{Ca}}) \tag{2.41}$$

where r is the nanodomain radius, F the Faraday constant, D_{Ca} the calcium diffusion coefficient, k_B^+ the intracellular buffer rate constant. $[B]_{tot}$ represents the initial total intracellular buffer concentration, according to the EBA approximation, and i_{Ca} is the calcium current through a single open CaV, given by Eq. 2.41. In Eq. 2.41 g_{sc} is the single-channel conductance, assumed equal to 40 pS for both L-type and P/Q-type calcium channels [?], and $V_{\text{Ca}} = 60$ mV is the equilibrium potential for calcium [139]. $[Ca^{2+}]_i^{closed}$ was assumed equal to 0.05 μM [1].

Intracellular calcium model in SK channels SK channels are regulated by intracellular calcium changes in a micrometric domain surrounding the channel itself [204]. Therefore, they are influenced not only by the neighbouring calcium channels but also by the dynamics of Sarco-Endoplasmic Reticulum Calcium ATPase (SERCA) uptake, the flux through Na^+-Ca^{2+} exchangers, and the flux through the plasma membrane Ca^{2+}-ATPases [236]. In this work, the intracellular calcium is modelled according to [232], with a simplified description in which its changes are governed by a first order differential equation (Eq. 2.42). Equation 2.42 describes the intracellular calcium dynamics as the result of two competing processes: an increase of concentration due to voltage-gated calcium currents (first term in Eq. 2.42), and a net decrease (second term in Eq.2.42) due

to the cited intracellular processes (SERCA) uptake, flux through Na$^+$-Ca^{2+} exchangers, and flux through the plasma membrane Ca^{2+}-ATPases) [236].

$$\frac{d[Ca^{2+}]_i(t)}{dt} = f\left[-\alpha I_{Ca} - k_{Ca}[Ca^{2+}]_i\right] \tag{2.42}$$

$$\alpha = \frac{1}{2V_{cell}F} \tag{2.43}$$

$$\tag{2.44}$$

In Eq. 2.42, α is the conversion factor between current and flux, calculated according to 2.43, f is the free intracellular calcium fraction, whereas k_{Ca} represents the calcium removal rate. In Eq. 2.42, F is the Faraday constant, and V_{cell} represents the entire neuron volume obtained from the Neuromorpho[3] database.

Table 2.1 reports the parameters used to simulate BK and SK channels activity. 2.1

Parameter	Value
D_{Ca}	250 μm^2 s^{-1}
r	13 nm
k_B^+	500 μM^{-1} s^{-1}
$[B]_{total}$	30 μM
F	96485 C mol^{-1}
f	0.001
k_{Ca}	0.03 ms^{-1}

Table 2.1: Parameter values used to model calcium concentration in the nano-, Eq. 2.40, and micro-domains, Eqs. 2.42 and 2.43.

Intracellular calcium modelling in the olfactory process

The transduction of an olfactory stimulus is a complex process realized by a cascade of biochemical reactions that result in an initial inhibition of the neuron when the odour is presented, followed by its activation when the odour is removed [13]. Concerning the chemosensory circuit of *C. elegans* here studied, the sensing role is played by AWC. An accurate biophysical model of the intracellular calcium dynamics during the AWC-mediated olfaction has been developed by Usuyama et al. [1], using a combination of mass balance equations and Hill equations that describe the cascade of reactions at the basis of the olfactory stimulus transduction. However, in this model [1] the electrical dynamics of the neuron is described in simplified way that does not account for the contribution of single ionic channels. In this work, the Usuyama model [1] has been coupled to the model of AWC electrical dynamics here developed to obtain a comprehensive view of the neuron functioning [1, 38, 40] (Fig. 2.2).

---

[3] http://neuromorpho.org/
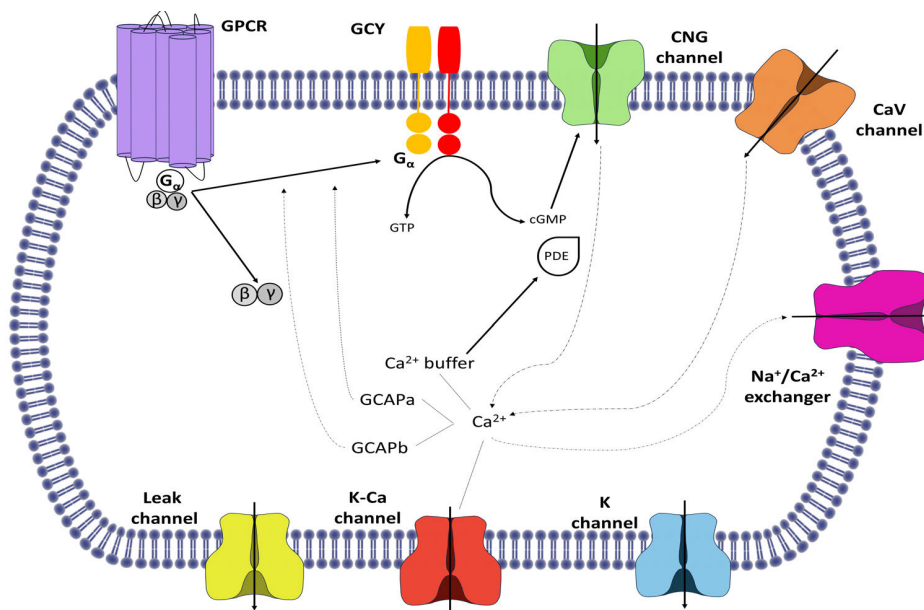
Figure 2.2: **Sensory stimuli transduction pathway in AWC^{ON} neurons**. Odorant binding to the GPCR promotes the dissociation of the G-protein complex into G_α and $G_{\beta\gamma}$ subunits. The G_α subunit inhibits the Guanaylate Cyclase (GCY) activity, and enzyme that converts GTP into cGMP. This inhibition results in a net reduction of cGMP levels in the cell and the consequent closure of CNG channels. The closure of CNG channels implicates a reduction of the intracellular calcium and the membrane potential. The cell hyperpolarization due to CNG closure is further reinforced by CaV channels closure induced by the more negative potential. Once the chemical stimulus is removed, the G_α inhibition is ceased, and a consequent transient calcium increase and a membrane depolarization are observed. The return to the resting state is then allowed by the activation of sodium-calcium exchanges (NCX), calcium buffers and potassium channels. Notably, the influence of G_α subunits on GCY is also regulated by the activity of two proteins, the guanylate cyclase-activating proteins, GCAPa and GCAPb, that regulate the excitation and the inhibition of the enzyme [1]

For the sake of clarity, the general formulations of the mass-action law and Hill functions are discussed in the following. For the complete list of equations and parameters of the AWC chemical response, the reader can refer to [1].

The interaction of chemicals and macromolecules to form different compounds can be described using the law of mass action. By means of this law, it is possible to describe the rate at which a compound is formed starting from the initial species. Each reaction proceeds in both directions. Given two species X and Y that react to form the compound Z, the reaction can be written as:

$$X + Y \underset{k_-}{\overset{k_+}{\rightleftharpoons}} Z \tag{2.45}$$

The rate of change of the X species can be described by a first order differential equation:

$$\frac{d[X]}{dt} = k_-[Z] - k_+[Y][X].$$
(2.46)

On the right side of the equation, the first term represents the increase of the [X] due to Z dissociation, while the second term represents the X consumption, due to the Z compound formation.

Some of the processes involved in AWC olfaction, such as the activation of voltage-gated calcium channels and cyclic-nucleotide-gated channels (CNG), work at time scales faster than that of biochemical reactions following the odour stimulation, e.g., the activation of CNG channels. In this case, the most suitable description uses a Hill equation. The Hill equation describes the cooperative binding processes of ligands to macromolecules (proteins or channels) as a function of the ligand concentration, as stated by Eq. 2.47.

$$\theta = \frac{[L]^n}{K_L^n + [L]^n} = \frac{1}{1 + \left(\frac{K_L}{[L]}\right)^n},$$
(2.47)

where K_L is the ligand concentration that produces half occupation, and n is the "Hill coefficient". The Hill coefficient reflects the cooperativity of the process, i.e. how the presence of already bounded ligands influences the binding of new. If the coefficient is 1, the binding processes are independent, if it is > 1 there is positive cooperativity, i.e., the biding of new ligands is facilitated by the presence of other ligands, while if it is < 1 the cooperativity is negative, which means that new bindings are discouraged by the already present ligands.

By combining these two laws, Usuyama et al. [1], obtained a complete description of the cascade of processes depicted in Fig. 2.2. As an example, the equation for intracellular calcium changes is reported below:

$$
\begin{aligned}
\frac{d[\text{Ca}](t)}{dt} = &-K_{+1,GCAPa+Ca}[GCAPa][\text{Ca}] + K_{-1,GCAPa+Ca}[GCAPa::\text{Ca}] \\
&- K_{+1,GCAPb+Ca}[GCAPb][\text{Ca}] + K_{-1,GCAPb+Ca}[GCAPb::\text{Ca}] \\
&- K_{+1,CaM+\text{Ca}_1}[CaM][\text{Ca}] + K_{-1,CaM+\text{Ca}_1}[CaM::\text{Ca}_1] - K_{+1,CaM::\text{Ca}_1+Ca}[CaM::\text{Ca}_1][\text{Ca}] \\
&+ K_{-1,CaM::\text{Ca}_1+Ca}[CaM::\text{Ca}_2] - K_{+1,CaM::\text{Ca}_2+Ca}[CaM::\text{Ca}_2][\text{Ca}] \\
&+ K_{-1,CaM::\text{Ca}_2+Ca}[CaM::\text{Ca}_3] - K_{+1,CaM::\text{Ca}_3+Ca}[CaM::\text{Ca}_3][\text{Ca}] \\
&+ K_{-1,CaM::\text{Ca}_3+Ca}[CaM::\text{Ca}_4] \\
&+ Ef_{CNG} \cdot \frac{I_{CNG,MAX} \cdot [cGMP]^{n_{CNG}}}{[cGMP]^{n_{CNG}} + K_{CNG}^{n_{CNG}}} \cdot (V_{CNG} - V) \\
&+ Ef_{CaV} \frac{(V_{\text{Ca}} - V)}{1 + \exp\frac{(V_{\text{Ca}}^{0.5} - V)}{K_{CaV}}} \\
&- Ef_{CaX} \frac{[\text{Ca}]}{1 + \left(\frac{[CaM::\text{Ca}_4]}{K_{NCX}}\right)}
\end{aligned}
$$
(2.48)

Eq. 2.48 describes the intracellular calcium changes determined by guanylate-cyclase-activating proteins (GCAPa and GCAPb), calcium buffer (calmodulin CaM), cyclic nucleotide gated channels (CNG), voltage-gated calcium channels (CaV), and sodium-calcium exchangers. The last three contributions are modelled with Hill functions that reflect their fast kinetics. For the complete list of equations and parameters, refer to [1]. The intracellular calcium modelled as in Eq. 2.2 has been coupled to the electrical model of AWC here developed [38]. In particular, with respect to [1], the parameters for the flux of CaV are recalculated from the I-V relation of calcium currents of the AWC model [38].

2.1.4 Whole-cell modelling

The model of whole-cell response to different stimulation protocols, including voltage, current, and chemical stimulations, has been constructed by combining the elements of interest for the description of the desired neuron dynamics. Single cells are modelled in a single-compartment approximation, in which the spatial dynamics is not considered. This approach constitutes a strong simplification; indeed, the electrical properties of neuronal cells are also critically dependent on cell morphology. Nevertheless, single-compartment models are widely used to study electrophysiological properties of a wide variety of cells and constitute a valid starting point to study complex neuronal phenomena. Concerning the electrical responses simulations the whole-neuron dynamics is obtained by solving the ordinary differential equation that governs the equivalent electrical circuit for the neuron.

$$C\frac{dV(t)}{dt} = -(I_{ext}(t) + I_{ion}(V,t)) \tag{2.49}$$

where I_{ext}, if present, is the externally applied current to the neurons and represents the analogous of the stimulus applied to the neuron during patch-clamp experiments performed in the current-clamp mode. The cell capacitance C is selected from available experimental data for *C. elegans* [19, 24?]. In Eq. 2.49, I_{ion} contains all the significant ionic currents included in the model of the considered neurons. For each modelled neuron the set of ionic currents to be included in the model is chosen according to the gene expression profiles extracted from the Wormbase[4] and CeNGEN[5] databases and literature reporting expression patterns of the specific genes. Therefore, I_{ion} can be expressed as:

$$I_{ion} = \sum_x I_x, \tag{2.50}$$

where I_x is the current associated with a specific kind of ion channels, modelled within the Hodgkin-Huxley formalism previously described. In each modelled neuron is included the intracellular calcium dynamics associated with CaV channels activity, modelled according to Eq. 2.43, even in the absence of SK channels. While the description of the intracellular calcium in the CaV centred nanodomain is included only when BK channels are selected for the modelling of the considered neuron.

---

[4]`https://wormbase.org`
[5]`https://cengen.shinyapps.io/SCeNGEA`

In AWC^{ON} olfaction model, the coupling between the electrical and chemical responses is performed by substituting the simplified description of the intracellular calcium given by Eq. 2.43 with the more detailed description of Ca^{2+} dynamics of the Usuyama model (Eq. 2.48) [1]. Concerning the electrical dynamics, Eq. 2.49 is still valid, but with I_{ext} substituted by an inward calcium current mediated by cyclic-nucleotide-gated (CNG) channels modelled as in [1] (Eq. 2.51).

$$I_{CNG} = \frac{I_{CNG,MAX} \cdot [cGMP]^{n_{CNG}}}{[cGMP]^{n_{CNG}} + K_{CNG}^{n_{CNG}}} \cdot (V - V_{CNG}) \qquad (2.51)$$

where $[cGMP]$ is the intracellular cyclic GMP concentration in μM, n_{CNG} and K_{CNG} are the Hill function exponent and slope describing the channel kinetics, and V_{CNG} is the reversal potential for CNG channels. Also, the parameters used in calculation the CaV-related flux in Eq. 2.48 are changed to reproduce the I-V curve for calcium channels computed from the electrical model.

$$J_{Cav}^{original} = 1\frac{(30 \text{ mV} - V)}{1 + e^{\frac{(-10 \text{ mV}-V)}{4 \text{ mV}}}} \longrightarrow J_{Cav}^{new} = 1\frac{(60 \text{ mV} - V)}{1 + e^{\frac{(-0.49 \text{ mV}-V)}{9.65 \text{ mV}}}} \qquad (2.52)$$

Therefore, in the model proposed here, the neuron is not stimulated by the application of an external current or voltage stimulus. Rather it is activated by the processes that downstream the odorant-binding to the GPCR. The receptor activation upon odor presentation has been modelled, according to [1, 237], with a fist order differential equation:

$$\frac{d[R_{active}]}{dt} = K_{+1,R}[odorant]([R_{total}] - [R_{active}]) - K-1, R[R_{active}], \qquad (2.53)$$

where $[R_{active}]$ is the fraction of activated receptors, $[R_{total}]$ is the amount of receptors, *odorant* is the chemical stimulus, and $K_{+1,R}$ and $K_{-1,R}$ represent the rate constants for odor-receptor association and dissociation, respectively. For the parameter values in Eqs. 2.51, 2.48, and 2.53 please refer to [1]

2.1.5 Biophysical modelling of neurons network

The single neurons models developed as previously described have been used to build a minimal circuit composed of six neurons: AWC, AIY, RIM, RMDL, RMDDL, RMDVL. The six selected neurons have been connected with both chemical and electrical synapses (or gap junctions). AWC and AIY neurons communicate through an inhibitory glutamate-mediated synapse [13, 44]. AWC neurons continuously release glutamate that inhibits AIY interneurons by gating the GLC-3 glutamate-gated chloride channels [44]. Concerning the other neurons of the circuit, a possible pathway of connection through gap junctions is retrieved from the Wormwiring database[6].

Due to the complexity of the intracellular processes that regulate the glutamate production in neurons, the inhibitory synapse between AIY and AWC neurons is modelled as

---

[6]https://www.wormwiring.org/

a graded synapse, in which the synaptic current delivered to the postsynaptic neuron is directly related to the intracellular calcium concentration in the presynaptic neuron [43]. The synaptic current is therefore given by Eq. 2.54

$$I_{syn} = n_{syn} \cdot k \cdot \text{Ca}_{pre}^3 \cdot (V_{post} - E_{syn}), \tag{2.54}$$

where n_{syn} represents the strength of the synaptic connection, k is the conversion factor of the calcium concentration into electrical current, Ca_{pre} is the intracellular calcium concentration, V_{post} is the postsynaptic cell membrane potential, and E_{syn} is the reversal potential for the synapse. The inhibitory or excitatory character of the synapse is defined by the value of E_{syn} with respect to the postsynaptic cell resting potential. If $V_{post}^r < E_{syn}$ the synapse is inhibitory, while if $V_{post}^r > E_{syn}$, the synapse is excitatory. In the present work, E_{syn} is set equal to -70 mV.

Gap junctions are electrical connections between cells formed by the clustering of several channels in two adjacent cells. Gap junction communication is faster and less complex than the communication mediated by chemical synapses. This simplicity is reflected also at the mathematical modelling level. In the present work, gap junction currents are modelled in the following way [43]:

$$I_{gap} = n_{syn} \cdot g_{gap} \cdot (V - E_{gap}), \tag{2.55}$$

where n_{syn} represents the number of synaptic channels, g_{syn} is the conductance of the single hemichannel, and E_{gap} is the potential of the presynaptic cell.

2.2 Tools and algorithms

In this section, the computational tools and optimization algorithms applied in this work are described. The model of single-currents and whole-neurons has been implemented both in NEURON and XXPAUT. The experimental data and simulation results are analysed in Matlab. Once the model equations are defined, a key point for obtaining a model that correctly reproduces the observed electrophysiological recordings is the definition of an optimal set of conductances. This problem falls in the class of optimization problems. Optimization problems are a particular class of problems in which both the model and the desired output are known, and the task is to find the input that leads to the desired output (Fig. 2.3).

In this work, two optimization strategies have been applied to derive the optimal set of ionic conductances to be used in single neuron models. The fist strategy is based on manual searching, performed by manually changing the parameter values until the desired result is reached. However, this strategy has two main disadvantages: it is time consuming and does not allow to explore wide parameter spaces. In this context, the development of an effective optimization routine assumes crucial importance. Among the many algorithms that could be applied to solve the problem, genetic algorithms have been selected for their wide range of applicability and their capability to explore a vast parameter space.

2.2. TOOLS AND ALGORITHMS
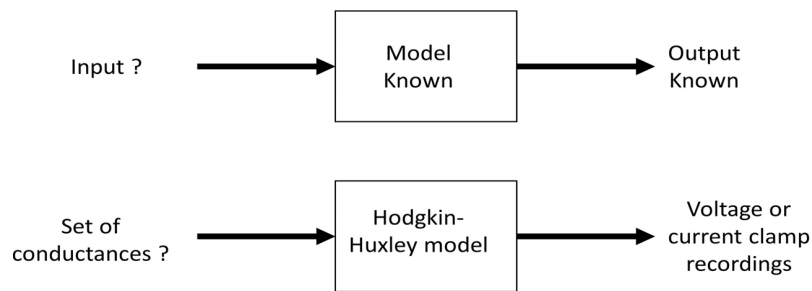
Figure 2.3: **Optimization problem scheme.** Scheme representing the optimization algorithm process. In the second row is schematically represented the specific case here studied. (Adapted from [238])

Four main tools have been used in this work to implement the models and analyse simulation results, as well as experimental data: MATLAB, XPPAUT, NEURON and Python with its libraries.

MATLAB is an environment for numerical computation and multi-paradigm programming language developed by MathWorks. This software is particularly suitable for matrix computation, graphical illustration production, and algorithm implementation [239]. It is equipped with many built-in functions and toolboxes specifically designed for scientific and industrial applications, such as statistical and image analysis, model development, and optimization. In the present work, MATLAB has been widely used in the derivation of single current model parameters by fitting experimental data for activation and inactivation variables and time constants, and also for BK channels model optimization through genetic algorithm (available in the Curve Fitting Toolbox).

XPPAUT is a widely used tool that allows a simple implementation and solutions of differential equations, diffusion equations, delay equations, functional equations, boundary value problems, and stochastic equations [240]. The software is coupled with AUTO, a program specifically developed for the study continuation and bifurcation problems with ordinary differential equations. Compared to other ODEs solver software, XPPAUT guarantees an easy implementation of the equations and has many built-in integration methods suitable for a wide range of problems. Moreover the graphical interface allows an immediate visualization and analysis the simulation results. In this work XPPAUT has been applied to build and solve single currents modelling as well as for whole-neurons simulations. Moreover, the program AUTO, within XPPAUT, is used to conduct detailed analyses of AWC and RMD neurons bistable behaviour.

NEURON is a simulation environment that has become a widely used tools among computational neuroscientists. The characteristics that made it so widely employed are its flexibility, the possibility to extend the basic mechanisms, the possibility to use Python as interpreter and to include network parallelization with MPI [43, 241]. NEURON can be used both by using a graphical interface and by a scripting language called "hoc". It allows managing a wide variety of problems ranging from single-cell biophysical models up to large network scale. Compared to other software, NEURON allows an easy imple-

mentation of customized libraries of biophysical mechanism models, e.g. ionic currents, synaptic currents, or chemical reactions. All the ionic currents, synaptic connections, and intracellular calcium model here used (except the AWC olfactory response model) have been implemented in NEURON and used in combination with the genetic-algorithm based routine and for the network simulation.

Python is an object-oriented high-level programming language developed in the 90s by Guido van Rossum [242]. Python is extremely flexible and possesses a wide assortment of basic functions as well as of standard and advanced libraries. Among its many advantages, a key one is that it can easily interact with NEURON, allowing both the use of .hoc files and NEURON tools inside Python directly. Thereby, it allows simple management of simulation data analysis and also the implementation of optimization routines based on Genetic Algorithms (GA). In this work, the optimization of model parameters has been performed using the Inspyred Library, an open-source, freely available library [243]. It provides implementations of many widely used Evolutionary Algorithms (EA), including but not limited to Genetic Algorithms, Evolutionary Strategy, Simulated Annealing, Particle Swarm Optimization, and Pareto Archived Evolution strategy. Also, Inpyred supports user defined functions for the evaluation and the generation of the candidates, and allows recording the complete computation history by offering specific functions, called observers, to save the generated candidates as well the statistics for each generation. Moreover, a very complete and well-written documentation is available, which allows a easy customization of the algorithms. Given the nowadays increasing interest in evolutionary programming, in particular in its application to optimization problems, for the interested readers, an overview of the basic working principles of genetic algorithms is given in Appendix C.

For the sake of clarity in Fig. 2.4 the basic operational scheme of GA is reported. In this work, the Inspyred library has been applied in combination with NEURON to find the optimal set of conductances in particular for AWC and AIY neurons.

2.3 Model implementation

In this section the details of models implementation are presented. The implementation can be divided in four steps, that will be discussed in detail in the following subsections

- Single currents parameter fitting in MATLAB.

- Single current models development in XXPAUT and NEURON.

- Whole-neuron models development in XPPAUT and NEURON.

- Circuit model.

2.3.1 Single currents parameter fitting and modelling

For each of the selected currents, experimental data points are obrained from literature and, when necessary, fitted to derive the steady-state variables and/or time constants
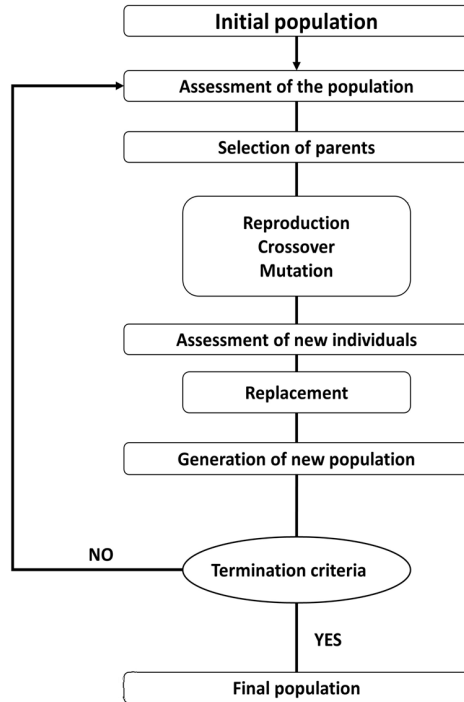
Figure 2.4: **Genetic algorithm operation scheme.** The diagram represents the basic operational scheme of a GA-based optimization. The initial population is evaluated based on user-defined criteria. The best individuals in the population are selected for mating. The generation of new individuals is performed by crossover and mutation operators that mimic the respective biological processes. The new population is then assessed and if the termination criteria are met the algorithm stops; otherwise, the same evolution process is repeated until the desired result is obtained. For further details on the working schemes of single operators applied in this work, the reader is referred to Appendix C.

expressions as a function of voltage. Curves are fitted in MATLAB (R2017b, R2019b, R2020a) using a least-squares non-linear fitting procedure that adopts a Trust-Region-Reflective algorithm ("lsqcurvefit" in MATLAB).

In the case of BK channels, the model parameters are fitted applying a hybrid genetic algorithm fitting procedure, which performs a further minimization of the GA result using the "fmincon" function [233]. Model parameters are obtained by fitting simultaneously the activation variable and time constants [152, 153]. The objective function for the optimization is chosen according to [233], as follows:

$$
\begin{aligned}
min^{\phi}_{\text{slo-}1/2,\,j} \;=\; & \sum_{j}\sum_{i}\left[m^{j}_{\text{BKs},\infty}(V_i) - \overline{m}^{j}_{\text{BKs},\infty}(V_i)\right]^2 \\
& + \left[\tau^{j}_{m_{\text{BKs}}}(V_i) - \overline{\tau}^{j}_{m_{\text{BKs}}}(V_i)\right]^2
\end{aligned}
\tag{2.56}
$$

where ϕ is the set of parameters, $m_{\mathrm{BKs},\infty}^{j}$ and $\tau_{m_{\mathrm{BKs}}}^{j}$ are the values of steady-state activation variable and time constant for the j-th calcium concentration ($Ca = 1, 10, 100, 1000\,\mu\mathrm{M}$ for SLO1 [152], and $Ca = 10, 60, 300\,\mu\mathrm{M}$ for SLO2 [153]). Finally, $\overline{m}_{\mathrm{BKs},\infty}^{j}$ and $\overline{\tau}_{m_{\mathrm{BKs}}}^{j}$ represent the simulated values of steady-state activation and time constant, respectively. Once the curve for steady-state variables and time constants has been obtained, the model of the ionic currents are implemented in XPPAUT and solved using a " stiff" solver (based on Rosenbrock discretization schemes), known to be suitable when dealing with coupled dynamics that work at different timescales [244]. Restrictive values of numerical tolerances ($\sim 1\mathrm{e}\text{-}8$) are set to ensure accurate results. Further restrictions on such setting do not cause significant differences in numerical results, indicating that a suitable accuracy is achieved. The single currents models have also been implemented in NEURON using the NMODL language. ODEs for single currents models are solved using the cnexp method and compared to XPPAUT output and experimental data to confirm the validity of the model. The full list of single-current model equations is reported in Appendix A, while the list of the parameter values can be found in Appendix B, Tables B1-B2.

2.3.2 Single neuron models

Single neuron models are developed in a single-compartment approximation, using both XPPAUT and NEURON. The specific set of ion channels to be included in the model is defined based on the gene expression profiles extracted from the Wormbase [5] and CeNGEN [37] databases and literature. AWC, RIM, and RMD neuron models are developed in XPPAUT, and the set of optimal conductances is derived by manually tuning the values of the conductances of single channels. In some cases, the kinetic parameters had to be manually varied to match the temporal characteristics of the neuron dynamics. The modified parameters are listed in Appendix B, between brackets. The system of ODEs describing the neuron is a " stiff" solver, and restrictive values of numerical tolerances ($\sim 1\mathrm{e}\text{-}8$) are set to ensure accurate results. AIY model is initially developed in NEURON and also translated in XPPAUT. Also, AWC, RIM, and RMD models have been translated to NEURON to allow GA optimization and circuit modelling. In the NEURON implementation, the length and diameter of the compartment have been chosen so that the total volume of the compartment corresponds to the total volume of the cell taken from the Neuromorpho database. The simulations are run both using the "hoc" implementation and inside Python. In particular, the use of NEURON implemented mechanisms under Python allowed the construction of a GA-based routine that has been used to derive the AIY neuron model and refine the model of AWC neurons. In the following paragraph the GA-implementation is discussed.

Genetic Algorithms implementation in Python

Optimization routines of single neurons parameters are implemented in Python, using the "Inspyred" library [7] [243]. The GA routing here implemented is based on a combination

---

[7] http://aarongarrett.github.io/inspyred/

of built-in Inspyred functions and customized functions written by the candidate. For all neurons, the initial population of parameters, in this case, the set of conductances, has been generated randomly, with a customized generator function, between specified boundary values. The population size is equal to $10 \cdot N_{par}$, where N_{par} is the number of parameters to be determined. The boundary values are specified in nS and converted to S/cm^2, the default unit for conductances used by NEURON, using a customized function. The initial population is then passed to the GA routine that performs the optimization. For each candidate, a voltage/current clamp simulation is performed using customized functions that call NEURON inside Python. The specific stimulation protocol, i.e., voltage-or current-clamp, used in the simulations has been defined to match the reference experimental recordings for the considered neurons. Finally, the simulation output is passed to the evaluator function, written by the candidate, that computes the fitness of each candidate ψ.

Based on the specific type of the available experimental data, i.e., complete voltage/current-clamp recordings or I-V curves (IVs) for peaks and steady-state, three fitness functions have been defined. All are based on the calculation of root mean distance between the experimental and the simulated data (Eqs. 2.57-2.59). In the case of voltage/current clamp recordings, the root mean distance between the experimental and the corresponding simulated trace is calculated at each time step and for all the applied voltage/current stimuli. Then the calculated distances are summed over time and voltage and normalized with respect to the number of time and voltage/current steps to obtain the fitness score ψ, for each candidate (Eqs. 2.57 and 2.58).

$$\psi^2 = \frac{1}{MN} \sum_{i=1}^{M} \sum_{j=1}^{N} \left(I_{EXP}^{ij} - I_{SIM}^{ij}, \right) \tag{2.57}$$

$$\psi^2 = \frac{1}{MN} \sum_{i=1}^{M} \sum_{j=1}^{N} \left(V_{EXP}^{ij} - V_{SIM}^{ij}, \right) \tag{2.58}$$

where I_{EXP} (V_{EXP}) is the experimental current (voltage), and I_{SIM} (V_{SIM}) is the output of the simulation. M and N are the numbers of voltage/current steps in the stimulation protocol and the number of points per trace, respectively. This fitness function is applied whenever whole-cell recordings are available.

In some cases, the only available data are the I-V curves derived from voltage-clamp recording. Therefore the fitness function has been adapted to minimize the root mean distance between the experimental and the simulated I-V curve for peaks and steady state. Eq. 2.59 gives the fitness score, ψ, assuming an equal weight for peaks and steady-state IVs.

$$\psi = \sum_{j=1}^{N} \left[\frac{(IV_{peaks,EXP}^{j} - IV_{peak,SIM}^{j})^2}{2} + \frac{(IV_{ss,EXP}^{j} - IV_{ss,SIM}^{j})^2}{2} \right] \tag{2.59}$$

Each tested candidate, as well as its fitness value (ψ) and the statistics of the population are saved in separate files, to allow eventual post-processing of the data. Once the

termination criteria are met, the final population is sorted and the best individual is chosen as the final candidate. For each modelled neuron, more than one GA run has been performed. The best candidate is selected based on the fitness value and the overall electrophysiological characteristics. The specific settings for GA optimization, as well as be final set of parameters of each neuron, are reported in the corresponding section of the results, i.e., Chapter 5, section 5.3, and Chapter 6, section 6.1.
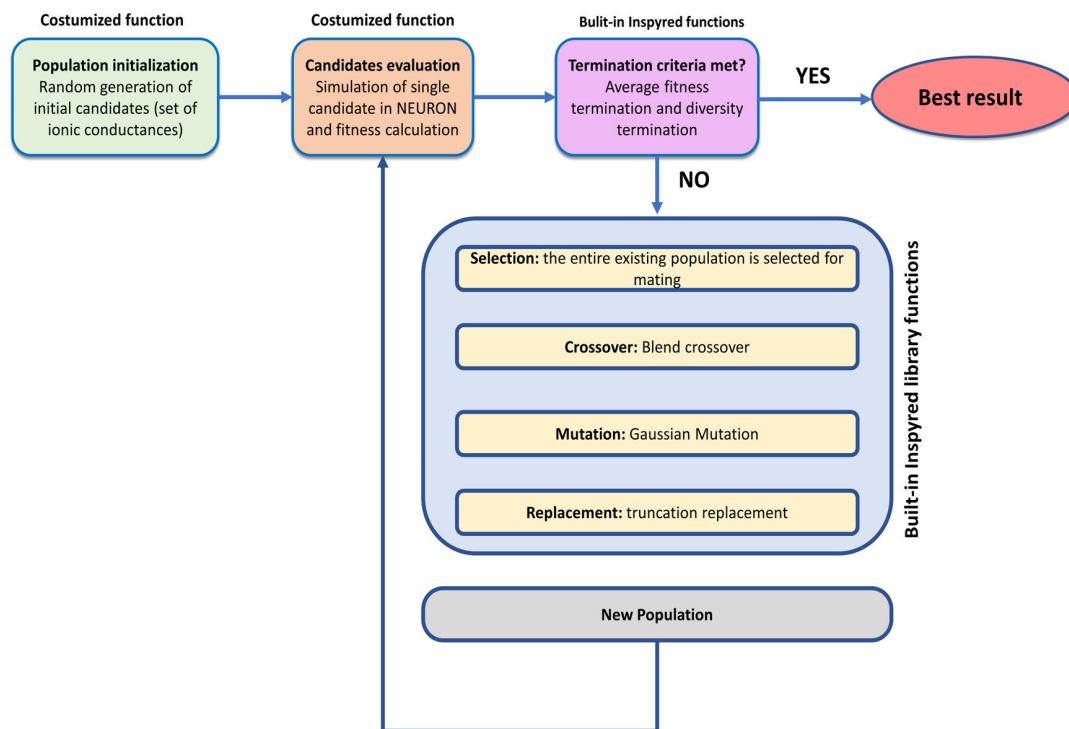
Figure 2.5: **GA optimization workflow in Python.** The optimization routine has been implemented in Python by using a combination of customized (written by the candidate), functions (generator, evaluator, fitness function) and built-in python functions (selection, crossover, mutation, and replacement operators). All the generated candidates as well as the best results and the statistics of each population are saved to allow further reconstruction.

2.3.3 Circuit model implementation

Once all the single-neuron and the synaptic connection models have been implemented in NEURON, the construction of the circuit is performed by inserting the synaptic connections between the selected neurons. As already specified in Section 2.5, due to the lack of specific experimental data and the complexity of mechanisms behind the glutamate production in AWC^{ON} neurons, the chemical synapses have been modelled using the standard model of graded synaptic transmission, taken from [43]. Similarly, the

gap junction connections have been modelled according to standard formulation of the gap junction currents reported in [43]. The voltage and intracellular calcium responses of the neurons involved in the circuit are then exported and analysed in MATLAB.

2.3.4 Simulation results analysis

Final models of single neurons are analysed by computing the steady-state and peaks I-V curves from the voltage clamp data and using *in silico* knockout simulations both in the voltage and current clamp configuration. I-V curves describe the relation between the recorded current and the applied voltage stimulus and therefore are indicative of the peculiar characteristic of the neuron. Peak I-V curves are computed by calculating the maximum of the current in a small interval (not greater than 100 ms) near the stimulus onset, while steady-state I-V cureves are computed by taking the mean of the whole-cell current in the last 5 ms of the stimulus. *In silico* knockout analysis allows the dissection of the contribution of the single ionic currents to the overall response of the neuron. *In silico* knockout have been built by suppressing the contribution of one channel at a time, while leaving unchanged the contribution of the others. This procedure mimic *in silico* the action of pharmacological agents, usually named "channels blockers", that are commonly used in patch-clamp experiments to selectively block a specific class of ion channels.

Chapter 3

Experimental methods and calcium imaging data.

55

This research work is born from a collaboration between the Campus Bio-Medico University of Rome and the Center For Life NanoScience (CLNS@Sapienza) of the Italian Institute of Technology (IIT). All the calcium imaging results that will be described in the chapter have been performed at the CLNS@Sapienza. In particular, experiments on wild-type (WT) and mutants worms have been conducted to clarify the sensory ability of AWC^{ON} to detect chemical and mechanical stimuli.

The candidate participated to some of the experiments, analysed the data, and contributed to results interpretation. In this chapter, her contribution to the work will be explicitly stated when present. Otherwise, the work has been performed by the CLNS@Sapienza group coordinated by Dr. Viola Folli. In particular, Dr. Silvia Schwartz and Giuseppe Ferrarese provided the strains and performed genetic cross, Dr. Davide Caprini designed the microfluidic devices and conducted calcium imaging experiments, Dr. Enrico Lanza built the imaging system, and Valeria Lucente conducted the experiments and analysed the data.

The chapter is divided into two main sections, the first dedicated to the description of the experimental procedures and data analysis methods, the second to the presentation of the results of calcium imaging experiments performed on AWC^{ON} neurons.

Moreover, given the extensive use in this work of published electrophysiological recordings performed with the patch-clamp technique, a brief resume of its working principles has been added to experimental methods. It has to be noted that all the patch-clamp data used in this work have been taken from literature and thereby not acquired at the CLNS@Sapienza.

3.1 Experimental methods

In the following the experimental methods used in calcium imaging experiments are described. In particular the paragraph is organized as follows. In subsection 3.1.1 the procedures for worm growth and maintenance are described; while subsections 3.1.2, 3.1.3, and 3.1.5 focus on the description of microfluidic device, optical setup, and imaging data analysis, respectively.

3.1.1 *C. elegans* strains preparation and maintenance

In calcium imaging experiments here showed, transgenic animals harboring the GCaMP5a fluorophore in the AWC^{ON} sensory neuron have been used to study its responses to chemical and mechanical stimuli. In particular, the following strains have been used in the experiments: CX17256 (*kyIs722[str-2p::GCaMP5(D380Y) + elt-2::mCherry]*, VC3113 *tax-4 (ok3771)*, JD21 *cca-1 (ad1650)*, VC9 *nca-2 (gk5)*, CX10 *osm-9 (ky10)*, and MT1212 *egl-19 (n582)*. All the strains have been obtained from the Caenorhabditis Genome Center which is funded by NIH Office of Research Infrastructure Programs (P40 OD010440). In order to monitor the activity of AWC^{ON} neurons, the transgenic strains have been genetically crossed to CX17256 strain to obtain mutants harboring the GCaMP5a fluorophore on the desired neuron (Table 3.1). Briefly, for each cross, 8-10 males from

3.1. EXPERIMENTAL METHODS

CX17256 have been crossed to 2 hermaphrodites from each mutant strain. After 3-4 days, at least 20 F1 fluorescent animals have been cloned individually in 35 mm petri dishes and left to lay eggs. From these 20 F1 worms, two different worms have been chosen to select the fluorescent F2 progeny. F2 animals were individually placed in 35 mm Petri dishes and after 3-4 days, all F2 worms have been subjected to PCR amplification for the gene of interest. Homozygous worms have been selected and kept for the experiments,and confirmed either on agarose gel, for deletion mutants, or Sanger sequencing, for amino acid substitution changes.

Strain name	Molecular change
AWCGcAMP/*tax-4*	Deletion in *tax-4* gene
AWCGcAMP/*cca1-1*	Deletion in *cca1-1* gene
AWCGcAMP/*nca-2*	Deletion in *nca-2* gene
AWCGcAMP/*osm-9*	Amino acid substitution
AWCGcAMP/*egl-19*	Amino acid substitution

Table 3.1: List of mutants trains obtained by genetic cross.

In addition to the above mentioned strains, calcium imaging experiments have also been performed on *unc- 13(e51) I; kyEx2595 [str2::GCaMP2.2b, unc-122::gfp]* and *unc-31(e928) IV; kyEx2595 [str2::GCaMP2.2b, unc-122::gfp]*, both kindly provided by Professor Chalasani (Salk Institute for Biological Studies, La Jolla, CA).

Single worm DNA extraction and Polymerase chain reaction (PCR) Standard PCR has been performed in order to amplify the genes of interest and select the correct mutant strain after genetic crosses. Briefly, the DNA template has been obtained by performing single worm DNA extraction as follows. Single worms are picked into 5 μl of worm Lysis Buffer (50mM KCl 10 mM Tris (pH 8.3) 2.5 mM MgCl2 0.45% NP-40 (IGEPAL) 0.45% Tween-20 0.01% Gelatin, 0.1 mg/mL of proteinase K added before use) in a 0.2 ml tube, rapidly centrifuged to pellet the worms and incubated at -80°C for at least 30 minutes. The tubes are then incubated at 60°C for 60 minutes. PCRs have been performed using the following standard procedure. A 25 μl reaction is prepared (GoTaq® Flexi DNA Polymerase) using specific primers for the genes of interest (Table 3.2). The thermal cycle for amplification consists in the following steps: initial denaturation at 95°C for 2 minutes x 1 cycle, denaturation at 95°C for 30 seconds x 1 cycle, annealing at 42–65°C, according to the primers melting temperature (Tm) for 50 seconds x 30 cycles, extension at 72°C 1min/kb x 30 cycles, and final extension at 72°C for 5 minutes x 1 cycle. The final step at 4°C indefinite. The PCR products are then run via agarose gel (2%) electrophoresis.

***C. elegans* maintenance and preparation for the experiments** All the strains are cultured under standard conditions at 20°C on nematode growth media (NGM) in 60 mm Petri dishes seeded with Escherichia coli strain OP50 as a food source. Worms

Strain name	Forward primer	Reverse primers	Internal primer	Tm	Elongation time [minutes]
tax-4	tctcattggaccatcttccc	tgtctcatgcctacacacgg	na	60°C	1:00
cca1-1	gggtgtggagtaccatcaac	actctcctcaaacttctgcc	atcgaagagcaggcatgaag	62°C	0:45
nca-2	ttccaagttttccgaattgc	gccaaaatcccgataacgtg	caagaatgacggcaacgaag	54°C	1:00
osm-9	tcggccttgctattcagaagc	atcttccagaacgtgcaactcg	na	62°C	0:40
egl-19	tgctgaagatcctctacaagc	atattctccacggcattctgc	na	62°C	0:45

Table 3.2: List of PCR primers used to amplify the genes of interest

are synchronized by placing 10 adult hermaphrodites on NGM plates for four hours to lay eggs. The plates were placed in an incubator at 20°C, after the hermaphrodites have been removed. Since their deposition rate is lower than of CX17256, unc-13 and unc-31 mutants are directly collected from the culture plates. On the day of the experiment, 15-20 fluorescent adults are collected and put in 35 mm Petri dishes, washed three times with S-basal (NaCl 0.1 M, potassium phosphate 0.05 M, pH6) and then injected into the microfluidic device. Animals are paralyzed inside the chip using levamisole hydrochloride (Sigma-Aldrich PHR1798) diluted in Milli-Q® water at a final concentration of 1 mM. In experiments with chemical stimuli, Isoamyl alcohol (Sigma-Aldrich 8.18969) diluted in S-basal buffer at a final 10-5 dilution, is used.

3.1.2   Microfluidic device

Microfluidic devices are fabricated in 1:10 PDMS (Polydimethylsiloxane Silgrad 184) using the soft lithography technique. The chips are obtained by casting and curing PDMS into a mould fabricated with a SU-8 negative obtained with conventional photolithography. After the casting process, the mould is cured, and a 0.6 mm puncher is used to make inlet and outlet holes. The PDMS mould is bonded on a microscope glass slide through an air-plasma treatment and thermal recovery on a hot plate. Experiments are carried out in a revised and miniaturized version of the pulse arena originally developed by Larsh et al. [41, 245], here called "mini-pulse arena". The inlet channels are designed to allow the administration of chemical stimuli using fluidic valves. Also, the chip possesses a loading channel used to inject the worms and an outlet channel that drains the fluid excess from the chip. The inlet channels are connected to two mutually exclusive pressurized fluid reservoirs through Tygon tubes, and the switch between them is regulated by digitally controlled electromechanical valves.

3.1.3   Optical setup

Calcium imaging experiments are performed on WT and mutant nematodes carrying the GCaMP5a on AWC[ON] neuron at 475 nm. The experiments are performed on a custom-designed inverted epifluorescence microscope (Eclipse Ti, Nikon, Melville, NY). Excitation light is reflected on the sample through a high power LED (470 nm - M470L2, Thorlabs, Newton New Jersey) with FITC excitation filter (MF475-35, CWL=475 nm, BW=35 nm, Thorlabs) and a condenser (ACL2520U-A, Thorlabs). The fluorescence signals are collected via a digital CMOS camera (ORCA-Flash4.0 C11440, Hamamatsu,

Hamamatsu City, Japan) through a dichroic mirror with a pass-band FITC/TRIC filter (59004x, Chroma, Bellows Falls Vermont) using a 4X objective with a numerical aperture 0.28 (XFLUOR4X/340, Olympus, Tokyo, Japan) for a field of view of $3.25X3.25$ mm^2. During the experiment, the area of the arena is selected using a motorized stage (MLS203-1, Thorlabs) and of a 660 nm-transmission channel (high-power LED, ML660L4, Thorlabs). During the experiments, the area is illuminated by blue-light (470 nm) only during the exposure time (100 ms) to reduce phototoxicity effects and maximize the temporal resolution. The fluid dynamics inside the arena is controlled by a set of electrovalves connected to the inlet reservoirs and digitally controlled (NI-DAQmX PCI-6221, National Instrument Controller, National Instruments, Austin, Texas). The synchronization of illumination, image acquisition, and fluid controlling is achieved through a custom software developed in MATLAB (Mathworks. Natik, Massachusset) (Fig. 3.1).
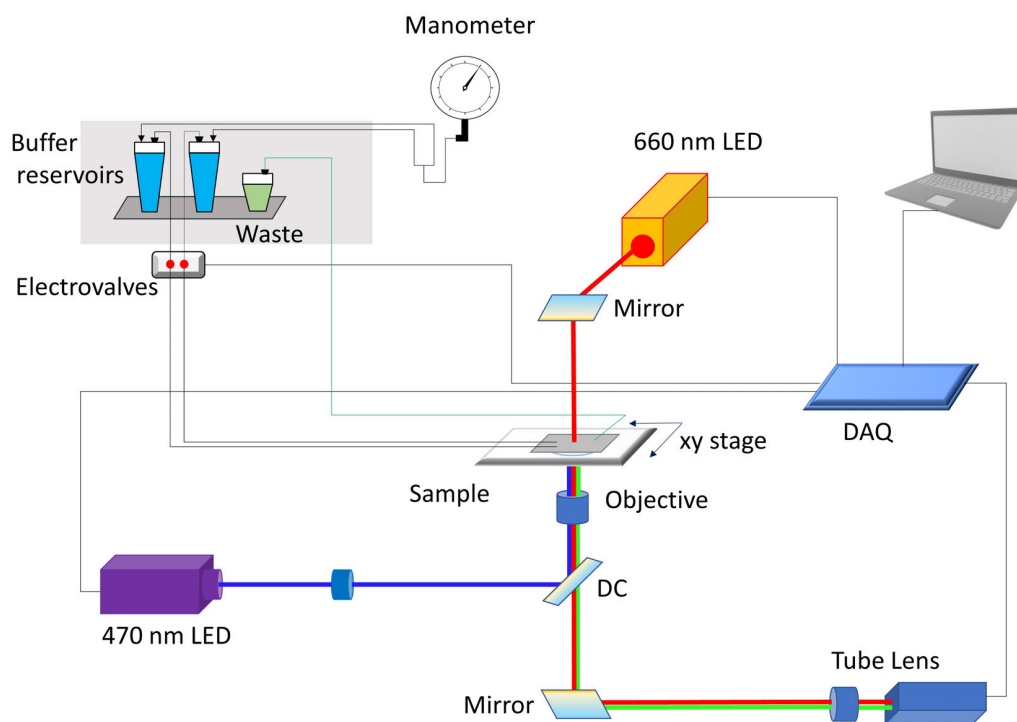
Figure 3.1: **Scheme of the calcium imaging setup**.

3.1.4 Protocols for calcium imaging experiments

The day of the experiment, the microfluidic chip is degassed in a vacuum chamber for at least 15 minutes, in order to prevent air bubble transfer from the PDMS to the chip.

Then the device is placed on an XY-microscope stage and connected to the pressurized reservoirs (Fig. 3.1). The chip is completely filled with buffer solution until a drop emerges from both inlets, while the outflow port is connected to the outflow reservoir. Then the two inlets are connected to Tygon tubing drop-to-drop connection. After few minutes of buffer flush inside the arena, approximately 10-15 worms are gently loaded into the chip with a tygon tube connected to a syringe. Eventual residual bacteria are removed by continuously flushing buffer solution. The worms are paralysed using levamisole hydrochloride (1 mM). After twenty minutes of levamisole administration, the paralysing agent is washed out by flushing buffer solution. In this work calcium imaging experiments have been performed using two different stimulation protocols: one designed to administrate chemical stimuli, and the other to provide mechanical stimuli.

In the chemical stimulation experiments, one of the two reservoirs (Fig. 3.1) is filled with the desired odorant, while the other contains buffer solution (S-basal). The switch of flow rates between odour and buffer is actuated by slowly (about 2 sec) opening and closing of the Tygon tubes connected to the reservoirs to prevent the propagation of dangerous shock waves in the tubes, generated by fast closure of conventional electromagnetic valves. The worms are exposed to three cycles of administration of IAA (10^{-5}). Each administration has a duration of 25 s and is followed by 25 s of buffer solution administration to allow AWC$^{\text{ON}}$ activation after the odour removal. Before the first chemical stimulus, the buffer solution is administrated to allow the identification of the fluorescence baseline.

In mechanical stimulation experiments, the two reservoirs are filled with neutral solution (S-basal) and maintained both at the same pressure throughout the experiment. Experiments are performed at four values of supply pressure: 100 mbar, 200 mbar, 300 mbar, and 400 mbar. The mechanical stimulus is obtained through a fast (<100 ms) switch of the supply reservoir, i.e. one reservoir is closed and simultaneously the other is opened, and vice versa (Dr. D. Caprini, private communication) [41]. In this way, the nematodes experience transient changes of the pressure and flow velocity at every opening and closing of the valves [41]. The pressure stress (normal component) and shear stress (tangential component) inside the arena are studied with dedicated simulations (Dr. D. Caprini, private communication) to test the effect of electrovalves closing and opening [41]. These simulations show that, after the reservoir switch, the stationary regime inside the chip is restored in less than 100 ms, providing a short mechanical stimulus to the neuron. During the experiments, the nematodes are exposed to six consecutive mechanical stimuli, delivered with 25 s intervals. The intensity of the mechanical stimulus was regulated by changing the supply pressure between 100 mbar and 400 mbar [41].

3.1.5 Data analysis

Collected fluorescence data are analysed employing in-house developed MATLAB scripts. The images are pretreated by subtracting a mean background averaged over the 10 initial background frames and reducing noise with an averaging filter. A graphical interface (GUI) allows drawing the region of interest (ROI) containing the nematode head at a reference frame. Based on this information, the software tracks this position in both

temporal directions by searching the maximum intensity averaged in a region of 10x10 pixels area within 30 pixels from the assigned neuronal position. The normalized calcium response is calculated as:

$$I(t) = \frac{\Delta F(t)}{F_0},\qquad(3.1)$$

where $F(t)$ is the fluorescence recorded at a time t, $\Delta F(t) = F(t) - F_{background}$ is the background corrected and integrated fluorescent trace, and F_0 is calculated as the mean fluorescence in the first 5 s of a stimulus free window. Normalized traces are averaged across 3-5 trials for each animal. Further analyses performed on the traces such as the calculation of the mean response across different animals and temporal characteristic analysis have been performed standard built-in MATLAB functions.

3.1.6   Patch-clamp technique

The patch-clamp technique is widely used method to study the electrophysiological properties of biological cells. This technique invented by Erwin Neher and Bert Sakmann, in 1976, determined a revolutionary breakthrough in the understanding of cellular and molecular biology [246]. In patch-clamp experiments, a recording AgCl electrode is placed inside a glass pipette filled with a suitable solution, that is pressed on the cell surface (Fig. 3.2). In the right conditions, the cell membrane attaches to the pipette forming the so-called "tight seal". In this way, the small patch of the membrane is insulated from the rest of the membrane and the environment. This approach considerably reduces the noise compared to the previous recording technique, in which the tissue is impaled with a sharp electrode. The patch-clamp technique allows the study of both whole-cell currents (in the cell-attached and whole-cell configurations) and single-channel currents (in the inside-out and outside-out configurations), depending on the chosen configuration. Most of the experimental data used as a reference for this work have been acquired in the whole-cell configuration. In this configuration, both intra- and extra-cellular environments can be controlled during the experiment(Fig. 3.2). Patch-clamp experiments can be performed by delivering to the cell two different kinds of stimuli. In the "voltage-clamp" mode, the membrane potential is clamped to a fixed value imposed by the experimenter, so that the total ionic current of the cell can be recorded by the same electrode. Conversely, in the "current-clamp" mode the cell is stimulated by injecting a current pulse of fixed amplitude, so that the membrane voltage could be recorded. Also, since both the intracellular and extracellular environments can be fully controlled, it is possible to administrate specific pharmacological agents to selectively block different channels, thereby allowing the dissection of their contribution to the overall cell behaviour.
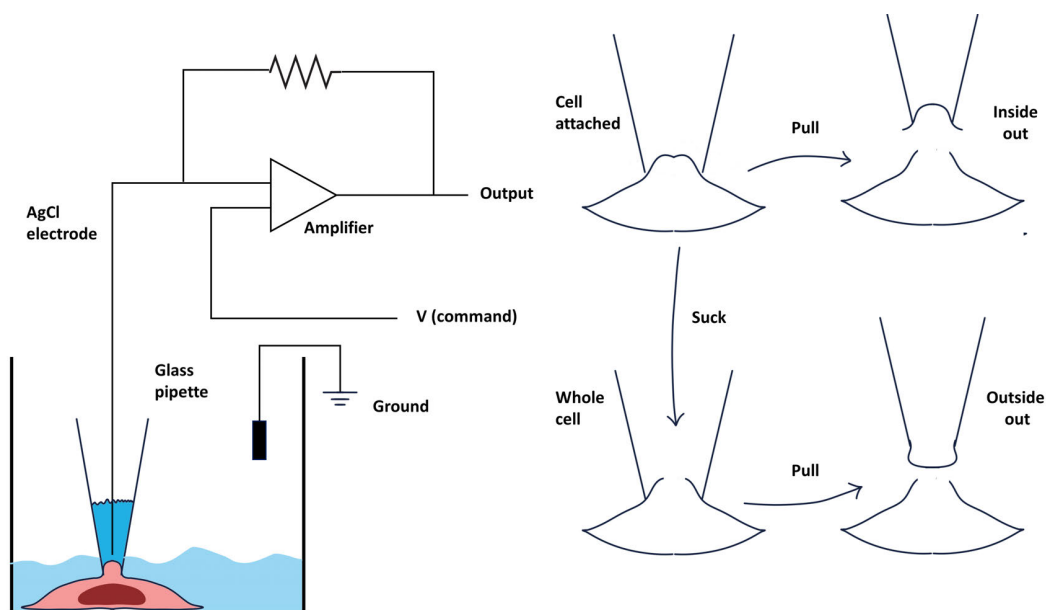
Figure 3.2: **The patch-clamp technique** The illustration shows the basic principles of the patch-clamp technique as well as the different configurations that are used in experimental recordings. On the left, the basic configuration of single-electrode patch-clamp is shown. In the single-electrode patch-clamp the AgCl electrode is used to stimulate the cells and record the current/voltage. On the right, the different configurations are shown. The cell-attached configuration is the precursor of all the configurations and is reached by pressing a glass micropipette on the cell surface and so that a small patch of membrane attaches to the pipette forming the "Giga seal" (1-10 GΩ). Then by pulling the pipette, the isolated patch is detached from the cell, reaching the inside-out configuration, which is particularly suitable for studying single-channels whose gating is modulated by internal ligands. If in cell-attached configuration a gentle suction is applied, the patch breaks and access to cell interior is gained. This configuration is called "whole-cell" configuration and is widely used to record both whole-cell ionic currents or the voltage in response to current injection. From the whole-cell configuration, the outside-out configuration can be reached by pulling the pipette until the two pieces of the membrane are torn from the cell and reconnect to leave the exterior surface exposed to the bath solution. This configuration is suitable for single-channel recordings on channels modulated by external ligands.

3.2 Calcium imaging results

In this section, experimental results on WT and mutants worms, based on calcium imaging experiments are presented. In the following, a brief description of the traces and of the acquisition protocol is reported, while the discussion and interpretation of the results, with respect to the computational results obtained by the candidate, are given in Chapter 5, Section 5.4.

3.2.1 AWC^{ON} neurons sensing of chemical and mechanical stimuli

Calcium imaging experiments performed on WT and mutant worms harbouring the GCaMP5a indicator have been performed at the CLNS@Sapienza-IIT, using two stimulation protocols to deliver chemical and mechanical stimuli, respectively.

The first set of experiments has been performed on WT worms, using the chemical stimulation protocol (Fig. 3.3).
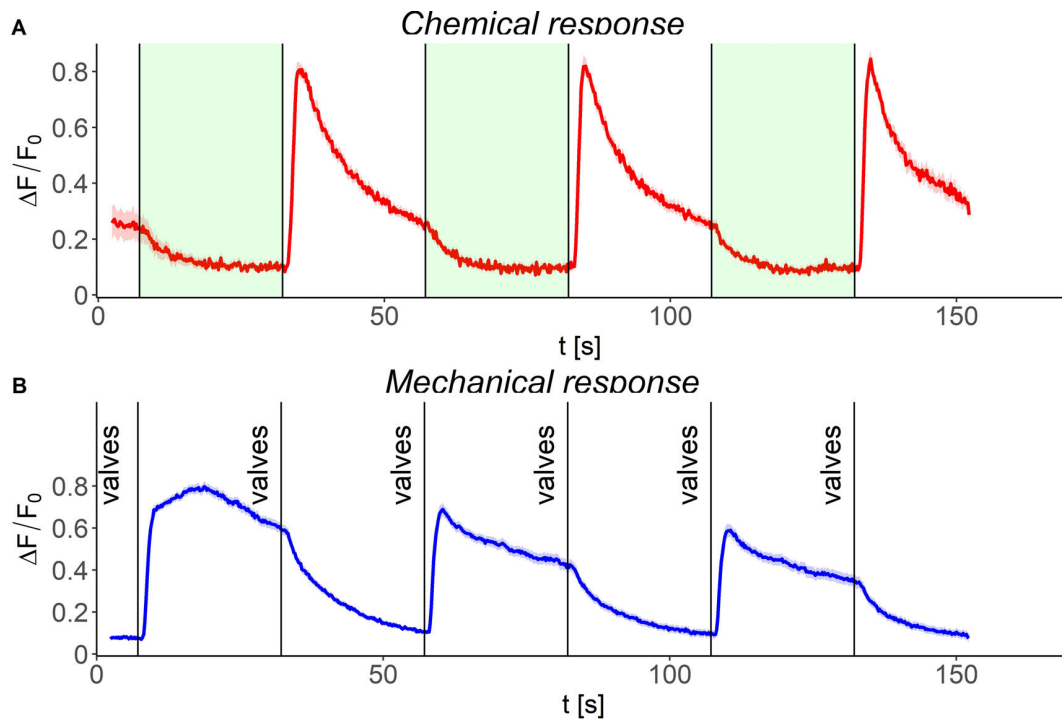
Figure 3.3: **AWC^{ON} response to chemical and mechanical stimuli**. **A) Chemical response** The panel shows the response of the neuron to chemical stimuli (IAA 10^{-5}) recorded in the mini-pulse arena of n>10 animals. The shaded green area indicates the odorant administration, while the shaded red area represents the standard error of the mean. **B) Mechanical response** The panel shows the mean (n>10) fluorescence responses of AWC^{ON} neurons to sequential mechanical stimuli (100 mbar) recorded in the mini-pulse arena. The shaded blue area represents the standard error of the mean. Experiments have been performed at the CLNS@Sapienza-IIT. The candidate has analysed the row traces to compute the average traces and s.e.m.

Upon chemical stimulation, the neuron undergoes to a decrease of intracellular calcium below the resting level, followed by a transient increase when the stimulus is removed (Fig. 3.3 A). Once the peak is reached, the calcium slowly returns to the initial level with an exponential decay (Fig. 3.3 A). This behaviour represents the characteristic ODOR-OFF response of AWC^{ON} neurons, widely reported in literature (e.g., [13, 42, 100]). Interestingly, AWC^{ON} neurons are capable of responding to mechanical stimuli

delivered by fast (<100 ms) opening and closing of the valves that regulate flow rate
inside the mini-pulse-arena (Fig. 3.3 B). Upon mechanical stimulation, the neuron seems
to display plateau-like responses of the intracellular calcium. When the stimulus is
applied, AWC^{ON} undergoes a calcium increase followed by a plateau phase, in which
the calcium stabilises in a high-concentration state until a second mechanical stimulus
is delivered (Fig. 3.3 B).

To investigate the role of voltage-gated calcium channels in AWC^{ON} neuron responses,
calcium imaging experiments on mutants for *egl-19*, *cca-1*, and *nca-2* have been per-
formed in both the experimental configurations (Fig. 3.4).
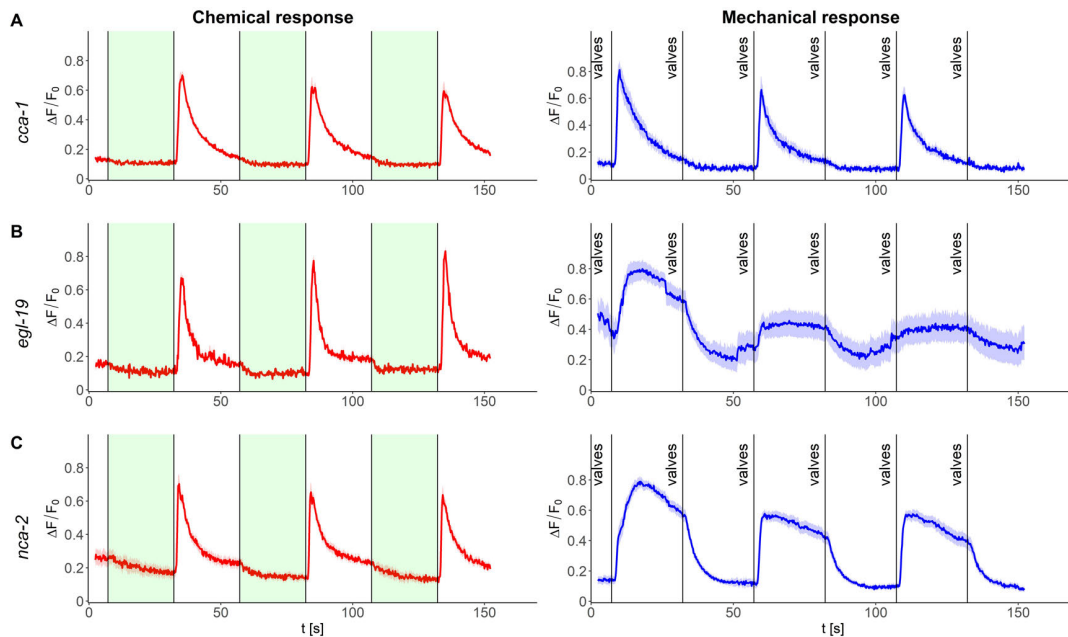
Figure 3.4: ***egl-19*, *cca-1*, and *nca-2* mutant responses to chemical and mechanical
stimuli. A)-C). *cca-1*, *egl-19* and *nca-2* responses**. Panels on the left show the mean
($n > 5$) ±s.e.m responses to IAA 10^{-5} of *cca-1* (A), *egl-19* (B), and *nca-2* (C) mutants. In
the right column the mean ($n > 5$) ±s.e.m. responses to a mechanical stimulus (100 mbar of
supply pressure) of *cca-1*, *egl-19*, and *nca-2* mutants. Experiments have been performed at the
CLNS@Sapienza-IIT. The candidate has analysed the raw traces to compute the average and
s.e.m. Same data of Fig. 5.21 in Chapter 5.

cca-1 mutants chemical responses are not considerably altered (Fig. 3.3 A), and display
the classic ODOR-OFF behaviour (Fig. 3.4 A left). Instead, the responses to mechanical
stimuli display a transient behaviour (Fig. 3.3 A right). The mechanical stimulation
elicits the neuron activation, but after the initial increase, the calcium returns to the
initial level, instead of stabilizing into the higher plateau. Notably, the neuron still
activates at alternating stimuli, indicating that the neuron is still in a non-excitable
state, when the second stimulus is delivered.

egl-19 mutants display the classical chemical responses with no appreciable alterations

compared to WT (Fig. 3.3 B left). Upon mechanical stimulation, *egl-19* mutants still show the plateau responses. However, compared to the WT responses these mutants display a slower rising phase and decreased fluorescence responses, especially after the second stimulus (Fig. 3.3 B right). The responses directly reach the plateau level without exhibiting the initial peak observed in the WT (Fig. 3.3 B right).

Finally, *nca-2* mutants display almost normal chemical and mechanical responses resembling those of WT (Fig. 3.3 C, and Fig. 3.3).

The experimental results presented above highlighted a possible role of AWC^{ON} neurons as mechanosensory neurons. To further elucidate this aspect, other calcium imaging experiments have been performed.

Firstly, the responses of the neurons have been tested for different intensities of the mechanical stimulus (Fig. 3.5).
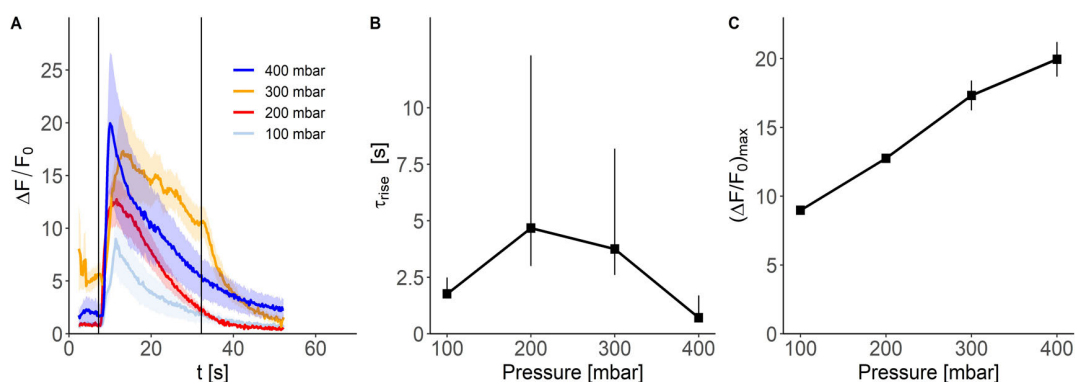
Figure 3.5: **AWC^{ON} response to mechanical stimuli. A) Recorded fluorescence traces at different supplied pressure in the mini-pulse arena**. The panel shows the mean responses $\pm$s.e.m of WT worms subjected to four different mechanical stimuli. The supply pressure is between 100 mbar and 400 mbar. **B) Time to peaks analysis**. The rising time is calculated by performing a linear fit on the linearised fluorescence traces obtained by taking the natural logarithm of the signal. The error bars represent the 95% confidence interval. **C) Fluorescence peak intensity of the recorded traces as a function of pressure**. The peak intensity for each trace reported in Panel A is calculated as the maximum of the signal and plotted with its s.e.m. The experiments have been performed at CLNS@Sapienza-IIT. The candidate has analysed the row traces to compute the average and s.e.m. She also performed the analyses shown in panels B and C. Same data of Fig. 5.18 in Chapter 5.

In these experiments the intensity of the mechanical stimulus is varied by changing the the supply pressure of the reservoirs between 100 mbar and 400 mbar. The buffer is delivered for 10 s from the first reservoir, then for 25 s from the second reservoir, and finally for 20 s from the first reservoir. All the tested animals respond to valve switches with increased fluorescence values for each tested pressure (Fig. 3.5 A). Notably, the peak intensity for the 100 mbar curve is almost 50% lower than that of the 400 mbar, indicating that higher pressure elicits higher responses in the neurons (Fig. 3.5 A and C). The rising phase of the peak is influenced by the pressure, with a non-linear trend (Fig. 3.5 B).
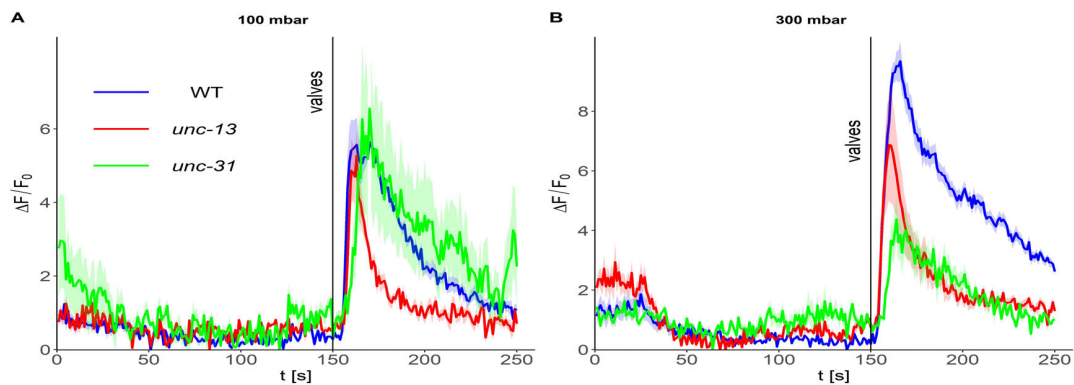
Figure 3.6: **Unc-13 and unc-31 mutant responses to mechanical stimuli**. **A) Average responses for 100 mbar supply pressure**. The panel shows the average ($n > 5$) responses of WT, *unc-13* and *unc-31* mutants to a mechanical stimulus delivered with a 100 mbar supply pressure in the reservoirs. The shaded areas represent the standard error of the mean. **B) Average responses for 300 mbar supply pressure**. The panel shows the average ($n > 5$) WT responses, *unc-13*, and *unc-31* mutants to a mechanical stimulus delivered with a 300 mbar supply pressure in the reservoirs. The shaded areas represent the standard error of the mean. The experimental recordings and data analysis have been performed at the CLNS@Sapienza-IIT. Same data of Fig. 5.19 in Chapter 5

Secondly, to elucidate whether these responses to mechanical stimuli are intrinsic or not, two mutants, defective for synaptic communication, have been selected for testing. *unc-13* and *unc-31* are involved in small and dense-core synaptic vesicles release, respectively [17, 247, 248], and thereby their suppression guarantees an almost complete separation of the neurons from the network that may elicit their mechanical responses. *unc-13* and *unc-31* mutants have been tested in the same experimental conditions of WT worms at 100 mbar and 300 mbar. At 100 mbar no significant differences have been observed between WT and mutant worms, while at 300 mbar the mutants responses are considerably reduced in magnitude (Fig. 3.6 A-B). These results suggest that AWC^{ON} mechanosensitivity is intrinsic for low intensity stimuli. While at increasing stimuli, additional sensory mechanisms may be involved, for example those responsible for the harsh touch sensation.

Finally, as the staring point of an extensive investigation of the mechanisms at basis of AWC^{ON} putative mechanosensitivity, *osm-9* and *tax-4* mutants have been tested.

OSM-9 channels are a class of TRPV channels known to be involved in *C. elegans* mechanosensation and are expressed in AWC^{ON} [249, 250, 251]. The *tax-4* gene encoded for a class of cyclic-nucleotide-gated channels that in AWC^{ON} neurons downstream the GPCRs signalling pathway [252]. Calcium imaging experiments on *osm-9* mutants show that the mutants still respond to mechanical stimuli with no significant differences from WT, and show normal chemical responses (Fig. 3.7 A-B). In contrast, *tax-4* mutants do not respond to both chemical and mechanical stimuli, suggesting that these channels are involved in both the signalling transduction pathways (Fig. 3.7 C-D).
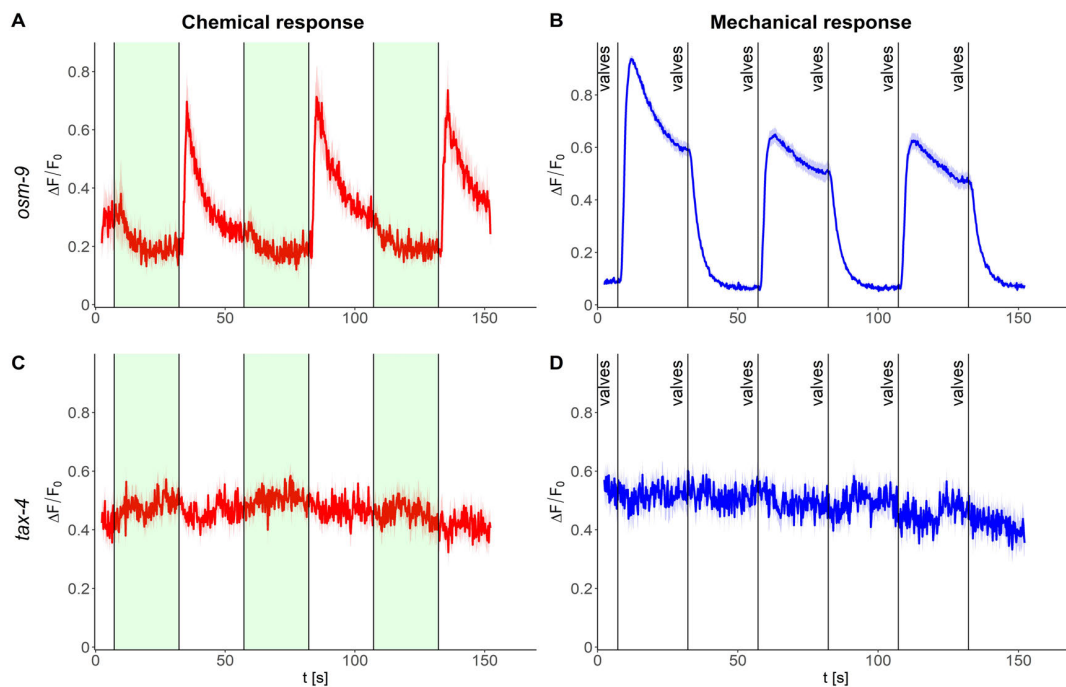
Figure 3.7: *osm-9* and *tax-4* mutant responses to mechanical and chemical stimuli.
A)-B) *osm-9* responses to chemical and mechanical stimuli. The panels show the average
responses ($n > 10$) of the *osm-9* mutant to chemical (A, IAA 10^{-5}) and mechanical stimuli (B,
100 mbar of supply pressure). The shaded areas indicate the s.e.m. **C)-D)** *tax-4* responses to
chemical and mechanical stimuli. The panels show the average responses ($n > 10$) of the *tax-4* mutant to chemical (A, IAA 10^{-5}) and mechanical stimuli (B, 100 mbar of supply pressure).
The shaded areas indicate the s.e.m. The experiments have been performed at CLNS@Sapienza-
IIT. The candidate has analysed the row traces to compute the average and s.e.m.

Chapter 4

Ionic currents modeling

69

In this chapter, the models of the single ionic currents that are known to participate in the nematode neuronal and muscular electrical activity are described. For each ionic current, the salient electrophysiological characteristics are described, and the corresponding figures report the activation and/or inactivation steady-state curves and time constants, as well as the simulated currents. If not otherwise stated in the description of the specific current, the equations used to model the currents are reported below. For further details about the modelling procedure and parameter fitting see Chapter 2 Sections 2.1.2, 2.2 and 2.3

$$I_x \quad = g_x m_x^p h_x^q (V - V_x) \tag{4.1}$$

$$\frac{dm_x}{dt} \quad = \frac{m_{x,\infty}(V) - m_x}{\tau_{m_x}(V)} \tag{4.2}$$

$$\frac{dh_x}{dt} \quad = \frac{h_{x,\infty}(V) - h_x}{\tau_{h_x}(V)} \tag{4.3}$$

$$m_{x,\infty}(V) \quad = \frac{1}{1 + e^{\left[\frac{-(V - V_{0.5})}{k_a}\right]}} \tag{4.4}$$

$$h_{x,\infty}(V) \quad = \frac{1}{1 + e^{\left[\frac{(V - V_{0.5})}{k_i}\right]}} \tag{4.5}$$

$$\tau_{m_x}(V) \quad = \tau_{h_x}(V) = \frac{a}{1 + e^{\frac{(V - b)}{c}}} + d \,. \tag{4.6}$$

In the following description, the genes encoding for the membrane channels are denoted in *italic*, the corresponding proteins in capital roman letters (e.g., *egl-19* encodes for EGL-19 channels) The corresponding ionic currents are denoted in capital roman letter without the dash between the gene name and the number (e.g., EGL-19 channels carry EGL19 currents).

4.1 Potassium channels

4.1.1 2TM family

IRK1/3 IRK channels are inward rectifier channels that give rise to sustained currents at very negative potentials, i.e., below -80 mV. This peculiar characteristic is reflected by the activation curve with an half activation voltage of -82 mV and saturation to 1 at potentials more negative than -100 mV, indicating that the complete activation of the channels is reached (Fig. 4.1 A). Activation time constants range between 4 ms and 8 ms and display a bell shape dependence described by Eq. 4.7 (Fig. 4.1 B).

$$\tau_{m_{\text{IRK}}}(V) = \frac{a}{e^{\frac{-(V - b)}{c}} + e^{\frac{(V - d)}{\tilde{e}}}} + f \tag{4.7}$$

When the delivered voltage stimulus is above the potassium resting potential (-80 mV) the current becomes outward and shows a sharp initial peak followed by a small steady-state current (Fig 4.1 C). This behaviour is consistent with that observed for *C. elegans*
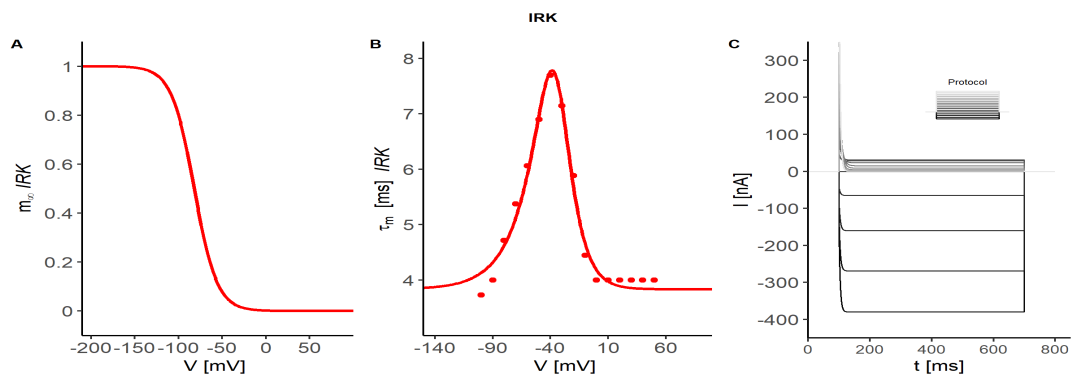
Figure 4.1: **IRK currents model**. **A)** Steady state activation curve for IRK currents ($V_{0.5}^a = -82$ mV, $K_a = 13$ mV) . **B)** Activation time constants fitting results. Experimental data from [151] are fitted to Eq. 4.7 ($a = 17.08$ ms, $b = -17.82$ mV, $c = 20.32$ mV, $d = -43.44$ mV, $e = 11.17$ mV, and $f = 3.83$ mV). **C).** Simulated IRK currents. The panel shows IRK currents obtained during a voltage clamp simulation consisting of 17 voltage steps between -120 mV and 40 mV with a duration of 600 ms and a holding potential of -80 mV. The simulation has been performed in XPPAUT using the "stiff" integration method. Figure Adapted from [38].

IRK-1 channels expressed *Xenopus* oocytes [149]. However, in the absence of a detailed characterization of their kinetics, reference data from rat and *Aplysia californica* are used to build the model [150, 151]. The complete list of model equations is reported in Appendix A, Eqs. A1-A3 and the corresponding parameters are listed in Appendix B Table B1.

4.1.2 6 TM family

SHK1
Patch-clamp data from cultured *C.elegans* myocytes show that *Shaker* is a rapidly activating and slowly inactivating current [138]. Steady-state activation and inactivation curves are shifted to more positive potentials and steeper compared to that of *Shal* currents (Fig. 4.2 A, and Fig. 4.5 A in the SHL1 currents section), indicating a very low contribution of SHK-1 currents at negative potentials. Activation time constants exhibit a voltage dependence described by a bell-shaped curve with a maximum of ~ 17 ms at -35 mV (Eq. 4.8 and Fig. 4.2 B). For higher and lower potentials, the activation time exponentially decreases up to less than 5 ms for voltages below -70 mV and above 0 mV. In contrast, inactivation time is voltage-independent [141] and in the seconds scale, being considerably slower than the activation time scale ($\tau_{h_{\text{SHK1}}} = 1400$ ms). Specific equations and parameters used to fine-tune *Shaker* activation and inactivation variables [138] and time constants [141] are listed in Appendix A, Eqs. A5-A8, and Appendix B Table B1, respectively.

$$\tau_{SHK1}^m = \frac{a}{e^{\frac{v-b}{c}} + e^{\frac{-(v-b)}{d}}} + e. \tag{4.8}$$
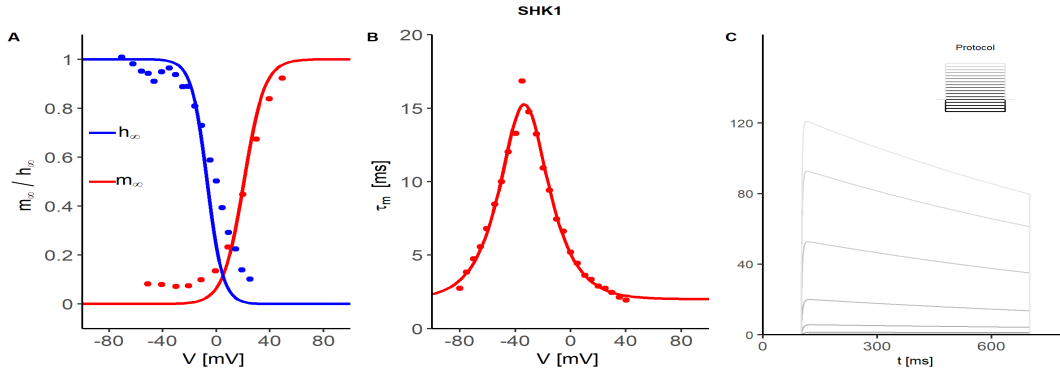
Figure 4.2: **SHK1 currents model**. **A)** Steady state activation (red) and inactivation (blue) curves [138] and corresponding experimental points from [138] ($V_{0.5}^a = (20.4 \pm 2)$ mV, $K_a = (7.7 \pm 1, 1)$ mV, $V_{0.5}^i = (-6.95 \pm 1.7)$ mV, and $K_i = (5.8 \pm 0.5)$ mV). **B)** Activation time constants fitting results. Experimental points from [141] (points) are fitted to Eq. 4.8 ($a = 26.6$ ms, $b = -33.7$ mV, $c = 15.8$ mV, $d = -33.7$ mV, $\tilde{e} = 15.4$ mV, and $f = 2.0$ ms). **C)** Voltage clamp simulation of SHK1 currents. The simulation protocol, sketched in the inset, consisted of 17 voltage steps between -120 mV and 40 mV lasting 600 ms. The maximal conductance was set to $\bar{g}_{SHK1} = 1.1$ nS to reproduce the experimental currents showed in [138], and the holding potential was $V_h = -80$ mV. The simulation is conducted in XPPAUT using the "stiff" integration method. Figure Adapted from [38].

EXP2

EXP-2 channels are voltage-gated channels peculiar to *C. elegans* [171]. EXP2 currents behave similarly to human ether-a-go-go channels, being essential for muscular action potential repolarization [142]. When subjected to a depolarizing stimulus between -60 mV and 60 mV, EXP-2 channels give rise to little outward currents (Fig. 4.3 D) [142, 171, 172, 253, 254] with a midpoint of activation at -17 mV. [142, 171] (Fig. 4.3 A). Activation time constants show a strong voltage dependence ranging from $\sim$50 ms at 20 mV to 788 ms at -20 mV. A second repolarizing stimulus of -120 mV elicits large tail currents, characteristic of the inward rectifier channels. EXP2 currents inactivation is characterized by ultrafast and voltage-dependent time constants in the sub-millisecond scale (Fig. 4.3 C). In absence of an explicit report of steady-state inactivation curve for EXP2, the steady-state inactivation function is modelled to reproduce the recorded currents [142] (Fig. 4.3 A); thus the midpoint of activation is chosen at -33.5 mV and the slope at -15.8 mV, according to [255]. Activation and inactivation time constants from [171] are fitted to Eqs. 4.10 and 4.11, respectively (Fig. 4.3 B-C). Model equations and parameters are listed in Appendix A, Eqs. A9-A13, and Appendix B Table B1, respectively.

$$\tau_{EXP2}^m = \frac{a}{e^{\frac{(V-b)}{c}} + e^{\frac{-(V-d)}{e}}} + f \qquad (4.9)$$

$$\tau_{\text{EXP2}}^h = \left\{ \frac{a}{1 + e^{\frac{(V-b)}{c}}} + d \right\} \cdot \left\{ \frac{a}{1 + e^{\frac{-(V-b)}{c}}} + d \right\}, \tag{4.10}$$

$$I_{\text{EXP2}} = \bar{g}_{\text{EXP2}} \cdot m \cdot h^3 \cdot (V - V_K) \tag{4.11}$$
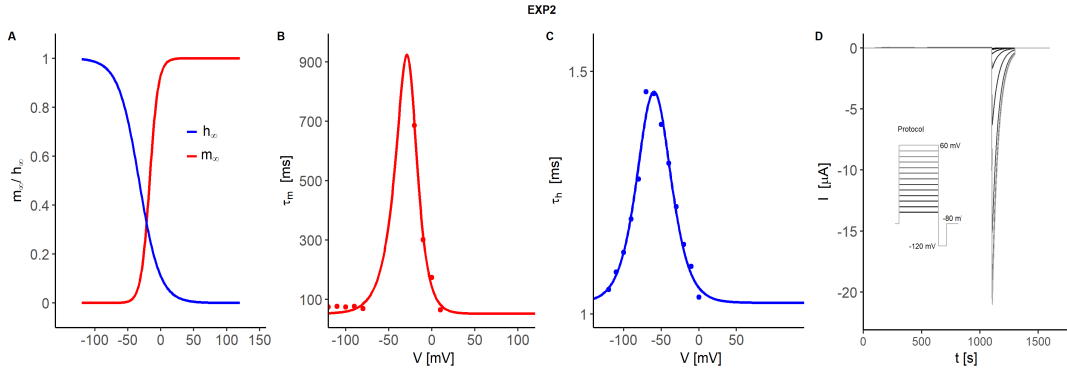
Figure 4.3: **EXP2 currents model**. **A)** Steady state activation (red) and inactivation (blue) curves ($V_{0.5}^a = (-17 \pm 2)$ mV, $K_a = (6.5 \pm 0.3)$ mV, $V_{0.5}^i = -50$ mV, $K_i = 10$ mV). The activation curve parameters are taken from [142, 171], while the inactivation curve parameters are defined by hand to match experimental data [142, 171]. **B)** Activation time constants as a function of voltage. Experimental points from [171] are fitted to Eq. 4.9 ($a = 209.11$ ms, $b = -7.53$ mV, $c = 9.18$ mV, $d = -55.20$ mV, $e = 13.46$ mV, $f = 51.22$ ms) (Errors on parameter fitting are not reported due to the lack of sufficient data to ensure an accurate fitting). **C)** Inactivation time constants as a function of voltage. Experimental points from [171] are fitted to Eq. 4.10 ($a = (1.31 \pm 0.08)$ ms, $b = (-59.77 \pm 2.02)$ mV, $c = (15.03 \pm 2.93)$ mV, $d = (0.55 \pm 0.04)$ ms). **D)** Voltage clamp simulation of EXP2 currents. The simulation protocol, sketched in the insert, consists in two voltage steps. The first step has a duration of 1000 ms and its amplitude has been ranged between -60 mV and 60 mV. The second step has a fixed amplitude of 120 mV and a duration of 200 ms. The simulation protocol has been defined according to [142, 171]. The maximal conductance was $\bar{g}_{\text{EXP2}} = 0.6$ mS, and the holding potential was $V_h = -80$ mV. The simulation has been conducted in XPPAUT using the "stiff" integration method.

EGL36.

Patch-clamp recordings on EGL-36 (KV3) channels, expressed in *Xenopus* oocytes, suggest that *C.elegans Shaw* currents are similar to Kv3.1 and Kv3.2 mammalian currents, showing fast activation and no inactivation (Fig 4.4C). The current activates at high voltages, being almost totally deactivated at negative potentials. Current waveforms, evoked by voltage depolarizing steps, are fitted by three exponential functions, with different characteristic time scales, indicating the contribution of fast, medium, and slow activation processes. The three time constants, from about 10 ms up to 350 ms, are all insensitive to voltage [143].
Kv3 channel contribution is modelled with a non-inactivating Hodgkin-Huxley type current, including three almost equally-weighted components, activating at the afore-

mentioned time scales. For the sake of convenience, the expressions for the activation
variables, time constants, and ionic current are reported below:

$$m^{\mathrm{f}}_{\infty}(V) = m^{\mathrm{m}}_{\infty}(V) = m^{\mathrm{s}}_{\infty}(V) = \frac{1}{1 + e^{\frac{-(V - V_{0.5})}{k_a}}} \tag{4.12}$$

$$\tau^{\mathrm{f}}_{m} = \tau^{\mathrm{m}}_{m} = \tau^{\mathrm{s}}_{m} = a \tag{4.13}$$

$$I_{\mathrm{EGL36}} = \bar{g}_{\mathrm{EGL36}} \cdot \left(w_1\, m^{\mathrm{f}} + w_2\, m^{\mathrm{m}} + w_3\, m^{\mathrm{s}} \right) \cdot (V - V_K) \tag{4.14}$$

where $w_1 = 0.33$, $w_2 = 0.36$, and $w_3 = 0.39$ are the weights of the three activation
components [143]. The full list of equations and parameter values here obtained for *C.
elegans* EGL36 currents are reported in Appendix A, Eqs. A14-A16, listed in Appendix B
Table B1.
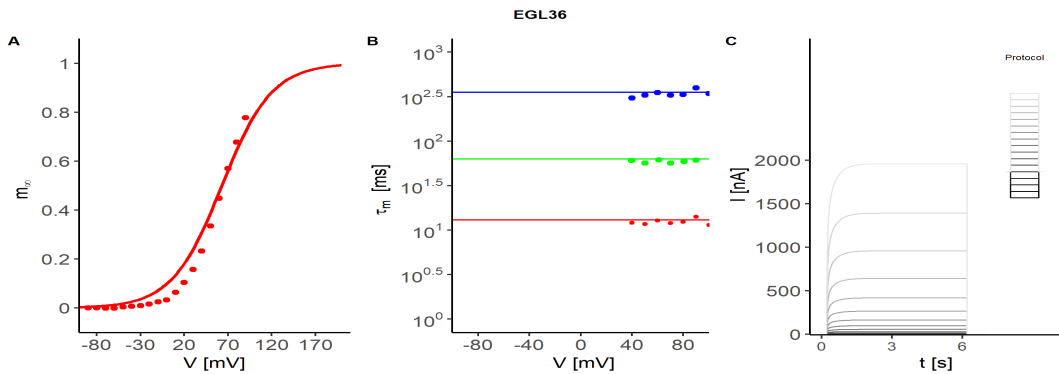
Figure 4.4: **EGL36 currents model**. **A)** Steady-state activation curve of EGL36 currents. The
curve and corresponding experimental points are obtained from [143] ($V_{0.5} = 63$ mV, $K_a = 28.5$
mV). **B)** Activation time constants from [143]. $\tau^{\mathrm{s}}_m = 355$ ms (in blue), $\tau^{\mathrm{m}}_m = 63$ ms (in green),
and $\tau^{\mathrm{f}}_m = 13$ ms (in red). **C)** Voltage clamp simulation of EGL36 currents. The simulation
protocol, consisted of 17 voltage steps between -120 and 40 mV, lasting 6 s. The maximal
conductance was set to $\bar{g}_{\mathrm{EGL36}} = 50$ nS to reproduce the experimental currents showed in [143],
and the holding potential was $V_h = -80$ mV. The simulation was performed in XPPAUT using
the "stiff" integration method. Figure Adapted from [38].

SHL1.

In response to depolarizing voltage steps, *Shal* currents are characterized by rapid activa-
tion and biexponential inactivation, with fast and slow components accounting for 70%
and 30% of the total current (Eq. 4.15), respectively [138]. SHL1 currents are modelled
based on voltage-clamp recordings in cultured *C.elegans* myocytes [138]. Steady-state ac-
tivation and inactivation are strongly voltage-dependent (Fig. 4.5 A, Eqs. 4.1 and 2.20),
as well as their respective time constants (Fig. 4.5B). The activation is characterized
by a time constant $\tau_m \simeq 18$ ms at V=-10 mV (Fig. 4.5 B), while fast and slow inac-
tivations are characterized by time constants of about 40 ms and 200 ms, respectively,
at depolarizing potentials (Fig. 4.5 C). Experimental data from [138] are used to fit

the equations 4.16 and 4.17. The full list of equations and parameter values here obtained for *C. elegans* SHL1 currents are reported in Appendix A, Eqs. A17-A21, listed in Appendix B Table B1.

$$I_{\text{SHL1}} = \overline{g}_{\text{SHL1}} \cdot m_{\text{SHL1}}^3 \cdot (0.7\, h_{\text{SHL1}}^{\text{f}} + 0.3\, h_{\text{SHL1}}^{\text{s}}) \cdot (V - V_K); \quad (4.15)$$

$$\tau_{SHL1}^m(V) = \frac{a}{e^{\frac{-(v-b)}{c}} + e^{\frac{(v-d)}{e}}} + f; \quad (4.16)$$

$$\tau_{SHL1}^{h_{f,s}}(V) = \frac{a}{e^{\frac{-(v-b)}{c}}} + d. \quad (4.17)$$
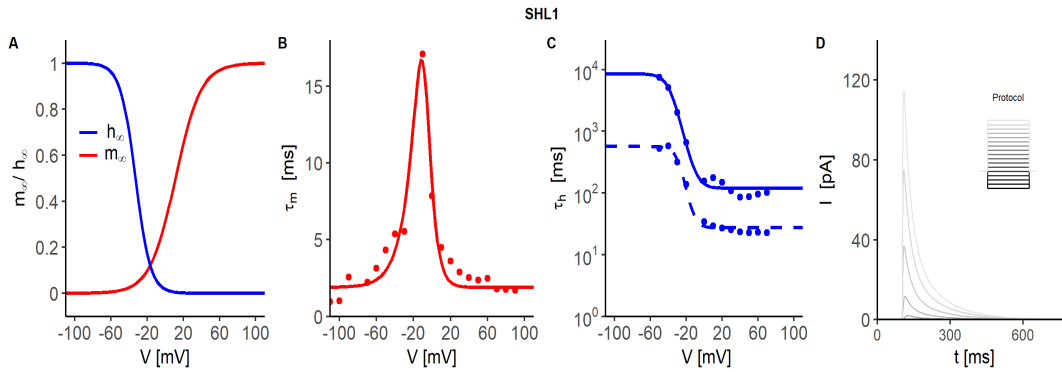
Figure 4.5: **SHL1 currents model**. **A)** Steady state activation (m_∞, red) and inactivation(h_∞, blue) curves from [138] ($V_{0.5}^a = (11.2 \pm 1.5)$ mV, $K_a = (14.1 \pm 1.04)$ mV, $V_{0.5}^i = (-33.1 \pm 1.20)$ mV, $K_i = (8.3 \pm 0.7)$ mV). **B)** Activation time constants. Experimental points are extracted from [138] (points) and fitted to Eq. 4.16 ($a = (13.80 \pm 1.2 \cdot 10^6)$ ms, $b = (-17.51 \pm 1.13)$ mV, $c = (12.92 \pm 10.39)$ mV, $d = (-3.71 \pm 0.57 \cdot 10^6)$ mV, $e = (6.49 \pm 7.57)$ mV, $f = (1.89 \pm 0.60)$ ms). **C)** Inactivation time constants fitting results. The experimental data from [138] are fitted to Eq. 4.17 ($a_f = (539.16 \pm 70.53)$ ms, $b_f = (-28.20 \pm 2.66)$ mV, $c_f = (4.92 \pm 2.39)$ mV, $d_f = (27.28 \pm 22.55)$ mV, $a_s = (8.42 \cdot 10^3 \pm 238.57)$ ms, $b_s = (-37.74 \pm 0.51)$ mV, $c_s = (6.38 \pm 0.33)$ mV, $d_s = (118.90 \pm 28.81)$ mV). The dashed and the solid lines represent the fitting curves for fast and slow constants, respectively. **D)** Voltage clamp simulation of SHL1 currents. The simulation protocol consists of 17 voltage steps between -120 mV and 40 mV. The step duration is 600 ms and the holding potential is $V_h = -80$ mV. The maximal conductance was set to $\overline{g}_{\text{SHL1}} = 1.8$ nS to reproduce the experimental currents showed in [138], and the holding potential was $V_h = -80$ mV. The simulation was conducted in XPPAUT using a stiff solver. Figure adapted from [38].

Based on experimental recordings on AWA neurons [21], a further model of SHL1 currents has been developed. The parameters for activation variable and inactivation time constants are derived by fitting experimental data for AWA neurons SHL1 currents [21], while activation time constants and inactivation variable parameters are manually tuned starting from the previous model to reproduce the currents. Also, with respect to the previous model, the weights of fast and slow components have been modified. In the AWA-derived model the fast component accounts for 80% of the total current and the slow for 20% (Eq. 4.18). Also, the exponent of the activation variable is changed to 1

(Eq. 4.18). The new parameters are listed in Appendix B Table B1 between brackets. In the single-neuron simulations, both the models of SHL1 currents have been used. The first model of SHL1 currents has been used in the model of AWC$^{\text{ON}}$ and RMD neurons, while the second model is inserted in the AIY and RIM neurons. When used in the AWC$^{\text{ON}}$ and RMD neurons, the new model of SHL1 currents does not cause significant changes in the neuronal dynamics.

$$I_{\text{SHL1}} = \bar{g}_{\text{SHL1}} \cdot m_{\text{SHL1}} \cdot (0.8 \, h_{\text{SHL1}}^{\text{f}} + 0.2 \, h_{\text{SHL1}}^{\text{s}}) \cdot (V - V_K); \qquad (4.18)$$

KQT.

In *C.elegans*, KQT channels give rise to M-type currents characterized by a slow activation [145]. Due to the lack of electrophysiology data on KQT2 currents, in the present work, only KQT1 and KQT3 models are presented.

   KQT1. When heterologously expressed in *Xenopus* oocytes, KQT-1 channels give rise to slowly-activating and non-inactivating outward rectifier currents [145] (Fig. 4.6 C). The currents activate at negative potentials with a half activation at -16 mV [145] (Fig. 4.6 A). Activation time constants have a sigmoidal dependence on voltage and range between ~ 5 s at negative potentials to ~ 500 ms at positive potentials (Fig. 4.6 B) [145]. The activation threshold is comparable with that of KQT3 currents, while the activation time constants are slower than KQT3 ones at the same voltage (Fig. 4.6 A-B and Fig 4.7 A-B). KQT1 activation variable and time constants are described with the standard Eqs. 4.4 and 4.6, and the corresponding parameters are listed in Appendix B Table B1. The full list of model equations is reported in Appendix A, Eqs. A22-A24.
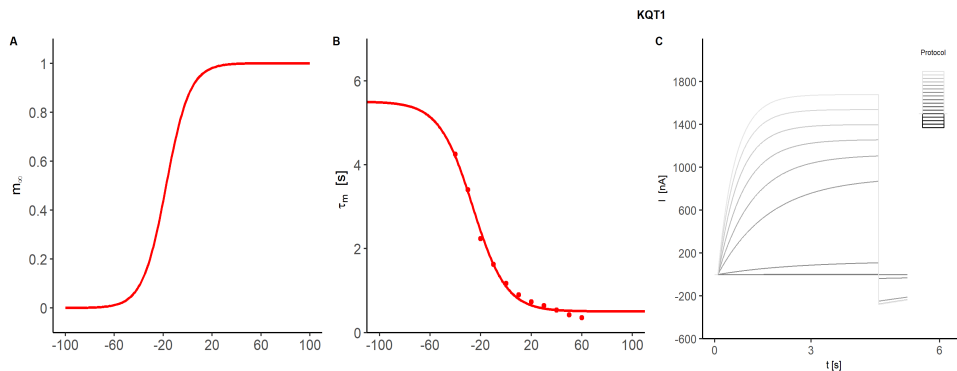
Figure 4.6: **KQT1 currents model**. **A)** Steady state activation curve ($V_{0.5}^{a} = -16$ mV, $K_a = 2.3$ mV) from [145]. **B)** Activation time constants fitting results. Experimental points from [145] are fitted to Eq. (Fitting parameters: $a = (5.0 \pm 1.9)$ s, $b = (-26.4 \pm 10.7)$ mV, $c = (13.3 \pm 5.7)$ mV, and $d = (0.5 \pm 0.2)$ s) **C)**. KQT-1 currents simulation. The simulation protocol consists of 17 voltage steps between -120 mV and 40 mV. The step duration is 6 s and the holding potential is $V_h = -80$ mV. The maximal conductance is set to $\bar{g}_{\text{KQT1}} = 14$ nS to reproduce the experimental recordings [145]. The simulation was conducted in XPPAUT using the stiff solver.

   KQT3. KQT3 currents recorded from heterologous expression in *Xenopus* oocytes

show a slow activation ($\tau_m \simeq 200$ ms), with a midpoint of -13 mV, and an almost absent inactivation, characteristic of M-type currents [145]. Given the absence of experimental data for time constants and inactivation kinetics on *C. elegans* KQT3, the model here presented is based on the one developed by [180] for KCNQ1, the mammalian homologue of KQT3. This model includes two activating components working at fast and slow time scales (m_f and m_s) and two inactivation variables (w and s, Eq. 4.21) (Fig. 4.7 A-C).
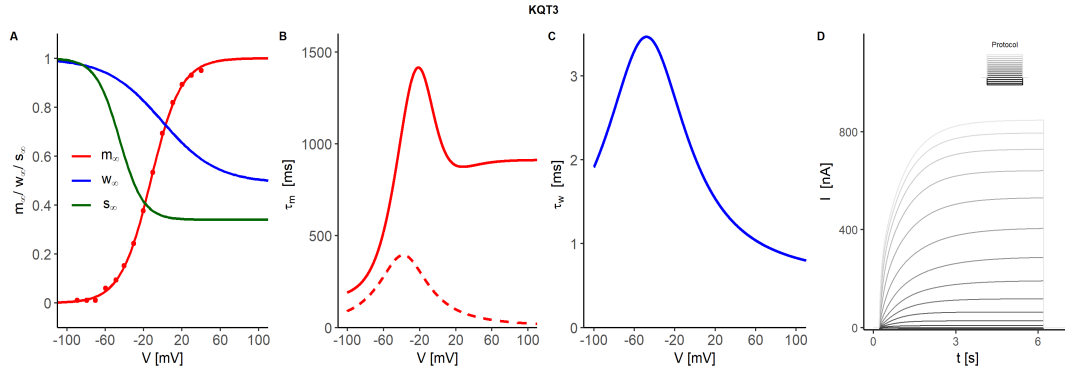
Figure 4.7: **KQT3 currents model**. **A)** Steady state activation (red) and incativation (blue and green) curves ($V_{0.5}^a = -12.8$ mV, $K_a = 15.8$ mV, $V_{0.5}^w = -1.1$ mV, $K_w = 28.8$ mV, $a_w = 0.5, b_w = 0.5$, $V_{0.5}^s = -45.3$ mV, $K_s = 12.3$ mV, $a_s = 0.3, b_s = 0.7$) from [145, 180]. **B)** Fast (dashed line) and slow (solid line) activation time constants as functions of voltage (Eqs. 4.19 and 4.20, for the parameter list see Appendix B, Table B1) [180]. **C)**. Inactivation time constants voltage-dependence described by Eq. 4.22 from [180]. **D)** Voltage clamp simulation of KQT3 currents. The simulation protocol consists of 17 voltage steps between -120 and 40 mV. The step duration is 6 s and the holding potential is $V_h = -80$ mV. The maximal conductance was set to $\bar{g}_{KQT3} = 36.5$ nS, to reproduce the experimental currents showed in [180]. The simulation is performed in XPPAUT using the a stiff solver. Figure adapted from [38].

The fast and slow components of activation account respectively for 30% and 70% of the total current, as in [180] (Eq. 4.23). The time constants for fast and slow activation and inactivation (w) show a voltage dependence described by Eqs. 4.19, 4.20 and 4.22, according to [180] (Fig. 4.7 B-C).

$$\tau_{KQT3}^{m,fast}(V) = \frac{a}{1 + \left(\frac{V+b}{c}\right)^2} \tag{4.19}$$

$$\tau_{KQT3}^{m,slow}(V) = a + \frac{b}{1 + 10^{-c(d-V)}} + \frac{e}{1 + 10^{-f(g+V)}} \tag{4.20}$$

$$w_{KQT3,\infty}(V) = s_{KQT3,\infty}(V) = a + \frac{b}{1 + e^{\frac{(V-V_{0.5})}{k_i}}} \tag{4.21}$$

$$\tau_{KQT3}^{w}(V) = a + \frac{b}{1 + \left(\frac{V-c}{d}\right)^2}, \tag{4.22}$$

$$I_{KQT3} = g_{KQT3}\left[0.3 m_f(t) + 0.7 m_s(t)\right] w(t)\, s(t)\,(V - V_K). \tag{4.23}$$

The time constant for s inactivation is chosen equal to 5 s, according to [180]. The parameter values for m_∞ are taken from [145], while the parameters for s_∞, w_∞ and the relative time constants are taken from [180]. The complete list of equations and parameters used is given Appendix A, Eqs. A25-A29, and in Appendix B Table B1.

Eag currents

EGL2. In response to voltage steps, EGL2 current shows similar properties compared to the mouse homologue *mEag*, and it is characterized by slow activation and absence of inactivation. EGL2 currents are here modelled with a single activation curve, fitted to reproduce the experimental data [146], and replicate the almost complete deactivation of the current at voltages below $\simeq -50$ mV (Fig. 4.8 A-C). Activation time constants show a marked voltage dependence at negative potentials and saturate around 1.5 s for voltages greater than -50 mV (Fig. 4.8 B). EGL2 model equations, and the corresponding parameters are listed in Appendix A, Eqs. A32-A34, and Appendix B, Table B1, respectively.
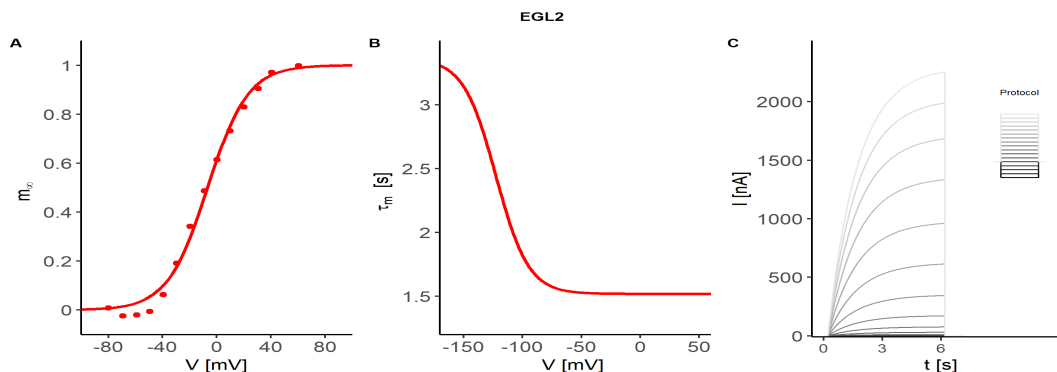
Figure 4.8: **EGL2 currents model**. **A)** Steady state activation curve. Experimental points from [146] are fitted to 4.4 ($V_{0.5}^a = (-6.9 \pm 2.20)$ mV, $K_a = (14.9 \pm 1.98)$ mV). **B)** Activation time constants as a function of voltage (Eq. 4.6, $a = 1845.8$ ms, $b = -122.6$ mV, $c = 13.8$ mV, and $d = 15.17.74$ ms). **C)** Voltage clamp simulation of EGL2 currents. The simulation protocol consists of 17 voltage steps between -120 mV and 40 mV. The stpe duration is 6 s, and the holding potential is $V_h = -80$ mV. The maximal conductance is set to $\bar{g}_{\text{EGL2}} = 20$ nS, to reproduce the experimental recordings in [146]. The simulation is conducted in XPPAUT using stiff solver. Figure adapted from [38].

UNC103. In the absence of a specific electrophysiological characterization of *C. elegans* UNC103 currents, the model here presented is based on electrophysiology data for the delayed rectifier currents of mammalian cardiac muscles [147]. In response to depolarizing voltage pulses, the currents start to activate at negative potentials around -50 mV with a steep voltage dependence (Fig. 4.9 A and D). Activation time constants show a bell-shaped voltage dependence, described by Eq. 4.24, and range between ∼100 ms and 1.7 s(Fig. 4.9 B). The currents increase progressively until -10 mV when the inactivation begins, and then starts to decrease. The return to the holding potential is characterized by large tail currents that saturate at 10 mV(Fig. 4.9 D). Inactivation time constants are

fast (the slowest is 18 ms) and voltage-dependent, as described by Eq. 4.25 (Fig. 4.9 C). The full list of equations and parameter values for activation/inactivation variable and time constants are reported in Appendix A, Eqs. A35-A39, and in Appendix B, Table B1, respectively.

$$\tau^m_{\text{UNC103}} = \left\{ \frac{a}{1 + e^{\frac{(V-b)}{c}}} + d \right\} \cdot \left\{ \frac{a}{1 + e^{\frac{-(V-b)}{c}}} + d \right\}, \quad (4.24)$$

$$\tau^h_{\text{UNC103}} = \left\{ \frac{a}{1 + e^{\frac{(V-b)}{c}}} + d \right\} \cdot \left\{ \frac{a}{1 + e^{\frac{-(V-b)}{c}}} + d \right\}, \quad (4.25)$$

$$I_{\text{UNC103}} = \bar{g}_{\text{UNC103}} \cdot m \cdot h \cdot (V - V_K) \quad (4.26)$$
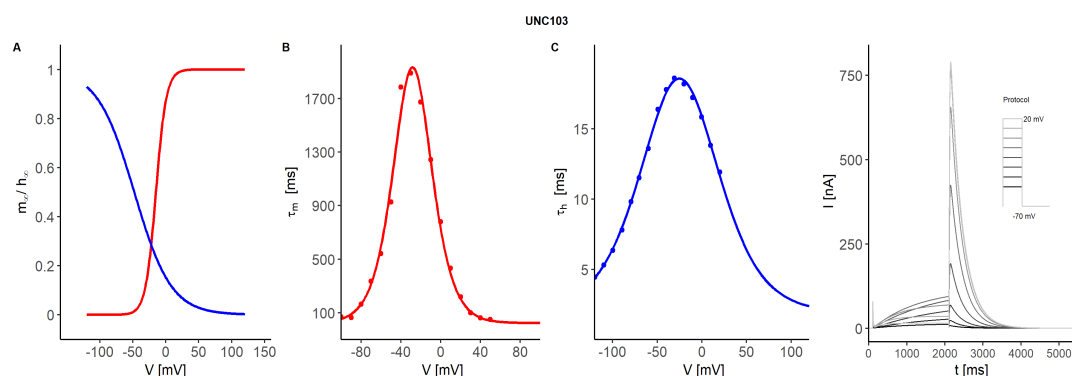
Figure 4.9: **UNC103 currents model**. **A)** Steady state activation and inactivation curves from [147] ($V^a_{0.5} = -15.1$ mV, $K_a = 7.85$ mV, $V^i_{0.5} = -49$ mV, $K_i = 28$ mV). **B)** Activation time constants as function of voltage. Experimental data from [147] are fitted to Eqs. 4.6 (Fit parameters: $a = (87.40 \pm 2.45)$ ms, $b = (-28.33 \pm 1.21)$ mV, $c = (13.10 \pm 1.13)$ mV, and $d = (0.26 \pm 0.70)$ ms). **C)** Inactivation time constants as function of voltage. Experimental data from [147] are fitted to Eqs. 4.6 (Fit parameters: $a = (8.16 \pm 0.21)$ ms, $b = (-25.19 \pm 0.96)$ mV, $c = (29.51 \pm 1.96)$ mV, and $d = (0.23 \pm 0.11)$ ms). **D)** Voltage clamp simulation of UNC103 currents. The simulation protocol, sketched in the insert, consists of 7 voltage steps between -50 mV and 20 mV. The step duration is 2 s, and the holding potential is $V_h = -70$ mV. The maximal conductance is set to $\bar{g}_{\text{UN103}} = 300$ μS to reproduce the experimental currents of [147]. The simulation is performed in XPPAUT using the "stiff" integration method.

KVS1.

KVS1 are A-type currents that activate at positive potentials and show almost no inactivation at negative potentials (Fig. 4.10 A, D). The currents start to activate at higher potentials compared to SHK1 and SHL1 currents, with a midpoint of 57.1 mV and a slope of 25 mV (Fig. 4.10 A) [144]. Also, inactivation is shifted to high potential with a midpoint of 47.3 mV and is steeper than the activation ($k_i = 11.1$ mV). Both activation and inactivation time constants display a sigmoidal dependence from voltage with activation time constants considerably faster than inactivation ones ($\tau_m = 4.36$ ms and

$\tau_h = 80.65$ ms at 60 mV) [144] (Fig. 4.10 B and C). The complete list of equations and parameters of the model is reported in Appendix A Eqs. A40-A43 and in Appendix B Table B1.
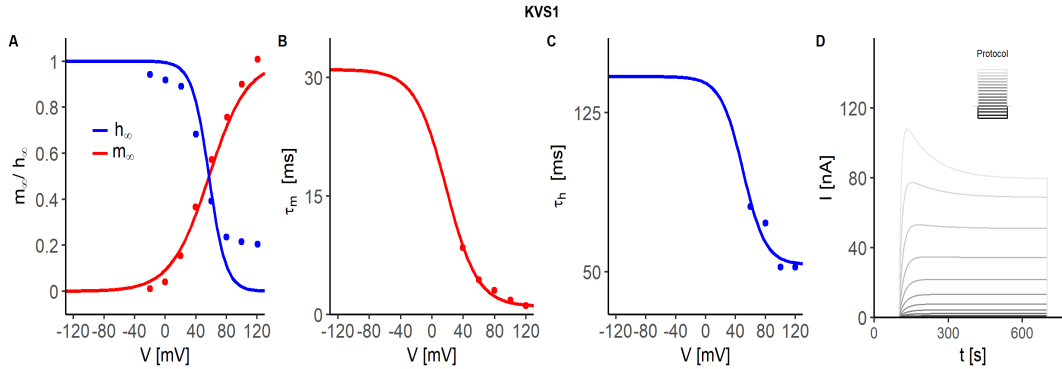
Figure 4.10: **KVS1 currents model**. **A)** Steady state activation (red) and inactivation (blue) curves with experimental data points [144] ($V_{0.5}^a = (47.3 \pm 4)$ mV, $K_a = (11.1 \pm 3.0)$ mV, $V_{0.5}^i = 57.1 \pm 6$ mV, $K_i = (25.0 \pm 2.0)$ mV). **B)** Activation time constants fitting results. Experimental data from [144] (points) are fitted to Eq. 4.6 (). **C)**, Fitting for inactivation time constants. The experimental values are extrated from [144] and fitted to Eq. 4.6. (Fit parameters: $a = (88.46 \pm 2.46)$ ms, $b = (50.00 \pm 1.21)$ mV, $c = (-15.00 \pm 1.12)$ mV, and $d = (53.41 \pm 0.10)$ ms). **D)** Voltage-clamp simulation of KVS1 currents. The simulation protocol, sketched in the inset, consists of 17 voltage steps between -80 mV and 40 mV. The step durations is 600 ms, and the holding potential is $V_h = -80$ mV. The maximal conductance was set to $\bar{g}_{SHL1} = 3.0$ nS to reproduce the experimental currents [144]. The simulation is conducted in XPPAUT using the stiff solver. Figure adapted from [38].

Calcium-regulated potassium channels

SLO1 and SLO2. SLO-1 and SLO-2 represent the big-conductance channels in *C. elegans* [162]. As their mammalian counterparts, SLO-1 and SLO-2 channels form complexes with L-type (EGL-19) and P/Q-type (UNC-2) CaVs [256]. As first step of the model development, isolated BK currents are modelled to reproduce the experimental data in [152] and [153]. Afterwards, the model of isolated SLO1 and SLO2 currents are coupled with the model of UNC2 and EGL19 currents (Section 4.2), assuming a 1:1 stoichiometry, to recreate the complex formed by the two channel species. As said, the chloride modulation of SLO2 [23, 206] is disregarded in this model due to the lack of reference data. The isolated BK channel model is developed according to [233], and the complete set of equations used to model the channels is reported in Chapter 2, Section 2.1.2. The model contains eight parameters, w_0^+, w_0^-, w_{yx}, w_{xy}, n_{yx}, n_{xy}, K_{yx}, and K_{xy}, as a function of which the half activation voltage and the slope of the activation curve can be written (Eqs. 2.25 and 2.28).
Model parameters are obtained by fitting simultaneously the activation variable and time constants [152, 153], using a hybrid genetic algorithm approach [233] (See Chapter 2 Section 2.3.1).
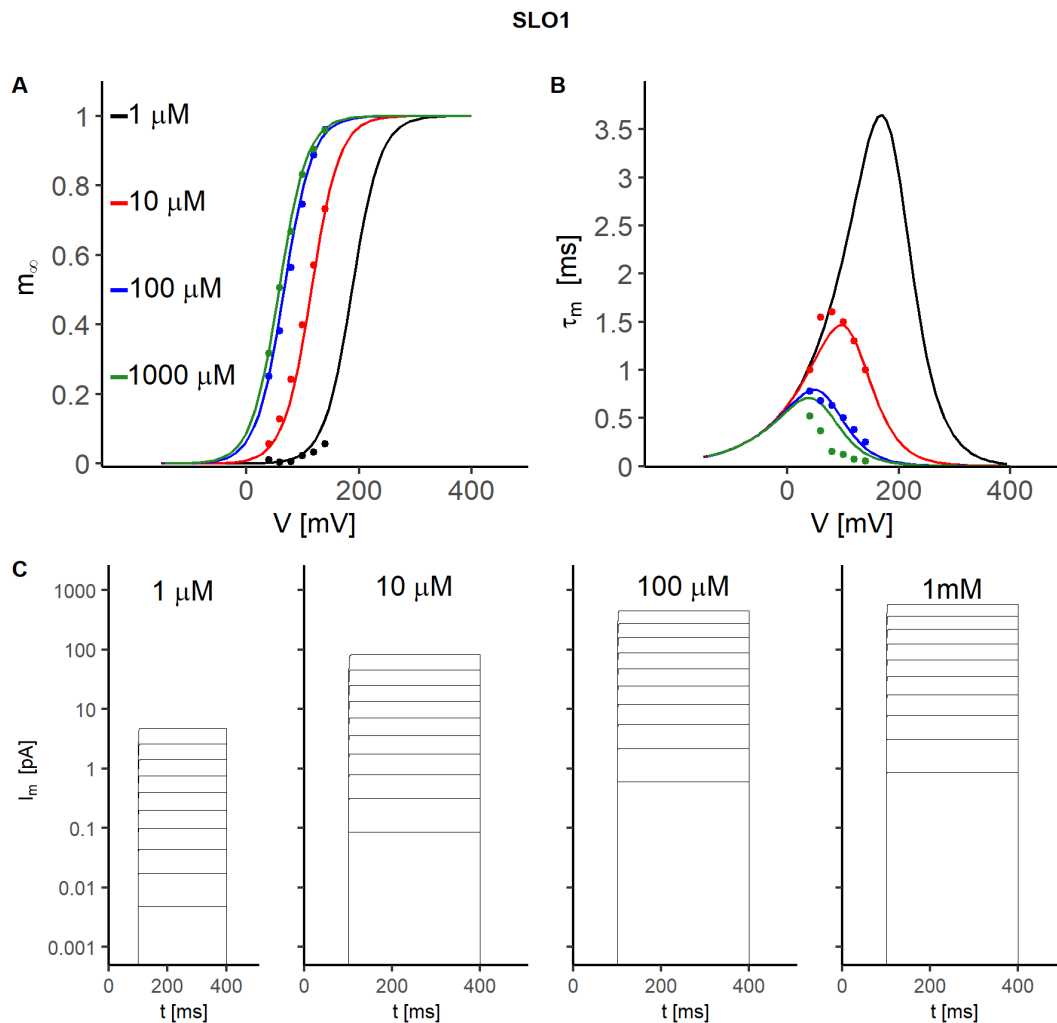
Figure 4.11: **Isolated SLO1 currents model. A)** Steady state activation fitting. Experimental data from [152] are fitted to Eqs. 2.25- 2.28. **B)** Activation time constants fitting. Experimental data [152] (points) are fitted to Eq. 2.28. **C).** Simulation of isolated SLO1 currents at $Ca^{2+} = 1, 10, 100, 1000\,\mu M$. The stimulation protocol consists in 13 voltage pulses ranging between -80 mV and 40 mV and. The step duration is 200 ms and the holding potential is $V_h = -80$ mV. The maximal conductance is assumed equal to $\bar{g}_{SLO1} = 15$ nS. The simulation is conducted in XPPAUT using the stiff integration method. Figure adapted from [38].

The simulated currents of isolated BK channels, as well as the fitting results, are reported in Figs. 4.11 A,B and 4.12 A,B. Both SLO1 and SLO2 activation (m_∞) curves and time constants display a similar behaviour at decreasing calcium concentrations, consisting of a left shift of the m_∞ curve and an increase in the activation time constants. However,
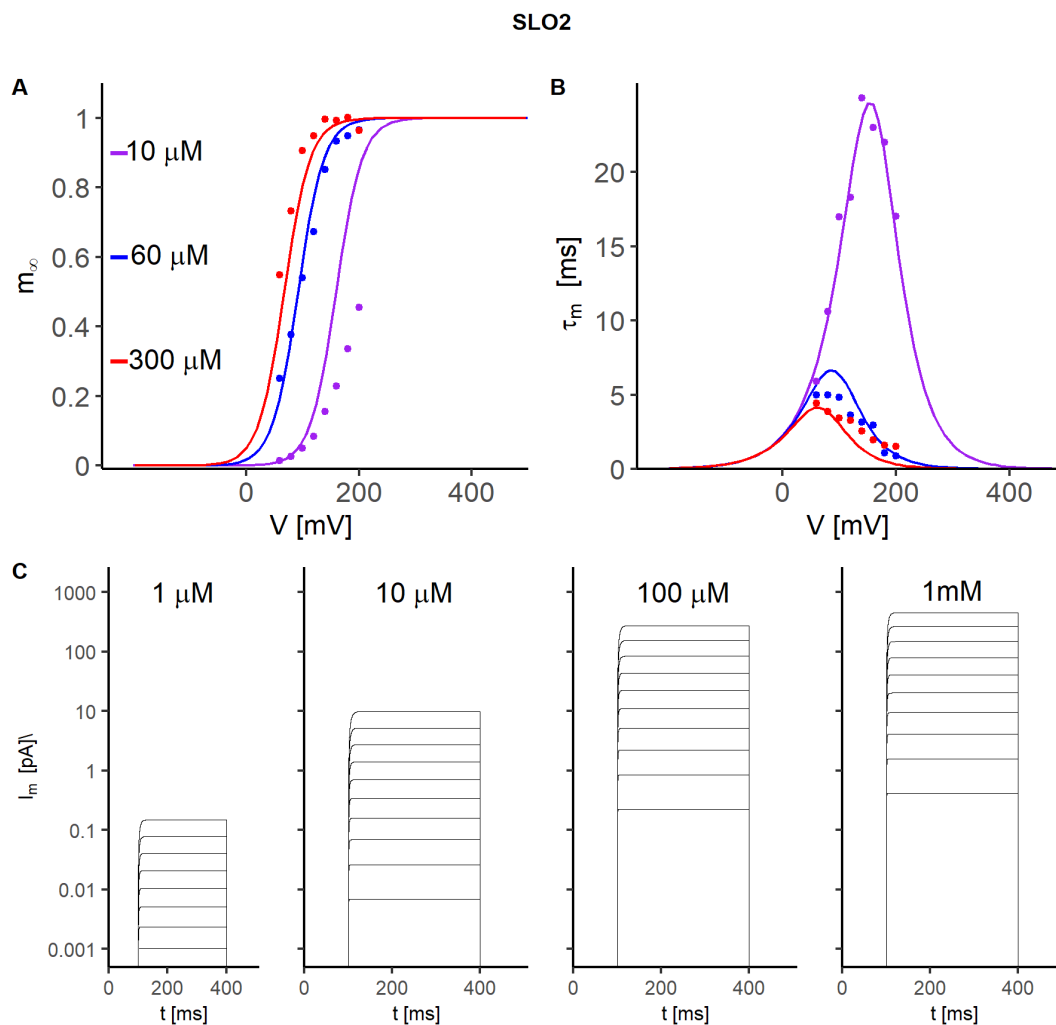
Figure 4.12: **Isolated SLO2 currents model**. **A)** Steady-state activation variable fitting. Experimental data from [153] are fitted to Eqs. 2.25- 2.28. **B)** Activation time constants fitting. Experimental data from [153] (points) are fitted to Eq. 2.28. **C)**. Simulation of isolated SLO2 channels at $Ca^{2+} = 1, 10, 100, 1000\,\mu$M. The stimulation protocol consisted in 13 voltage pulses ranging between -80 mV and 40 mV and. The step duration is 200 ms, and the holding potential is $V_h = -80$ mV. The maximal conductance is assumed equal to $\bar{g}_{SLO2} = 15$ nS. The simulation is conducted in XPPAUT using the stiff integration method. Figure adapted from [38].

SLO2 currents, compared to SLO1 ones, activate at more negative potentials and with slower time constants (at Ca = 10 μM $\tau_m^{SLO1} = \sim 1.5$ ms and $\tau_m^{SLO2} = \sim 20$ ms). As expected, both SLO1 and SLO2 currents are non-inactivating and increase at increasing intracellular calcium concentrations (Figs. 4.11 C and 4.12 C). Calcium changes affect

more SLO2 than SLO1 currents, with a maximum current varying between $\sim$0.1 pA at
Ca=1 μM and $\sim$1000 pA at Ca=1 mM, for SLO2, and between $\sim$10 pA and $\sim$1000 pA,
in the case of SLO1 (Figs. 4.11 C and 4.12 C).

In the *C. elegans* case, experimental observations suggest that SLO-1 and SLO-2 channels
form complexes with both EGL-19 and UNC-2 channels, but not with CCA-1 [23, 152,
205, 256, 257]. Therefore, only the model of SLO-1 and SLO-2 complexes with EGL-19
and UNC-2 is developed in this work. In contrast with the isolated case, when coupled to
CaV, both SLO1 and SLO2 currents inactivate with a kinetics that resembles that of the
associated CaV (Fig. 4.14). SLO1-UNC2 and SLO2-UNC2 currents inactivate rapidly
once the peak is reached, while SLO1-EGL9 and SLO2-EGL19 show little inactivation,
consistently with the EGL19 inactivation characteristics (Figs. 4.14 A-D, 4.15 A-D,
and 4.16 A-D). The full list of equations and the corresponding parameters are reported
in Appendix A, Eqs. A44-A48, and in Appendix B, Table B2.
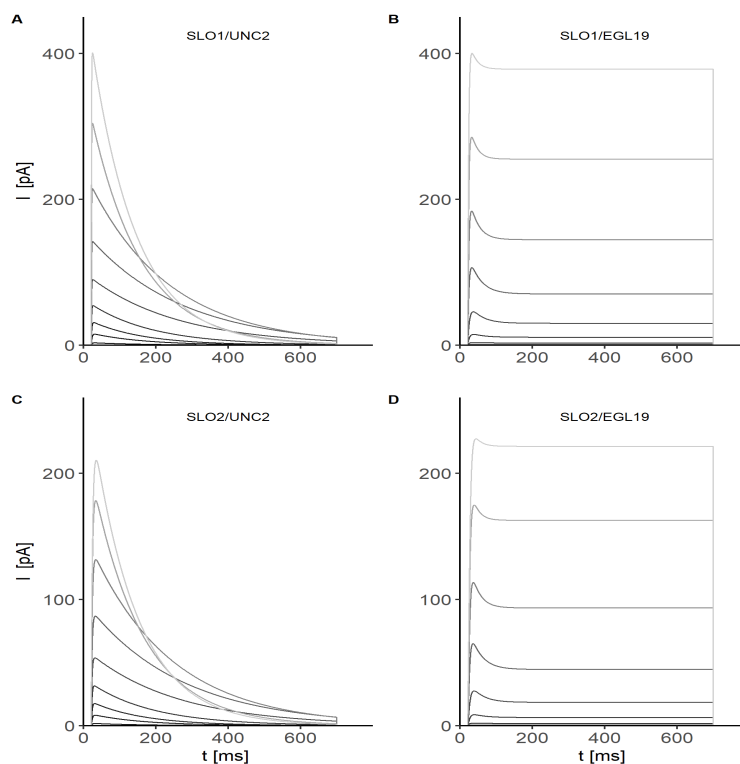
Figure 4.13: **SLO1 and SLO2 channels complexes**. All simulations protocols consisted in 13
voltage steps between -80 mV and 40 mV. The step duration is 200 ms, and the holding potential
is $V_h = -80$ mV. The maximal conductance is $\bar{g}_{BK} = 15$ nS, while the the corresponding CaV
conductance is set to 1 nS ($\bar{g}_{EGL19} = \bar{g}_{UNC2} = 1$ nS). Figure adapted from [38].

KCNL. Since there are no available electrophysiological data on *C. elegans* SK chan-
nels, the model of KCNL currents here presented is based on that developed for mam-
malian SK channels [232]. The activation variable is modelled using a Hill function of
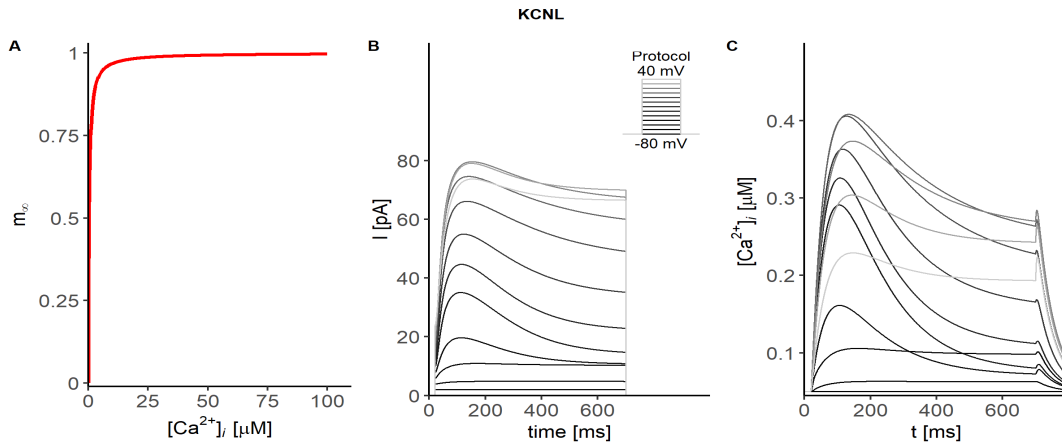
Figure 4.14: **KCNL currents model**. **A)** Activation variable as function of intracellular calcium concentration. **B).** Simulated KCNL currents in response to 13 depolarizing voltage pulses between -80 mV and 40 mv lasting 680 ms. The maximal conductance is $\bar{g}_{\mathrm{BK}} = 1.5$ nS and the holding potential is set equal to -80 mV. **C).** Intracelluar calcium during the voltage-clamp simulation shown in panel B. The intracellular calcium is calculated according to Eqs. 2.42 and 2.43, where the volume of the compartment is chosen equal to the AWC$^{\mathrm{ON}}$ neuron volume ($V_{cell} = 31.16\ \mu\mathrm{m}^3$). To properly reproduce the KCNL currents and intracellular calcium dynamics, EGL19, UNC2, and CCA1 currents are included in the simulation. The maximal conductance of CaV channels is set equal to 1 nS. Figure adapted from [38].

the calcium concentration with a Hill coefficient equal to 1 (Eq. 4.27)

$$m_\infty = \frac{[\mathrm{Ca}]}{K_{\mathrm{Ca}} + [\mathrm{Ca}]} \tag{4.27}$$

$$I_{SK} = g_{k,Ca} \cdot \frac{[\mathrm{Ca}]}{K_{\mathrm{Ca}} + [\mathrm{Ca}]} \cdot (V - V_K), \tag{4.28}$$

where $K_a = 100\mu\mathrm{M}$ is defined as the ratio between k_- and k_+ in the following kinetic equation:

$$C + Ca \underset{k_-}{\overset{k_+}{\rightleftharpoons}} O, \tag{4.29}$$

where the letters C and O indicate the closed and the open state of the channels, respectively.

4.2 Calcium channels

In the following paragraphs are described the models of the three calcium channels in
C. elegans: EGL-19, UNC-2, and CCA-1.

EGL19.
The model of EGL-19 currents is based on electrophysiological data for *C.elegans* body
wall muscles [139] and pharynx [140]. EGL19 currents activate at high voltages compared
to CCA1 and UNC2 (described in the following paragraphs) with a midpoint of activation
at 5.6 mV. Also, compared to the other CaVs, EGL-19 channels show a little inactivation
and an inactivation variable h_∞ with a peculiar inverted bell-shaped curve, described
by 4.30.

$$h_{\text{EGL19},\infty}(V) = \left\{ \frac{a}{1 + e^{\frac{-(V - V_{0.5})}{k_i}}} + b \right\} \cdot \left\{ \frac{c}{1 + e^{\frac{\left(V - V_{0.5}^b\right)}{k_i^b}}} + d \right\} \tag{4.30}$$

When subjected to voltage pulses between -80 mV and 40 mV, EGL-19 starts to activate
around -40 mV, giving rise to inward currents with fast activation and little inactivation
(Fig. 4.15 D).
The current progressively increases until 10 mV when the maximum is reached, then
progressively decreases as the voltage approaches the reversal potential for calcium
(Fig. 4.15 D). Due to the peculiar shape of the inactivation variable, the currents ap-
preciably inactivate only at intermediate voltages (between -20 mV and 20 mV) when
h_∞ reaches its minimum (Fig. 4.15 A and D). Also, activation and inactivation time
constants show a peculiar voltage dependence that is modelled, according to [258], using
a combination of two Gaussian and Boltzmann, functions respectively (Fig. 4.15 B, C
and Eqs. 4.31, 4.32).

$$\tau_{m_{\text{EGL19}}}(V) = \left\{ a\, e^{-\left(\frac{V - b}{c}\right)^2} \right\} + \left\{ d\, e^{-\left(\frac{V - \tilde{e}}{f}\right)^2} \right\} + g \tag{4.31}$$

$$\tau_{h_{\text{EGL19}}}(V) = a \left\{ \frac{b}{1 + e^{\frac{(V - c)}{d}}} + \frac{\tilde{e}}{1 + e^{\frac{(V - f)}{g}}} + h \right\} \tag{4.32}$$

Steady-state activation and inactivation curves are derived from data in [139], while
experimental data for time constants are taken from [140]. The complete list of equa-
tions and parameters of the model is reported in Appendix A, Eqs. A52-A56, and in
Appendix B Table B3.

UNC2.
UNC2 channels generate P/Q-type current that activates rapidly and inactivates at in-
termediate time scales. In response to voltage steps ranging from -80 mV to 40 mV,
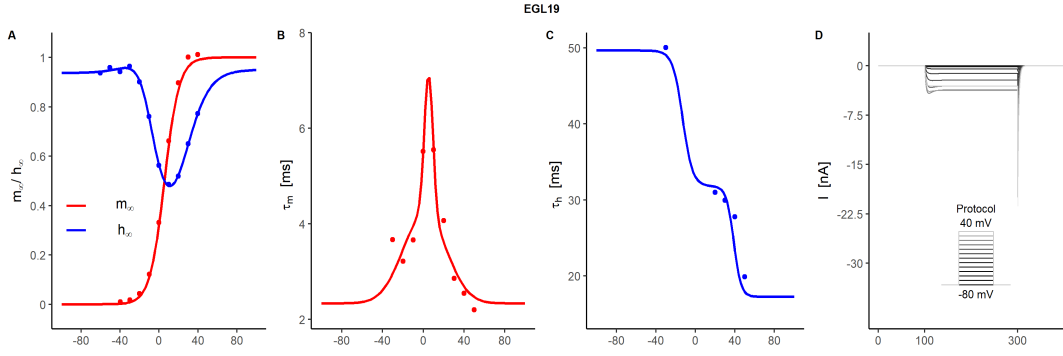
Figure 4.15: **A)** Steady-state activation (red) and inactivation (blue) curves with experimental data from [139] ($V_{0.5}^a = 5.6$ mV, $K_a = 7.5$ mV, $a = 1.43$ ms, $V_{0.5}^i = 24.86$ mV, $k_i = 11.95$ mV, $b = 0.14$ ms, $c = 5.96$ ms, $V_{0.5}^b = -10.54$ mV, 8.06 mV, $d = 0.60$ ms). **B)** Activation time constants fitting. Experimental data from [140] (points) are fitted to Eq. 4.31. (Fit parameters: $a = 2.34$ ms, $b = 5.2$ mV, $c = 6.0$ mV, $d = 1.9$ ms, $\tilde{e} = 1.4$ mV, $f = 28.7$ mV, $g = 3.7$ mV, and $h = 43.1$ ms) **C)** Inactivation time constant fitting. Experimental data from [144] are fitted to Eq. 2.21 ($a = 0.4$ ms, $b = 44.6$ mS, $c = -23.0$ mV, $d = 5.0$ mV, $\tilde{e} = 36.4$ ms, $f = 28.7$ mV, $g = 3.7$ mV, and $h = 43.1$ ms). **D)** Voltage clamp simulation of EGL19 currents. The simulation protocol, sketched in the inset, consisted of 17 voltage steps between -120 mV and 50 mV. The step duration is 200 ms, and the holding potential is $V_h = -80$ mV. The maximal conductance is set to $\bar{g}_{EGL10} = 3.0$ nS to reproduce the experimental currents shown in [144]. The simulation is conducted in XPPAUT using the "stiff" integration method. Figure adapted from [38].

UNC2 currents activate at -40 mV and increase progressively until 0 mV when the intensity of the peak begins to decrease (Fig. 4.16 D). Activation and inactivation variables for UNC-2 channels are modelled according to the data for rat brain P/Q-type channels [155], that are the mammalian homologue of UNC-2 channels. Both activation and inactivation time constants are voltage dependent, with activation times considerably faster than inactivation ones (Fig. 4.16 B, C). Experimental data for time constants from [157] are fitted to equations 4.33 and 4.34, and have been multiplied by factors 2.2 and 3, respectively, to reproduce the currents in [155]. The complete list of equations and parameters is reported in Appendix A Eqs. A57-A61 and in Appendix B Table B3.

$$\tau_{UNC2}^m(V) \;=\; \frac{a}{e^{\frac{-(v-b)}{c}} + e^{\frac{(v-\tilde{e})}{f}}} + f \tag{4.33}$$

$$\tau_{UNC2}^h(V) \;=\; \frac{a}{e^{\frac{-(v-b)}{c}}} + \frac{d}{1 + e^{\frac{(v-d)}{\tilde{e}}}} \tag{4.34}$$
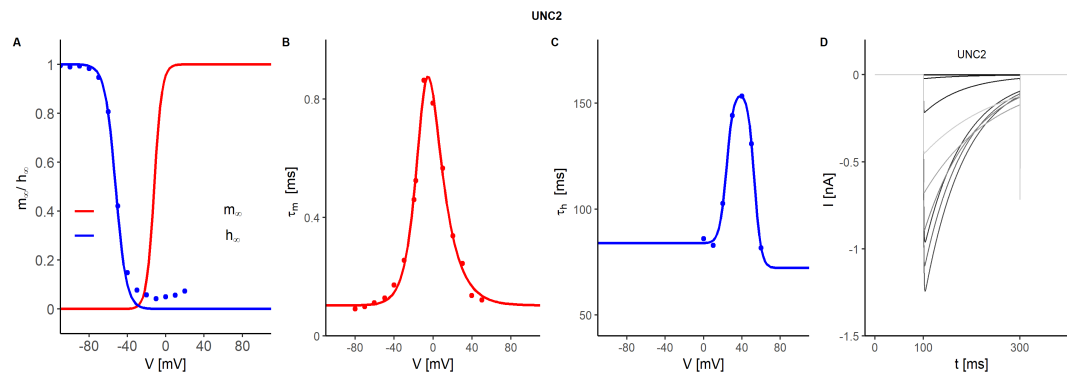
Figure 4.16: **UNC2 currents model**. **A)** Steady state activation (red) and inactivation (blue) curves with data points extracted from [155] ($V_{0.5}^a = (-12.17 \pm 0.17)$ mV, $K_a = (3.97 \pm 0.11)$ mV, $V_{0.5}^i = (-52.47 \pm 0.18)$ mV, $K_i = (5.6 \pm 0.1$ mV)). **B)** Activation time constants fitting. Experimental data from [157] (points) are fitted to Eq. 4.33. (Fit parameters: $a = (1.50 \pm 0.11)$ ms, $b = d = (-8.18 \pm 1.01)$ mV, $c = (9.08 \pm 1.91)$ mV, $e = (15.35 \pm 2.78)$ ms, $f = (0.10 \pm 0.02)$ mV) **C)**. Inactivation time constants fitting. Experimental data from [157] are fitted to Eq. 4.34. (Fit parameters: $a = (83.80 \pm 33.36)$ ms, $b = (52.90 \pm 16.30)$ mV, $c = (4.46 \pm 7.54)$ mV, $d = (72.10 \pm 61.73)$ mV, $e = (23.90 \pm 13.87)$ mV, $f = (3.591 \pm 9.34)$ ms). **D)** Voltage clamp simulation of UNC2 currents. The simulation protocol, sketched in the inset, consisted of 12 voltage steps between -80 mV and 40 mV. The step durations is 600 ms, and the holding potential is $V_h = -80$ mV. The maximal conductance is set to $\bar{g}_{\text{UNC2}} = 23$ nS to reproduce the experimental currents showed in [155]. The simulation is conducted in XPPAUT using the "stiff" integration method. Figure adapted from [38].

CCA1.

CCA1 currents are T-type calcium currents characterized by fast activation and inactivation. In response to sequential voltage steps, CCA1 currents begin to activate at -60 mV and show inward currents that increase in amplitude until -10 mV, when the maximum peak is observed. For voltage pulses above -10 mV, the currents start to decrease in amplitude and show a faster inactivation kinetics, according to the shortening of inactivation time constants at high voltages (Fig.4.17 A, C, D). Both activation and inactivation variables display a strong voltage dependence, and the two curves overlap around -70 mV, giving rise to a sustained inward current, usually called " window current" (Fig. 4.17 A). Activation and inactivation time constants are both voltage dependent, as shown in Fig. 4.17 B-C. Activation time constants are in the ms range for the considered voltages and shorten at increasing potentials, saturating at 0.7 ms for voltages greater than 50 mV (Fig.4.17 B, Eq. 4.6). Inactivation time constants display the same voltage dependence of the activation ones, but they are two orders of magnitude slower at the same voltage (around 20 ms at 50 mV, Fig.4.17 C, Eq. 4.6). In absence of a complete electrophysiological characterization of *C.elegans* cca1 currents, the model here presented is based on data for rat CaV3.1 currents, which are the mammalian counterparts of CCA1 [158]. To reproduce the peculiar activation scheme of the currents, the activation variable is elevated to the second power in the expression for

the total current, as shown by 4.35. The complete list of equations and parameters used to model the currents is reported in Appendix A, Eqs. A62-A44 and in Appendix B, Table B3.

$$I_{\text{CCA1}} = \bar{g}_{\text{CCA1}} \cdot m_{\text{CCA1}}^2 \cdot h_{\text{CCA1}} \cdot (V - V_{Ca}) \tag{4.35}$$
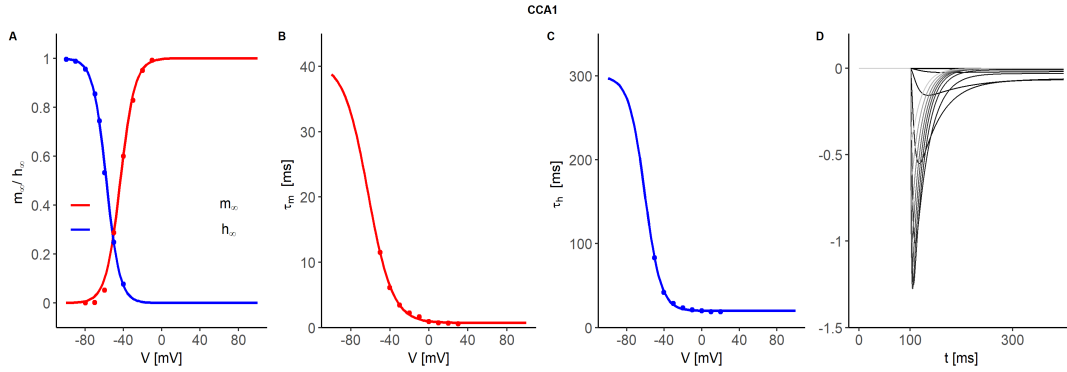
Figure 4.17: **CCA1 currents model. A)** Steady state activation and incatvation curves. Data points extracted from [158]. (Fit parameters: $V_{0.5}^a = (-43.44 \pm 0.88)$ mV, $K_a = (7.55 \pm 0.67)$ mV, $V_{0.5}^i = (-58.04 \pm 0.64)$ mV, $K_i = (6.98 \pm 0.57)$ mV) **B)** Activation time constants fitting. Experimental points are extracted from [158] (points) and fitted to Eq. 4.6. (Fit parameters: $a = (40 \pm 95)$ ms, $b = (-62.94 \pm 46.07)$ mV, $c = (12.48 \pm 6.34)$ mV, $d = (0.70 \pm 0.42)$ ms) **C)**. Inactivation time constant fitting. Experimental points are extracted from [158] and fitted to Eq. 4.6. (Fit parameters: $a = (280 \pm 958)$ ms, $b = (-60.73 \pm 43.03)$ mV, $c = (8.52 \pm 4, 62)$ mV, $d = (19.75 \pm 1.65)$ ms) **D)** Voltage clamp simulation of CCA1 currents. The simulation protocol, sketched in the inset, consisted of 13 voltage steps between -80 mV and 40 mV lasting 600 ms. The maximal conductance was set to $\bar{g}_{\text{CCA1}} = 25$ nS to reproduce the experimental currents showed in [158], and the holding potential was $V_h = -80$ mV. The simulation was conducted in XPPAUT using a stiff solver. Figure adapted from [38].

4.3 Conclusion

The models of some important channels, developed in this Ph.D. work, and involved in the nematode neuronal dynamics have been presented. In particular, 9 voltage-gated potassium channels, 3 voltage-gated calcium channels, and 3 calcium-regulated potassium channels have been developed, based on available experimental data from literature for *C. elegans* and other organisms expressing similar channels. Each model is developed in a Hodgkin-Huxley formalism and correctly reproduces the peculiar characteristics of the currents recorded for *C. elegans*.

The models here presented constitute an important basis for an extensive modelling of *C. elegans* cells, in particular neurons and muscles. The single-current models will be combined in the following chapters, based on gene expression data, to reproduce *in silico* the behaviour of four neurons, AWC$^{\text{ON}}$, AIY, RIM, and RMD neurons. These

4.3. CONCLUSION

ion channels models represent also the key ingredients for the future development of the whole-cell models of other neurons of interest, such as the AWA, AFD and ASE sensory neurons, the interneurons AVA, and the VA5, VB5 and VD6 motor neurons.

Chapter 5

Biophysical model of AWC$^{\text{ON}}$ sensory neuron

91

In this chapter, the computational studies conducted on the AWC^{ON} neuron with the aim to characterize its behaviour in terms of electrical and calcium responses are presented. The final objective of this part of the work is to obtain a comprehensive and biophysically accurate model of the AWC^{ON} neuron behaviour to be used as a tool for the investigation of the molecular mechanisms at the basis of sensory information processing. Indeed, AWC^{ON} is one of the most important sensory neurons, being responsible for effective food procurement and sexual attraction in males [259, 260].
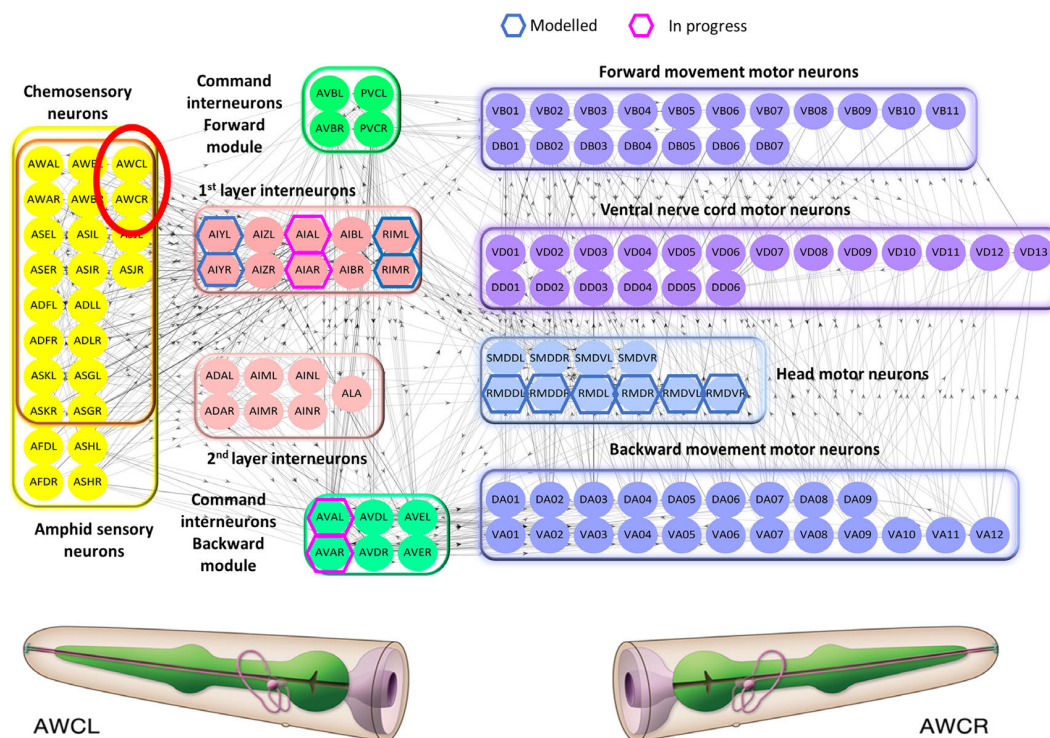
Figure 5.1: **AWC neurons in the olfactory circuit**. The top panel shows the olfactory network of the nematode. AWC neurons are highlighted in red. The lower panel is reproduced from WormAtlas[1]

Despite AWC neurons are among the most studied and well characterized at molecular level, until today, there is only one published patch-clamp recording by Ramot et al. [19] that reports the whole-cell currents, without a dissection of the specific contributions. In this work, a great modelling effort has been dedicated to the development of a biophysical model to elucidate the AWC^{ON} biophysics.

In this chapter, three models of the AWC^{ON} neurons are presented. Two models concern the electrical behaviour of the neuron and the third describes the coupling between the detailed models of electrical and intracellular calcium dynamics.

In the first section, the biophysical model of AWC^{ON} neurons' electrical dynamics, de-

veloped based on the single-current models presented in Chapter 4, is described [38]. This first model reproduces the salient characteristics of the AWC^{ON} neuron electrical responses and allows the study of the contribution of single currents to the overall dynamics of the neuron. The role of single ionic currents is elucidated by means of *in silico* knockout neurons and conductance analyses [38]. *In silico* knockout neurons are defined as neurons in which the contribution of one ionic current is suppressed while the others remain unchanged. In this way, the effect of channel blockers cab be mimicked, allowing the dissection of the single current contributions. It has to be noted that *in silico* knockout neurons do not directly correspond to mutated neurons. However, some information from these models can be also extracted with respect to mutated cases.

Afterwards (Section 5.2), the detailed model of the electrical response [38] is coupled with a detailed model of the intracellular calcium dynamics in AWC^{ON} neurons developed by Usuyama et al. [1]. In this way, a complete and biophysically accurate description of the AWC^{ON} functioning from odor stimulation to electrical responses is obtained [40]. The model correctly reproduces the responses of AWC^{ON} neurons in a wide range of odorant concentrations and exposure times. Also, the dose-response curves characterizing both the intracellular calcium and the membrane voltage responses of the neuron are computed [40].

Finally, the electrical model of the AWC^{ON} neurons is further refined by applying a genetic-algorithm based optimization routine. The refined model, tested in current-clamp conditions, shows an unexpected putative bistable behaviour, previously unobserved in AWC^{ON} neurons. This interesting behaviour is further characterized with *in silico* knockout neurons simulations and a bistability analysis.

In the last section of the Chapter, the results of calcium imaging experiments showing that AWC^{ON} are capable of responding to transient mechanical stimuli [41]. The putative AWC^{ON} mechanosensitivity is also investigated through calcium imaging experiments on mutant worms to dissect its molecular origin. The results here presented suggest that the AWC^{ON} mechanosensitivity is intrinsic rather than synaptic in origin [41]. Finally, the role of two voltage-gated calcium channels and of a sodium leak channel in the mechanical and chemical responses is investigated, highlighting their different role in the two sensory modalities.

Concerning the model implementation, the first model of AWC^{ON} is developed in XP-PAUT, and then translated into NEURON language to allow a further refinement using the genetic algorithm; while, the coupling between the electrical model and the calcium dynamics is performed in XPPAUT. Moreover, it is important to note that in some cases, the parameters of single current models are changed to match the specific behaviour of the neuron. This fact is not surprising, indeed many of the single current models are based on patch-clamp recording on heterologously expressed channels. Indeed the heterologous expression of *C. elegans* ionic channels in other cells, such as *Xenopus* oocytes is, on the one hand, a powerful instrument to characterize their properties, but on the other hand, some of these properties could be altered by non-native components of the cellular environment [261].

5.1 AWC$^{\text{ON}}$ WT electrical model

The Hodgkin-Huxley model here presented of the AWC$^{\text{ON}}$ neuron is based on experimental voltage-clamp recordings from [19] (Fig. 5.2).
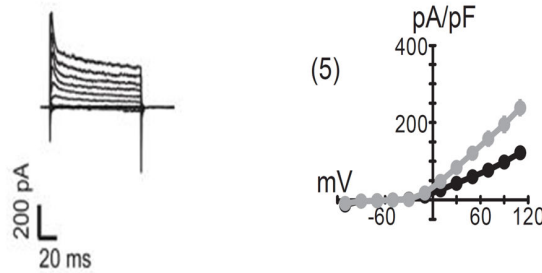
Figure 5.2: **Experimental voltage-clamp recording on AWC$^{\text{ON}}$ neurons**. The figure shows whole-cell voltage-clamp recordings on AWC$^{\text{ON}}$ neurons performed by Ramot D. et al [19]. The neuron is stimulated with 12 voltage steps between -110 mV and 110 mV lasting 100 ms. On the right the corresponding peaks (grey) and steady-state (black) I-V curves are shown. Adapted by permission from [Springer Nature]: [Nature/Springer/Palgrave] [Nature Neuroscience] [Bidirectional temperature-sensing by a single thermosensory neuron in *C. elegans*, D Ramot et al.], [4975231135814] (2008).

The ionic currents included in the model are selected from a combination of the gene expression profiles obtained from Wormbase [262] and literature [145, 146, 155, 201, 205, 256]. According to this criterion, the following ion currents are included in the model: SHL1, SHK1, KVS1, EGL2, KQT3, IRK, EGL19, UNC2, CCA1, SLO1, SLO2, KCNL, NCA (Eq. 5.1)[2].

$$
\begin{aligned}
I_{ion}^{AWC} ={}& I_{SHL1} + I_{\text{KVS1}} + I_{\text{SHK1}} + + I_{\text{KVS1}} + I_{\text{EGL2}} + I_{\text{KQT3}} + I_{\text{IRK}} \\
& + I_{\text{EGL19}} + I_{\text{UNC2}} + I_{\text{CCA1}} \\
& + I_{\text{SLO1/EGL19}} + I_{\text{SLO1/UNC2}} + I_{\text{SLO2/EGL19}} + I_{\text{SLO2/UNC2}} \\
& + I_{\text{KCNL}} + I_{\text{NCA}} + I_{\text{LEAK}}.
\end{aligned}
\tag{5.1}
$$

To correctly reproduce the experimental currents [19], it has been necessary to modify some parameters of single channels models: their values are reported in Appendix B, Tables B1-B3, while the ionic conductances for the different channels species are listed in Table 5.1.

---

[2]After the submission of this work the candidate has found that the new release of the CeNGEN database includes also the EXP-2 channels in the list of expressed channels. The candidate is working to update the model on the basis of the new information.

Table 5.1: **Ionic conductances for AWC$^{\text{ON}}$ neurons.** The following reversal potentials are used for potassium, calcium sodium and leakage currents, respectively: $V_K = -80$ mV, $V_{Ca} = 60$ mV and $V_{Na} = 30$ mV, $V_L = -90$ mV. The final set of conductances is obtained by a fine tuning of the values for each current, to match the experimental I-V curves [19].

Current	Conductance ($\bar{g}_x$) [nS] AWC$^{\text{ON}}$
SHL1	2.9
SHK1	0.1
KVS1	0.8
EGL2	0.85
KQT3	0.55
EGL19	1.55
UNC2	1
CCA1	0.7
SLO1/EGL19	0.11
SLO1/UNC2	0.11
SLO2/EGL19	0.10
SLO2/UNC2	0.10
KCNL	0.06
NCA	0.06
IRK	0.25
LEAK	0.27

5.1.1 AWC$^{\text{ON}}$ WT whole-cell electric model

As the first step, a voltage-clamp simulation is performed using the same stimulation protocol of [19] and the steady-state I-V curve is obtained from the simulated traces (Fig. 5.3 A-B). The voltage-clamp protocol consists of 12 voltage steps between -110 mV and 110 mV, starting from a holding potential of -70 mV. At negative command potentials, the neuron has a nearly passive behaviour, while for intermediate stimuli (between -60 mV and -20 mV) the current rapidly reaches the peak and decreases, reaching a local minimum, before stabilizing to the steady-state value (Fig 5.3 A). At increasing potentials, the currents become outward with increasing peaks degrading into a plateau phase (Fig. 5.3 A). The peculiar behaviour at intermediate command potentials is evident also in steady-state I-V curve that, similarly to ASER neurons [18], shows in this region a non-linear behaviour, determined by the interplay between inward and outward currents (Fig. 5.3 B).

Current stimuli between -4 pA and 20 pA evoke threshold-like responses characterized by a fast upstroke followed by a plateau phase (Fig. 5.3 C). The observed responses resemble the robust activation displayed by AWC under chemical stimulation [13, 91]. Moreover, other sensory neurons in *C. elegans* have been shown to display threshold-like responses mediated by voltage-gated calcium and potassium channels [18, 21, 22].
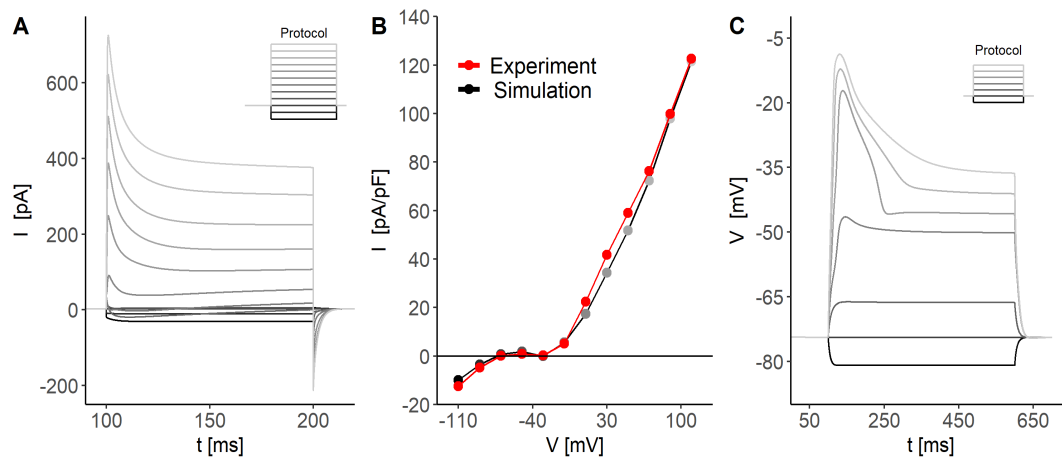
Figure 5.3: **AWC voltage- and current-clamp simulation**. Figure adapted from [38]. **A) Voltage-clamp simulation**. The panel shows the simulated whole-cell current obtained by stimulating the neuron with the same protocol of the experimental recordings [19]. The protocol, sketched in the insert, consists of 12 voltage steps ranging between -110 mV and 110 mV, with a duration of 100 ms. The holding potential is set to -70 mV **B) Steady-state I-V curves analysis**. The steady-state I-V curve (in black) is computed from the simulated currents with the same procedure of the experimental I-V (in red) to allow the comparison between the simulation and the experimental data from [19]. **C) Current-clamp simulation of AWC^{ON}**. The model is tested with a current-clamp protocol by applying sequential current steps from a holding current of 0 pA. Each current step has a duration of 500 ms, and the injected current is varied between -4 pA and 20 pA to ensure the activation of the neuron. No reference current-clamp recordings on AWC^{ON} neurons have been found in literature. The cell capacitance is set to 3.1 pF, according to [19], and corresponds to 1.3 μF/cm^2 when scaled on the total cell surface ($S_{\text{AWC}^{ON}} = 238.16$ μm^2, from Neuromorpho). This value agrees with that reported for other sensory neurons, for example, the ASE neurons [18].

5.1.2 AWC^{ON} conductance and *in silico* knockouts analyses

To clarify whether AWC^{ON} responses also rely on a combination of voltage-gated potassium and calcium currents, the role of each ionic current is studied by analysing the single-current activation and inactivation dynamics (Fig. 5.4). For this study, a stimulus of 15 pA, lasting 500 ms, has been selected to ensure the neuron activation, i.e., the generation of large excursions of the membrane potential. To further elucidate the role of each ionic current, the response of *in silico* knockout neurons to the same 15 pA stimulus has been studied (Fig. 5.4).

The analysis of Fig. 5.4 allows to describe in great detail the overall dynamics of WT AWC^{ON} neurons. When a depolarizing stimulus is applied, the neuron undergoes a fast depolarization supported by the sequential activation of CCA1, UNC2, and EGL19 currents (Fig. 5.4 Ba-Da). CCA-1 channels activate mostly in the upstroke and repolarization phases and moderately also in the late phase of the plateau, indicating their prominent role in fast depolarizations and repolarization phases (Fig. 5.4 Ba). *In silico*

5.1. AWC^{ON} WT ELECTRICAL MODEL
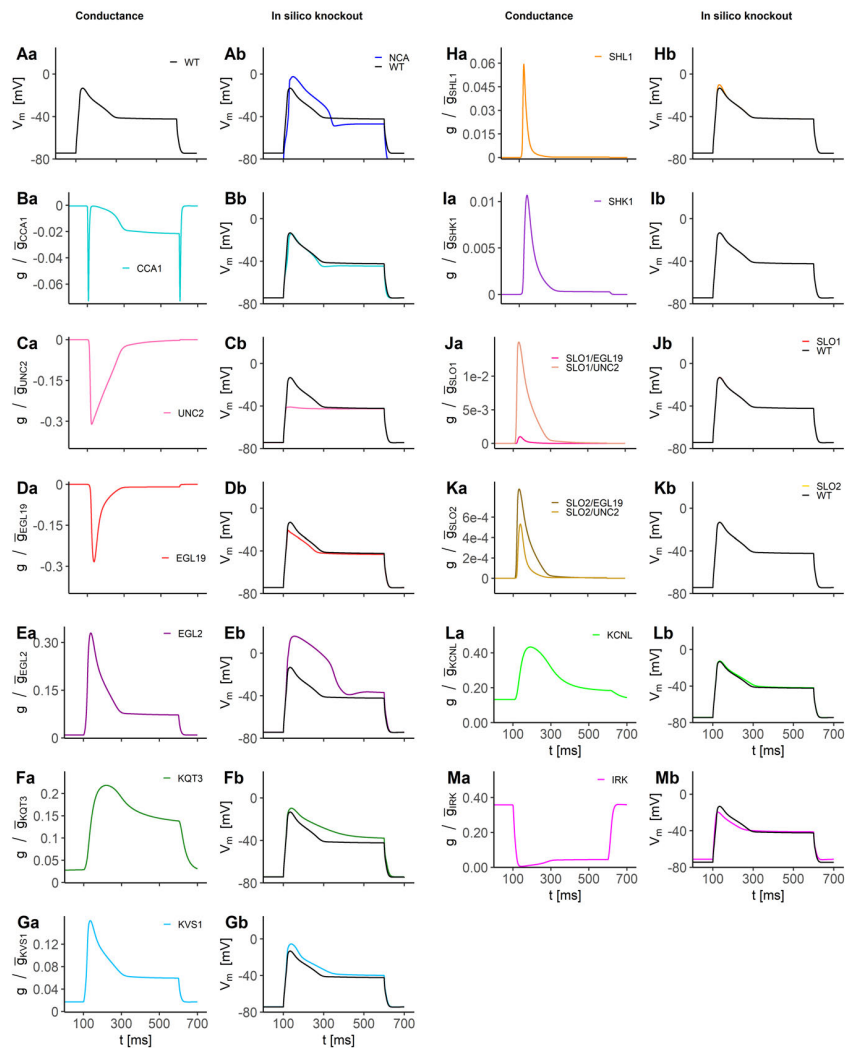
Figure 5.4: **AWC conductance and knockout analysis**. **Aa) WT response**. Simulation of WT response to a 15 pA stimulus. **Ba-Ma) Normalized single-currents conductances**. The normalized conductance is defined as the product of the activation and inactivation variable. Panels Ba, Ca, and Da show the normalized conductance of voltage-gated calcium currents. In these panels $g_x/\bar{g}_x$ is multiplied by -1 to reproduce the sign of the current. Panels Ea-La show the normalized conductances for voltage-gated and big-conductance, and small-conductance potassium channels. **Ab-Mb)** *In silico* **knockout responses**. Simulated response of *in silico* knockout neurons. The simulation protocol consists in a single-current pulse of 15 pA lasting 500 ms. The black curve in all the panels represents the WT simulation, while the coloured traces represent the response of *in silico* knockout for the same current analysed in the left (a) panel.

knockout neurons show no significant alterations of the peak intensity, but the upstroke phase is slower compared to the WT case (Fig. 5.4 Bb). Also, consistently with the conductance behaviour, the plateau level is slightly shifted to potentials more negative than the WT due to the reduced inward flux of calcium (Fig. 5.4 Bb). UNC-2 channels are predominantly active during the upstroke, being almost inactive in the plateau (Fig. 5.4 Ca), as confirmed by the *in silico* knockout responses, in which the initial peak is completely suppressed (Fig. 5.4 Cb). EGL-19 channels are mainly active in the upstroke phase, giving a little contribution to the plateau (Fig. 5.4 Da). The *in silico* knockout simulation confirms the conductance analysis, showing a reduced peak and an almost unchanged plateau (Fig. 5.4 Db). Inward currents carried by calcium channels are counterbalanced by outward potassium fluxes (Figs.5.4 Ea/b-Ma/b).

Concerning the potassium channels, the conductances analysis suggests that the upstroke phase is mainly influenced by EGL-2, KQT-3, KVS-1, and less by SHL1 (Fig 5.4 Ea-Ha). Instead, SHK1 does not cause significant changes even in the overall response since their activation level is lower compared to other outward currents (Fig 5.4 Ia). Also SLO1 and SLO2 do not significantly contribute to the responses, probably due to too low levels of intracellular calcium levels at the nanoscale (Fig 5.4 JA-Ka).
EGL2, KQT3 and KVS1 are robustly activated in the plateau phase, and their deletion leads to increased peaks and plateau levels (Fig 5.4 Eb-Gb). Also, KQT3 and KVS1 deletions affect the responses in a similar way by slowing down the plateau stabilization (Fig. 5.4 Fb-Gb). EGL-2 knockout shows the most altered voltage response, characterized by an initial peak reaching positive potentials, followed by a slow repolarization phase terminating in a plateau (Fig 5.4 Eb). This result suggests that EGL-2 channels are essential for counterbalancing the CaV activity and determining the shape of electrical responses in the repolarization phase.
Despite their modest activation KCNL channels, do not affect significantly the response, probably due to low intracellular calcium levels (Fig. 5.4 La/b). Consistently with their inward rectifier, properties IRK channels are more active before and after the current pulse than during the pulse (Fig. 5.4 Ma). The knockout simulations further confirmed their role in tuning the resting potential of the cell. Indeed IRK deletion shifts the resting potential to more -71.1 mV (Fig. 5.4 Mb).
Finally, NCA deletion significantly affects both the resting potential and the shape of the response, suggesting their important role in tuning the neuron excitability (Fig. 5.4 Ab). Indeed, the resting potential (-74.4 mV) is considerably affected by NCA deletion, being shifted to -71.1 Mv and -84.1 mV, respectively.

As the last step of the analysis, the voltage-clamp simulations for the *in silico* knockout neurons have been performed. This analysis, similarly to the *in silico* knockout analysis in the current-clamp configuration, allows to dissect the contribution of each current to the overall response of the neurons. However, compared to the current clamp case, this analysis covers a wider range of voltages, thereby offering the possibility to study phenomena not revealed by the previous analysis. Figs. 5.5 and 5.6 show both the total

current and the I-V curves for peaks and steady state computed for all the knockout
neurons.
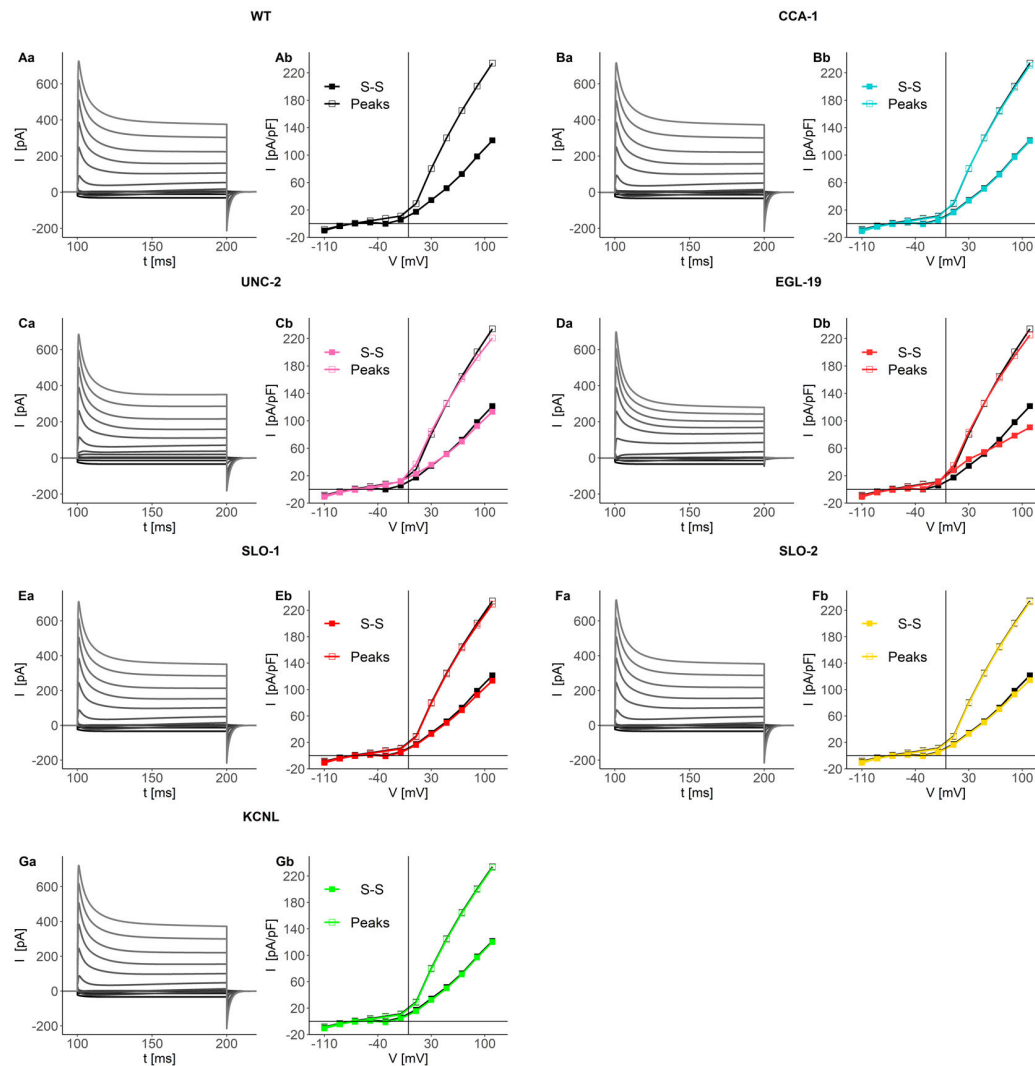
Figure 5.5: **Voltage clamp of CaV and K-Ca currents *in silico* knockout. Aa-Ga)
Simulated whole-cell currents** The panels show the simulated whole-cell currents of WT
(Panel Aa), CaV knockouts (Panels Ba, Ca, and Da), and K-Ca knockouts (Panels Ea, Fa, and
Ga). **Ab-Gb) Peaks and steady-state I-V curves for CaV and KCa knockouts**. I-V
curves are derived from the simulated currents showed in Panels Aa-Ga. For the sake of clarity,
in each panel the WT peaks (empty black squares) and steady-state (filled black squares) I-V
curves are reported. The simulation protocol is the same of Fig. 5.3A, i.e., 12 voltage steps
between -110 mV and 110 mV with a duration of 100 ms delivered from a holding potential of
-70 mV

The analysis of the I-V curves highlights that the above mentioned non-linearities at
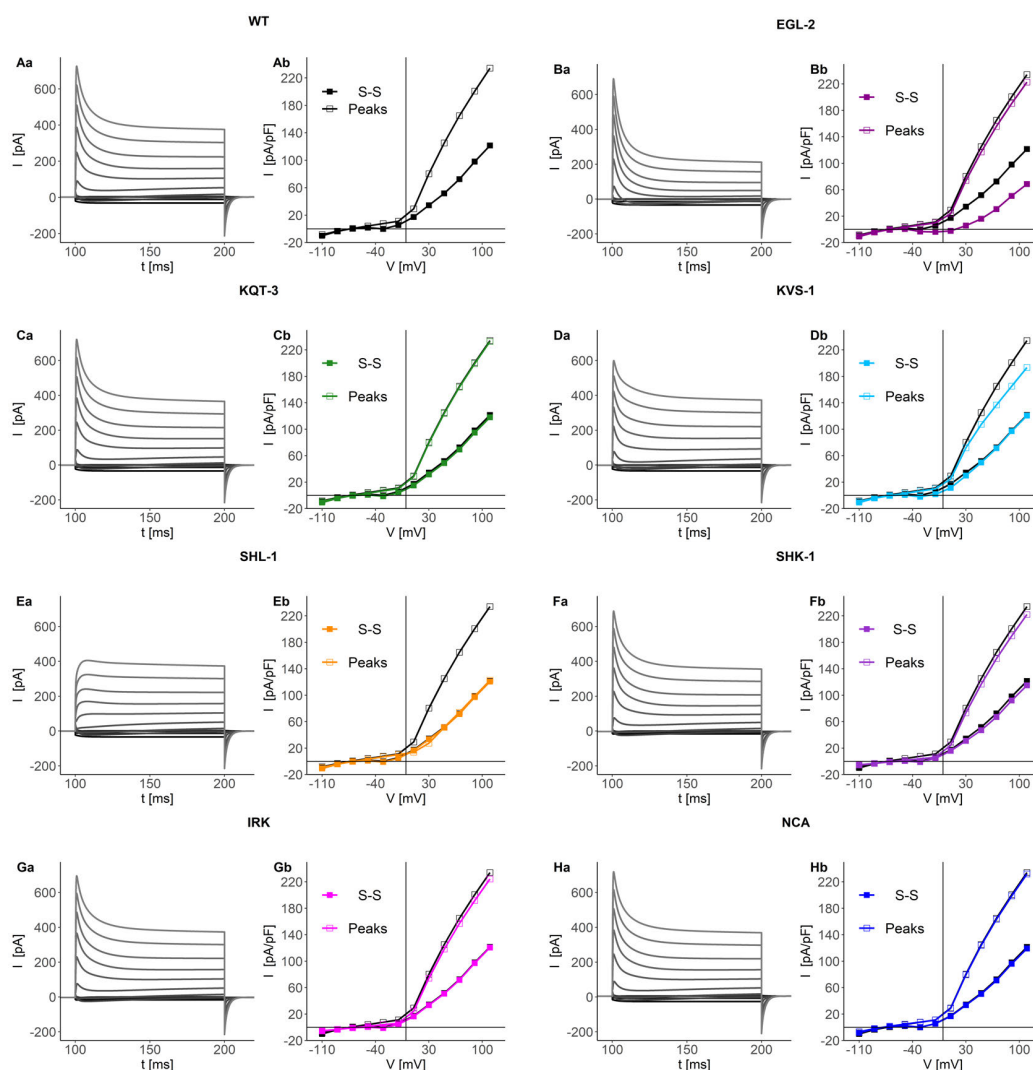
Figure 5.6: **Voltage clamp of KV currents *in silico* knockout**. **Aa-Ha)** Simulated whole-cell currents of WT (Panel Aa), KV knockouts (Panels Ba-Ga), and NCA knockout (Panel Ha). **Ab-Hb) Peaks and steady-state I-V curves for KV knockouts**. I-V curves are derived from the simulated currents showed in Panels Aa-Ha. For the sake of clarity, in each panel the WT peaks (empty squares) and steady state (filled squares) I-V curves are reported. The simulation protocol is the same of Fig. 5.3A, i.e., 12 voltage steps between -110 mV and 110 mV with a duration of 100 ms delivered from a holding potential of -70 mV.

intermediate voltages (from -60 mV to -20 mV, see Fig. 5.3 B) are determined by the interplay between calcium currents carried by UNC-2 and EGL-19 and outward rectifier potassium currents of EGL-2 channels (Figs. 5.5 Ca/b, Da/b, and 5.6 Ba/b). In accordance to the inward character of the calcium currents, the steady-state I-V curve for

EGL19 and UNC2 knockouts shows increased steady-state currents with respect to WT,
and in the case of UNC-2 knockout also a small increase in the peak current (Fig. 5.5 Cb
and Db). As already suggested by the current-clamp simulations (Fig. 5.4 Eb), EGL-2
channels are the main contributors to the outward potassium currents. Indeed, their
deletion removes the most important contribution that counterbalances the inward cal-
cium current leading to decreased steady-state currents and increased cellular excitability
(Figs. 5.4 Eb and 5.6 Ba/b). UNC-2, EGL-19, and EGL2-2 deletion mainly affects the
steady-state I-V curve, while, the peaks I-V shows less marked changes (Fig. 5.5 Ba/b-
Ca/b and Fig. 5.6 Ba/b). Peak currents are mainly carried by SHL-1 channels, with
minor contributions of KVS1 and SHK-1 (Figs. 5.6 Da/b, Ea/b, and Fa/b). In particu-
lar, SHL-1 deletion leads to a almost complete removal of the fast transient component
in the total current, and to the collapse of the peaks I-V on the steady-state curve
(Fig. 5.6 Ea/b).

The other currents inserted in the model have a secondary role in shaping the whole-cell
currents. Indeed, their deletion causes minor changes in both the peaks and I-V curves
compared to EGL19, UNC2, EGL2, and SHL1 deletions. In accordance with the current-
clamp analysis, CCA1 currents do not significantly alter the total current, and thus the
I-V curves (Fig. 5.5 Ba-Bb). Small alterations in the intermediate region are caused
by KQT3, KVS1, SHK1, IRK, and KCNL (Figs. 5.5 Ga/b and 5.6-Ca/b, Da/b, Fa/b,
and Ga/b). Concerning the KCa channels, both SLO-1 and SLO-2 channels deletion
influences only the steady-state I-V at high potentials (V > 50 mV), confirming that their
irrelevance in the voltage response (Fig. 6.3 Jb-Kb) is due to their very low activation at
negative membrane potentials (Fig 5.4 Jb and Kb). KCNL channels slightly influence
the steady-state current by reducing it of few pico-amperes, especially in the region
between -40 mV and 30 mV (Fig. 5.5 Ga/b).

Finally, in accordance with knockout current-clamp simulations and with their known
physiological role, IRK channels mainly affect the neuronal behaviour at negative po-
tentials by shifting the resting potential to more positive values (from -74.4 mV to
-71.1 mV). The negative tail of the I-V curves is also influenced by NCA currents that
tune the intersection with the zero current line, which represents the resting potential of
the cell. In particular, as already observed in the current-clamp analysis (Fig. 5.4 Ab),
its value is shifted to more negative potentials (-84.4 mV) (Fig. 5.6 Ha/b).

5.2 Coupling of calcium and electrical dynamics in AWC^{ON} neurons.

Once the model of the electrical dynamics has been obtained, it has been coupled with
the detailed mathematical model of AWC^{ON} response to chemical stimuli developed by
Usuyama et al. [1]. This model reproduces the AWC^{ON} responses to chemical stimuli
through a set of ordinary differential equations (ODEs) that account for the dynamics of
the biochemical processes that downstream the GPCRs activation [1]. In particular, this
chemotaxis model is able to describe the characteristic ODOR-OFF responses of AWC
observed in calcium imaging experiments [13]. However, despite its ability to describe in

great detail many intracellular processes triggered by chemical stimulations, including the intracellular calcium dynamics, the description of the membrane voltage dynamics is extremely simplified and do not allow to dissect the role of single ionic currents. Therefore, the coupling of this model [1] with the model of the electrical responses here developed [38], would allow a complete and detailed reconstruction of the AWC^{ON} behaviour upon chemical stimulation. The coupling of the two descriptions is performed by substituting the simplified calcium dynamics (Eq. 2.42) used in the electrical model with that computed in the model of Usuyama et al. [1] (Eq. 2.48). Moreover, in the chemotaxis model, the membrane potential dynamics is substituted with the electrical model of AWC^{ON} here developed. The parameters used in the calculation of the CaV-related flux have been optimized to reproduce the I-V curve for calcium channels as computed from the electrical model.

$$J_{Cav}^{original} = 1\frac{(30 \text{ mV} - V)}{1 + e^{\frac{(-10 \text{ mV} - V)}{4 \text{ mV}}}} \longrightarrow J_{Cav}^{new} = 1\frac{(60 \text{ mV} - V)}{1 + e^{\frac{(-0.49 \text{ mV} - V)}{9.65 \text{ mV}}}} \qquad (5.2)$$

To test the coupled model, the intracellular calcium and membrane voltage responses have been calculated at different odor concentrations and exposure times. The first analysis is performed studying the dependence of AWC^{ON} response on different odor concentrations. Simulations have been performed by delivering step-like odor stimuli with a concentration between 20 μM and 250 μM and a duration of 60 s (Fig. 5.7).
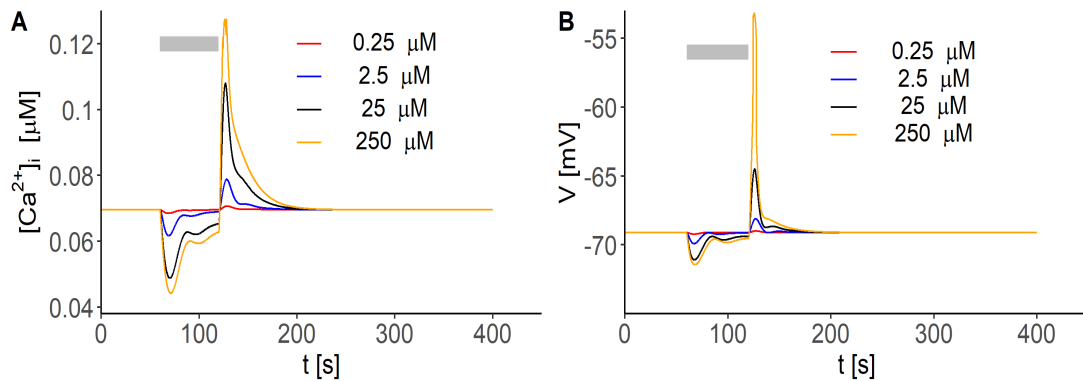
Figure 5.7: **AWC^{ON} responses to different odor concentrations. A) Intracelluar calcium response at different odor concentrations**. The neuron is stimulated with odor concentrations between 0.25 μM and 250 μM for 60 s (gray bar). The curves show the intracellular calcium concentration calculated through Eq. 2.48. **B) Membrane voltage responses of AWC neurons**. Membrane voltage responses corresponding to calcium traces shown in panel A. The simulations are conducted in XXPAUT using the stiff integration method with a time step of 0.01 s. Figure adapted from [40]

.

The range of concentration is chosen to match the most common experimental protocols for calcium imaging and chemotaxis assays [13]. As expected, odor application induces a membrane hyperpolarization and calcium decrease due to the inhibition of CGN channels

(Fig. 5.7 A-B). The calcium slowly decreases, reaching a minimum in 8.7 s (250 μM)-10.5 s (0.25 μM), and then undergoes a transient increase after the stimulus removal, reaching the maximum in 8.7 (0.25 μM)-6.2 s (250 μM). The membrane voltage dynamics follows the intracellular calcium behaviour, showing a hyperpolarization during the odor presentation, followed by a transient increase after the stimulus removal. The membrane voltage response and the corresponding intracellular calcium trace for the highest odour concentration (250 μM) show peculiar characteristics unobserved at lower odor concentrations (Fig. 5.7 A-B). The membrane voltage curve shows a steep increase resembling a threshold-like response, which is probably related to a robust activation of voltage-gated calcium channels, e.g. CCA1 channels (Fig. 5.7 B).

In the corresponding calcium trace in place of the single maximum, two local maxima appear (Fig. 5.7 A and Fig. 5.8). Their insurgence is ascribed to non-linear voltage-calcium feedback on calcium fluxes that results in an inhibition of the intracellular calcium production in the peak region (Fig. 5.8).
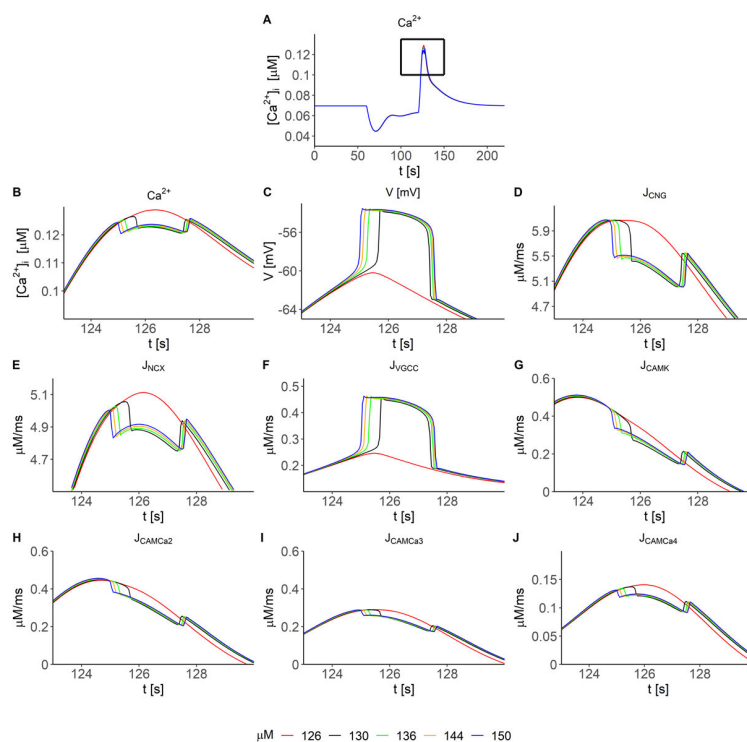
Figure 5.8: **Analysis of calcium fluxes in the peaks region**. The anomalous peaks in the calcium trace arise for odour concentrations above 126 μM with 60 s of exposure. The panels show the different fluxes involved in the intracellular calcium dynamics (Eq. 2.48) for odor concentrations between 126 μM and 150 μM. For the sake of clarity, only an enlargement of the depolarization peak is showed. For a detailed description of the specific role of each flux in the overall calcium dynamics the reader is referred to [1]

.

In particular, the steep increase in the membrane voltage seems to induced an inhibition of different fluxes, including the flux mediated by CNG channels, that is not properly counterbalanced by the increase of the flux associated to voltage-gated calcium channels (Fig. 5.8). This effect will be further investigated with future studies, dedicated in particular to the fine tuning of the parameters that influence the coupling between the electrical and chemical response model. Despite the spurious peaks appearing in the calcium curves, the model correctly reproduces the overall behaviour of AWC observed in calcium imaging experiments [13].

The second aspect here addressed, is the dependence of AWC^{ON} responses on the duration of odorant exposure. The AWC^{ON} responses are tested at a fixed odor concentration of 25 μM with a variable exposure time (20 s, 60 s, 140 s, and 300 s), and also with a multistep protocol, in which a second odor step is delivered after the first stimulus (Fig. 5.9).
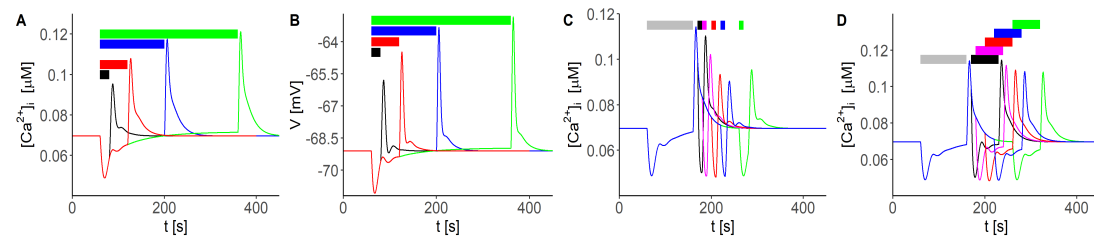
Figure 5.9: **AWC responses at different exposure time. A)-B)** Panel A shows the computed calcium during a simulation performed at a fixed calcium concentration of 25 μM and with an exposure time variable between 20 s and 300 s. In panel B are shown the corresponding membrane voltage curves. **C)** The panel shows the calcium response to a double-step protocol. The second stimulus has a duration 10 s and is delivered 10 s, 20 s, 40 s, or 60 s after the preconditioning stimulus. The preconditioning stimulus is administrated at 25 μM for 100 s. **D)** The panel shows the calcium response to a double-step protocol. The second stimulus has a duration 60 s and is delivered 10 s, 20 s, 40 s, or 60 s after the preconditioning stimulus. The preconditioning stimulus is administrated at 25 μM for 100 s. The preconditioning stimulus is administrated at 25 μM for 100 s. The simulation is performed in XPPAUT using a stiff integration method with a time step of 0.01 s. Panels A-C are adapted from [40].

In accordance with experimental data, the simulated neurons show increasing calcium and voltage responses at increasing exposure times (Fig. 5.9 A-B), indicating that AWC^{ON} responses depend both on odor concentration and exposure time. In the multistep simulations, a facilitation effect is observed (Fig. 5.9 C-D). These simulation are performed by delivering a preconditioning stimulus of 25 μM for 100 s, followed by a second stimulus at the same concentration applied 10 s, 20 s, 40 s, 60 s, or 100 s after the first stimulus with a duration of 10 s (Fig. 5.9 C). Interestingly, the calcium peak amplitude is greater at low delays and progressively decreases at increasing delay times (Fig. 5.9 C). This observation suggests the presence of a facilitation effect that promotes higher responses when the neuron is in a partially activated state induced by the first stimulus, and also of an adaption process that works at longer time scales compared to

that of the calcium dynamics. To verify that this facilitation effect does not depend on
the second stimulus duration, simulations at different durations of the second step have
been performed. Notably, even extending the duration of the second step up to 60 s the
effect is preserved, supporting the hypothesis that the facilitation is not related to the
specific duration of the stimulus (Fig. 5.9 D).

To grasp a complete picture of the dependence of AWC$^{\text{ON}}$ responses on odor concentra-
tion and exposure time, the dose-response curves are built for both intracellular calcium
and membrane voltage (Fig. 5.10 A-B).
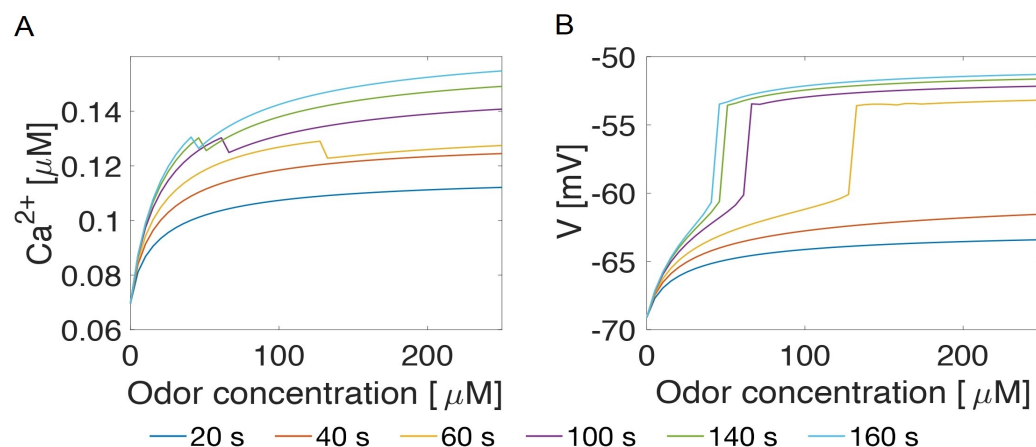
Figure 5.10: **Dose response curves for AWC neurons** Panels A and B show respectively the
intracellular calcium and membrane voltage peak intensities as a function of exposure time at
different odor concentrations. For calcium curves exhibiting the additional peaks, the reported in-
tensity represents the value of the central maximum. Figure reproduced with permission from [40]
(©2020 IEEE, DOI: 10.1109/MetroInd4.0IoT48571.2020.9138174).

Both curves show a saturation effect at high odor concentrations and high exposure
times, indicating that the neuron is more sensitive in the intermediate range of odor
concentrations (below 100 μM). Notably, for exposure times above 60 s, the calcium
curve shows a discontinuity related to the appearance of the local maxima in calcium
response (Fig 5.10 A). Such discontinuity is also reflected in the membrane voltage
response curve that shows a steep increase probably related to the the activation of
voltage-gated calcium channels (Fig. 5.10 B). Indeed, the membrane voltage values fall
in a range suitable for the activation of CCA1 currents (See Chapter 4, Section 4.2). A
possible interpretation of this phenomenon is that non-linear voltage-calcium feedback
on calcium fluxes that results in an inhibition of the influx through cyclic-nucleotide-
gated channels, as suggested by the analysis of single fluxes contributing to the calcium
dynamics in the peak region (Fig 5.8). However this aspect deserves further investigation
with additional simulations to clarify the role of each model entity in the overall response.

5.3 A refinement of the AWC^{ON} model with GA optimization

In the AWC^{ON} electrical model presented in Section 5.1, the set of conductances used in the electrical model is derived by a fine tuning, by hand, of the values of the single conductances, until the desired result is reached. In view of the future development of other neuron models, an optimization routine, based on genetic algorithms, has been implemented in Python as a part of this work (see Chapter 2, Section 2.3, and Appendix C for further details). The models of single currents, already implemented in XPPAUT, have been translated in NEURON using the *nmodl* language. The automatic model parameter optimization is driven by Python scripts, using NEURON to solve the model equations. The experimental steady-state and peaks I-V curves (Fig. 5.2) for AWC^{ON} [19] obtained from [19] are used as reference data to compute the fitness of each individual, according to Eq. 2.59. The specific settings of the GA are used to derive the optimal set of parameters are listed in Table 5.2, while the final set of conductances is reported in Table 5.3.

Table 5.2: **AWC^{ON} GA optmization settings.** In this table are listed the specific settings of the GA used to derive the optimal set of parameters listed in Table 5.3. The subscripts EXP and SIM denote experimental and simulated data, respectively.

	Specific setting
Reference data	Peaks and Stead-state I-V curves from [19]
Fitness calculation	$\psi = \sum_{j=1}^{N} \left[\frac{(IV_{peaks,EXP}^{j} - IV_{peak,SIM}^{j})^2}{2} + \frac{(IV_{ss,EXP}^{j} - IV_{ss,SIM}^{j})^2}{2} \right]$
Population size	10
Number of generations	300
Mutation	Guassian mutation with mean $\zeta = 0$ and $\sigma = 1$ mutation rate 0.3
Crossover	Blend crossover crossover rate: 1 $\alpha = 0.1$ (See Fig. C6)
Elitism	1

Table 5.3: **List of optimized conductances** The first and the second columns report the list of ionic currents used in the model and the optimized set of conductances, respectively; while in the last two columns the upper and lower limits used in the GA optimization are listed. These limits are chosen in a suitable range defined after multiple preliminary runs of the GA routine.

Current	Conductance ($\bar{g}_x$) [nS] AWC^{ON}	Lower Limit [nS]	Upper Limit [nS]
SHL1	2.93	2	3.5
SHK1	0.99	0.05	1
KVS1	0.88	0.05	1
EGL2	0.10	0.1	1.5
KQT3	0.7	0.7	1
EGL19	0.89	0.1	1.8
UNC2	0.30	0.1	0.7
CCA1	0.52	0.1	1
SLO1/EGL19	0.16	0.05	1
SLO1/UNC2	0.98	0.05	1
SLO2/EGL19	0.23	0.05	1
SLO2/UNC2	0.05	0.05	1
KCNL	0.04	0.01	0.7
NCA	0.08	0.05	0.1
IRK	1.0	0.1	1
LEAK	0.11	0.1	1

5.3.1 AWC^{ON} WT refined model whole-cell simulations- The AWC^{ON} bistability

The resulting set of parameters properly replicates the experimental peaks and steady-state I-V (Fig. 5.11). The overall behaviour of the currents is the same observed in the experimental data and in the first model of AWC [19, 38] (see Section 5.1). The neuron shows inward rectifier behaviour for voltage stimuli below the resting, while for high potential the dynamics is dominated by outward rectifier potassium currents (Fig. 5.11 A-C). Concerning the peaks I-V curve, there are no significant differences between the two sets of parameters; indeed, the SHL1 conductance, which is the main responsible for peak currents, is almost unchanged (Fig. 5.11 B-C). In contrast, the experimental steady-state I-V curve is better reproduced by the new set of conductances, in particular between -10 mV and -50 mV, where the old set of parameters was overestimating the currents with respect to the experimental data (Figs. 5.3 B and 5.11 C).

Also in this case, a current-clamp simulation has been performed by applying current steps between -4 pA and 20 pA (Fig. 5.11 C). Surprisingly, the current-clamp simulation highlighted a previously unobserved behaviour of the neuron that seems to possess two resting states of the membrane potential. Interestingly, the high stable state is reached when the neuron is stimulated with intermediate currents, between 0 pA and 15 pA, while for stimuli higher than 15 pA, the neuron repolarizes to the lowest resting state
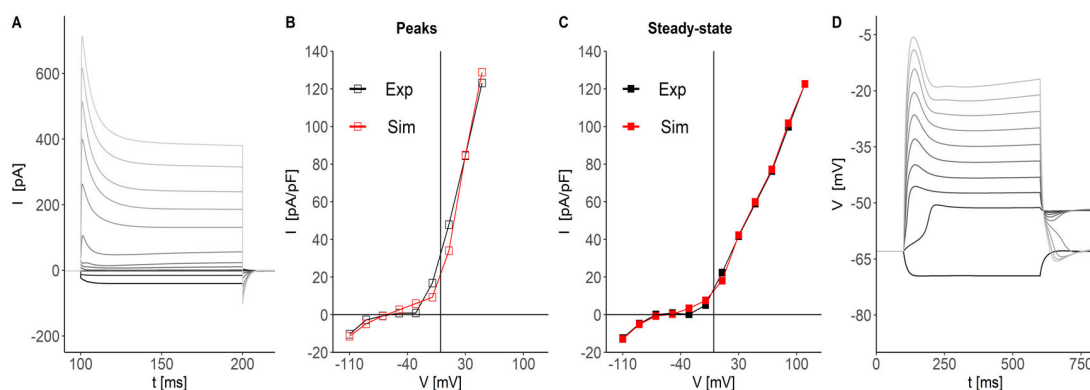
Figure 5.11: **Genetic algorithm optimization on AWC^{ON}. A) Voltage-clamp**. Simulated whole cell currents obtained with the same protocol of [19], i.e., 12 voltage steps ranging from -110 mV to 110 mV. The simulated currents are coloured with shades of greys that represent the intensity of the applied stimulus. The darkest shade encode for the most negative, and the brightest for the highest voltage step. **B) Peaks I-V**. The panel shows the comparison between experimental (black) and simulated (red) peak current. Experimental points (in black) from [19] are compared to the same curve obtained from the simulated currents reported in panel A. **C) Steady-state I-V**. The experimental steady-state I-V curve (black) from [19] is compared to the same curve obtained from the simulated currents reported in panel A. **D) Current-clamp simulation** The panel shows the response of the neuron to sequential current steps ranging between -2 pA and 20 pA. The simulation highlights a bistable behaviour characterized by two stable resting potentials. The high resting state can be reached from the low by applying a stimulus current. Notably, only intermediate stimuli are effective in producing the switch between the two states.

(Fig. 5.11 C). This last peculiar feature distinguishes the AWC^{ON} bistability from the kind of bistability observed in other neurons, such as the RMD *C. elgans* neurons (see Chapter 6, Section 6.3) and mammalian thalamocortical (TC) and nucleus reticularis thalamus (NRT) neurons [20, 219, 220]. Therefore, specific current-clamp simulations have been performed with the aim to clarify the role of stimulus intensity and duration on the post-stimulus state (Fig. 5.12). The current-clamp protocol has been designed to control the duration of the repolarization phase through a current ramp that restores the holding value of current in a linear manner ($i_h = 0$ pA) (Fig. 5.12). The simulation results suggest that, in addition to the intensity of the stimulus, also its temporal characteristics are essential in determining the switch between the two states. Indeed, for ramp durations above 26.1 ms, the neuron, after a depolarizing stimulus of 20 pA, re-polarizes into the high resting state, while for faster repolarization times the lower state is chosen (Fig. 5.12 B).

This result constitutes, to the best of the candidate knowledge, the first report of AWC^{ON} bistability, and therefore it deserves a further investigation from both the computational and experimental point of view. In the following, the results of the computational analysis conducted to elucidate the origin of this behaviour, are discussed, also with respect to the experiments that have been performed at CLNS@Sapienza-IIT to test the model
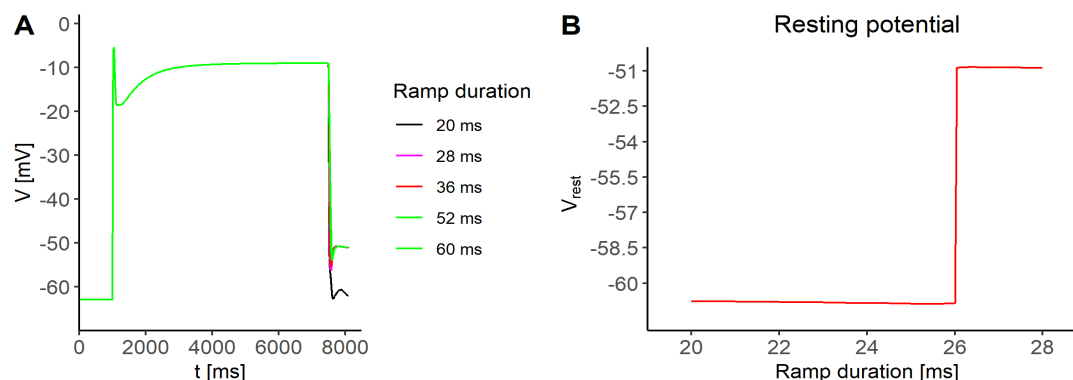
Figure 5.12: **AWC^{ON} bistability: repolarization phase analysis**. **A). AWC^{ON} responses to different re-polarizing ramps**. The neuron is stimulated with a 20 pA step lasting 7.5 s from an holding current $i_h = 0\ pA$. The return to the holding current is realized via a linear ramp with a duration between 20 ms and 60 ms. **B) Resting state as function of the ramp duration**. The region near the transition point has been analysed by fine tuning the ramp duration. The critical value for the switch between the two post-stimulus states is 26.1 s.

predictions. It is worth to note that something resembling a bistable behaviour is also present in AWC^{ON} calcium imaging data, upon chemical and mechanical stimulation, as shown in Chapter 3, Fig. 3.3.

Whole-cell simulations, alone, are not sufficient to elucidate the biophysical origin of the behaviour, i.e., the involvement of specific ionic currents in the bistability of AWC^{ON}. This peculiar behaviour is further investigated by means of *in silico* knockout simulations in voltage- and current-clamp configuration and by means of bifurcation diagrams.

5.3.2 Voltage and current clamp analysis of *in silico* knockouts of AWC^{ON} refined model

The first analysis conducted on the new model consisted in voltage and current clamp simulation of *in silico* knockouts to dissect the contribution of each current to the overall dynamics. With respect to the same analysis on the previous model (Figs. 5.5 and 5.6 in Section 5.1.2), the role of most of the channels in shaping the peaks and steady-state I-V curves is preserved (Figs. 5.13, and 5.14). The most striking differences between the two models are observed for SHK1 and EGL2 (Fig. 5.6 Ba/b and Fa/b, Fig. 5.14 Ba/b and Fa/b). In the new model, EGL2 removal does not cause significant alterations of the steady-state I-V curve, indicating a minor contribution to the steady-state currents (Fig. 5.14 Ba/b). SHK1 currents have replaced the role of EGL2 in the new model, becoming the major carriers of the steady-state potassium currents (Fig. 5.14 Fa/b). Indeed, their removal significantly reduces the steady-state currents and consequently shifts half of the I-V curves to lower currents than the WT (Fig 5.14 Fb).

To gain a first insight on the bistability origin, activation and inactivation dynamics of single currents and *in silico* knockout analyses are performed in the current clamp

---

109
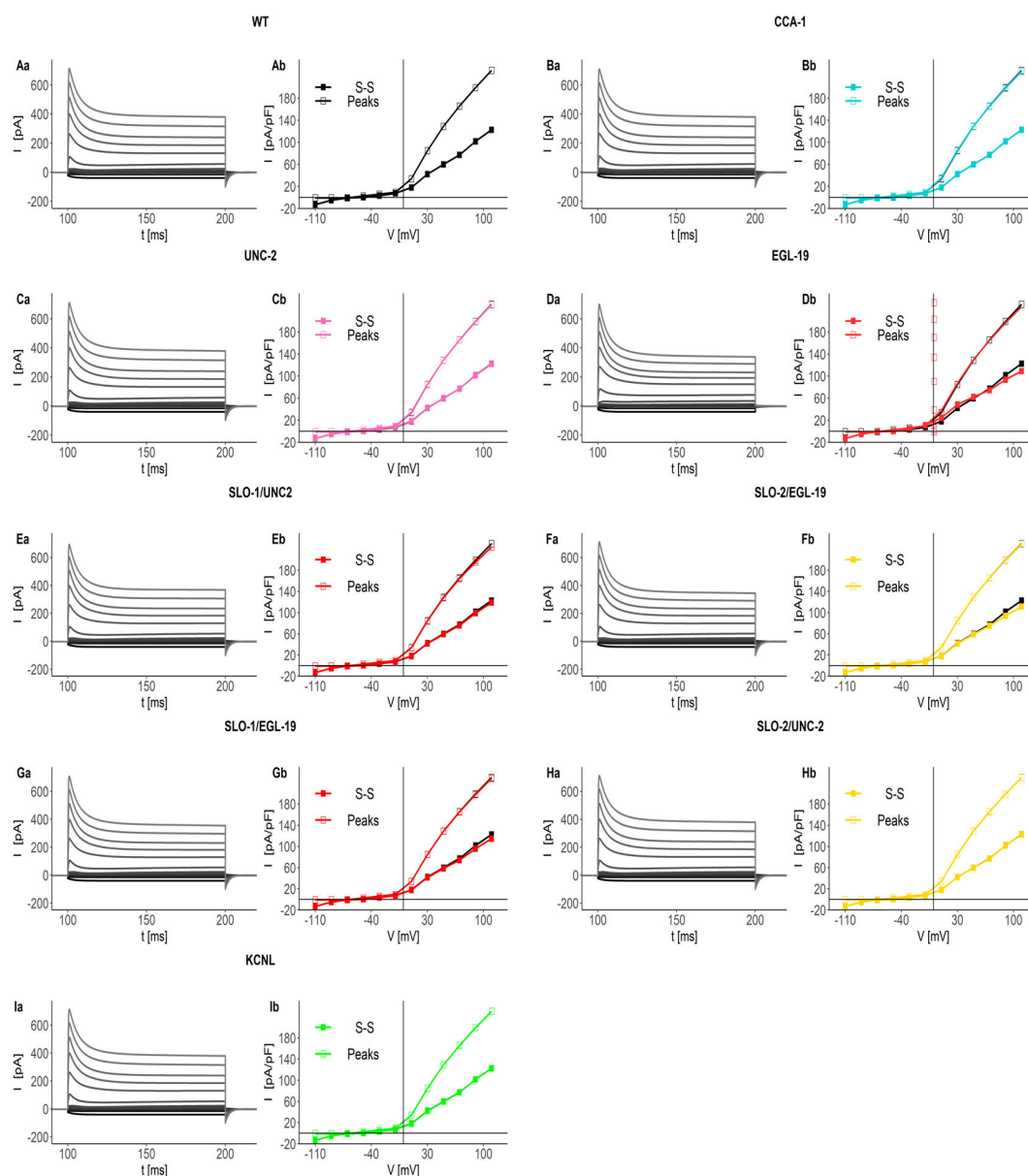
Figure 5.13: **Voltage clamp of CaV and K-Ca currents *in silico* knockout. Aa-Ia)** Simulated whole-cell currents of WT (panel Aa), CaV knockouts (panels Ba, Ca, and Da), and K-Ca knockouts (Panels Ea, Fa, Ga, Ha, Ia). **Ab-Ib) Peaks and steady-state I-V curves for CaV and KCa knockouts**. I-V curves are derived from the simulated currents showed in panels Aa-Ia. For the sake of clarity, in each panel the WT peaks (empty squares) and steady state (filled squares) I-V curves are reported. The simulation protocol is the same of Fig. 5.11A, i.e., 12 voltage steps between -110 mV and 110 mV with a duration of 100 ms and delivered from a holding potential of -70 mV.
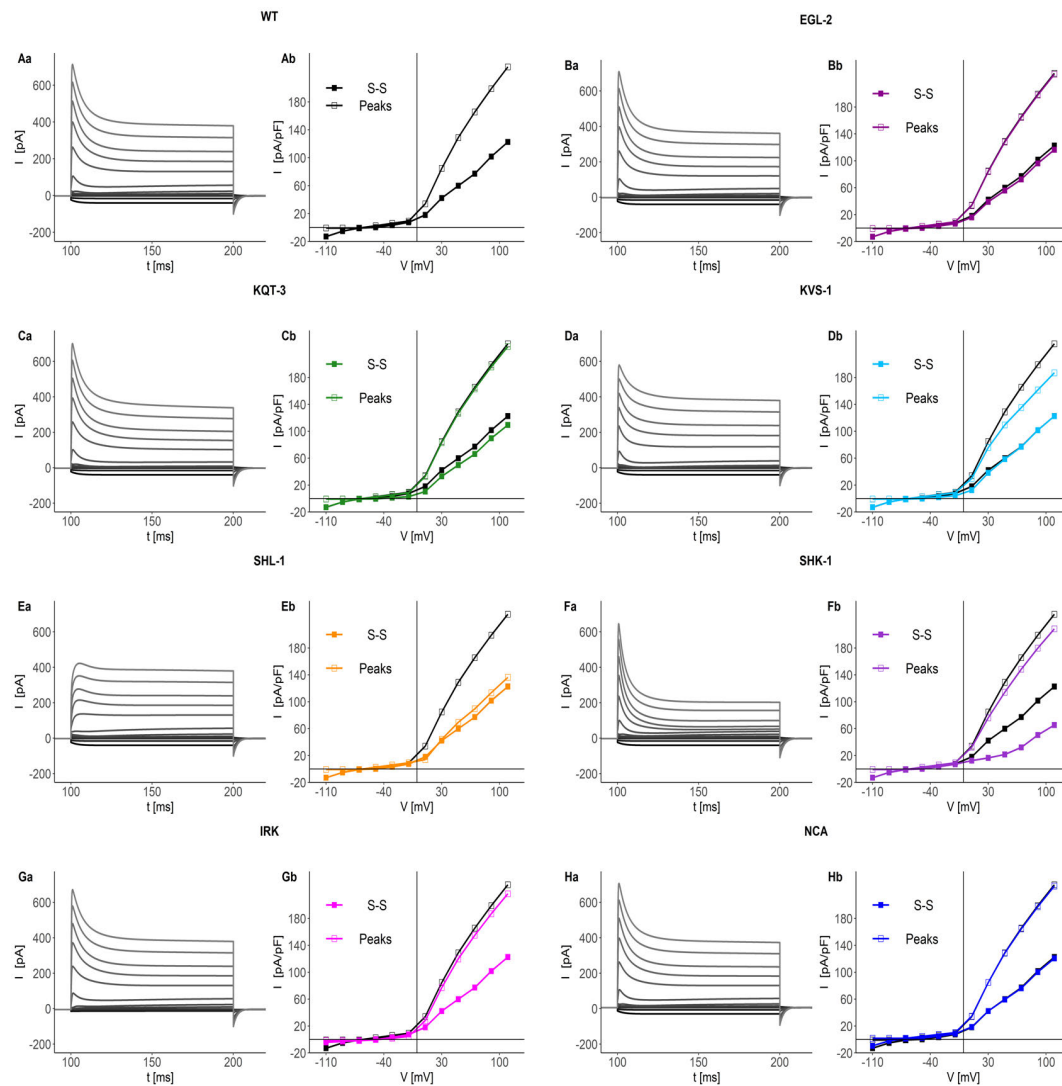
Figure 5.14: **Voltage clamp of KV currents *in silico* knockout. Aa-Ha)** Simulated whole-cell currents of WT (Panel Aa), KV. **Aa-Ha)** Simulated whole-cell currents of WT (panel Aa), KV knockouts (panels Ba-Ga), and NCA knockout (Panel Ha). **Ab-Hb) Peaks and steady-state I-V curves for KV knockouts**. I-V curves are derived from the simulated currents showed in panels Aa-Ha. For the sake of clarity, in each panel the WT peaks (empty squares) and steady state (filled squares) I-V curves are reported. The simulation protocol is the same of Fig. 5.11A, i.e., 12 voltage steps between -110 mV and 110 mV with a duration of 100 ms and delivered from a holding potential of -70 mV.

configuration by applying a current stimulus of 10 pA to elicit the transition between the two states. The computed normalized conductances for each ionic current are shown in Fig. 5.15, panels Ba-Ma; while the *in silico* knockout responses are reported in Fig. 5.15,

panels Ab-Mb and Na/b.
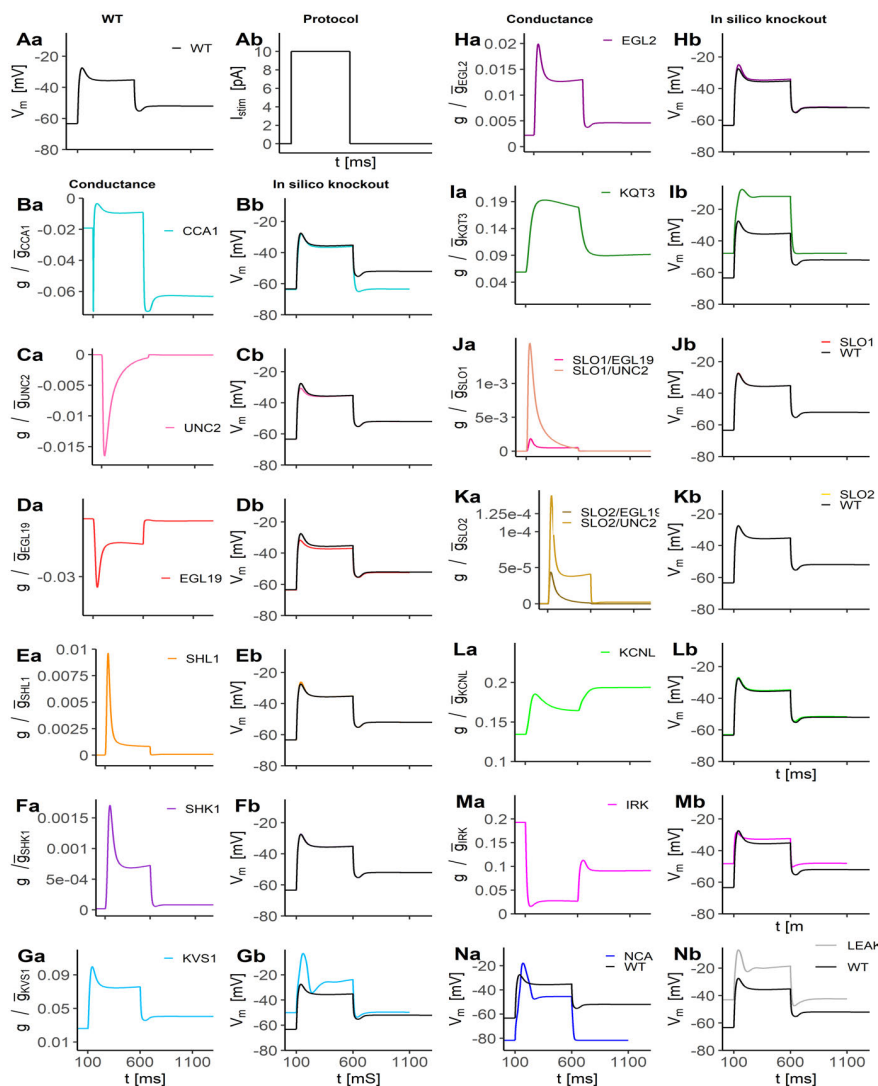
Figure 5.15: **AWC conductance and knockout analysis**. **Aa) WT response**. Simulation of the WT response to a 10 pA stimulus. **Ba-Ma) Normalized single-currents conductances**. The normalized conductance is defined as the product of the activation and inactivation variable. Panels Ba, Ca, and Da show the normalized conductance of voltage-gated calcium currents. In these panels $g_x/\bar{g}_x$ is multiplied by -1 to reproduce the sign of the current. Panels Ea-La show the normalized conductances for voltage-gated, big-conductance, and small-conductance potassium channels. **Ab-Mb) *In silico* knockout responses**. Simulated response of *in silico* knockout neurons. The simulation protocol consisted in a single-current pulse of 10 pA lasting 500 ms. The black curve in the panels represents the WT simulation.

Similarly to the first model (Fig. 5.4 in Section 5.1.2), the typical response of AWC neurons to a 10 pA stimulus consists of a fast upstroke phase followed by a slow repolarizing

phase that stabilizes in a plateau. However, in this case, after the stimulus removal, the neuron does not return to the initial resting state (-63.38 mV), instead, it falls into a second stable resting state at -52.21 mV.

The upstroke phase is characterized by the activation of CCA1 and UNC2 channels, that is counterbalanced by SHL1, KVS1, SHK1, and EGL2, with a little contribution of SLO1 and SLO2 currents (Fig. 5.15 Ba, Ca, Ea-Ha and Ia-Ja). The main calcium flux in the plateau phase is carried by EGL19, with a slowly decreasing contribution of UNC2 (Fig 5.15 Ca-Da). KQT3 currents are the most active in the plateau phase, with other contributions from EGL2, KVS1, and SHK1 (Fig. 5.15 Ha-Ia), while IRK channels are mainly active in the resting state, and inactivate during the stimulus phase. The post-stimulus phase seems to be supported by CCA1, KVS1, KQT3, and IRK currents that remain active after the stimulus removal (Fig. 5.15 Ba, GA, Ia, and Ma).

The remaining ionic currents inactivate almost completely in the post-stimulus phase (Fig. 5.15 Ca, Da, Ea, Fa, and Ja-La), suggesting that CCA1, KQT3, KVS1 and IRK channels may play a key role in the bistability. The hypothesis that the interplay between CCA1 currents and outward potassium fluxes from KQT3, KVS1, and IRK mediates the bistability is further supported by the *in silico* knockout analysis (Fig. 5.15 Bb-Mb). The removal of these channels suppresses the bistable behaviour, and in the case of potassium currents. it significantly alters the resting potential by shifting it to high potentials ($V_{WT}^R = -63.38$ mV, $V_{KVS1}^R = -50.07$ mV, $V_{KQT3}^R = -47.89$ mV, and $V_{IRK}^R = -48.29$ mV). In addition to the above mentioned currents, the *in silico* knockout analysis highlighted also the role of NCA and LEAK currents in the bistability mechanism.

5.3.3 Bistability analysis

To further elucidate the bistable behaviour of the neuron, a bistability analysis is performed. For each of the ionic currents that have been suggested to be critical for the bistability by the previous *in silico* knockout analysis, the steady-state stability of the system is investigated by characterizing the resting state of the system upon modulation of their conductances.

As first step, a characterization of the membrane potential stability at different applied stimuli is performed in WT and knockout cases (Fig. 5.16). This analysis is performed in AUTO within XPPAUT by computing the steady-state solutions of the ODEs system for different values of the stimulus current. In the diagrams shown in Fig 5.16, each point of the curves represents the steady-state value of the membrane potential for a certain applied stimulus. In particular, the most interesting information for the bistability analysis is the value of membrane potential at $I_{stim} = 0$ pA, which corresponds to the resting potential of the cell. As shown in Fig. 5.16 A, the WT curve (black) intercepts the $I_{stim} = 0$ pA line (vertical dashed) three times, indicating that three equilibrium points exist for the system. The two extremal points represent the stable resting potentials $V_r^l = -63.38$ mV and $V_r^u = -52.13$ mV, while the intermediate point represents an unstable equilibrium $V_r^i = -58.36$ mV. As expected, knockouts for KQT3, KVS1,

CCA1, LEAK, and NCA currents show only one intersection with $I_{stim} = 0$ pA line, i.e., only one stable resting potential exists (Fig. Fig 5.16 A). The other knockouts still display the three intersection distinctive of the bistable behaviour (Fig. Fig 5.16 B).
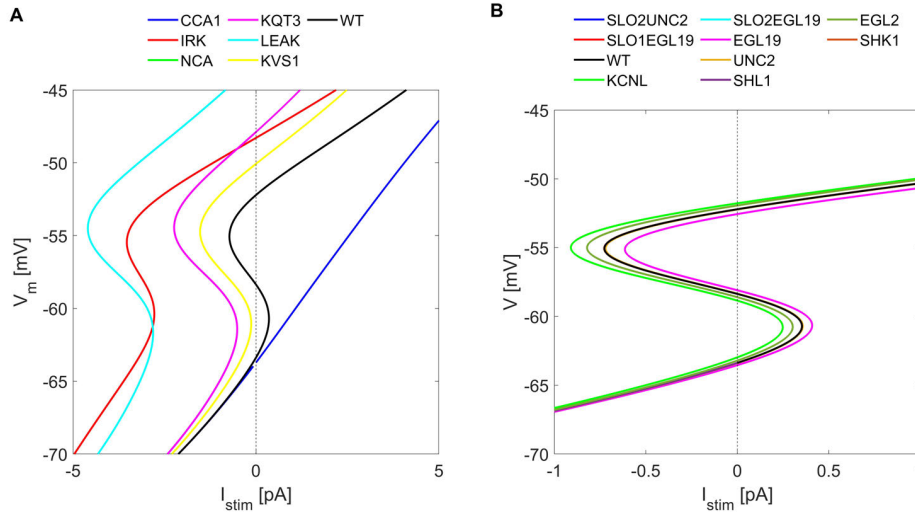
Figure 5.16: **Resting potential study for AWC neurons. A)-B) Steady-state V-I curve for *in silico* knockouts**. Diagrams are computed using AUTO within XPPAUT. Each curve represents the steady-state value of the membrane potential for a given stimulus current. For $I_{stim} = 0$ pA the diagram gives the resting potential of the neuron. In panel A are shown the curves computed for the knockouts of CCA1, KQT3, KVS1, NCA, and LEAK. Each curve has a unique intersection with the axis $I_{stim} = 0$ pA, and thereby a single resting potential. Panel B shows the curves computed for the bistable knockouts.

To achieve a complete picture of the complex interplay between channels, the equilibrium points of the system are studied by varying the parameters $\bar{g}_{CCA1}$, $\bar{g}_{IKR}$, $\bar{g}_{KQT3}$, $\bar{g}_{KVS1}$, and $\bar{g}_{NCA}$. In Fig. 5.17 A-F the computed bifurcation diagrams for channels involved in the bistability are shown. Notably, all the diagrams display two saddle-node bifurcations (fold or limit point (LP)). When the conductance $\bar{g}_x$ is below the value reached at the leftmost bifurcation point ($\bar{g}_x < x_{LP}^{left}$) the system displays only one stable solution V_r, while for increasing values of the conductance, the system undergoes a saddle-node bifurcation, from which two solutions arise, one stable V_s and one unstable V_u. At increasing values of the $\bar{g}_x$ parameter, a second saddle-node bifurcation point is reached. At this point, the unstable branch collides with the lower stable branch, giving rise to a unique high-voltage stable state. When the control parameter, $\bar{g}_x$, falls between the two LP points, the neuron has two stable resting potentials that can be reached by perturbing the neuron with a current stimulus. The range of $\bar{g}_x$ for which the bistability is observed is different for each of the currents, suggesting that the bistable behaviour is achieved by a complex interplay of currents.

All together these results suggest that AWC^{ON} neurons display a putative bistable be-
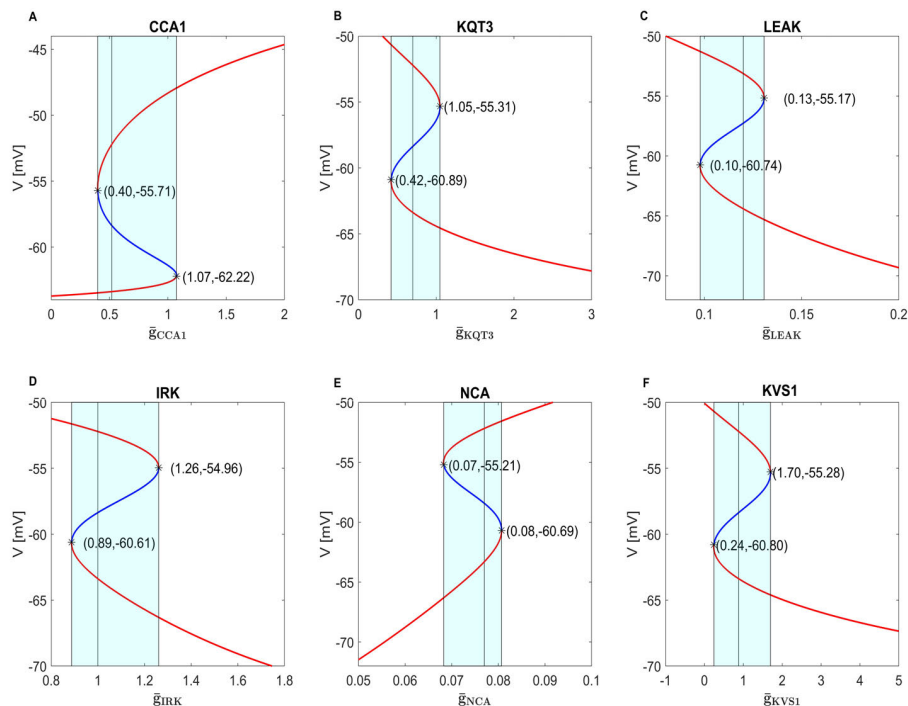
Figure 5.17: **Bifurcation diagrams for AWC neurons**. Bifurcation diagrams showing the equilibrium points of membrane potential evolution upon variation of $\bar{g}_x$. All diagrams show similar feature with two saddle-node-bifurcation arising for certain values of the conductances. The red lines represent the high (V_s) and low (V_r) branches, while the blue lines represent the unstable branch (V_u). The vertical grey line indicates the value of the conductance selected in the AWC model, and the light blue filled area highlights the region of bistability. Outside the bistability region the neuron has only one resting state given by V_r or V_s. All diagrams have been computed using AUTO within XPPAUT.

haviour that may be ascribed to the interplay between voltage-gated potassium and calcium currents, i.e. CCA1, KQT3, KVS1, IRK, and LEAK currents. These results constitute the first report of a bistable behaviour in *C. elegans* sensory neurons. However, this is not the absolute first report of bistable behaviours in the nematode neurons. Indeed, a similar behaviour has been experimentally observed in RMD motor neurons [20] (see also Chapter 6, Section 6.3). Given the potential relevance of this result on AWC^{ON}, dedicated patch clamp experiments similar to that performed for RMD neurons [20] should be performed to validate the modelling results.

5.4   Some insights on AWC$^{\text{ON}}$ putative mechanosensitivity

In this section the experimental results reporting a novel sensory behaviour of AWC$^{\text{ON}}$ neurons are described. These experiments have been performed at the CLNS@Sapienza-IIT, with the collaboration of the candidate, who followed the work and contributed to data acquisition and analysis.

AWC$^{\text{ON}}$ neurons are among the most important chemosensory neurons in *C. elegans* [83], however as many other sensory neurons the are not uniquely specialized to detect volatile chemical compounds, rather they are capable of detecting electric fields, light and temperature [19, 61, 84]. Here is reported a previously unobserved ability of AWC$^{\text{ON}}$ to detect mechanical stimuli delivered as pressure changes inside a microfluidic device. All the details regarding the experimental materials and protocols are given in Chapter 3.

As first step in elucidating the putative mechanosensory ability of AWC$^{\text{ON}}$ neurons, the responses of WT AWC$^{\text{ON}}$ neurons, harbouring the GCaMP5a genetically-encoded calcium indicator, to mechanical stimuli at increasing intensities have been recorded to characterize the sensitivity of the neuron. Worms are imaged in the mini-pulse arena when subjected to a transient (< 100 ms) mechanical stimuli delivered by opening and closing the valves of buffer reservoirs according to a specific temporal scheme (see Chapter 2, Section 3.1.2).

All the tested animals respond to valves switches with increased fluorescence values for each tested pressure (Fig. 5.18 A).
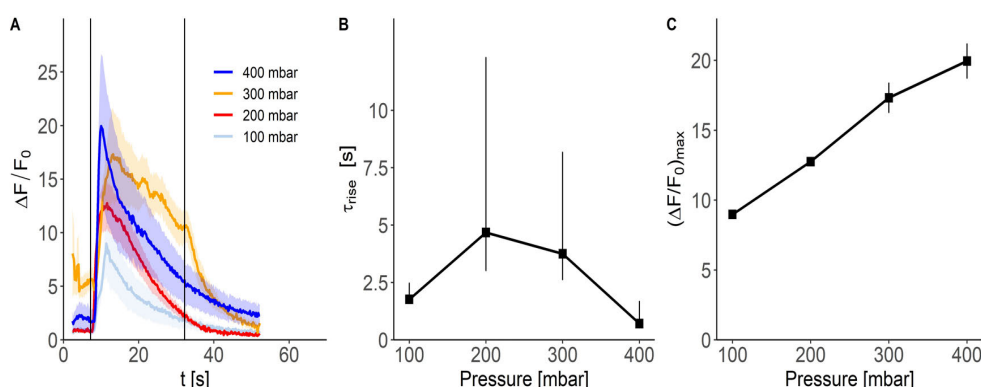
Figure 5.18: **AWC$^{\text{ON}}$ response to mechanical stimuli. A) Recorded fluorescence traces at different supplied pressure in the mini-pulse arena**. The panel shows the mean responses $\pm$s.e.m of WT worms subjected to four different mechanical stimuli. The supply pressure is between 100 mbar and 400 mbar. **B) Time to peaks analysis**. The rising time is calculated by performing a linear fit on the linearized fluorescence traces obtained by taking the natural lorgarithm of the signal (This analysis has been performed by the candidate). The error bars represent the 95% confidence interval. **C) Fluorescence peak intensity of the recorded traces as a function of pressure**. The peak intensity for each trace reported in Panel A is calculated as the maximum of the signal and plotted with its s.e.m. (this analysis has been performed by the candidate). Same data of Fig. 3.5 in Chapter 3.

5.4. SOME INSIGHTS ON AWC^{ON} PUTATIVE MECHANOSENSITIVITY

The peak intensity for the 100 mbar curve is almost 50% lower than that of the 400 mbar, indicating that higher pressure elicits higher responses in the neuron (Fig. 5.18 A and C). The response at 300 mbar shows a plateau-like behaviour, while the other responses are transient. This fact is not surprising; indeed, during the experiments, a variability in the responses is observed, so that not all the tested worms display a plateau upon mechanical stimulus application [41]. It has been observed that, upon mechanical stimulation, some worms respond with a transient increase of calcium, while some others display plateau-like responses [41]. This variability is observed not only among different animals tested in a single experiment but also among the responses of a single animal to repetitive stimulations, suggesting that the mechanical responses of AWC^{ON} neurons might be less robust to environmental factors than the chemical ones [41]. Moreover it is also possible that for the 300 mbar pressure a 25 s interval between the two stimuli is too short to allow the relaxation of the calcium to the baseline. Compared to chemical responses that display a saturating behaviour at increasing stimulus intensities (Fig. 5.10 A in Section 5.2), mechanical responses seem to increase linearly with the stimulus strength (Fig. 5.18 C). However, it has to be noted that the range of mechanical stimuli here tested is very limited compared to the range of concentrations used to compute the dose-response curves for chemical stimuli (Fig. 5.10, [40]). Thus, further experiments should be performed to uncover eventual saturation effects also arising in the case of mechanical responses. The intensity of the stimulus also affects the rising phase of the peak, but in a non-linear trend (Fig. 5.18 C).

The ability of AWC^{ON} neurons to respond to mechanical stimuli could be the result of their intrinsic properties or a consequence of the information received from the surrounding network. In the first scenario, AWC^{ON} mechanosensitivity is intrinsic, and thereby the neuron must express some mechanoreceptors that enable it to sense mechanical stimuli. In the second case, AWC^{ON} behaves as an interneuron activated by mechanosensory neurons. The two scenarios are equally probable, indeed, despite their primary sensory character, AWC^{ON} neurons could be recruited as interneurons by other sensory circuits, for example, the salt sensation circuit [17]. On the other hand, there are other sensory neurons that display a polymodal behaviour, being able to respond to short (500 ms) mechanical stimuli with robust and sustained intracellular calcium changes [61, 263]. Therefore, in light of these considerations, a key step in the computational model validation is to establish whether the experimentally observed responses are intrinsic or not.

To clarify this point, two mutants with defective synaptic communication in AWC^{ON} neurons have been selected, the *unc-31* and *unc-13* mutants [17]. *unc-13* and *unc-31* are involved in small and dense-core synaptic vesicles release, respectively [17, 247, 248]. Thereby their suppression guarantees an almost complete separation of the neurons from the network that may elicit AWC^{ON} mechanical responses, at least as far the chemical signalling is concerned. Further studies should be performed to investigate the eventual role of gap-junction signalling in the mechanical responses. *unc-13* and *unc-31* mutants have been tested in the same experimental conditions of WT worms at 100 mbar and 300 mbar. At 100 mbar, no significant differences have been observed between WT

117

and mutant worms, while at 300 mbar the mutants responses are considerably reduced
in magnitude (Fig. 5.19 A-B). These results suggest that AWC$^{\text{ON}}$ mechanosensitivity
might have an intrinsic component for low-intensity stimuli, while for increasing stimuli,
additional sensory mechanisms may be involved, for example, those responsible for the
harsh touch sensation.
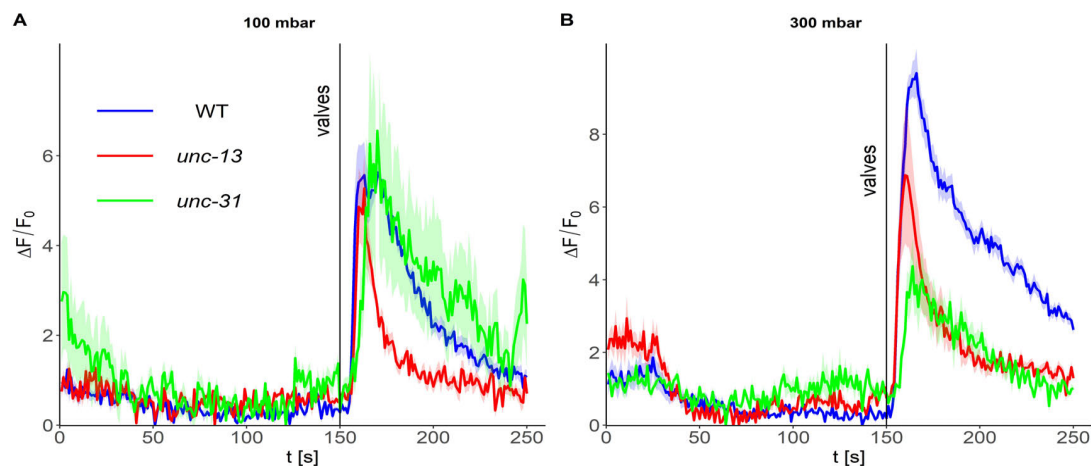
Figure 5.19: **unc-13 and unc-31 mutant responses to mechanical stimuli**. **A) Average
responses for 100 mbar supply pressure** The panel shows the average ($n > 5$) responses
of WT, *unc-13* and *unc-31* mutants to a mechanical stimulus delivered with a 100 mbar supply
pressure in the reservoirs. The shaded areas represent the standard error of the mean. **B)
Average responses for 300 mbar supply pressure**. The panel shows the average ($n > 5$)
responses of WT, *unc-13* and *unc-31* mutants to a mechanical stimulus delivered with a 300 mbar
supply pressure in the reservoirs. The shaded areas represent the standard error of the mean.
The experimental recordings and data analysis have been performed at the CLNS@Sapienza.
Same data of Fig. 3.6 in Chapter 3.

AWC$^{\text{ON}}$ neurons may express on their surface some mechanoreceptors that enable them
to sense pressure changes. However the exact nature of such receptors is still unknown.
Based on the rationals below, two mutants, *osm-9* and *tax-4*, have been selected, to gain
more information on the molecular mechanisms of AWC$^{\text{ON}}$ mechanosensation.
In *C. elegans* ciliated mechanosensory neurons (ASH, ADE, CEP, FLP, IL1, OLQ, and
PDE) the detection of mechanical stimuli is allowed by a combination of TRP and
DEG/ENaC channels [264, 265]. One of these TRP channels, the OSM-9 channel, is
also expressed in AWC$^{\text{ON}}$ neurons [266, 267, 268]. OSM-9 channels are expressed in
the nematode mechanosensory neurons, where they co-assemble with other TRPV chan-
nels, encoded by the *ocr-1, ocr-2* and *ocr-3* genes [269, 270]. OSM-9 and OCR proteins
function in a interdependent manner, so that the suppression of one subunit disrupts
the functionality of the others [269, 270, 271]. In particular, OCR proteins are essential
for the proper localization of OSM-9 in the cilia of mechanosensory neurons [270]. In
contrast to mechanosensory neurons, AWC$^{\text{ON}}$ does not express the *ocr* genes that are
essential for the *osm-9* localization in the cilia; rather, it expresses homomeric OSM-

9 channels in the soma where they regulate the olfactory plasticity, being responsible of the long term adaption to odors [267]. Due to its role in mechanosensory neurons, OSM-9 has been chosen for the experiments. However, the considerations above, in particular those related to the lack of expression in AWC^{ON} cilia, make it unlikely that OSM-9 channels are responsible for AWC^{ON} mechanosensation. Calcium imaging experiments on *osm-9* mutants confirmed this hypothesis. Indeed, *osm-9* mutant responses to mechanical stimuli resemble those of the WT worms and display the prototypical mechanosensitive behaviour, suggesting that OSM-9 channels are not responsible for AWC^{ON} mechanosensitivity (Fig. 5.20 B,F).
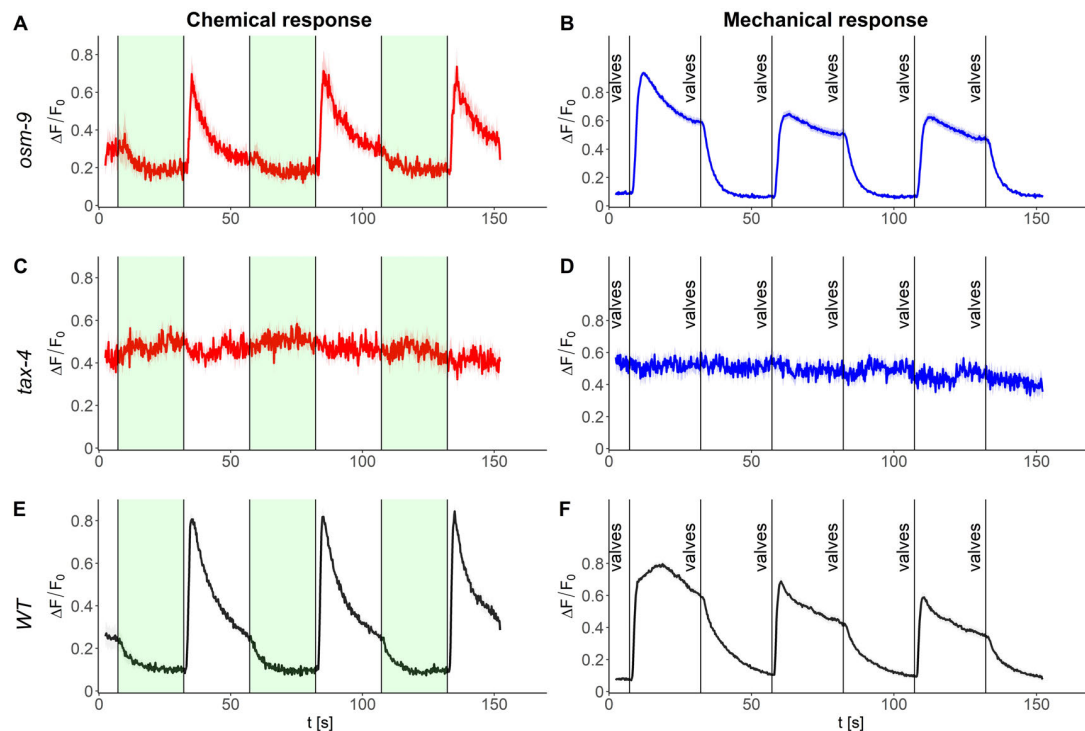
Figure 5.20: ***osm-9* and *tax-4* mutant responses to mechanical and chemical stimuli**. **A)-B) *osm-9* responses to chemical and mechanical stimuli**. The panels show the average responses ($n > 10$) of the *osm-9* mutant to chemical (IAA 10^{-5}, panel A) and mechanical stimuli (100 mbar of supply pressure, panel B). The shaded areas indicate the s.e.m. **C)-D) *tax-4* responses to chemical and mechanical stimuli**. The panels show the average responses ($n > 10$) of the *tax-4* mutant to chemical (IAA 10^{-5}, panel C) and mechanical stimuli (100 mbar of supply pressure, panel D). **E)-F) WT responses to chemical and mechanical stimuli**. The panels show the responses of WT worms to repetitive chemical (IAA 10^{-5}, panel E) and mechanical stimuli (supply pressure 100 mbar, panel F). The shaded areas indicate the s.e.m. The experiments have been performed at CLNS@Sapienza-IIT. Same data of Figs. 3.3 and 3.7 in Chapter 3.

The results on *osm-9* mutants and the absence of expression in AWC^{ON} neurons of other known mechanosensitive channels, such as DEG/ENac channels or other mechanosensi-

tive TRP channels, suggest that AWC^{ON} mechanosensitivity relies on a different mechanism. There are growing evidences that GPCRs can act as mechanoreceptors to detect stretch-induced deformations of the membrane [272, 273, 274]. Different works have shown that mammalian olfactory neurons could also detect mechanical stimuli sharing the transduction pathway with the olfactory one [275, 276, 277]. Also, AWC^{ON} neurons express in their cilia 22 GPCRs, some of which have been predicted to have a structure similar to that of mechanosensitive GPCRs [272, 278]. Altogether, these considerations could suggest an involvement of the GPCRs in AWC^{ON} mechanosensation.

As the first step in elucidating a possible GPCR-mediated mechanotransduction pathway in AWC^{ON}, the mechanical responses of *tax-4* mutants have been tested and compared with the chemical responses measured in the same mutants. The *tax-4* gene encodes for CNG channels subunits that are essential in defining both the morphological features and sensing ability of many sensory neurons, including AWC^{ON} [131, 279, 280]. CNG channels activate downstream to the metabotropic receptor signalling pathway so that their suppression disrupts the responses of AWC^{ON} to chemical stimuli (Fig. 5.20 C,E). Notably, *tax-4* mutants do not respond to mechanical stimuli (Fig. 5.20 D,F), suggesting that GPCRs may be involved in the transduction of mechanical stimuli. This result is in agreement with the results of Grosmaitre et al., showing that the suppression or blockade of the CNG channels eliminates both the chemical and mechanical responses in mouse olfactory neurons [277]. Despite these first encouraging experimental results, further studies should be performed to identify molecular components involved in AWC^{ON} mechanotransduction. AWC^{ON} neurons express many different GPCRs on their surface, and also it cannot be excluded that other mechanisms may be involved, such as gap-junction signalling from other neurons, mechanosensitive innexin hemichannels [281], or still unidentified cationic channels [263].

Other possible candidates to explain the mechanosensitivity are the voltage-gated calcium channels and potassium channels (VGCs). Indeed, many studies on the corresponding mammalian channels have shown that VGCs can sense deformations of the lipid bilayer [282, 283, 284, 285]. However, despite their ability to sense membrane stretch, VGCs channels are regulators of neuronal excitability rather than primary mechanoreceptors [283]. Furthermore, there is no report of their specific expression on AWC^{ON} cilia, making it even more unlikely that the AWC^{ON} mechanosensitivity depends on VGCs channels. To test the role of these channels in the AWC^{ON} chemosensation and mechanosensation calcium imaging experiments have been performed in *egl-19(n582)*, *cca-1(ad1650)* mutants. Also, the *nca-2(gk5)* have been tested to clarify the role of these Na^{+} permeable channels.

egl-19, *cca-1* and *nca-2* mutants respond to chemical and mechanical stimuli with large calcium excursions (Fig. 5.21 A-F). Upon chemical stimulation, the mutants do not display significant differences from WT (Fig. 5.21 A,C,E and Fig. 5.20E); while in the case of mechanical stimuli some differences are observed, in particular for *cca-1* mutants (Fig. 5.21 B and Fig. 5.20 F). *cca-1* mechanical responses lack the prototypical plateau observed in WT. *egl-19* mutants responses lack the initial fast rising but still show the plateau (Fig. 5.21 D and Fig. 5.20 F); while *nca-2* responses are almost unchanged

(Fig. 5.21 F and Fig. 5.20 F). Altogether these data suggest that EGL-19 and CCA-1 channels are involved in the transduction of mechanical stimuli, but, as expected, they are not primary mechanosensors.
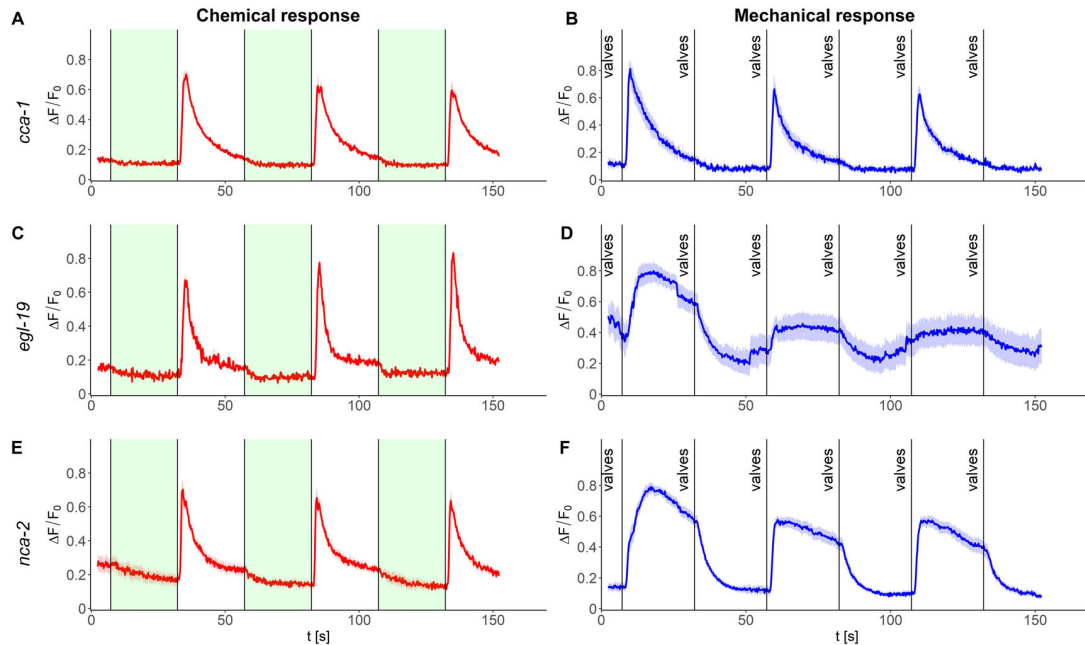
Figure 5.21: **egl-19, cca-1, and nca-2 mutants responses to mechanical stimuli. A)-B). cca-1 mutants responses**. Panel A shows the mean ($n > 5$) ±s.e.m responses to IAA 10^{-5}, while panel B reports the mechanical responses (supply pressure: 100 mbar). **C)-D) egl-19 mutants responses.** Panel C shows the mean ($n > 5$) ±s.e.m responses to IAA 10^{-5}, while panel D reports the mechanical responses (supply pressure: 100 mbar). **E)-F) nca-2 mutants mechanical responses**. Panel E shows the mean ($n > 5$) ±s.e.m responses to IAA 10^{-5}, while panel F reports the mechanical responses (supply pressure: 100 mbar).

Finally, an interesting feature of the AWC$^{\text{ON}}$ mechanical responses is the flip-flop-like behaviour exhibited upon repetitive mechanical stimuli delivered with 25 s intervals (Fig. 5.20 F). This behaviour may recall the bistable dynamics of the resting potential observed in current clamp simulations (Fig. 5.15). In particular the first mechanical stimulus could induce the transition to the upper resting state, while the second stimulus allows the return to lower one. The result on cca-1 and egl-19 mutants seem to confirm the model predictions. Indeed, cca-1 mutants do not display the flip-flop behaviour, i.e. the bistability is suppressed, that is instead maintained in egl-19 mutants. In contrast with the modelling predictions, nca-2 mutants show a bistable-like behaviour. The results on cca-1 and egl-19 are encouraging, however it must be underlined that calcium imaging experiments are not suitable to definitely validate the model predictions. Indeed, as observed for OLL neurons, the calcium signals dynamics might be considerably slower (tens of seconds) compared to the extremely fast dynamics (in the milliseconds range) of the mechano-gated currents induced by mechanical stimuli [263]. A proper validation

of the model predictions would require a dedicated set of patch-clamp experiments to test the membrane voltage-bistability and its eventual relationship with the putative mechanosensory behaviour of AWC$^{\text{ON}}$.

5.5   Conclusion

AWC$^{\text{ON}}$ neurons are among the most important sensory neurons in *C. elegans*, being responsible for effective food procurement and sexual attraction in males [259, 260]. Moreover, many studies have highlighted the polymodal nature of AWC neurons, which are involved in thermal [19], chemical [13, 83, 84, 286] and electrical stimuli [75].
In this work, a detailed biophysical model of AWC$^{\text{ON}}$ has been developed, reproducing the salient characteristics observed in voltage-clamp experiments [19]. The model is obtained by combining the models of single ionic currents (presented in Chapter 4), and the set of optimal conductances is fine-tuned to reproduce the experimental behaviour. The high level of detail included in the model allowed to analyse for the first time the contribution of single ionic currents to the overall neuron dynamics, both in the voltage and current-clamp configurations. In particular, the simulations performed in the current clamp configuration highlighted the ability of AWC$^{\text{ON}}$ neurons to generate threshold responses shaped by the interplay between calcium currents carried by EGL-19 and UNC-2 channels and potassium currents from KVS-1 and EGL-2 channels. Moreover, voltage-clamp simulations of *in silico* knockout neurons suggested that the main carrier of the fast transient outward rectifier currents are the SHL-1 channels and that SLO1 and SLO2 currents play a minor role in the generation of the responses of AWC$^{\text{ON}}$ neurons, similarly to ventral motor [23, 38].

The detailed model of the electrical response developed by the candidate has been coupled with a detailed model of the G-protein signalling pathway regulating the AWC$^{\text{ON}}$ olfaction developed by Usuyama et al. [1] to obtain a biophysically accurate description of the AWC$^{\text{ON}}$ neurons functioning. Despite the spurious peaks appearing at high odor concentrations, the model correctly reproduces the experimental observations [13, 40, 42]. The neuron responds to chemical stimuli in a dose-dependent manner in which the higher is the odor concentration, the higher is calcium responses. Moreover, the intensity of the response and its rising time depends on the exposure time, with higher responses arising at longer exposure times. Finally, an extended sensitivity analysis has been performed, with respect to [1], to characterize both the membrane voltage and the intracellular calcium responses in a wide range of odor concentrations and exposure times. This model constitutes a useful tool to investigate the effect of intracellular signalling processes on the electrical behaviour and allows the direct comparison of model predictions with the experimental calcium imaging data. Despite the encouraging results, there are some aspects that deserve further investigation. The first concerns the study of the influence of voltage-gated calcium channels in shaping both the intracellular calcium and the membrane voltage responses. The second aspect, which is probably connected to the first, is the appearance of discontinuities in dose-response curves in correspondence

of membrane voltage values suitable to activate voltage-gated T-type calcium channels. The last aspect studied is the appearance of spurious peaks in the calcium responses at high concentrations. These aspects will be addressed with additional computational studies to clarify the role of each calcium flux in the overall dynamics and by further refinement of the coupled model parameters, also with respect to experimental data.

As the last step of the computational study of AWC^{ON} neurons, the parameters of the electrical model have been refined by applying a genetic-algorithm based routine implemented in Python specifically for this purpose. This analysis allowed to obtain a new set of conductance that better reproduces the experimental results [19] with respect to the first model. In the new model, the role of the ionic channels is almost preserved, except for an inversion of the roles of EGL-2 and SHK-1 currents. Interestingly, current clamp simulations performed with the new set of parameters revealed the existence of two stable resting states in the membrane potential of AWC^{ON} neurons. A detailed analysis, performed *via* conductance and bistability studies and *in silico* knockout simulations, suggests that AWC^{ON} bistability relies on a complex interplay of calcium and potassium currents, carried by CCA-1 and KQT-3, KVS-1, and IRK channels, respectively. Moreover, the bistability is further tuned by leakage conductances (LEAK and NCA currents).

Finally, a previously unobserved sensory function of AWC^{ON} is investigated through calcium imaging experiments performed with the collaboration of CLNS@Sapienza. The study has been conducted through calcium imaging experiments on WT and mutant worms harbouring the GCaMP5a. Experiments performed in a microfluidic device, the mini-pulse arena (see Chapter 3), showed that AWC^{ON} neurons are capable of responding to transient mechanical stimuli, delivered as changes in the fluid stream inside the microfluidic device. Worms defective for synaptic transmission (*unc-13* and *unc-31* mutants) still respond to mechanical stimuli, suggesting that the mechanosensitivity is mainly determined by the intrinsic properties of the cell. The molecular origin of these responses have been investigated by testing *osm-9* and *tax-4* mutants. In particular, the result on *tax-4* mutants suggests that a G-protein mediated pathway may be recruited in the AWC^{ON}-mediated mechanosensation, similarly to mammalian olfactory neurons [277]. However, further studies should be performed to dissect the specific pathway and the molecular players involved in the transduction of mechanical stimuli. Finally, the role of CCA-1, EGL-19, and NCA-2 channels in chemical and mechanical responses has been investigated. *cca-1*, *egl-19*, and *nca-2* mutants display almost normal chemical responses, while mechanical responses are altered, especially in *cca-1* mutants, indicating that these channels may be important for the transduction of mechanical stimuli. AWC^{ON} neurons display a flip-flop-like behaviour resembling a bistable regime. However, dedicated current-clamp experiments must be performed to validate the prediction on AWC^{ON} bistability.

Chapter 6

Interneurons and motor neurons modelling

125

In this chapter, the models of AIY, RIM, and RMD neurons are presented. In particular, the models of RMD and RIM neurons are built using XPPAUT, and the set of optimal conductances is derived by hand, while the AIY model is developed in NEURON and optimized using a GA routine implemented in Python (See Chapter 2). The specific ionic currents included in the single-neuron models are selected based on available electrophysiology data [20], in the case of RMD, and on gene expression profiles obtained from the Wormbase [5] and CENGeN [37] databases, in the case of AIY and RIM interneuron. The behaviour of each modelled neuron is analysed by means of *in silico* knockout simulations performed both in voltage and current clamp configurations, and of normalized conductance analysis. Moreover, the bistable behaviour of RMD neurons is further analysed with a dedicated bistability analysis to clarify its biophysical origin. This last analysis is performed in AUTO within XPPAUT and by means of voltage-clamp simulations.
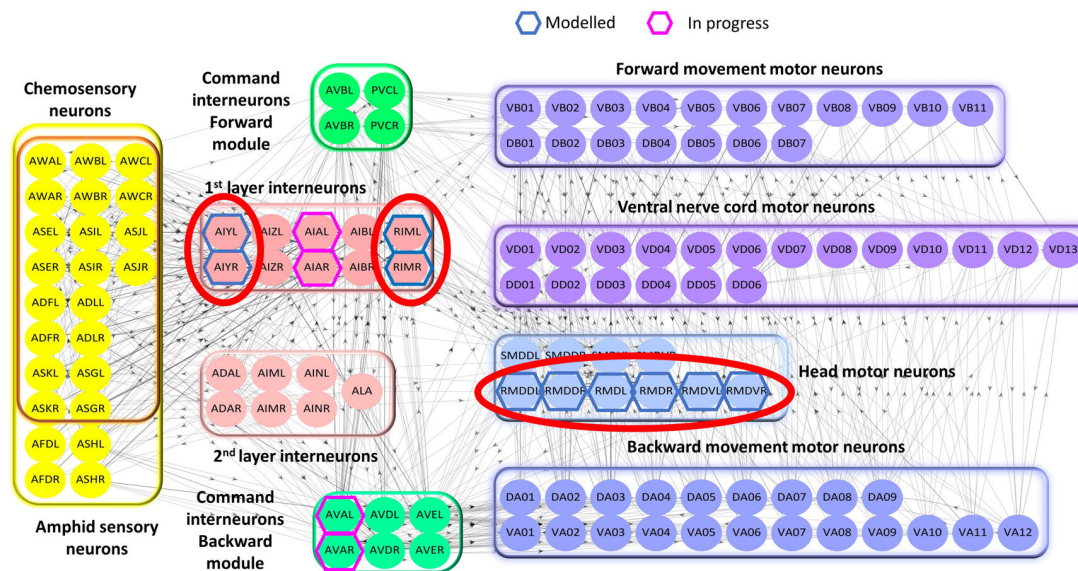
Figure 6.1: **Neurons modelled in Chapter 5**

6.1 AIY interneurons

AIY neurons are a class of interneurons whose primary function is the processing of sensory information received from many sensory neurons, including the AWC olfactory neurons. The model here presented is implemented in NEURON and optimized through a GA based routine implemented in Python, using as reference published whole-cell current and voltage-clamp recordings [21]. Despite the availability of whole-cell recordings, no further details are known about AIY physiology; in particular, the specific ion chan-

nels that give rise to the recorded currents are not known. Therefore, the set of ionic currents to be included in the model is selected based on the information collected from the CENGeN [37] database and includes UNC2, EGL19, SLO1, SLO2, SHL1, UNC103, KQT1, EGL2, KCNL, NCA, and IRK currents (Eq. 6.1)

$$
\begin{aligned}
I_{ion}^{AIY} =& I_{\mathrm{SHL1}} + I_{\mathrm{KQT1}} + I_{\mathrm{UNC103}} + I_{\mathrm{EGL2}} + I_{\mathrm{EGL19}} + I_{\mathrm{UNC2}} \\
& + I_{\mathrm{SLO1/EGL19}} + I_{\mathrm{SLO1/UNC2}} + I_{\mathrm{SLO2/EGL19}} + I_{\mathrm{SLO2/UNC2}} \\
& + I_{\mathrm{KCNL}} + I_{\mathrm{NCA}} + I_{\mathrm{LEAK}}.
\end{aligned}
\tag{6.1}
$$

Several preliminary runs of GA optimization have been performed, trying different fitness functions based on voltage and current clamp data and mean I-V curves. From these preliminary runs, a subset of conductances that is suitable for reproducing the I-V curves in the region between -70 mV and 10 mV, is derived and includes EGL19, UNC2 SLO2, SLO1, IRK, NCA, and KNCL conductances. The remaining conductances are determined with a GA-based optimization, using as reference data the mean I-V curves taken from [21]. In Table 6.1, the specific settings for the GA optimization are reported, while the final set of conductances is listed in Table 6.2.

Table 6.1: **AIY GA optmization settings.** In this table the specific settings of the GA are listed, used to derive the optimal set of parameters listed in Table 5.3. The subscripts EXP and SIM denote experimental and simulated data, respectively.

	Specific setting
Reference data	Peaks and Stead-state I-V curves from [19]
Fitness calculation	$\psi = \sum_{j=1}^{N} \left[\frac{(IV_{peaks,EXP}^{j} - IV_{peak,SIM}^{j})^2}{2} + \frac{(IV_{ss,EXP}^{j} - IV_{ss,SIM}^{j})^2}{2} \right]$
Population size	50
Number of generations	4
Crossover	Blend crossover crossover rate: 1 $\alpha = 0.1$
Replacement	Truncation replacement
Termination criteria	Combination of average fitness termination and diversity termination

Table 6.2: **List of optimized conductances for AIY**. The first and the second columns report the list of ion currents used in the model and the optimized set of conductances, respectively. The last two columns report the upper and lower limits for GA optimization. These limits are chosen in a suitable range defined after multiple preliminary runs of the GA routine. In this model, the second version of the SHL1 currents model is used (for further details see Chapter 4).

Current	Conductance ($\bar{g}_x$) [nS] AWC^{ON}	Lower Limit [nS]	Upper Limit [nS]
SHL1	0.41	0.1	1.1
UNC103	0.08	0.05	0.8
EGL2	0.233	0.1	0.6
LEAK	0.088	0.05	0.8
KQT1	0.198	0.1	0.5
EGL19	0.2	fixed	
UNC2	0.2	fixed	
SLO1/EGL19	0.3	fixed	
SLO1/UNC2	0.3	fixed	
SLO2/EGL19	0.3	fixed	
SLO2/UNC2	0.3	fixed	
KCNL	0.12	fixed	
NCA	0.045	fixed	
IRK	0.15	fixed	
LEAK	0.11	0.1	1

6.1.1 AIY WT whole-cell voltage and curret clamp

Fig. 6.2 shows the final results of GA optimization. In accordance with experimental observations [21, 24], in response to sequential voltage steps between -120 mV and 50 mV AIY interneurons display modest non-inactivating outward rectifier currents, and a small inward rectifier component arising at low voltages, with a transition between the two regimes around -30 mV (Fig. 6.2 A-C). The comparison between simulated and experimental I-V curves shows that the model correctly reproduces this behaviour, despite small inconsistencies in the intermediate region (-50 mV and 30 mV) of the I-V (Fig. 6.2 A-C).

During current-clamp simulation, the neuron shows large voltage excursions in response to stimuli between -15 pA and 35 pA. Notably, hyperpolarizing stimuli seem to be more effective in perturbing the neuron. Indeed, negative currents induce larger voltage excursions than that elicited by a positive stimulus of the same magnitude (blue traces in Fig. 6.2 C). Despite the large excursions in the voltage, both the experimental and simulated traces do not show any threshold-like responses. Upon current injection, the voltage undergoes a fast upstroke followed by a fast stabilization in a plateau. The contribution of single ionic currents to the whole-cell dynamics is studied by means of *in silico* knockout simulations and conductance analysis.
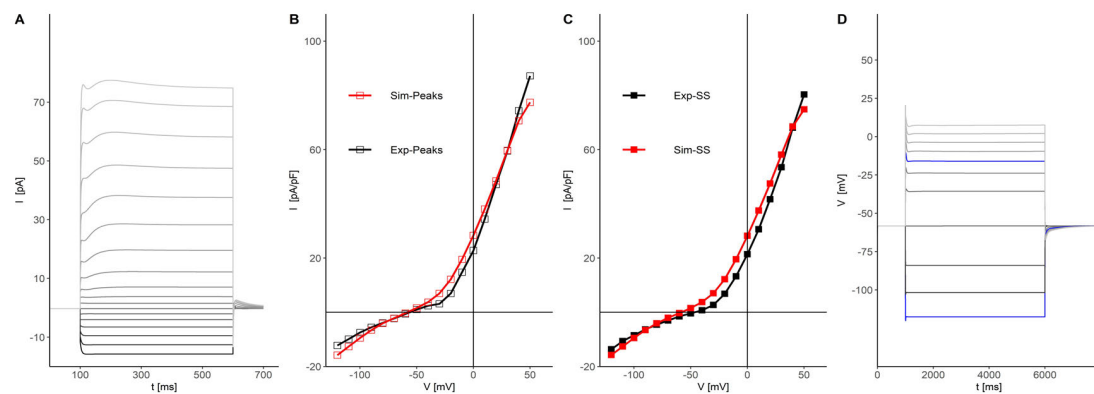
Figure 6.2: **AIY model: voltage- and current-clamp simulations**. **A) Simulated whole-cell currents of AIY interneurons.** The voltage-clamp simulation protocol consists of 17 voltage steps ranging between -120 mV and 50 mV with a duration of 500 ms, and delivered from a holding potential of -60 mV. In the panel the simulated whole-cell currents are shown. **B)-C) Experimental and simulated I-V curves comparison**. The panels report simulated (red) and experimental (black) steady-state (filled square) and peaks (empty squares) I-V curves for AIY neurons. Reference experimental data are obtained from [21]. **D) Current-clamp simulation**. In the panel the simulated voltage responses are reported. The current-clamp protocol consists of 11 current steps between -15 pA and 35 pA applied from and holding current of 0 pA. The step duration is 5 s. The cell capacitance is set to 1 $\mu F/cm^2$, that corresponds to 0.67 pF when scaled on the entire neuron surface (65.89 μm^2, from Neuromorpho). This value is in agreement with experimental measurements for AIY neurons [24]. All the simulations are performed in NEURON using the same protocols of experimental recordings [21].

6.1.2 *In silico* knockouts and conductance analysis

Voltage-clamp simulations of *in silico* knockout AIY neurons (Figs. 6.3-6.4) show that the outward rectifier behaviour of the neuron is mainly mediated by the potassium currents EGL2 and KQT1 (Fig. 6.3 Ba/b-Ca/b). EGL2 and KQT1 removal consistently affects both steady-state and peak currents by reducing the outward rectifier component (Fig. 6.3 Ba/b-Ca/b). SHL1, KCNL, and SLO1/EGL19 currents slightly affect the upper part of the I-Vs, by causing a small reduction in the outward current, while SLO2-UNC2, SLO1-UNC2, SLO1-EGL19 and UNC-103 do not significantly alter both steady-state and peak currents (Figs. 6.3 Da/b-Ea/b, and 6.4 Da/b-Ha/b). The inward rectifier behaviour at negative potentials is mainly determined by IRK and NCA currents (Fig. 6.3 Fa/b-Ga/b). In particular, NCA removal considerably shifts towards positive currents in the region of the I-V curves below 30 mV, suggesting that these channels could be essential in tuning the resting potential of the neuron. Calcium channels do not significantly affect both peaks and steady-state I-Vs, suggesting their minor involvement in the AIY dynamics (Fig 6.4 Ba/b-Ca/b).
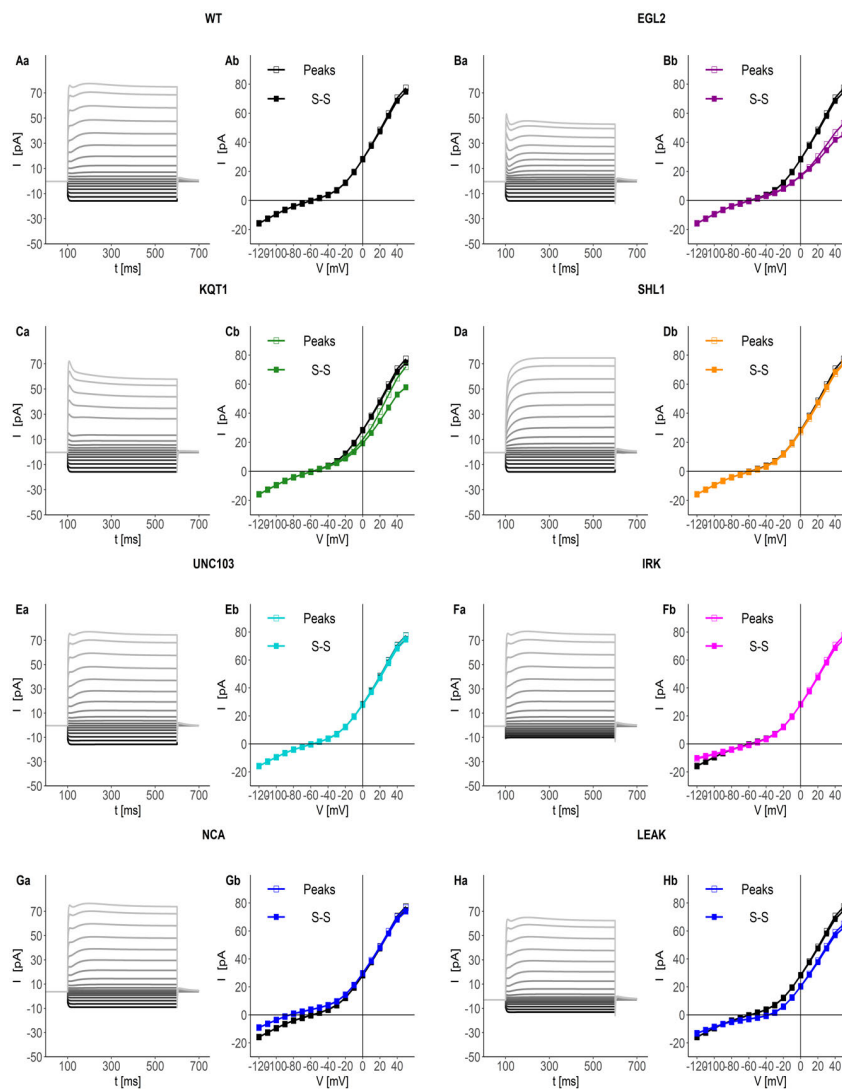
Figure 6.3: **AIY model: voltage and current clamp simulation**. All simulations are conducted in NEURON using the same protocol of experimental recording [21]. The protocol consists of 17 voltage steps ranging between -120 mV and 50 mV with a duration of 500 ms, delivered from a holding potential of -60 mV. **Aa/b) Simulated whole-cell currents of WT AIY interneurons.** Panel Aa shows the WT simulated currents, while panel Ab repotes the computed peaks (empty squares) and steady-state (S-S, filled squares) I-V curves. **Ba/b)-Fa/b) Potassium channels *in silico* knockouts**. These panels show the whole-cell currents (a) and the I-V curves (b) obtained from voltage clamp simulations of the KV channels *in silico* knockouts, i.e., EGL2 (Ba/b), KQT1 (Ca/b), SHL1 (Da/b), UNC103 (Ea/b), and IRK (Fa/b). **Ga/b)-Ha/b) *In silico* knockouts for NCA and LEAK currents**. Panels Ga/b and Ha/b show the whole-cell currents (a) and I-V curves (b) for NCA and LEAK knockouts.

6.1. AIY INTERNEURONS
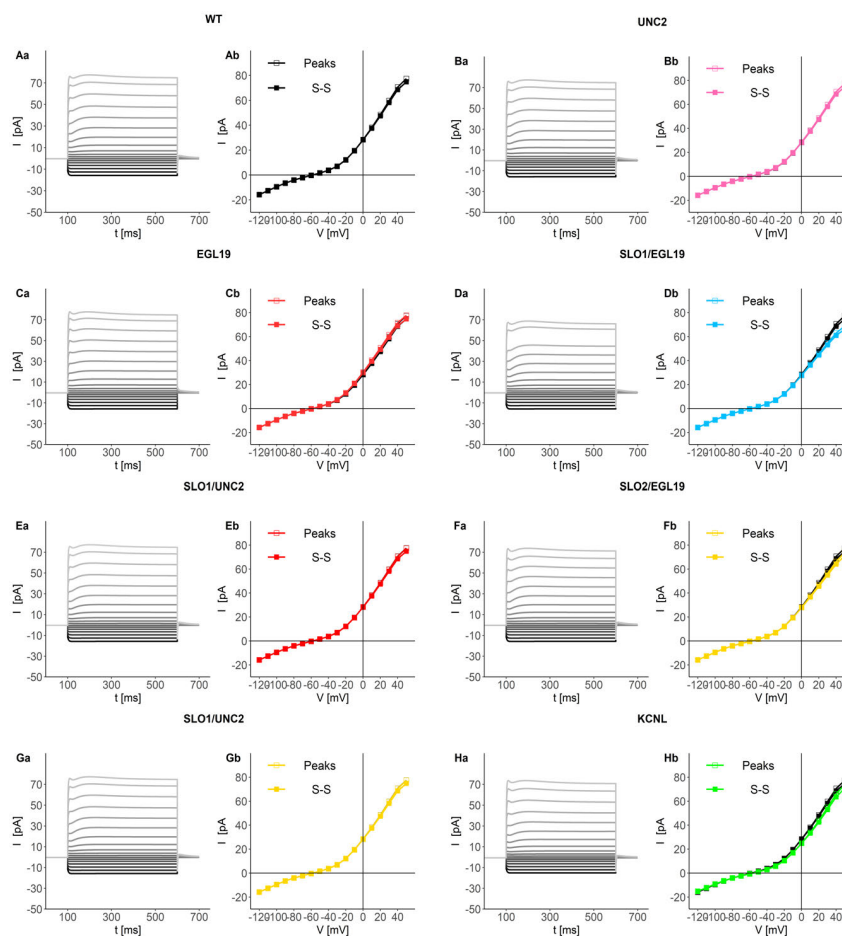
Figure 6.4: **AIY model: voltage and current clamp simulation.**All simulations are conducted in NEURON using the same protocol of experimental recording [21]. The protocol consists of 17 voltage steps ranging between -120 mV and 50 mV with a duration of 500 ms, delivered from a holding potential of -60 mV. **Aa/b) Simulated whole-cell currents of WT AIY interneurons.** Panel Aa shows the WT simulated currents, while panel Ab repotes the computed peaks (empty squares) and steady-state (S-S, filled squares) I-V curves. **Ba/b)-Ca/b) Calcium channels *in silico* knockouts**. In the panels are shown the whole-cell currents (a) and the I-V curves (b) obtained from voltage clamp simulations of the CaV currents *in silico* knockouts, i.e., UNC2 (Ba/b), and EGL19 (Ca/b). **Da/b)-Ha/b) Calcium-regulated potassium channels *in silico* knockouts**. These panels show the whole-cell currents (a) and the I-V curves (b) obtained from voltage clamp simulations of the K-Ca currents *in silico* knockouts, i.e., SLO1/EGL19 (Da/b), SLO1/UNC2 (Ea/b), SLO2/EGL19 (Fa/b), SLO2UNC2 (Ga/b), and KCNL (Ha/b).

A second analysis of *in silico* knockouts is performed in the current-clamp configuration by applying a current stimulus of 35 pA with a duration of 5 s. For each ionic current, the *in silico* knockout responses and the normalized conductances are analysed (Fig. 6.5).

131
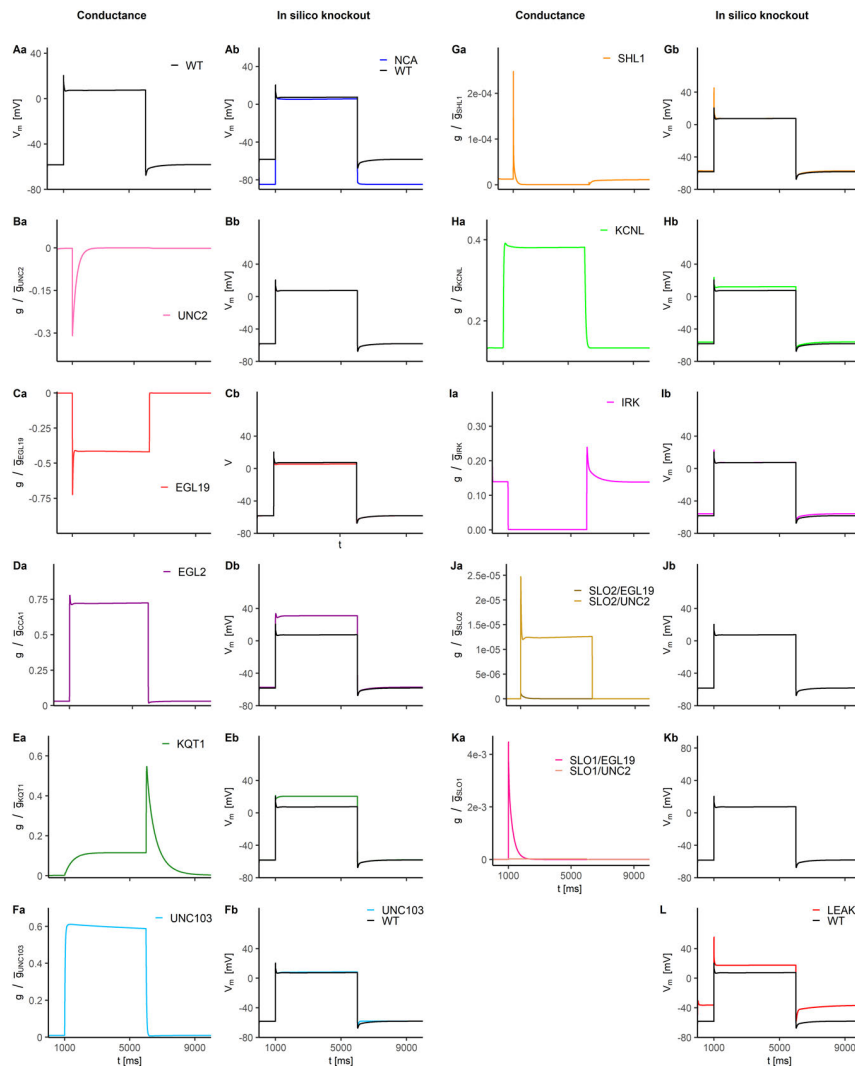
Figure 6.5: **AIY model: normalized conductance and in *in silico* knockout analysis. Aa) Simulated WT voltage response of AIY interneurons.** The panel shows the response of WT AIY interneurons to a 35 pA current step with a duration of 5 s and delivered from a holding current of 0 pA. **Ba)-Ka) Normalized conductance analysis**. The panels show the normalized conductances for all the channels included in the model during the WT simulation shown in panel Aa. In particular panels Ba and Ca report the conductances of voltage-gated calcium channels (multiplied by -1 to reproduce the sign of the current), while panels Da-Ga and Ia report those of voltage gated potassium current, and panels Ja-Ka and Ha show the normalized conductances of calcium regulated potassium channels. **Ab)-Kb) and L)** *In silico* **knockout simulations**. The panels show the responses of *in silico* knockout neurons to a 35 pA current step lasting 5 s and delivered from a holding current of 0 pA. All the simulations here shown have been performed in NEURON.

Concerning *in silico* knockouts, the most notable changes are observed in EGL2, KQT1, and LEAK knockouts (Fig. 6.5 Db, Eb, and L). Their removal considerably increases the plateau value, and in the case of LEAK currents, it also causes a 20 mV increase in the resting potential (Fig. 6.5 Jb, $V_r^{WT} = -56.09$ mV). In accordance with these observations, the normalized conductance analysis shows that EGL2 currents are mostly active in the plateau phase, while KQT1 display a modest activation during the plateau and undergo a transient increase when the stimulus is removed (Fig. 6.5 Da/b-Ea/b).

In contrast with other *C. elegans* neurons, such as RMD, AWC, AWA or ASE [18, 20, 21, 22, 38], AIY dynamics is not considerably affected by voltage-gated calcium channels (Fig. 6.5 Ba/b-Ca/b). *In silico* knockouts for EGL19 and UNC2 currents show little alterations of the responses (Fig. 6.5 Bb-Cb). In particular, EGL19 deletion reduces the plateau level of few millivolts, consistently with the removal of a inward calcium flux (Fig. 6.5 Cb). The conductance analysis confirms that EGL19 currents remain active during the plateau phase, while UNC2 contribute mostly to the fast upstroke phase (Fig. 6.5 Ba-Ca). The upstroke phase is also influenced by SHL1 currents that counterbalance the inward contribution given by EGL19 and UNC2 (Fig. 6.5 Ga/b). SHL1 knockout shows an increased intensity of the initial peak, while the plateau is almost unchanged (Fig. 6.5 Gb). This result is further confirmed by the conductance analysis that shows a sharp peak in correspondence of the stimulus onset, followed by an almost complete inactivation during the plateau phase (Fig. 6.5 Ga). IRK currents are mostly active before and after the stimulus, and completely inactivate during the stimulus (Fig. 6.5 Ia). Their removal causes small alterations of the resting potential by shifting it to more positive values ($V_r^{IRK} - 55.89$ mV, Fig. 6.5 Ib).

The most significant alterations of the resting potential are caused by NCA removal, which shifts the resting potential below the potassium reversal potential, confirming the results of voltage clamp simulations (Fig. 6.5 Ab, V_r^{NCA} =-84.65 mV). UNC103 currents suppression mainly affects the repolarization phase by accelerating the recovery of the resting potential (Fig. 6.4 Fb). UNC103 currents show a robust activation during the stimulus but give only a small contribution to the plateau level definition (Fig. 6.5 Fa/b). Finally, K-Cas are not particularly critical for AIY responses. Deletion of KCNL, SLO1-EGL19 and SLO2-UNC2 slightly increases the plateau, with a maximum alteration of $\sim$4.7 mV observed for KCNL.

6.2 RIM interneurons

RIM neurons are a class of interneurons that innervate the head. RIM neurons are involved in locomotion by regulating the reversal behaviour together with AVA, AVD, and AVE [102, 287]. Despite their importance for locomotion, few is known about their physiology. To date, only whole-cell current- and voltage-clamp recordings have been published [21], but few is known about the specific ion currents giving rise to the observed responses. To adequately reproduce the characteristic behaviour of RIM neurons, a set of ionic conductances has been obtained from the CENGeN [37] database, and the corresponding channels have been included in the model implemented in XPPAUT. The final set of conductances includes SHL1, EGL36, EGL2, EXP2, IRK, CCA1, UNC2, EGL19, KCNL and NCA channels (Eq. 6.2)[1]

$$
\begin{aligned}
I_{ion}^{RIM} =& I_{\mathrm{SHL1}} + I_{\mathrm{EGL2}} + I_{\mathrm{EGL36}} + I_{\mathrm{EXP2}} \\
& I_{\mathrm{EGL19}} + I_{\mathrm{UNC2}} + I_{\mathrm{KCNL}} + I_{\mathrm{CCA1}} + I_{\mathrm{NCA}}.
\end{aligned}
\tag{6.2}
$$

This set of conductance is derived by fine-tuning the conductances of the different channels by hand. For this specific neuron, several attempts to optimize the model with GA have been performed; however, the final results were unsatisfing. Some of the obtained parameter sets reproduced quite well the behaviour of the neuron during a current clamp simulation, but they failed to reproduce the peculiar features of RIM currents observed in the voltage-clamp experiments, in particular for what concerns the steady-state behaviour. These peculiarities could be instead well described with the first "manual" model, whose set of conductances is reported in Table 6.3

6.2.1 RIM WT whole-cell current- and voltage-clamp

RIM neurons are classified as outward rectifier neurons [21]. During voltage-clamp experiments, they give rise to fast activating and inactivating currents with a small outward component in the steady-state (Fig. 6.10 A). The simulated currents correctly reproduce the initial transient phase as well as the steady-state currents, as confirmed by the good agreement between the experimental and steady-state I-V curves (Fig.6.6 B-C) [21]. In response to voltage stimuli between -100 mV and 50 mV, the neuron exhibits an inward rectifier behaviour switching to outward rectifier around -30 mV. Above -30 mV, transient currents start to activate and increase progressively, giving rise to sharp peaks that rapidly degrade within 10 ms to the steady-state value.
The agreement between experimental and simulated data in the current clamp is worse than in the voltage-clamp case (Fig. 6.7).
The recorded voltage [21] traces show large excursions in response to both positive and negative current stimuli (Fig. 6.7 A). This behaviour is qualitatively reproduced

---

[1]After the submission of this work the candidate has found that EXP2 channel are not expressed in RIM, according to the new release of the CeNGEN database. The candidate is working to update the model on the basis of the new information.

Table 6.3: **RIM model parameters.** The following reversal potentials are used for potassium, calcium sodium currents and leakage currents, respectively: $V_K = -80$ mV, $V_{Ca} = 60$ mV and $V_{Na} = 30$ mV. The final set of conductances is derived by fine-tuning the values for each current to match the experimental I-V curves [21]. In this model, the second version of the SHL1 currents model is used (for further details see Chapter 4). Also, the time constants of EGL2 currents are rescaled by multiplying the parameters a and d by 7 (see Appendix A, Eq. A33 and Appendix B, Table B1) to match the specific temporal characteristics of the recorded currents.

Current	Conductance ($\bar{g}_x$) [nS]
	RIM
SHL1	1.71
EGL2	0.16
EGL36	0.15
EXP2	0.75
EGL19	0.25
UNC2	0.37
CCA1	0.1
KCNL	0.2
NCA	0.05
IRK	0.25
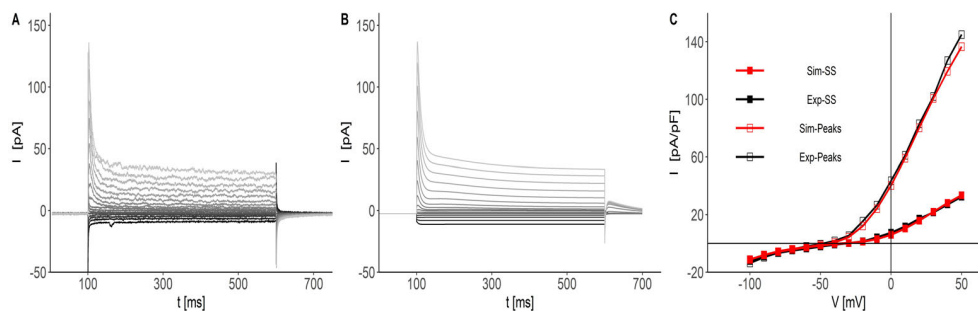
Figure 6.6: **RIM model: voltage-clamp simulation**. **A) Experimental voltage clamp**. Experimental currents from [21]. The curves have been recoded in a voltage-clamp experiment, by delivering sequential voltage steps between-100 mV and 50 mV with 10 mV increments and a step duration of 500 ms [21] The holding potential is -60 mV.**B) Simulated whole-cell currents for RIM**. The voltage clamp simulation has been performed in XPPAUT using the same stimulation protocol of the experimental recordings. **C) I-V curves comparison**. In this panel simulated (red) and experimental (black) steady-state (S-S, filled square) and peaks (empty squares) are compared. Simulated curves are in good agreement with the experimental traces. The simulation has been performed in XXPAUT using the stiff solver.

also in the simulated voltage traces; however simulated responses show an initial peak followed by a slight decrease to a plateau, which is not observed in the experimental recordings (Fig. 6.7 B). Also, the *in silico* neuron displays an anomalous behaviour during the repolarization. Indeed, upon stimulus removal and before returning to its
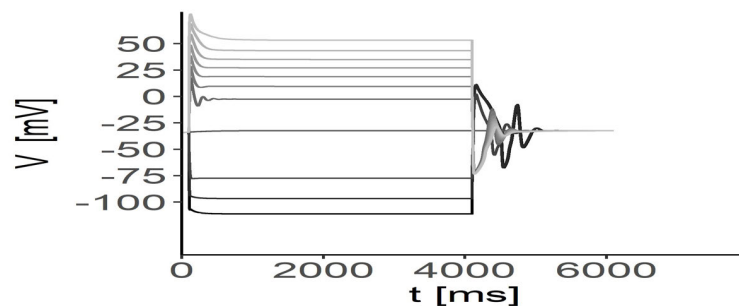
Figure 6.7: **RIM model: current-clamp simulation**. **A) Experimental current-clamp recording on RIM neurons** The panel show the voltage responses (from [21]) of the RIM neurons, recorded during a current-clamp experiment. The stimulation protocol used in experimental recordings consisted in sequential current pulses between -15 pA and 35 pA with 5 pA increments and a duration of 5 s [21]. The holding current was 0 pA **B) Simulated current-clamp recordings**. The panel shows the simulated voltage responses obtained during a current-clamp simulation performed using the same stimulation of the experimental recordings (panel A) [21]. The cell capacitance is set to $C = 1.03$ pF, that is equivalent to 1 μF/cm^2 when scaled to the entire surface of the neuron ($S = 103.34$ μm^2, obtained form Neuromorpho[2]). The simulations has been performed in XPPAUT using the stiff solver

resting state, the voltage exhibits positive or negative peaks, depending on the sign of the applied stimulus, that slowly degrades to the resting value, eventually giving rise to other small oscillations (Fig 6.6 F). This anomalous behaviour is investigated and clarified in the following by means of voltage-clamp and current-clamp simulations of the *in silico* knockout neurons.

6.2.2 *In silico* knockout neurons

First of all the *in silico* knockouts are studied in the voltage-clamp configuration to dissect the role of different channels in generating the whole-cell currents (Fig. 6.8). As expected, the transient outward behaviour is determined by the sole transient potassium current included in the model, the SHL1 current (Fig. 6.8 Na/b). Its deletion suppresses the peaks while preserving the steady-state outward component that is mainly determined by non-inactivating potassium channels such as EGL2, EGL36, and KCNL (Fig. 6.8 Ea/b, Ga/b and Na/b). Deletion of the potassium EXP2 currents and calcium EGL19, CCA1 and UNC2 currents cause very small alterations of both steady-state and peaks I-V curves in the intermediate and low part of the I-Vs, indicating that calcium currents have a relatively low influence in the RIM neurons dynamics (Fig. 6.8 Ba/b-Da/b and Fa/b). IRK and NCA currents mostly influence the lower part of the I-Vs being responsible for the inward rectifier character of the currents at very negative potentials (Fig. 6.8 La/b-Ma/b). Also, similarly to the AIY case, NCA currents removal shifts to higher currents the region of the I-V curved below 30 mV, suggesting their involvement in tuning the resting potential.
To elucidate the behaviour of the neuron under a current simulation, in particular to
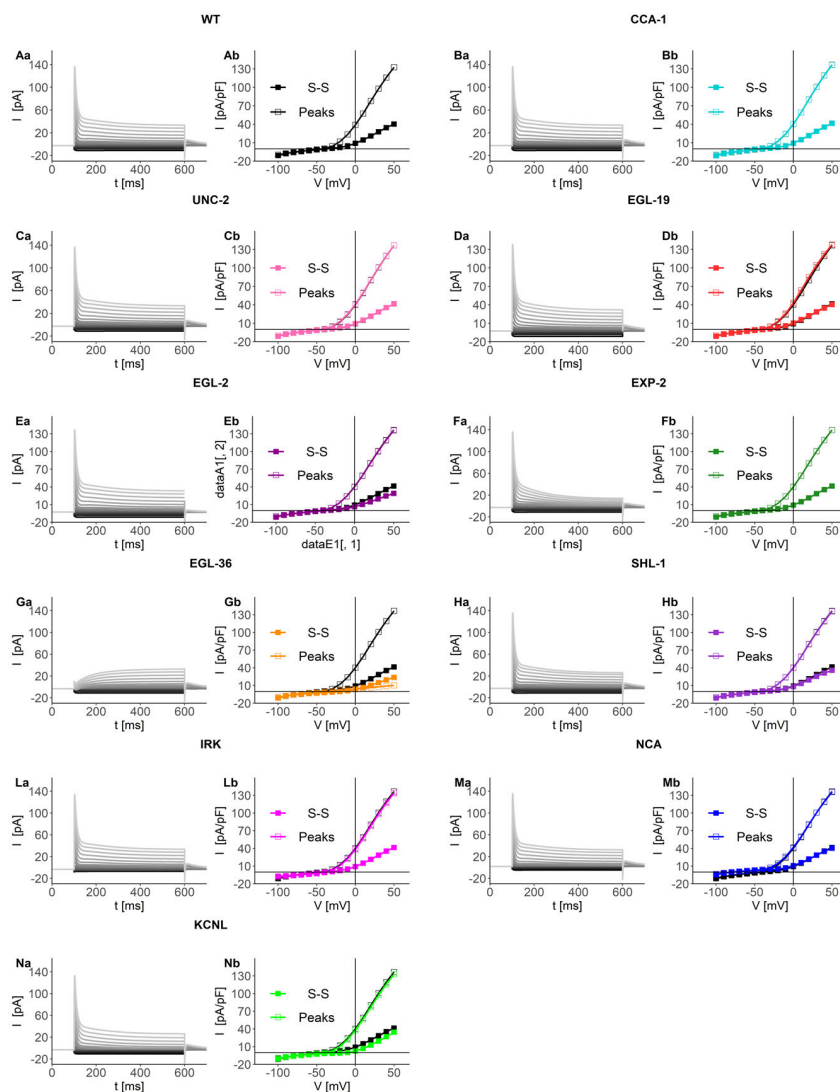
Figure 6.8: **RIM model:** *in silico* **knockout voltage-clamp simulation**. **Aa)-Na) WT and *in silico* knockouts simulated currents**. Panel Aa shows the simulated WT whole-cell currents in a voltage-clamp simulation performed with same protocol of Fig. 6.6 B. Panels Ba-Ha show the simulated currents of *in silico* knockout neurons during the voltage clamp simulation. **Ab)-Nb) WT and *in silico* knockouts I-V curves**. The panels show the computed steady-state (S-S, filled squares) and peaks (empty squares) I-V curves for the simulations showed in panels Aa)-Na). The black curves in each panel are the reference WT I-V curves. All the simulations have been performed in XPPAUT using the stiff solver.

clarify the origin of the observed anomalies in the current-clamp simulation, normalized conductances and *in silico* knockout neurons responses are analysed during a current-clamp simulation in which the neuron is subjected to a current step of 15 pA lasting

137
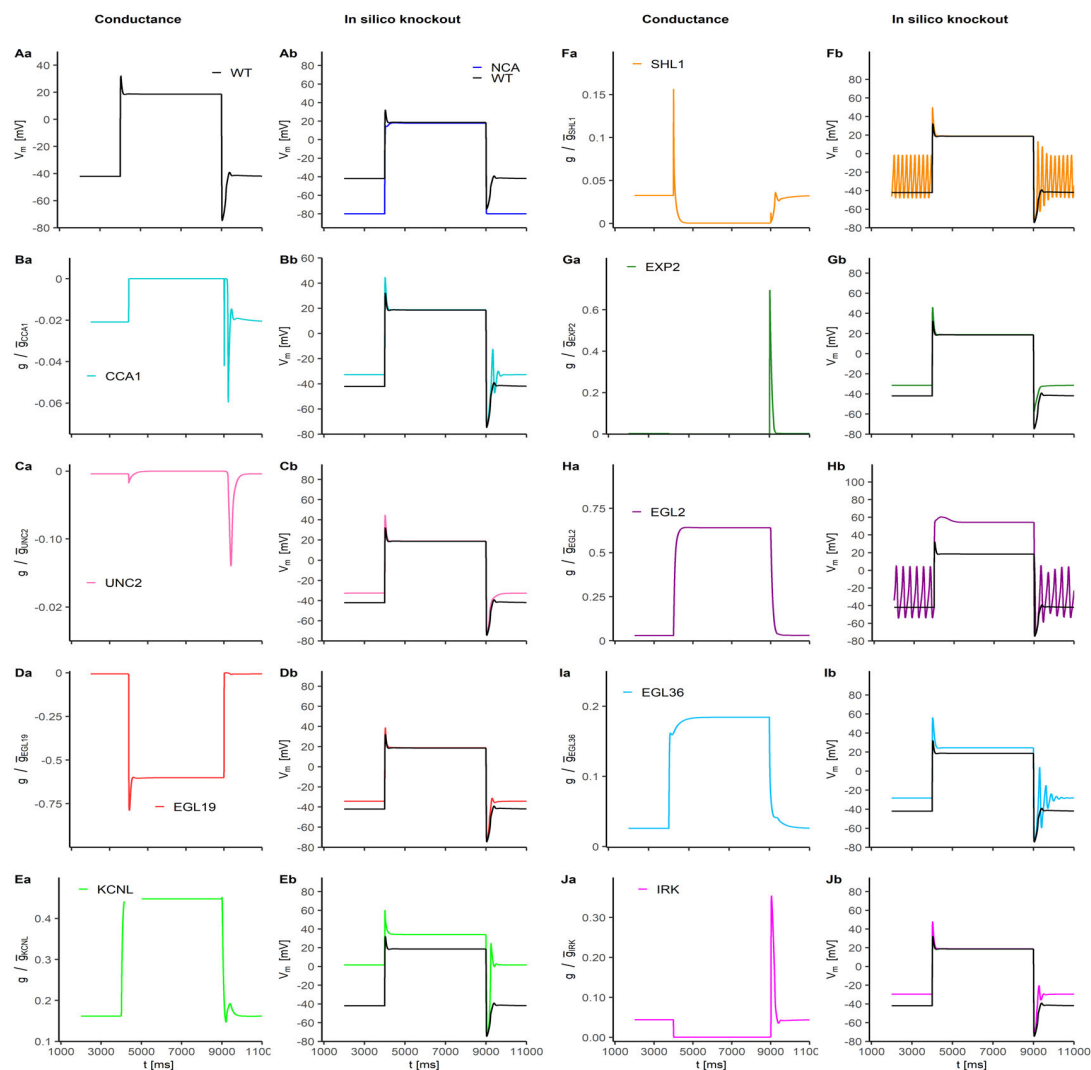
Figure 6.9: **RIM model: *in silico* knockouts and conductance analysis. Aa) WT response**. Panel Aa shows the response of WT RIM neurons to a current pulse of 15 pA, lasting 5 s and delivered from a holding current of 0 pA. **Ba)-Ja) Normalized conductance analysis in WT neurons**. The panels show the normalized conductances of all the ionic channels included in the WT model during the WT simulation shown in panel Aa. In panels Ba, Ca and Da the normalized conductance $g_x/\bar{g}_x$ is multiplied by -1 to reproduce the sign of the current. **Ab), Bb)-Jb) *In silico* knockouts voltage responses**. The panels show the *in silico* knockout membrane voltage responses to a 15 pA current step with a duration of 5 s and delivered from a holding current of 0 pA. All the simulations have been performed in XPPAUT using the stiff solver.

5 s (Fig.6.9 Aa). As expected, EGL2 and EGL36 currents activate during the plateau phase (Fig. 6.9 Ha and Ia), and their removal produces a considerable increase (between

20 mV and 40 mV) of the plateau level (Fig. 6.9 Hb and Ib). Also, EGL19 and KCNL currents are active in this phase (Fig. 6.9 Da and Ea). KCNL currents suppression shifts the plateau by 10 mV towards positive potentials and significantly affects the resting potential of the cell (Fig. 6.9 Eb). EGL19 suppression do not significantly change the plateau level, rather if affects the voltage peak and the resting potential (Fig. 6.9 Db). In the repolarization phase several currents activate including CCA1, UNC2, EXP2, and IRK (Fig. 6.9 Ba, Ca, and Ga).Their removal mainly affects the repolarization phase, accelerating the return to the resting state, while the upstroke and plateau regions are almost unaffected (Fig. 6.9 Bb, Cb, and Gb). Notably, in this phase EGL36 suppression induces oscillations of the membrane potential (Fig. 6.9 Hb and Ib). SHL1 currents activate during the upstroke phase and inactivate during the plateau phase (Fig. 6.9 Fa). Interestingly, SHL1 knockout show an increased peak intensity and periodic oscillations in the resting state (Fig. 6.9 Fb), confirming the important role of these currents in the RIM dynamics. Interestingly, also EGL2 knockouts show periodic oscillations in the resting state (Fig. 6.9 Hb) that deserve further investigation with future simulations. Finally, NCA channels deletion shifts the resting potentials at -80 mV and suppresses the initial peak, suggesting their important role in regulating the cellular excitability and resting potential (Fig. 6.9 Ab). Given that the suppression of NCA currents seems to remove the initial undesired upstroke, some trials have been performed in which the NCA conductance is reduced to match the current clamp recordings. However, the reduction of NCA conductance alters the voltage clamp results, especially in the region below -30 mV.

6.3 RMD motor neurons

The RMD neurons represent a class of ring motor neurons responsible for spontaneous foraging movements and head withdrawal reflex activated by the stimulation of the mechanosensory neurons OLQ and IL1 [288]. RMD neurons generate active responses. Based on experimental data [20] and expression profiles obtained from Wormbase [5] and CeNGEN [37], the following set of ionic current has been selected for RMD description[3]. SHL1, SHK1, EGL36, SLO1, SLO2, CCA1, UNC2, EGL19, KNCL, IRK, NCA. Thus the total ionic current is given by Eq. 6.3. As in the case of the fist AWC$^{\mathrm{ON}}$ and RIM, the set of conductances that correctly reproduces the RMD behaviour is obtained manually. The selected values are listed in Table 6.4, while the list of single channel parameters is reported in Appendix B Tables B1-B2.

$$
\begin{aligned}
I_{ion}^{RMD} =& I_{\mathrm{SHL1}} + I_{\mathrm{SHK1}} + I_{\mathrm{EGL36}} + I_{\mathrm{EGL19}} + I_{\mathrm{UNC2}} + I_{\mathrm{CCA1}} \\
&+ I_{\mathrm{SLO1/EGL19}} + I_{\mathrm{SLO1/UNC2}} + I_{\mathrm{SLO2/EGL19}} + I_{\mathrm{SLO2/UNC2}} \\
&+ I_{\mathrm{KCNL}} + I_{\mathrm{NCA}} + I_{\mathrm{LEAK}}.
\end{aligned}
\tag{6.3}
$$

---

[3]After the submission of this work the candidate has found that the new release of the CeNGEN database includes also the EXP-2 channels in the list of expressed channels. The candidate is working to update the model on the basis of the new information.

Table 6.4: **Ionic conductances for RMD neuron.** The following reversal potentials are used for potassium, calcium sodium currents and leakage currents, respectively: $V_K = -80$ mV, $V_{Ca} = 60$ mV and $V_{Na} = 30$ mV, $V_L = -80$ mV. The final set of conductances is derived by fine-tuning by hand the values for each current to match the experimental current clamp curves [20].

Current	Conductance ($\bar{g}_x$) [nS] RMD
SHL1	2.5
SHK1	1.1
EGL36	1.3
EGL19	0.99
UNC2	0.9
CCA1	3.10
SLO1/EGL19	0.30
SLO1/UNC2	0.30
SLO2/EGL19	0.3
SLO2/UNC2	0.3
KCNL	0.06
NCA	0.05
IRK	0.20
LEAK	0.40

6.3.1 RMD WT whole-cell and *in silico* knockouts current-clamp analysis

As the first step in the study of RMD neurons, a current clamp simulation is performed, following the same stimulation protocol used in the experimental recordings [20]. The protocol consists of two sequential pulses of current (Fig. 6.10 B). The first ranging between -2 pA and 10 pA, and the second at a fixed value of 15 pA. Experimental recordings on RMD neurons revealed a peculiar feature of their behaviour, the bistability, which is correctly reproduced by the model here presented (Fig. 6.10) [20, 38]. RMD neurons possess two stable resting states, one around -70 mV and the other at ∼-40 mV. The two states can be reached by applying a depolarizing or hyperpolarizing stimulus depending on the initial state of the neuron. Indeed for the switch from the lower to the upper state, a depolarizing stimulus is required, while a hyperpolarizing stimulus induces the inverse process. Notably, not all stimuli are effective in promoting the switch; instead, a threshold behaviour is observed. Current stimuli below 6 pA do not cause a voltage perturbation large enough to induce the jump (Fig. 6.10) [20, 38].

To investigate the origin of the RMD bistable behaviour, the single currents activation and inactivation dynamics is analysed. Also, to further clarify the role of each current in the whole-neuron response, the *in silico* knockout analysis is performed both in the current and voltage-clamp configurations. The first analyses to be conducted concern the study of activation and inactivation dynamics of single currents and the *in silico*
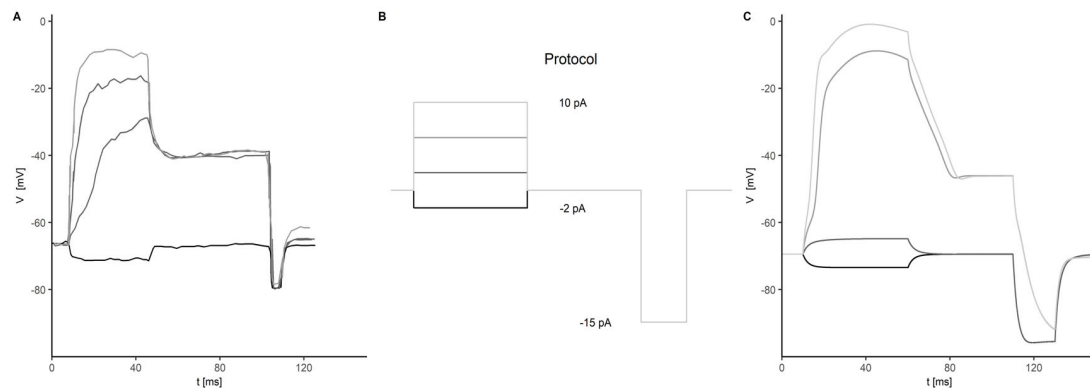
Figure 6.10: **RMD model: current-clamp**. Figure adapted from [38]. **A) Experimental current clamp**. Experimental current-clamp recordings on RMD neurons [20]. **B) Current-clamp protocol**. The protocol consists in 4 current pulses between -2 pA and 10 pA delivered from an holding potential of 0 pA and lasting 50 ms. After the first current step, a second hyperpolarizing step at -15 pA is delivered. **C) RMD current-clamp simulation**. Simulated RMD voltage responses to the stimulation protocol sketched in Panel B. The cell capacitance is set to 1.2 μF to match the experimental data. The simulation has been performed in XPPAUT using a stiff solver.

knockout responses during a single-step current-clamp. The WT and knockout neurons are stimulated with a 10 pA current pulse with a duration of 50 ms (Fig. 6.11 Aa).

Upon positive current injection, the neuron exhibit a threshold like response triggered by the sequential activation of CCA1, UNC2, and EGL19 currents (Fig. 6.11 Ba-Da). In particular, CCA1 currents are mostly active in the rising phase and inactivate almost completely in the plateau (Fig. 6.11 Ba). When the stimulus is removed, the decrease of the membrane potential reactivates the currents that remain consistently active also in the post-repolarization phase (Fig. 6.11 Ba). Notably, CCA1 removal suppresses the bistable behaviour, suggesting their crucial role in the RMD neuron dynamics (Fig. 6.11 Bb). This result is in accordance with observations in mammalian thalamocortical (TC) and nucleus reticularis thalamus (NRT) neurons, in which the bistable behaviour is mediated by T-type currents [219, 220]. UNC2 and EGL19 currents mainly support the plateau phase, which is significantly affected by their removal (Fig. 6.11 Ca/b-Da/b). Both UNC2 and EGL19 knockouts show decreased membrane potential and faster repolarization (Fig. 6.11 Cb-Db).

Concerning the influence of voltage-gated calcium channels in the RMD behaviour some considerations should be done, especially with respect to the results of the current-clamp experiments on mutants worms showed in [20]. Current-clamp recordings performed on *cca-1(ad1650)* null mutants are not bistable. In the experiments, *cca-1(ad1650)* mutants display a similar amplitude to that of WT [20]. This phenomenon seems to be not reproduced in the *in silico* knockout neurons, but, however this is only a graphical effect due to the fact that the same stimulus amplitude of WT simulations is maintained also in the knockouts simulation. Indeed, an increase of the stimulus amplitude of few

141
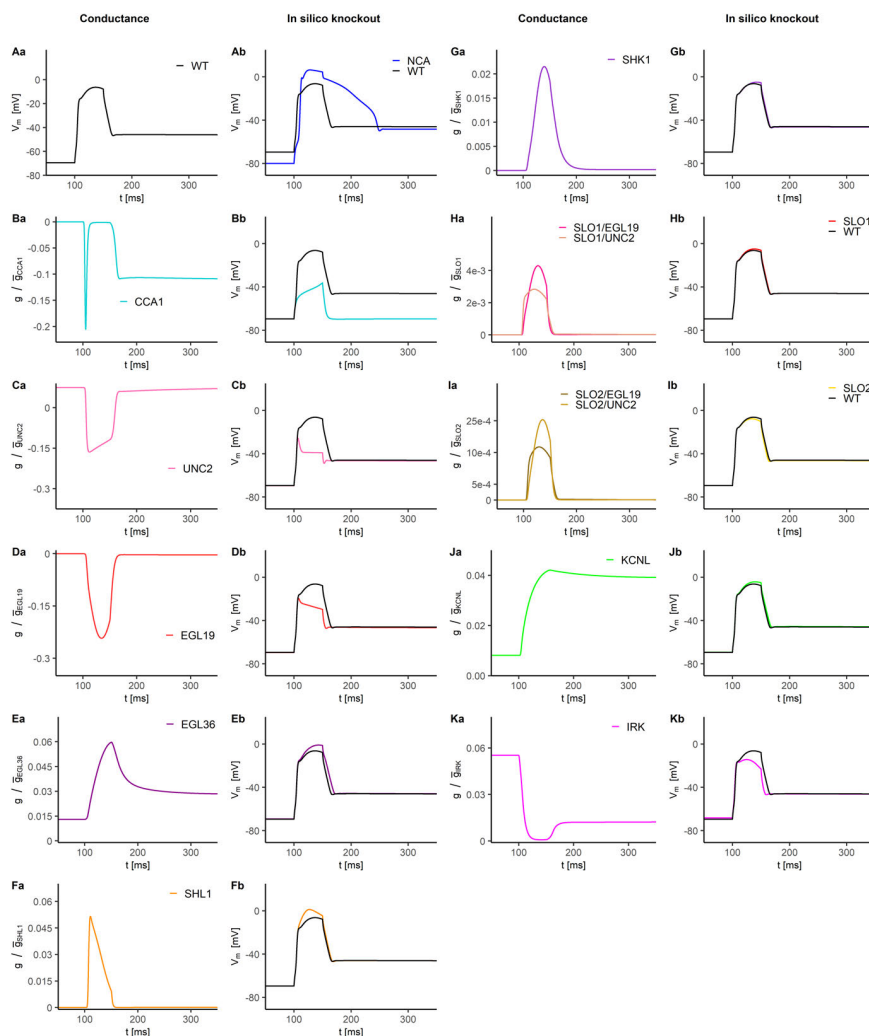
Figure 6.11: **RMD conductance and knockout analysis**. **Aa) WT response**. Simulation of the WT response to 10 pA stimulus. **Ba-Ka) Normalized single-currents conductances**. The normalized conductance is defined as the product of the activation and inactivation variable. Panels Ba, Ca, and Da show the normalized conductance of voltage-gated calcium currents. In these panels $g_x/\bar{g}_x$ is multiplied by -1 to reproduce the sign of the current. Panels Ea-Ka show the normalized conductances for voltage-gated (Panels Ea-Ga and Ka), big-conductance (Panels Ha-Ia), and small-conductance (Panel Ja) potassium channels. **Ab-Kb) *In silico* knockout responses**. Simulated response of *in silico* knockout neurons. The simulation protocol consisted in a single-current pulse of 10 pA lasting 50 ms. The black curve in the panels represents the WT simulation.

picoamperes (from 10 pA to 11 pA) is enough to produce action potentials with an amplitude comparable to that of WT, and, therefore, to reproduce the experimental recordings. Moreover, it is worth to note that also in the experimental recordings a

small variability in the activation threshold is observed among WT worms and mutants. Therefore, as far as is concerned CCA1 currents, the modelling results seem in agreement with the experimental observations.

Experimental data for *cca-1, unc-2, egl-19* and *nca-1/2* mutants showed in [20] do not display a bistable behaviour. However, some important considerations should be done in comparing the computational and the experimental results. First of all, it must be recalled that *in silico* knockout neurons do not exactly reproduce mutant or knockout worms, rather they mimic the effects of channel blockers. In mutants worms compensation effects may arise to overcome the dysfunctions caused by mutations.

Concerning UNC-2 channels, the simulation results for in silico knockout seem in disagreement with the single current-clamp recording for *unc-2(e55)* mutants reported in [20]. However, Mellem et al. also show that these mutants still display long lasting transitions between two state in absence of applied stimuli. This behaviour is accordance with that observed in WT worms and indicates that the bistability is preserved in *unc-2(e55)* mutants. The shape and the amplitude of the action potentials in UNC2 *in silico* knockout (Fig. 6.13 Cb) differ from that observed in the experiments [20]. To the best of the candidate knowledge, it is still not known whether compensatory effects arise in these mutants to overcome the loss of UNC-2 channels, but in case they could explain the observed differences. Moreover, by increasing in the simulations the stimulus amplitude up to 20 pA, the characteristic shape of the action potential is restored. In the model here presented (Fig 6.13 Db) the EGL19 *in silico* knockout display bistability and reduced responses that are not observed in the experiments [20]. However, it must be noted that the specific mutant strain *egl-19(n2368)*, is reported to carry a gain-of-function mutation of EGL-19 channels, producing an hyperactivation of the L-type channels [289, 290]. Therefore, the simulation results for EGL19 *in silico* knockout cannot be compared to the patch clamp data for *egl-19(n2368)* mutants [20], indeed the former represents a loss of functionality, while the latter an increased functionality. Concerning NCA currents, both mutants and *in silico* knockouts display action potentials but with striking differences that deserve further investigation through dedicated experiments.

A final observation about all the mutants data presented in [20] is that, except for *unc-2* mutants, there is no final evidence about the lack of bistability, indeed for *cca-1, egl-19*, and *nca-1/2* the recordings of spontaneous activity are not reported and it is not explicitly stated by the authors that those mutants are not bistable. Moreover, despite single current clamp recordings do not show bistability, it has to be considered that this phenomenon is observed only in the 55% (54 out of 98) of WT neurons, and in absence of information about the number of tested mutant worms it cannot be excluded that also these mutants are still bistable (as in the *unc-2* case). On the other hand, the hypothesis of CCA1-based bistability proposed in this work, is corroborated by observations in mammalian neurons, in which this behaviour is mediated by the interplay between of T-type calcium currents (carried by CCA-1 in the nematode) and leakage currents [219, 220]. In conclusion, a comparison between the mutants date presented in [20] and the in silico knockouts simulation results is not so easy and therefore dedicated

current clamp experiments using specific channel blockers must be performed in the future to ensure a proper validation of the computational results.

Compared to the AWC^{ON} case, the potassium channels seem to have a less strong influence on the neuron dynamics. As expected, the non-inactivating potassium currents carried by EGL-36, influence the late plateau and repolarization phases (Fig. 6.11 Ea/b), and also remain active in the post-stimulus resting state (Fig. 6.11 Ea). Consistently with the mammalian case [291], EGL-36 deletion leads to increased voltage responses with a slower repolarization compared to WT, confirming their role in tuning the cellular excitability (Fig 6.11 Eb). Similarly to the AWC^{ON} case, SHL1 currents mainly activate in the rising phase (Fig. 6.11 Fa), as confirmed by the knockout responses that show increased voltage levels in the early plateau (Fig. 6.11 Fb). SHK-1 channels activate during the late plateau and completely inactivate in the post-stimulus phase, and their deletion does not significantly alter the shape of the response (Fig. 6.11 Ga/b). SLO1 and SLO2 channels activate only during the stimulus phase and inactivate completely after its removal (Fig. 6.11 Ia-Ja). SLO1 and SLO2 knockouts show a little change (<1.4 mV) in the late plateau phase, while the upstroke and early plateau are unchanged (Fig. 6.11 Ib-Jb). Also, KCNL channels contribute mainly to the plateau and repolarization phase (Fig. 6.11 Ja). However, in contrast to BK and KV channels that inactivate in the post-stimulus phase, they remain active after the stimulus removal, showing almost no inactivation (Fig. 6.11 Ja). This residual activation of KCNL channels is related to the persistent activation of CCA1 currents in the post-stimulus state, which causes a calcium influx sufficient to keep KCNL channels open. KNCL knockout has a little influence in the plateau and repolarization phases of the response, causing a little increase (~2 mV) and broadening of the peak, respectively (Fig. 6.11 Jb). IRK currents are active in the resting state, and undergo inactivation during the stimulus and post-stimulus phases (Fig. 6.11 Ka). The most striking effects are observed in the NCA knockout. NCA suppression shifts the resting potential from -69.5 mV to -80.0 mV and produces broad responses with increased amplitude and prolonged repolarization phase (Fig. 6.11 Ab).

6.3.2   RMD WT and *in silico* knockout voltage-clamp analysis

To further elucidate the role of single currents in RMD neuron dynamics, a voltage clamp analysis of WT and *in silico* knockout neurons is performed. Voltage-clamp simulations with applied stimuli ranging from -120 mV to 60 mV have been used to derive the I-V curve of the neuron. At stimulus potentials below -70 mV, the WT neuron displays an inward rectifier behaviour probably related to IRK currents. (Fig. 6.12 A-C).

At intermediate potentials (-70 mV - -40 mV), the steady-state I-V relation show a non linear behaviour (Fig. 6.12 C). Given that the two resting states observed in the current-clamp fall in this region of the curve, a more in-depth analysis is performed through a voltage clamp simulation with a 2 mV step intervals. In the region between -70 mV and -40 mV the curve displays local maxima and minima and crosses the x-axis in three points at -69.5 mV, -59.8 mV and -46.6 mV (Fig. 6.12 C). In particular, the steady-state current is negative below -69.5 mV and between -59.8 mV and -46.6 mV. The leftmost and the rightmost intersections represent the two resting states observed in
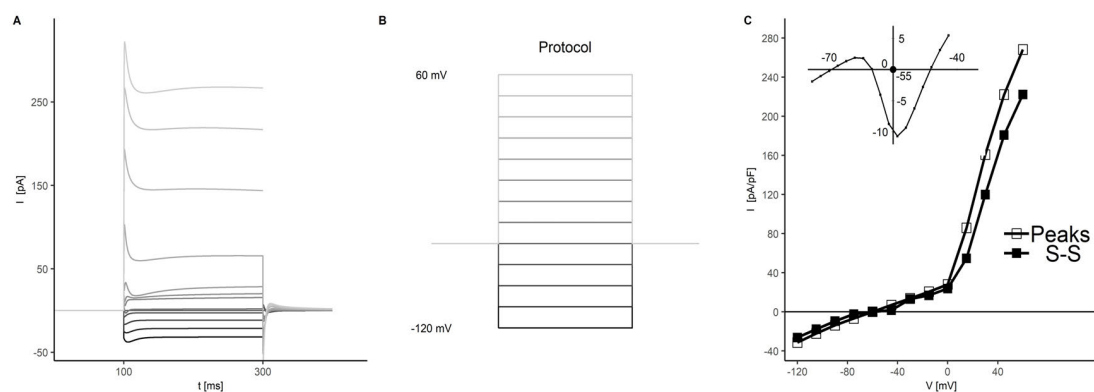
Figure 6.12: **RMD model: voltage-clamp simulation**. **A) Voltage-clamp simulation**. Whole-cell currents of the RMD neurons obtained in a voltage clamp simulation performed using the protocol sketched in panel B. **B) Voltage-clamp simulation protocol**. The protocol consists in 13 voltage steps between -120 mV and 60 mV with a duration of 1200 ms. The holding potential is -70 mV. **C) I-V curves for peaks and steady-state**. From the simulated currents (shown in panel A) the peaks and steady-state I-V curves are computed. To investigate the origin of the bistability a second voltage clamp simulation is performed with 2 mV increments between the voltage steps. This simulation shows that between -70 mV and -40 mV the steady-state current has a non linear behaviour with local maxima and minima. The three intersection points with the x-axis (i.e., I=0 pA) represent three equilibrium points of the system. The leftmost and rightmost intersections represent the two stable resting potential observed in the current-clamp, while the central one is an unstable equilibrium.

current-clamp simulation, while the intermediate intersection corresponds to an unstable equilibrium. At potential above 0 mV a clear outward rectifier behaviour, probably related to potassium currents, emerges(Fig. 6.12 C).

The *in silico* knockout voltage-clamp analysis allowed to clarify the role of each ionic current to the whole-cell responses, and confirmed that CCA1 currents are responsible for the RMD bistability. Their suppression leads to the disappearance of three zero crossings of the steady-state I-V (Fig. 6.13 Bb). UNC2 and EGL19 are active mainly in the intermediate voltage region between -50 mV and -30 mV, and their removal shifts the steady-state I-V to more positive currents (Fig. 6.13 Ca/b-Da/b). SLO1 and SLO2 currents deletion alters the I-V curve at high potentials consistently with their kinetics of activation (Fig. 6.13 Ea/b-Fa/b). KCNL channels cause only a little shift to negative currents of the steady-state I-V, consistent with the removal of an outward potassium current (Fig. 6.13 Ga/b). Concerning the other potassium currents, as expected the steady-state whole-cell current is mainly influenced by EGL36 and SHK1 (Fig. 6.13 Ba/b and Da/b). EGL36 and SHK1 knockout show decreased steady-state currents that indicate the suppression of an outward potassium contribution (Fig. 6.14 Ba/b and Da/b). Peak currents are mainly carried by SHL1 and SHK1, with a prominent contributions of SHL1 rather than SHK1 (Fig. 6.14 Ca/b-Da/b). Finally, as expected, IRK currents deletion reduces the inward current at negative potentials, while NCA suppression moves the resting potential to negative values around -80.0 mV
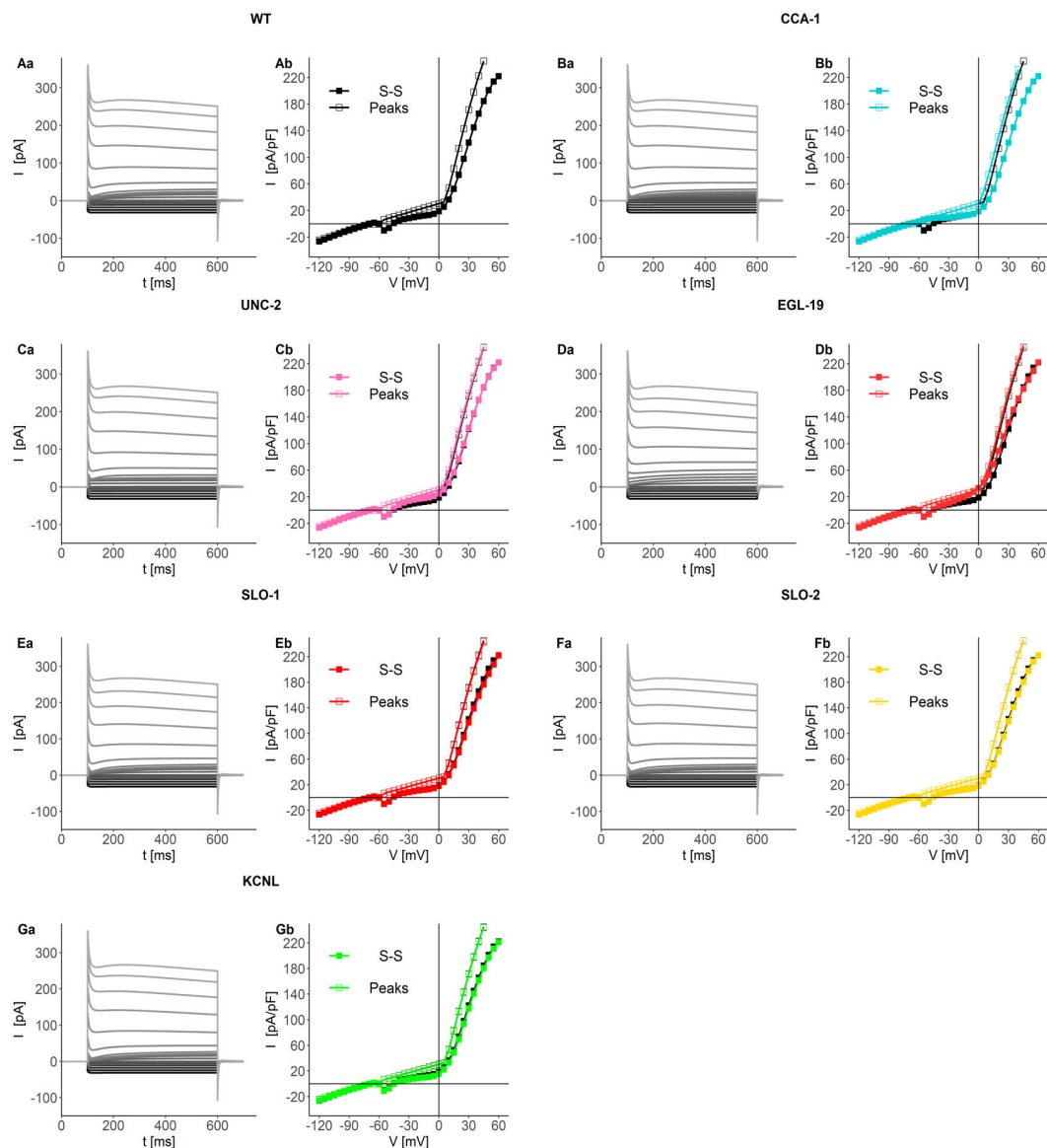
Figure 6.13: **Voltage-clamp of CaV and K-Ca currents *in silico* knockouts. Aa-Ga)** Simulated whole-cell currents of WT (Panel Aa), CaV knockouts (Panels Ba, Ca, and Da), and K-Ca knockouts (Panels Ea, Fa, and Ga). **Ab-Gb) Peaks and steady-state I-V curves for CaV and KCa knockouts**. I-V curves are derived from the simulated currents showed in Panels Aa-Ga. For the sake of clarity, in each panel the WT peaks (empty squares) and steady state (filled squares) I-V curves are reported. The simulation protocol consisted in 37 voltage steps between -120 mV and 60 mV with a duration of 500 ms and delivered from a holding potential of -70 mV. In panels Aa-Ga only half of the simulated traces are reported.
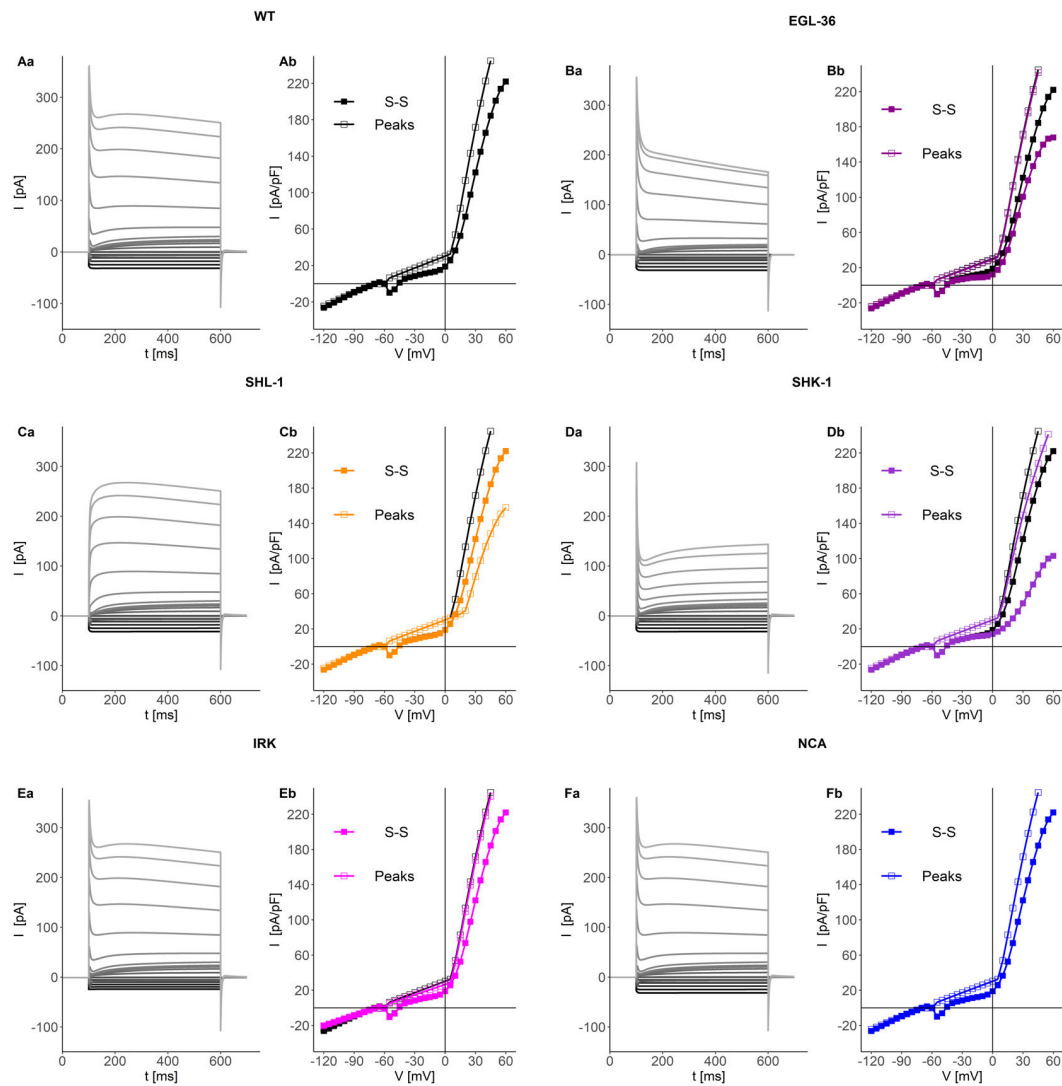
Figure 6.14: **Voltage-clamp of KV channels *in silico* knockout. Aa-Fa)** Simulated whole-cell currents of WT (Panel Aa), KV knockouts (Panels Ba-Ea), and NCA knockouts (Panel Fa). **Ab-Fb) Peaks and steady-state I-V curves for KV and NCA knockouts.** I-V curves are derived from the simulated currents showed in Panels Aa-Fa. For the sake of clarity, in each panel the WT peaks (black empty squares) and steady state (black filled squares) I-V curves are reported. The simulation protocol consists in 37 voltage steps between -120 mV and 60 mV with a duration of 500 ms and delivered from a holding potential of -70 mV. In panels Aa-Fa only half of the simulated traces are reported.

6.3.3 Bistability analysis

The role of CCA1 channels in the bistability is confirmed by current and voltage-clamp analyses. However this phenomenon deserves a deep investigation, to uncover the under-

ling mechanisms and the possible role of other channels. For this purpose, voltage-clamp and bifurcation studies have been performed to clarify their role in originating the bistability (Fig. 6.15).

Voltage clamp simulations at different values of $\bar{g}_{CCA1}$ (from 0.5 nS to 5 nS) show that the bistability emerges for values of the conductances above 1 nS when the steady-state current show only one intersection point with the x-axis (Fig 6.15 A). For decreasing $\bar{g}_{CCA1}$, the minimum of the I-V curve shifts to positive values and becomes less pronounced, determining the coalescence of the three zeros into one (Fig 6.15 A). The enlargement of steady-state I-V curves, in the region between -90 mV and -10 mV, clearly shows that only the suppression of CCA1 removes the three zeros intersections (Fig. 6.15 B). All-together these findings further support the key role of CCA1 in the RMD bistability. Steady-state stability is further characterized by computing the equilibrium points of the system as a function of $\bar{g}_{CCA1}$. The bifurcation diagram showed in Fig. 6.15 C describes the RMD equilibrium points at different values of $\bar{g}_{CCA1}$. When $\bar{g}_{CCA1}$ is below 1.1 nS the system has only one stable resting state. At increasing values of $\bar{g}_{CCA1}$ the system undergoes a saddle-node bifurcation (fold or limit point LP in Fig 6.15 C) from which two solutions arise, one stable solution V_s and one unstable solution V_u. At high values of $\bar{g}_{CCA1}$ the two solutions eventually collide with the lower stable resting state branch (V_r) through a second LP bifurcation, leading to a sole high-voltage stable state. This second regime is not described here due to the non-physiological value of the $\bar{g}_{CCA1}$ and with the experimental observations of [20]. The unstable state V_u acts as a threshold, regulating the switch between the two stable states.

Bistable dynamics has been observed in different types of neurons, including Purkinje cells, thalimc neurons, and motor neurons, and for the first time in AWC[ON] neurons [21, 41, 292, 293]. In these neurons, the bistability implicates the coexistence of different dynamic regimes such as different spking modes, non-oscillatory stable states, resting and spiking state, spiking and bursting states [219, 220]. Computational analyses performed by means of mathematical models of the single-neuron dynamics revealed that also leak channels are implicated in the bistability [219, 220]. For this reason, the bistability of RMD has been re-analysed to highlight a possible role of LEAK currents in the RMD dynamics. As first stage, steady-state I-V currents have been derived for different values of $\bar{g}_{LEAK}$ (Fig 6.15 D and 6.15 E). The steady-state curves have three different zeros at different ranges of the parameter. The two regions are separated by a region where the steady-state current has a single zero crossing (Fig 6.15D and 6.15E).

These findings suggest that the modulation of $\bar{g}_{LEAK}$ in even more complex than that of $\bar{g}_{CCA1}$, involving two different bistable regimes. To confirm this hypothesis, the bifurcation diagram with $\bar{g}_{LEAK}$ as control parameter has been computed (Fig. 6.15 F). The diagram shows two different regimes of bistability, the first arising for small values of the leak conductance, between 0.042 nS and 0.055 nS, and the other in the range ~ 0.25 nS -0.9 nS. In this last region, the bistability is originated by two LP bifurcations that give rise to two stable solutions separated by an unstable one (Fig. 6.15 F).
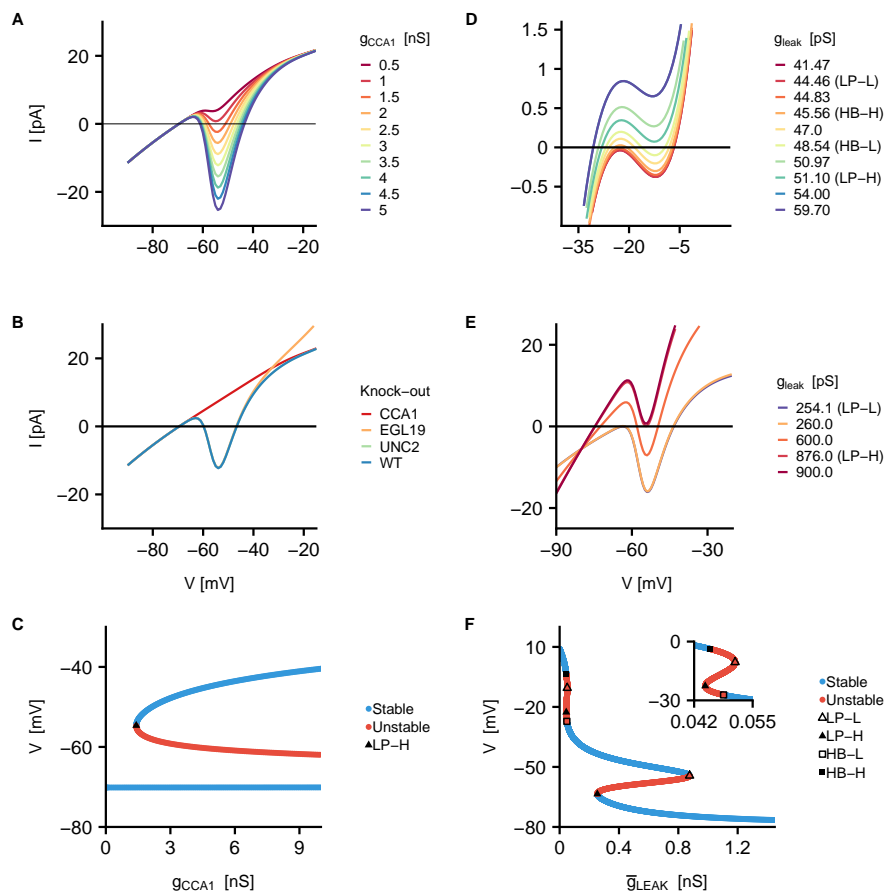
Figure 6.15: **RMD neurons bistability analysis**. **A) Steady-state I-V curves for different values of $\overline{g}_{CCA1}$.** Different voltage-clamp simulations have been performed between -90 mV and -10 mV, with 1 mV increments and with different values of $\overline{g}_{CCA1}$ between 0.5 nS and 5 nS with 0.5 nS increments. In the panel are shown the computed I-V curves. **B) Steady-state I-V curves for calcium channels *in silico* knockouts.** The curves are computed using the same voltage-clamp protocol of panel A in the case of *in silico* knockout for Cav channels. **C) Bifurcation diagram computed at varying $\overline{g}_{CCA1}$.** The system has three fixed points in correspondence of $\overline{g}_{CCA1}$ used in WT simulations. The two extremal points are stable while the middle one is unstable. At varying $\overline{g}_{CCA1}$ the system undergoes to a saddle-node bifurcation from which two solutions arise, one stable (blue) and one unstable (red). The black empty triangle indicates the bifurcation point [V, $\overline{g}_{CCA1}$]=[-59.5 mV, 1.14 nS]. At $\overline{g}_{CCA1} > 1.14$ nS the system exhibits three fixed points: two stable (V_r and V_s) and one unstable (V_u). **D)-E) Steady-state I-V curves computed at varying $\overline{g}_{LEAK}$.** Voltage clamp simulations at varying $\overline{g}_{LEAK}$ have been performed with sequential voltage steps ranging from -90 mV to -30 mV with 0.8 mV increments, in panel D, and from -35 mV to +5 mV with 0.8 mV increments, in panel E. The step duration is 1300 ms and the holding potential is $V_h = -70$ mV for both the panels. **F) Bifurcation diagram computed using $\overline{\mathbf{g}}_{LEAK}$ as parameter.** The bifurcation diagram has been computed by varying $\overline{g}_{LEAK}$ between 0 nS and 1.4 nS. In the range 0.25 nS$< \overline{g}_{LEAK} < 0.9$ nS the diagram is similar to that of panel C, with two saddle node bifurcations (LP-L) from which two stable solutions arise (blue), separated by an unstable solution (red). For values of 0.042 nS$< \overline{g}_{LEAK} < 0.055$ nS the behaviour is more complex, indeed two unstable solutions V_u' and V_s' arise from the saddle-node bifurcation (LP-H). For decreasing values of $\overline{g}_{LEAK}$, V_s' gains stability through a Hopf bifurcation (HB-L). By further decreasing $\overline{g}_{LEAK}$, V_u' and V_s' collapse in a second saddle-node bifurcation (LP-L), and V_s' remains the unique stable solution. Between the two Hopf bifurcation the system may display a second bistable regime. Figure reproduced with permission from [38].

149

For values of $\bar{g}_{\text{LEAK}}$ below 0.25 nS, another bistable regime originates from a combination of two LP and two Hopf bifurcations (HB). Notably, the presence of HB bifurcations suggests the existence of periodic solutions. Strikingly, the oscillatory solutions (Fig. 6.16) found for the RMD system display similar characteristics of action potential fired by AWA neurons [21]. The action potentials are fired from a plateau around -30 mV and a peak at ~5 mV with a period of ~200 ms. This results confirm that this model is also a good starting point to replicate also the experimental recordings on AWA neurons or pharyngeal action potentials [21, 137, 140].
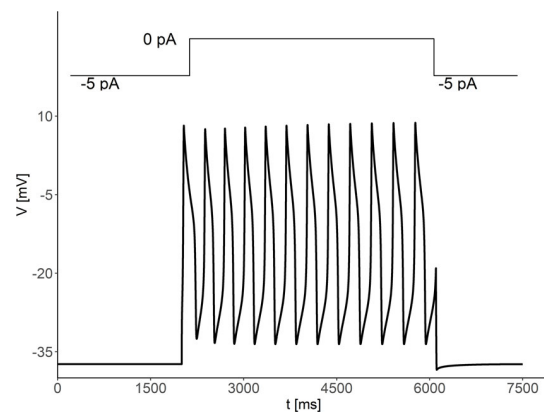
Figure 6.16: **Periodic solution in RMD neurons**. The figure shows the periodic solution arising in the grey area of Fig. 6.17

To achieve a complete picture of the RMD neurons dynamics, two dimensional bifurcation diagrams have been computed in the two regions of bistability highlighted by the study for the leakage current. The diagram shown in Fig. 6.17 A illustrates the behaviour of the model in the plane $\bar{g}_{\text{LEAK}} - \bar{g}_{\text{CCA1}}$.

At low values of $\bar{g}_{\text{CCA1}}$, the system has only one stable solution (V_s and V_s') or a bistable regime if g_{LEAK} is in the appropriate range. As $\bar{g}_{CCA1}$ increases, a torus bifurcation originates periodic solutions. In the narrow grey area, the stable solution V_s' coexist with a stable periodic solution (Fig. 6.17 A), which becomes the unique stable solution for values of $\bar{g}_{\text{LEAK}}$ between 0.045 nS and 0.08 nS. For values of $\bar{g}_{\text{LEAK}}$ between 0.15 nS and 1.2 nS, the behaviour of the dynamic system is described by the diagram showed in Fig. 6.17 B. When g_{LEAK} falls below the low LP (red dashed line) or above the high LP, the neuron has only one stable state V_s or V_r, respectively, while in the region between the two bifurcations the system display a bistable behaviour (Fig. 6.17 B, red area).
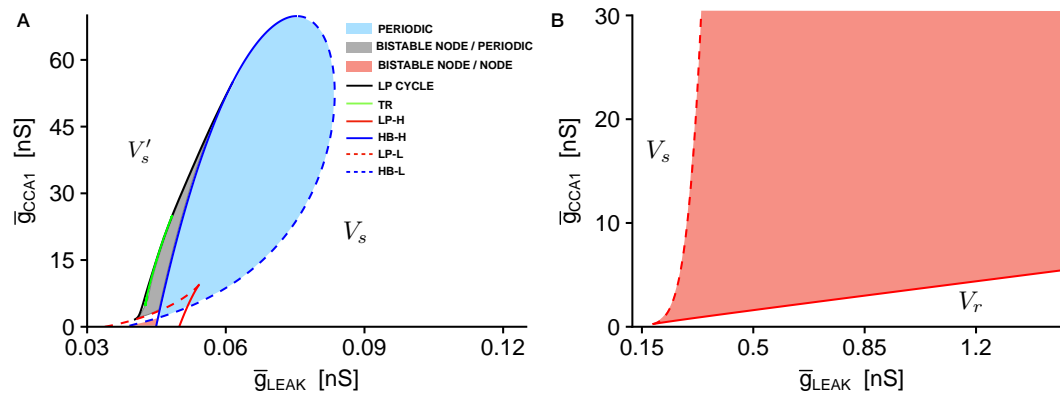
Figure 6.17: **Bifurcation diagram in the plane** $\overline{g}_{LEAK} - \overline{g}_{CCA1}$. **A) Two-dimensional bifurcation diagram at low** $\overline{g}_{LEAK}$ **values**. The red and blue curves denote the Fold (LP) and Hopf (HB) bifurcations, respectively. The torus and fold bifurcations cycles, i.e, the periodic solutions of the system, are highlighted in black and green. In the red area enclosed by HB-L and HB-H the system is bistable with V_s and V_s' as stable non-periodic states (nodes). For increasing values of $\overline{g}_{CCA1}$ two unstable cycles originate from a fold bifurcation cycle (LP cycle). At increasing values of $\overline{g}_{LEAK}$, one of these cycles collides with V_s' in the HB-H bifurcation. In the proximity of the fold bifurcation cycles, a large periodic solution becomes stable through a torus bifurcation (TR). Between TR and HB-H bifurcations the system has two different stable regimes (gray area), characterized by the coexistence of V_s' and a stable periodic solution. At increasing values of $\overline{g}_{LEAK}$, on the right of the HB-H only the oscillatory solution survives (blue area), and eventually disappears *via* a HB-L bifurcation. In the white areas a unique stable solution exists V_s' or V_s at low and high values of $\overline{g}_{LEAK}$, respectively. **B) Two-dimensional bifurcation diagram at high** $\overline{g}_{LEAK}$ **values**. The red dashed line represents the low-voltage fold bifurcation (LP-L). Below this bifurcation the neuron has a unique stable state V_s; while above the second LP bifurcation a second stable state V_r appears together with an unstable state V_u (red area, bistability region). For increasing values of $\overline{g}_{LEAK}$, the stable state V_s coalesces with V_u through a second LP-H bifurcation at high voltage represented by the continuous red line (LP-H). Thus, the system collapses in the unique stable state V_r. Figure reproduced with permission from [38]

6.4 Conclusion

In this chapter, three neurons belonging to the interneurons and motor neurons classes have been successfully modelled. The models have been developed in a Hodgkin-Huxley formalism, and analysed by means of *in silico* knockouts simulations and normalized conductance analysis to dissect the role of the different ionic channels in the whole-neuron dynamics.

The model of AIY neurons is developed in NEURON and the set of optimal conductances has been obtained by means of a GA-based routine implemented in python by the candidate. The model properly reproduces the typical behaviour of AIY neurons in voltage-clamp and current-clamp experiments [21]. The neuron displays an outward rectifier behaviour and is more sensitive to hyperpolarizing than to depolarizing stimuli,

without a threshold behaviour [21, 24]. However, to date, a complete experimental characterization of the ionic currents giving rise to the observed characteristics is still missing. In this work, the first dissection of the ionic currents contributing to AIY dynamics is performed based on *in silico* knockout and normalized conductance analyses. These analyses suggest that KQT1 and EGL2 currents determine the outward-rectifier character, while the inward rectification at hyperpolarizing potentials is mainly related to IRK and NCA currents. Although the main electrophysiological properties are correctly reproduced, the model still needs a further refinement to ensure a better match between the simulation and experimental results, especially at high potentials, where both steady-state and peak currents are underestimated.

The RIM model has been developed in XPPAUT, and the conductances have been manually fine-tuned. As in the AIY case, the model here presented constitutes the first biophysical model of the neuron. The *in silico* knockout and conductance analyses performed in this study suggest that the transient outward rectifier character observed in the experiments [21] is mediated by SHL1 currents, with a small contribution of EGL2 to the steady-state currents. The voltage-clamp recordings [21] are reproduced quite well by the model, as confirmed by the good agreement between simulated and experimental I-V curves. In contrast, current-clamp recordings are less well reproduced than the voltage-clamp ones, in particular during the upstroke and the repolarization phases. The conductance analysis suggested that NCA currents, in combination with voltage-gated potassium contributions, are the main responsible for the observed discrepancies. Therefore, further refinements of the model should be performed to fine-tune these parameters and match the observed voltage responses. This refinement will be performed in XPPAUT, but also new trials with a GA based routine will be performed.

Concerning the motor neurons, the model of RMD neurons here presented correctly reproduces the peculiar bistable behaviour observed for these neurons [20]. In contrast to other *C. elegans* neurons (AFD and AIA) showing a bistable behaviour only in presence of applied stimuli [21, 25], RMD neurons possess two stable states of the membrane potential in absence of applied stimuli [20]. The mechanisms through which the neuron selects the stable state are still unexplored. However, given that the neuron can switch between the two states depending of the applied stimulus, it can be argued that RMD chooses its resting state on the basis of the most resent input received from the surrounding network. These characteristics may confer to the neuron robustness and resilience to noise, ensuring an effective control of head movements. In this work the physiological origin of the bistability has been analysed through normalized conductance and *in silico* knockout studies. The first analysis highlighted the possible role of CCA-1 currents in ensuring the existence of the two stable states, that is further confirmed by in *in silico* knockout and bifurcation analyses. The bifurcation analysis revealed also an important role of LEAK currents in tuning the resting states of the neuron. Interestingly, the bistability analysis revealed also the potential of the model here developed to reproduce periodic oscillation and action potentials with characteristics very similar to that recently observed in AWA sensory neurons [21].

Chapter 7

The olfactory circuit model

153

In this chapter, biophysical models of miminal sensory circuit are presented. Firstly, the models of single neurons discussed in Chapters 5 and 6 are used to recreate a small circuit in which the sensory neuron AWC is connected though a chemical inhibitory synapse to the AIY neuron. Then, once the connection between AWC^{ON} and AIY neurons has been established, the RIM interneurons and the RMD motor neurons have been added in the circuit, by using gap junctions to connect RMD and RIM among them and with AIY (Fig. 7.1). The synaptic connections are modelled according to Chapter 2, section 2.1.5. The selected circuit represents half of the real biological network, indeed due to the left-right asymmetry in the worm, a specular circuit exists, whose primary sensory neuron is the AWC^{OFF} neuron. The circuit models have been implemented in NEURON and the results analysed in MATLAB.
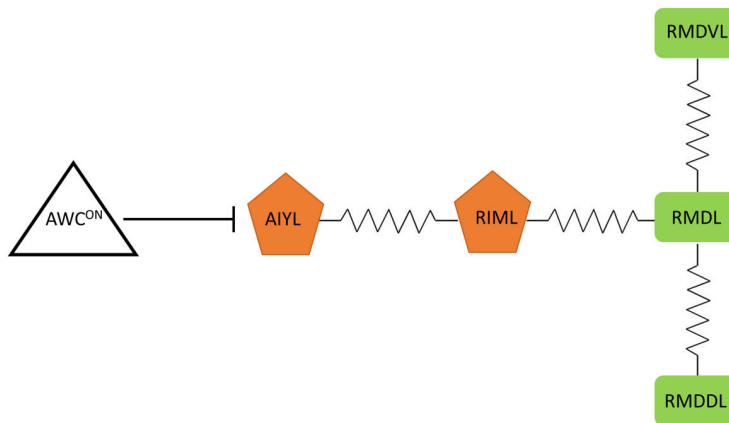
Figure 7.1: **Modelled six neurons circuit**. The modelled circuit includes six neurons AWC^{ON}, AIY, RIM, and three RMD neurons (RMDL, RMDDL, RMDVL). The synaptic connections to be included are selected on the basis of literature and of the information collected from the Wormwiring database[1].

7.1   AWC-AIY connection

As the first step to develop a biophysical model of a small sensory circuit, the connection between the sensory neuron AWC^{ON} and the AIY interneuron is modelled. This initial two-neuron circuit is created using the single-cell electrical models of AWC^{ON} (Chapter 5, Section 5.1) and AIY (Chapter 6, Section 6.1) with the simplified calcium dynamics (Eq. 2.42). AIY is one of the main synaptic targets of AWC neurons, with which it forms inhibitory synaptic connections mediated by the glutamate-gated chloride channels

GLC-3 [294]. AWC^{ON} neurons release glutamate in a continuous mode with the amount of released neurotransmitter proportional to the degree of activation of the neuron, and thereby to its intracellular calcium concentration [42, 44]. Due to the complexity of the processes at the basis of glutamate production in neuronal cells, a simplified model of the synaptic connection, based on the strict relation between glutamate release and calcium activity in the neuron [42, 44], is used. In particular, a standard model for graded synaptic release taken from [43], is implemented in NEURON. The synaptic current is dependent on the intracellular calcium concentration in the presynaptic neuron as stated by Eq. 7.1

$$I_{syn} = n_{syn} \cdot k \cdot \text{Ca}_{pre}^3 \cdot (V_{post} - E_{syn}), \tag{7.1}$$

where $n_{syn} = 220$ represents the strength of the synaptic connection, $k = 1 \cdot 10^{17}$ μS/M^3 is the conversion factor of the calcium concentration into electrical current, Ca_{pre} is the intracellular calcium concentration expressed in M, V_{post} is the membrane potential of the postsynaptic cell, and $E_{syn} = -70$ mV is the reversal potential for the synapse. The model parameters have been selected manually by ranging the values in wide space, spanning different order of magnitude, and the values that correctly reproduced the inhibitory behaviour of the synapse have been selected. As the fist step a mono-directional synapse is inserted in the circuit, so that the AWC^{ON} neuron sends an inhibitory current to the AIY interneuron.

The response of the circuit is tested by injecting two current pulses of 20 pA and -20 pA in the AWC^{ON} neuron to elicit a depolarization an hyperpolarization, respectively (Fig. 7.2 A left and C left). For both the neurons, the membrane voltage dynamics and the intracellular calcium responses have been analysed (Fig. 7.2 A and D). Concerning the AWC^{ON} neuron, the responses are consistent with that of the XPPAUT model, confirming the correctness of the NEURON implementation. The 20 VpA current pulse elicits in AWC^{ON} appreciable changes in the intracellular calcium, with a time course that follows the membrane voltage dynamics, but with slower time scales, especially in the repolarization phase (Fig. 7.2 B left). Notably, the large voltage excursions in the AWC^{ON} neurons induce small changes ($\sim$3 mV) in the AIY membrane potential (Fig. 7.2 A right). This result is in accordance with experimental observations performed with voltage sensitive dyes, that report little fluorescence changes in both the soma and neurite for hyperpolarizing and depolarizing stimuli [44, 45]. Also, in accordance with the single-cell model results, the neuron is more sensitive to hypepolarizing stimuli. Indeed, in correspondence of comparable voltage changes in AWC^{ON}, the neuron shows larger voltage excursions when receiving hyperpolarizing rather depolarizing stimuli ($\sim$3 mV Vs. 10^{-3} mV) (Fig. 7.2 A right and C right). Concerning the intracellular calcium dynamics, many calcium imaging experiments have demonstrated that AIY neurons display large changes in the intracellular calcium at the neurite level, while the soma remains almost inactive [44, 295, 296]. The simplified model of the intracellular calcium dynamics here adopted (Eq. 2.42 in Chapter 2, Section 2.1.3) seems to reproduce only the behaviour of the soma, despite it was meant to reproduce the whole-neuron dynamics (Fig. 7.2 B right and D right). This result highlights the limitations of both the synaptic

connection model and the intracellular calcium description that should be further refined. Also, it would be of particular interest for future development to include in the model the morphological features of AIY interneurons given the marked difference between the soma and neurite dynamics, going from a single-compartment model to a spatial description.
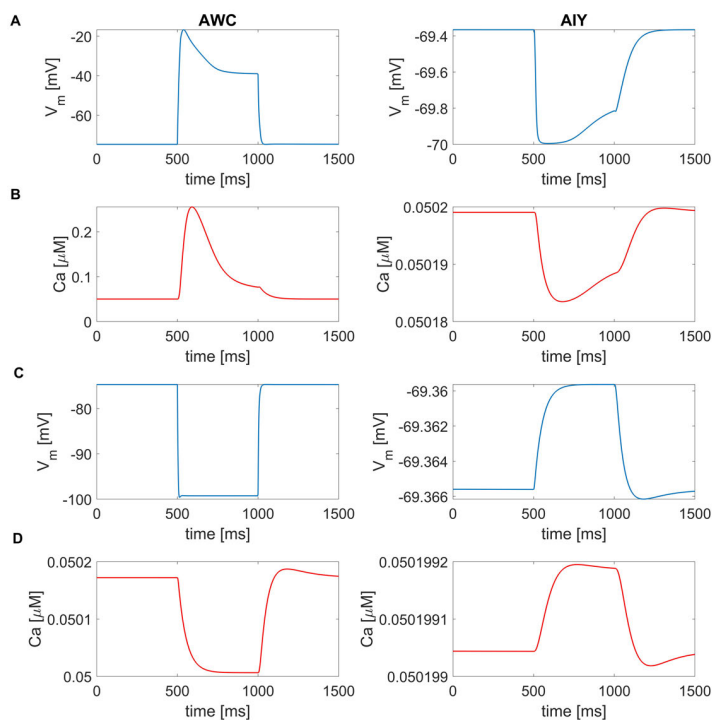
Figure 7.2: **AWC^{ON}-AIY inhibitory connection**. Panels A and B show the membrane voltage (A) and intracellular calcium (B) responses of AWC^{ON} (left) and AIY (right) neurons, respectively, to a depolarizing stimulus on the sensory neuron. The AWC^{ON} neurons is stimulated with a 20 pA current pulse for 500 ms. Panels C and D show the membrane voltage (C) and intracellular calcium (D) responses of AWC^{ON} (left) and AIY (right) neurons, respectively, to an hyperpolarizing stimulus on the sensory neuron. The stimulus consists of a -20 pA current pulse for 500 ms.

7.2   Six-neurons circuit

Once AWC^{ON} and AIY neurons have been connected, the RIM, and RMD neurons have been added to the circuit. The new neurons have been connected together and with the AIY neuron though a network of gap junction, as shown in Fig. 7.1, according to the information taken from the WormWiring database. In absence of a specific electro-physiological characterization for these connections, a standard model of gap junction is used:

$$I_{gap} = n_{syn} \cdot g_{gap} \cdot (V - E_{gap}), \qquad (7.2)$$

where $n_{syn} = 200$ represents the number of synaptic channels, $g_{syn} = 0.1 \cdot 10 - 3 \ \mu S$ is the conductance of the single hemichannel, and E_{gap} is the potential of the presynaptic cell. The model parameters have been selected manually by ranging the values in wide space, spanning different order of magnitude.

The response of the circuit is tested by delivering a current pulse of 20 pA to the AWC^{ON} neuron, to mimic its activation upon chemical stimulus removal. Contextually, the voltage on AWC^{ON} and on the other neurons in the circuit is recorded (Fig. 7.3). In the new circuit, both the intracellular calcium and the membrane voltage reponses of AIY neuron are unchanged, despite the addition of the feedback provided by the gap junction connections with RIM. As expected, the inhibition of AIY results in the inhibition of all the other neurons in the circuit. RIM interneurons and RMD motor neurons show little changes in the membrane voltage, around 0.7 mV, and no appreciable changes in the intracellular calcium (the changes are below $10^{-4} \ \mu M$). At these values of the membrane potential ($\sim$-67 mV), the voltage-gated calcium channels, that in this model are the unique carriers of calcium inside the cell, are almost inactive, and the stimulus received from the network is not sufficient to trigger their activation. To verify this hypothesis, a hyperpolarizing stimulus of -20 pA is delivered to AWC^{ON} neurons, to elicit depolarization in the downstream interneurons an motor neurons. However, also in this case no significant changes in the calcium is observed in all neurons, including AWC^{ON}.
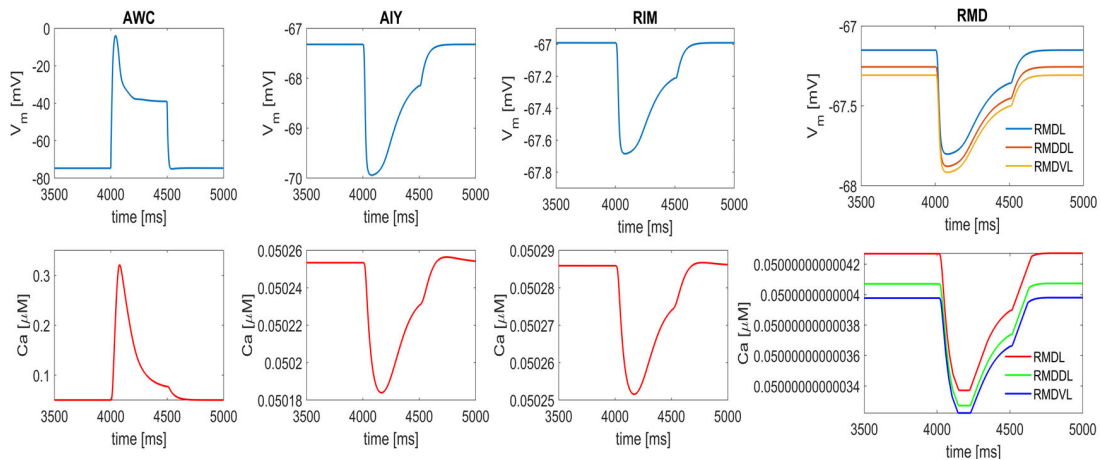
Figure 7.3: **Circuit response to 20 pA step injected on AWC^{ON}.** The panels show the membrane voltage (first row) and intracellular calcium (second row) responses of the six neurons to a 20 pA depolarizing step applied on the AWC^{ON} neuron.

In has to be noted that, in the case of RIM neurons some discrepancies between the model and the experiments exist. RIM neurons show an opposite behaviour with respect to that observed in calcium imaging experiments [16]. However, it has to considered that

AWC^{ON} neurons connect to RIM, not only through AIY neurons, but also trough a gap junction network formed with AVA and AIB neurons (here not modelled), with which they form excitatory synapses [13]. Thus, the input derived from that pathway may dominate on the inhibitory signals received from AIY neurons, and elicit the activation of RIM neurons in correspondence of AWC^{ON} activation (i.e. depolarization). Concerning the RMD neurons, to the best of the candidate knowledge, there are no experimental reports of RMD activity associated to AWC^{ON} dynamics. The small hyperpolarization observed is consistent with that observed in RIM neurons that send through the gap junction connection a small hyperpolarizing stimulus to RMDL.

7.3 Conclusion

In this chapter a preliminary study on a biophysical minimal sensory circuit of *C. elegans* is performed. The synaptic connections have been modelled with standard formulations [43]. The coupling between the sensory neuron AWC^{ON} and the AIY interneuron has been performed using a graded synaptic connection, in which the synaptic current is related to the intracellular calcium dynamics in the AWC^{ON} neuron. From the electrical point of view, the connection between the two neurons is correctly reproduced, while the intracellular calcium levels in the postsynaptic neuron are consistently underestimated, being inconsistent with experimental evidences that report large calcium excursions in the AIY neurites in correspondence of AWC^{ON} neurons inhibition [44, 45]. A refinement of both the synaptic connection and intracellular calcium models should be included, taking into account the specific gating characteristics of the GLC-3 channels, and by refining the model of intracellular calcium in the AIY interneurons. The same considerations are valid for the remaining part of the circuit, in particular for what concerns the intracellular calcium modelling. Regarding the characterization of gap junction connections, specific data for *C. elegans* could be used, when available for the connections here studied, to obtain a more realistic model.

The results here reported are very preliminary to the development of a complete biophysical model of the olfactory circuit. The inclusion in the circuit of other neurons, such as AWA, AVA, AIA, and AIB, that are also recruited in the olfactory circuit, may allow to grasp a more complete picture of single neurons function in the network. Currently, the candidate is developing the models of AWA, AIA and AVA, for which electrophysiological recording are available in literature [20, 21, 25]. The inclusion of these neurons in the circuit will also allow the inclusion of excitatory pathway that are also important for the *C. elegans* food searching behaviour.

Conclusions

159

In the last decades, many efforts have been devoted to the clarification and comprehension of *C. elegans* nervous system functioning. The comprehension of the molecular mechanisms at the basis of signal integration, generation and transmission could be of key importance for the study of the nematode nervous system, and constitutes a starting point for the comprehension of complex systems, such as the mammalian brain. In this scenario, mathematical models could provide an important tool to explain the observed phenomena both at the molecular and cellular level, to predict unexpected new behaviours and to guide future experiments.

To date, many computational model have been developed for the *C. elegans* nervous system. These models describe the neuronal dynamics of the nematode at different scales, from the single-cell [1, 36] up to the network and behavioural scale [27, 28, 29, 30, 31, 32]. However, these studies mainly focus on calcium dynamics in single neurons or on the network dynamics, while the electrical behaviour of single neurons is treated in a simplified way that does not account for the specific biophysical characteristics of the single cells. In the last decades, many works have highlighted the complexity of neuronal behaviours arising at the single-cell level in *C. elegans* neurons [18, 19, 20, 21, 22, 25]. In this context, the single-cell models could provide new insights into the single neuron dynamics.

To the best of the candidate knowledge, this work provides the first comprehensive framework for modelling the *C. elegans* neurons and muscles in a biophysically accurate way, taking into account the molecular origin of the neuronal responses.

The models of 15 important channels involved in the nematode neuronal dynamics have been developed in a Hodgkin-Huxley formalism. In particular, 9 voltage-gated potassium channels, 3 voltage-gated calcium channels, and 3 calcium-regulated potassium channels have been modelled, based on available experimental data from literature for *C. elegans* and other organisms expressing similar channels. All the models here presented correctly reproduce the experimental recordings of *C. elegans* ionic currents in their native membrane or when heterologously expressed in other cells.

The models of single ionic currents have been used to model four important neurons of the nematode: the AWC[ON] sensory neurons, the AIY and RIM interneurons, and the RMD motor neurons.

Concerning the AWC[ON] sensory neurons, both the electrical and the calcium dynamics have been studied in detail. A model of the AWC[ON] electrical behaviour has been developed [38]. It correctly reproduces the recorded whole-cell currents [19] and predicts active threshold responses in the voltage of AWC[ON] neurons. The origin of these responses has been investigated for the first time using *in silico* knockout simulations and conductance analysis, revealing a complex interplay between EGL19 and UNC2 calcium currents and EGL2 and KVS1 potassium currents.

The model of the electrical response developed by the candidate has been coupled with a pre-existing detailed model of the intracellular calcium dynamics [1], to obtain a biophysically accurate description of the AWC[ON] response to chemical stimuli. The membrane

voltage and the intracellular calcium responses have been analysed in a wide range of odour concentrations and exposure times to reconstruct the dose-response curves characterizing the sensory ability of the neuron. Overall, despite some aspects that deserve further investigation, the model correctly reproduces the behaviour of the neurons as observed in calcium imaging experiments [13, 42].

A refinement of the AWC^{ON} electrical model through a genetic algorithm-based optimization routine revealed a previously unobserved bistable behaviour of the neuron that exhibits two stable resting potentials. This behaviour has been investigated through *in silico* knockout and conductance analyses that highlighted the role of CCA1 calcium current, KQT3, KVS1, and IRK potassium currents, as well as of NCA and LEAK currents, in originating the bistability.

Calcium imaging experiments performed at the CLNS@Sapienza reported a previously unobserved ability of AWC^{ON} neurons to detect mechanical stimuli. Its origin is investigated with experiments on *osm-9, tax-4, unc-13*, and *unc-31*, suggesting that mechanical responses are intrinsic and possibly share the signalling pathway with GPCRs. Further experiments on *cca-1, egl-19*, and *nca-2* mutants showed that voltage-gated calcium channels are also important for the transduction of mechanical stimuli.

The models of AIY, RIM and RMD neurons have been developed with the same method used for AWC^{ON} [20, 21]. The three models correctly reproduce the main characteristics of the current and voltage-clamp recordings [20, 21], also as far as the bistable behaviour of the RMD neurons is concerned.

The models of the AIY and RIM could need some refinements. Indeed, some discrepancies emerged especially in RIM neurons, that display an anomalous peak in the repolarization phase deserving further investigation.

Concerning the RMD neurons, the model here developed successfully reproduced the bistability observed in current-clamp experiments [20]. The high level of detail of this model allowed to elucidate the origin of the bistability of RMD neurons through *in silico* knockout and bistability analysis. Similarly to the AWC^{ON} case, the bistable behaviour is mediated by CCA1 currents in combination with LEAK currents. A detailed analysis of the equilibrium states of the system also highlighted the existence of periodic solutions and action potential firing modes with characteristics similar to that of the recently recorded action potentials in AWA neurons [21].

Finally, the models of the four neurons have been connected in a small circuit, using standard models of graded synaptic gap junction connections. The inhibitory connection between AWC^{ON} neuron and AIY interneuron is well reproduced as far as the electrical behaviour is concerned, while the large calcium excursions observed in AIY neurons [44, 295, 296] are not correctly reproduced. Thus, future studies will focus on developing a suited model of the intracellular calcium dynamics in interneurons. The same considerations remain valid for the RIM and RMD connections, in particular in the case of the intracellular calcium dynamics. Concerning the characterization of gap junction connections, the lack of specific data for *C. elegans* constitutes an issue to be overcome with different kinds of models. The results here reported are very preliminary

to the development of a biophysical model of the olfactory circuit, in which also other important neurons, such as AWA, AVA, AIA, and AIB, should be included

This study constitutes the first attempt to develop a biophysical framework for the *C. elegans* nervous system modelling. However, there are some limitations in this study that should be pointed out and considered for future developments.

The first limitation of the model is that the whole-cell models have been developed in the single compartment approximation, disregarding the diffusive currents arising from the complex morphological structure of the cells and the heterogeneous distribution of the ionic channels in different cellular compartments. Single-compartment models have demonstrated in many years their effectiveness in reproducing the electrophysiological behaviour of different cell types. The obtained results demonstrate that the single isopotential compartment approximation also works in the *C. elegans* case. A possible future development is the inclusion of the morphological features of the neurons in the model, to account also for the spatial dynamics of membrane voltage and intracellular calcium, which is of particular importance, for example, in the case of AIY interneurons.

The second limitation concerns the simplified description of the intracellular calcium dynamics used in the electrical models. As confirmed by circuit simulations, the present description is too simplified to reproduce the calcium dynamics observed in imaging experiments. Therefore, for future studies, a refinement and specification of this model must be performed, in particular in the case of interneurons.

The third point concerns the coupling between the detailed description of intracellular calcium and electrical dynamics of AWC^{ON} neurons, which still deserves a fine-tuning of the parameters and a detailed investigation of the calcium fluxes to be performed through computational studies and experimental data fitting.

The last point to be noted concerns the synaptic connection modelling. Indeed, as already said the standard models implemented here are not suitable for adequately describing the observed dynamics, in particular with respect to the intracellular calcium responses. A dedicated computational study should be performed to develop more accurate models of synaptic connections in *C. elegans*, based on available electrophysiology data.

Despite the limitations described above, the single-neurons models developed in this work correctly reproduce the salient characteristics of AWC^{ON}, AIY, RIM, and RMD neurons and allow a detailed study of their electrophysiological properties in terms of single ionic currents. It is important to note that, except for RMD neurons [20], no electrophysiological experiments have been performed to dissect the role of the single ionic currents. In addition to that, in the case of AIY and RIM neurons, the specific set of ionic channels expressed in the neurons is less well characterized than in the AWC^{ON} and RMD case. Therefore, the models here developed could also constitute a guide for future experiments devoted to clarify the mechanisms of electrical response generation in sensory, motor, and interneurons.

In conclusion, this work provides a useful tool for extensive biophysical modelling of the

CONCLUSIONS

C. elegans nervous system both at the single cells and at the network level, opening the way for a comprehensive understanding of the nematode neurons functioning. Future work will be dedicated to refining the above-cited critical aspects, and developing the model of other neurons of the olfactory circuit such as the AWA, AIA, AVA, and ventral motor neurons for which electrophysiological data are available. In this way, the olfactory circuit of the nematode will be recreated *in silico*.

Acknowledgements

I am also deeply grateful to my supervisor Prof. Simonetta Filippi, my co-supervisors Dr. Letizia Chiodo and Dr. Viola Folli, and Dr. Alessandro Loppini for their invaluable advice, continuous support and patience. Their immense knowledge and plentiful experience have encouraged me in all the time of my academic research and daily life.

I would like to extend my sincere thanks to the CLNS@Sapienza group members, Dr. Silvia Schwarts, Dr. Davide Caprini, Dr. Enrico Lanza, Giuseppe Ferrarese and Valeria Lucente, for their technical support and the critical discussions. Without their competence and experience the experimental results presented in this study would not be obtained.

I would also like to thank Dr. Qiang Liu (Rockefeller University, New York) for the invaluable advice and support in the development of AIY neurons models.

A special thanks also goes to the other UCBM group members, Dr. Alessio Gizzi, Prof. Christian Cherubini, Dr. Alessandro Barone, and Margherita Matarrese for their advice, critical discussion, and support that have made my study experience at UCBM an incredible period of scientific and personal growth.

Finally, my deepest gratitude goes to my family and friends for their constant understanding and encouragement in the past few years, which has invaluably helped me to complete this study.

Appendices

167

Appendix A

For each modelled current x the full list of equations, including steady-state activation and/or inactivation variables and time constants, as well as the equation for the total current. When necessary, fast, medium, and slow components are denoted as m_x^{f}, m_x^{m}, m_x^{s} (h_x^{f}, h_x^{m}, h_x^{s}), while $\tau_{m_x}^{\mathrm{f}}$, $\tau_{m_x}^{\mathrm{m}}$, $\tau_{m_x}^{\mathrm{s}}$ ($\tau_{h_x}^{\mathrm{f}}$, $\tau_{h_x}^{\mathrm{m}}$, $\tau_{h_x}^{\mathrm{s}}$) denote the corresponding time constants. The corresponding parameters are listed Appendix B, Tables B1, B2, and B3.

Voltage-gated potassium currents IRK

$$m_{\mathrm{IRK},\infty}(V) = \frac{1}{1 + e^{\frac{(V - V_{0.5})}{k_a}}} \tag{A1}$$

$$\tau_{m_{\mathrm{IRK}}}(V) = \frac{a}{e^{\frac{-(V-b)}{c}} + e^{\frac{(V-d)}{\tilde{e}}}} + f \tag{A2}$$

$$I_{\mathrm{IRK}} = \overline{g}_{\mathrm{IRK}} \cdot m_{\mathrm{IRK}} \cdot (V - V_K) \tag{A3}$$

SHK1

$$m_{\mathrm{SHK1},\infty}(V) = \frac{1}{1 + e^{\frac{-(V - V_{0.5})}{k_a}}} \tag{A4}$$

$$\tau_{m_{\mathrm{SHK1}}}(V) = \frac{a}{e^{\frac{-(V-b)}{c}} + e^{\frac{(V-d)}{\tilde{e}}}} + f \tag{A5}$$

$$h_{\mathrm{SHK1},\infty}(V) = \frac{1}{1 + e^{\frac{(V - V_{0.5})}{k_i}}} \tag{A6}$$

$$\tau_{h_{\mathrm{SHK1}}} = a \tag{A7}$$

$$I_{\mathrm{SHK1}} = \overline{g}_{SHK1} \cdot m_{\mathrm{SHK1}} \cdot h_{\mathrm{SHK1}} \cdot (V - V_K) \tag{A8}$$

EXP2

$$m_{\mathrm{EXP2},\infty}(V) = \frac{1}{1 + e^{\frac{-(V - V_{0.5})}{k_a}}} \tag{A9}$$

$$\tau_{\mathrm{EXP2}}^m = \frac{a}{e^{\frac{(V-b)}{c}} + e^{\frac{-(V-d)}{e}}} + f \tag{A10}$$

$$h_{\mathrm{EXP2},\infty}(V) = \frac{1}{1 + e^{\frac{(V - V_{0.5})}{k_i}}} \tag{A11}$$

$$\tau_{\mathrm{EXP2}}^h = \left\{ \frac{a}{1 + e^{\frac{(V-b)}{c}}} + d \right\} \cdot \left\{ \frac{a}{1 + e^{\frac{-(V-b)}{c}}} + d \right\}, \tag{A12}$$

$$I_{\mathrm{EXP2}} = \overline{g}_{\mathrm{EXP2}} \cdot m \cdot h^3 \cdot (V - V_K) \tag{A13}$$

APPENDIX A

EGL36

$$m_{\text{EGL36},\infty}^{\text{f}}(V) = m_{\text{EGL36},\infty}^{\text{m}}(V) = m_{\text{EGL36},\infty}^{\text{s}}(V) = \frac{1}{1 + e^{\frac{-(V - V_{0.5})}{k_a}}} \tag{A14}$$

$$\tau_{m\text{EGL36}}^{\text{f}} = \tau_{m\text{EGL36}}^{\text{m}} = \tau_{m\text{EGL36}}^{\text{s}} = a \tag{A15}$$

$$I_{\text{EGL36}} = \bar{g}_{\text{EGL36}} \cdot \left(0.33\, m_{\text{EGL36}}^{\text{f}} + 0.36\, m_{\text{EGL36}}^{\text{m}} + 0.39\, m_{\text{EGL36}}^{\text{s}} \right) \cdot (V - V_K) \tag{A16}$$

SHL1

$$m_{\text{SHL1},\infty}(V) = \frac{1}{1 + e^{\frac{-(V - V_{0.5})}{k_a}}} \tag{A17}$$

$$\tau_{m_{\text{SHL1}}}(V) = \frac{a}{e^{\frac{-(V-b)}{c}} + e^{\frac{(V-d)}{\tilde{e}}}} + f \tag{A18}$$

$$h_{\text{SHL1},\infty}^{\text{f}}(V) = h_{\text{SHL1},\infty}^{\text{s}}(V) = \frac{1}{1 + e^{\frac{(V - V_{0.5})}{k_i}}} \tag{A19}$$

$$\tau_{h_{\text{SHL1}}}^{\text{f}}(V) = \tau_{h_{\text{SHL1}}}^{\text{s}}(V) = \frac{a}{1 + e^{\frac{(V-b)}{c}}} + d \tag{A20}$$

$$I_{\text{SHL1}} = \bar{g}_{\text{SHL1}} \cdot m_{\text{SHL1}}^3 \cdot (0.7\, h_{\text{SHL1}}^{\text{f}} + 0.3\, h_{\text{SHL1}}^{\text{s}}) \cdot (V - V_K) \tag{A21}$$

KQT1

$$m_{\text{KQT1},\infty}(V) = \frac{1}{1 + e^{\frac{-(V - V_{0.5})}{k_a}}} \tag{A22}$$

$$\tau_{m_{\text{KQT1}}}(V) = \frac{a}{1 + e^{\frac{(V-b)}{c}}} + d \tag{A23}$$

$$I_{\text{KQT1}} = \bar{g}_{\text{KQT1}} \cdot m_{\text{KQT1}} \cdot (V - V_K) \tag{A24}$$

KQT3

$$m_{\text{KQT3},\infty}^{\text{f}}(V) = m_{\text{KQT3},\infty}^{\text{s}}(V) = \frac{1}{1 + e^{\frac{-(V - V_{0.5})}{k_a}}} \tag{A25}$$

$$\tau_{m_{\text{KQT3}}}^{\text{f}}(V) = \frac{a}{1 + \left(\frac{V+b}{c}\right)^2} \tag{A26}$$

$$\tau_{m_{\text{KQT3}}}^{\text{s}}(V) = a + \frac{b}{1 + 10^{-c(d-V)}} + \frac{\tilde{e}}{1 + 10^{-f(g+V)}} \tag{A27}$$

$$w_{\text{KQT3},\infty}(V) = s_{\text{KQT3},\infty}(V) = a + \frac{b}{1 + e^{\frac{(V - V_{0.5})}{k_i}}} \tag{A28}$$

$$\tau_{w_{\text{KQT3}}}(V) = a + \frac{b}{1 + \left(\frac{V-c}{d}\right)^2} \tag{A29}$$

$$\tau_{s_{\text{KQT3}}} = a \tag{A30}$$

$$I_{\text{KQT3}} = \bar{g}_{\text{KQT3}} \cdot (0.7\, m_{\text{KQT3}}^{\text{f}} + 0.3\, m_{\text{KQT3}}^{\text{s}}) \cdot w_{\text{KQT3}} \cdot s_{\text{KQT3}} \cdot (V - V_K) \tag{A31}$$

EGL2

$$m_{\text{EGL2},\infty}(V) = \frac{1}{1 + e^{\frac{-(V - V_{0.5})}{k_a}}} \tag{A32}$$

$$\tau_{m_{\text{EGL2}}}(V) = \frac{a}{1 + e^{\frac{(V - b)}{c}}} + d \tag{A33}$$

$$I_{\text{EGL2}} = \overline{g}_{\text{EGL2}} \cdot m_{\text{EGL2}} \cdot (V - V_K) \tag{A34}$$

UNC103

$$m_{\text{UNC103},\infty}(V) = \frac{1}{1 + e^{\frac{-(V - V_{0.5})}{k_a}}} \tag{A35}$$

$$\tau_{\text{UNC103}}^{m} = \left\{ \frac{a}{1 + e^{\frac{(V - b)}{c}}} + d \right\} \cdot \left\{ \frac{a}{1 + e^{\frac{-(V - b)}{c}}} + d \right\}, \tag{A36}$$

$$h_{\text{UNC103},\infty}(V) = \frac{1}{1 + e^{\frac{(V - V_{0.5})}{k_i}}} \tag{A37}$$

$$\tau_{\text{UNC103}}^{h} = \left\{ \frac{a}{1 + e^{\frac{(V - b)}{c}} + d} \right\} \cdot \left\{ \frac{a}{1 + e^{\frac{-(V - b)}{c}}} + d \right\}, \tag{A38}$$

$$I_{\text{UNC103}} = \overline{g}_{\text{UNC103}} \cdot m \cdot h \cdot (V - V_K) \tag{A39}$$

KVS1

$$m_{\text{KVS1},\infty}(V) = \frac{1}{1 + e^{\frac{-(V - V_{0.5})}{k_a}}} \tag{A40}$$

$$h_{\text{KVS1},\infty}(V) = \frac{1}{1 + e^{\frac{(V - V_{0.5})}{k_i}}} \tag{A41}$$

$$\tau_{m_{\text{KVS1}}}(V) = \tau_{h_{\text{KVS1}}}(V) = \frac{a}{1 + e^{\frac{(V - b)}{c}}} + d \tag{A42}$$

$$I_{\text{KVS1}} = \overline{g}_{\text{KVS1}} \cdot m_{\text{KVS1}} \cdot h_{\text{KVS1}} \cdot (V - V_K) \tag{A43}$$

APPENDIX A

Calcium-regulated potassium currents   SLO1-SLO2

$$CaV = EGL19,\ UNC2$$

$$m_{\text{BK},\infty}(V, Ca) = \frac{m_{\text{CaV}} k_o^+ (\alpha + \beta + k_c^-)}{(k_o^+ + k_o^-)(k_c^- + \alpha) + \beta k_c^-} \tag{A44}$$

$$\tau_{m_{\text{BK}}}(V, Ca) = \frac{\alpha + \beta + k_c^-}{(k_o^+ + k_o^-)(k_c^- + \alpha) + \beta k_c^-} \tag{A45}$$

$$\alpha = \frac{m_{\text{CaV},\infty}}{\tau_{m_{\text{CaV}}}} \tag{A46}$$

$$\beta = \tau_{m_{\text{CaV}}}^{-1} - \alpha \tag{A47}$$

$$I_{\text{BK}} = \overline{g}_{\text{BK}} \cdot m_{\text{BK}} \cdot h_{\text{CaV}} \cdot (V - V_K) \tag{A48}$$

For k_o^+, k_o^-, k_c^- see Methods. Ca stands for the nano-scale calcium concentration close to CaV channels, i.e. $\left[\text{Ca}^{2+}\right]_{o,i}^n$ and $\left[\text{Ca}^{2+}\right]_{c,i}^n$ for $k_o^{+/-}$ and $k_c^{+/-}$, respectively.

KCNL

$$m_{\text{KCNL},\infty}(Ca) = \frac{Ca}{K_{Ca} + Ca} \tag{A49}$$

$$\tau_{m_{\text{KCNL}}} = a \tag{A50}$$

$$I_{\text{KCNL}} = \overline{g}_{\text{KCNL}} \cdot m_{\text{KCNL}} \cdot (V - V_K) \tag{A51}$$

For intracellular calcium calculation see Methods. Ca stands for the micro-scale calcium concentration, i.e. the intracellular calcium $\left[\text{Ca}^{2+}\right]_i^m$.

Voltage-gated calcium currents   EGL19

$$m_{\text{EGL19},\infty}(V) = \frac{1}{1 + e^{\frac{-(V - V_{0.5})}{k_a}}} \tag{A52}$$

$$\tau_{m_{\text{EGL19}}}(V) = \left[a \; e^{-\left(\frac{V - b}{c}\right)^2} \right] + \left[d \; e^{-\left(\frac{V - \tilde{e}}{f}\right)^2} \right] + g \tag{A53}$$

$$h_{\text{EGL19},\infty}(V) = \left[\frac{a}{1 + e^{\frac{-(V - V_{0.5})}{k_i}}} + b \right] \cdot \left[\frac{c}{1 + e^{\frac{\left(V - V_{0.5}^b\right)}{k_i^b}}} + d \right] \tag{A54}$$

$$\tau_{h_{\text{EGL19}}}(V) = a \left[\frac{b}{1 + e^{\frac{(V - c)}{d}}} + \frac{\tilde{e}}{1 + e^{\frac{(V - f)}{g}}} + h \right] \tag{A55}$$

$$I_{\text{EGL19}} = \overline{g}_{\text{EGL19}} \cdot m_{\text{EGL19}} \cdot h_{\text{EGL19}} \cdot (V - V_{Ca}) \tag{A56}$$

UNC2

$$m_{\text{UNC2},\infty}(V) = \frac{1}{1 + e^{\frac{-(V - V_{0.5})}{k_a}}} \tag{A57}$$

$$\tau_{m_{\text{UNC2}}}(V) = \frac{a}{e^{\frac{-(V - b)}{c}} + e^{\frac{(V - b)}{d}}} + \tilde{e} \tag{A58}$$

$$h_{\text{UNC2},\infty}(V) = \frac{1}{1 + e^{\frac{(V - V_{0.5})}{k_i}}} \tag{A59}$$

$$\tau_{h_{\text{UNC2}}}(V) = \frac{a}{1 + e^{\frac{-(V - b)}{c}}} + \frac{d}{1 + e^{\frac{(V - \tilde{e})}{f}}} \tag{A60}$$

$$I_{\text{UNC2}} = \overline{g}_{\text{UNC2}} \cdot m_{\text{UNC2}} \cdot h_{\text{UNC2}} \cdot (V - V_{Ca}) \tag{A61}$$

CCA1

$$m_{\text{CCA1},\infty}(V) = \frac{1}{1 + e^{\frac{-(V - V_{0.5})}{k_a}}} \tag{A62}$$

$$h_{\text{CCA1},\infty}(V) = \frac{1}{1 + e^{\frac{(V - V_{0.5})}{k_i}}} \tag{A63}$$

$$\tau_{m_{\text{CCA1}}}(V) = \frac{a}{1 + e^{\frac{-(V - b)}{c}}} + d \tag{A64}$$

$$\tau_{h_{\text{CCA1}}}(V) = \frac{a}{1 + e^{\frac{(V - b)}{c}}} + d \tag{A65}$$

$$I_{\text{CCA1}} = \overline{g}_{\text{CCA1}} \cdot m_{\text{CCA1}}^2 \cdot h_{\text{CCA1}} \cdot (V - V_{Ca}) \tag{A66}$$

NCA

$$I_{\text{NCA}} = \overline{g}_{\text{NCA}} \cdot (V - V_{Na}) \tag{A67}$$

APPENDIX A

LEAK

$$I_{\text{LEAK}} = \overline{g}_{\text{LEAK}} \cdot (V - V_L) \tag{A68}$$

Appendix B

Parameter list for single currents models In the following tables the parameters of single-current models are listed. The values between parenthesis are the modified values used in the single neurons models. The values between brackets are the parameters for the second model of SHL1 currents.

Parameter		Value	Unit
Voltage-gated K$^+$ currents			
IRK			
m_∞	$V_{0.5}$	-82	mV
	k_a	13	mV
τ_m	a	17.1	ms
	b	-17.8	mV
	c	20.3	mV
	d	-43.4	mV
	$\tilde{e}$	11.2	mV
	f	3.8	ms
SHK1			
m_∞	$V_{0.5}$	20.4	mV
	k_a	7.7	mV
h_∞	$V_{0.5}$	-7.0	mV
	k_i	5.8	mV
τ_m	a	26.6	ms
	b	-33.7	mV
	c	15.8	mV
	d	-33.7	mV
	$\tilde{e}$	15.4	mV
	f	2.0	ms
τ_h	a	1400	ms
EXP2			
m_∞	$V_{0.5}$	-17.0	mV
	k_a	6.5	mV
h_∞	$V_{0.5}$	-33.5	mV
	k_i	15.8	mV
τ_m	a	209.1	ms
	b	-7.53	mV
	c	9.18	mV
	d	-55.20	mV
	e	-13.46	mV
	f	51.22	ms
τ_h	a	1.3	ms
	b	-89.0	mV
	c	49.4	mV

APPENDIX B

	d	0.9	ms
	EGL36		
m_∞	$V_{0.5}$	63.0	mV
	k_a	28.5	mV
τ_m^{s}	a	355.0	ms
τ_m^{m}	a	63.0	ms
τ_m^{f}	a	13.0	ms
	SHL1		
m_∞	$V_{0.5}$	11.2 (-6.8) [10.26]	mV
	k_a	14.1 [16.25]	mV
h_∞	$V_{0.5}$	-33.1 [-40]	mV
	k_i	8.3 [8.3]	mV
τ_m	a	13.8 (1.4) [6.9]	ms
	b	-17.5 [-40]	mV
	c	12.9 [12.92]	mV
	d	-3.7 [-40]	mV
	$\tilde{e}$	6.5 [6.49]	mV
	f	1.9 (0.2) [0.94]	ms
τ_h^{f}	a	539.2 (53.9) [179.72]	ms
	b	-28.2 [-60]	mV
	c	4.9[4.9]	mV
	d	27.3 (2.7) [9.09]	ms
τ_h^{s}	a	8422.0 (842.2) [8422.0]	ms
	b	-37.7 [-60]	mV
	c	6.4 [6.38]	mV
	d	118.9 (11.9) [118.90]	ms
	KQT1		
m_∞	$V_{0.5}$	-16	mV
	k_a	2.3	mV
τ_m	a	5000	ms
	b	-26.4	mV
	c	13.3	mV
	d	5019.0	ms
	KQT3		
m_∞	$V_{0.5}$	-12.8 (7.7)	mV
	k_a	15.8	mV
w_∞	$V_{0.5}$	-1.1	mV
	k_i	28.8	mV
	a	0.5	
	b	0.5	
s_∞	$V_{0.5}$	-45.3	mV
	k_i	12.3	mV

	a	0.3	
	b	0.7	
τ_m^f	a	395.3 (39.5)	ms
	b	38.1	mV
	c	33.6	mV
τ_m^s	a	5503.0 (550.3)	ms
	b	-5345.4 (-534.5)	ms
	c	0.0283	mV^{-1}
	d	-23.9	mV
	$\tilde{e}$	-4590 (-459.1)	ms
	f	0.0357	mV^{-1}
	g	14.2	mV
τ_w	a	0.5	ms
	b	2.9	ms
	c	-48.1	mV
	d	48.8	mV
τ_s	a	500	ms
EGL2			
m_∞	$V_{0.5}$	-6.9	mV
	k_a	14.9	mV
τ_m	a	1845.8 (8.39)	ms
	b	-122.6	mV
	c	13.8	mV
	d	1517.74 (4.04)	ms
UN103			
m_∞	$V_{0.5}$	-15.1	mV
	k_a	7.85	mV
h_∞	$V_{0.5}$	-49	mV
	k_i	28	mV
τ_m	a	1845.8 (8.39)	ms
	b	-122.6	mV
	c	13.8	mV
	d	1517.74 (4.04)	ms
KVS1			
m_∞	$V_{0.5}$	57.1 (27.1)	mV
	k_a	25.0	mV
h_∞	$V_{0.5}$	47.3 (17.3)	mV
	k_i	11.1	mV
τ_m	a	30.00	ms
	b	18.12	mV
	c	-20.00	mV
	d	1.00	ms

APPENDIX B

τ_h	a	88.46	ms
	b	50.00	mV
	c	-15.00	mV
	d	53.41	ms

Table B1: **Voltage-gated potassium channels model parameters**

Parameter		Value	Unit
Calcium regulated K^+ currents			
SLO1			
w_{yx}		0.013	mV^{-1}
w_{xy}		-0.028	mV^{-1}
w_0^-		3.15	ms^{-1}
w_0^+		0.16	ms^{-1}
K_{xy}		55.73	μM
n_{xy}		1.30	
K_{yx}		34.34	μM
n_{yx}		10^{-4}	
SLO2			
w_{yx}		0.019	mV^{-1}
w_{xy}		-0.024	mV^{-1}
w_0^-		0.90	ms^{-1}
w_0^+		0.027	ms^{-1}
K_{xy}		93.45	μM
n_{xy}		1.84	
K_{yx}		3294.55	μM
n_{yx}		10^{-5}	
KCNL			
K_{Ca}		0.33	μM
τ_m	a	6.3	ms
Intracellular calcium			
g_{sc}		40	pS
V_{Ca}		60	mV
r		13	nm
F		96485	C mol^{-1}
D_{Ca}		250	μ^2m s^{-1}
k_B^+		500	μM^{-1} s^{-1}
$[B]_{\text{tot}}$		30	μM
$[\text{Ca}^{2+}]_{c,i}^n$		0.05	μM
V_{cell}		31.16 (AWC), 5.65 (RMD)	μm^3
f		0.001	
τ_{Ca}		50	ms
$[\text{Ca}^{2+}]_{\text{eq}}^m$		0.05	μM

Table B2: **List calcium-regulated potassium channels model parameters**

APPENDIX B

Parameter		Value	Unit
Voltage-gated $Ca^{2}+$ currents			
EGL19			
m_∞	$V_{0.5}$	5.6 (-4.4)	mV
	k_a	7.5	mV
h_∞	$V_{0.5}$	24.9 (14.9)	mV
	k_i	12	mV
	$V_{0.5}^b$	-10.5 (-20.5)	mV
	k_i^b	8.1	mV
	a	1.43	
	b	0.14	
	c	5.96	
	d	0.60	
τ_m	a	2.9	ms
	b	5.2 (-4.8)	mV
	c	6.0	mV
	d	1.9	ms
	$\tilde{e}$	1.4 (-8.6)	mV
	f	30.0	mV
	g	2.3	ms
τ_h	a	0.4	
	b	44.6	ms
	c	-23.0 (-33.0)	mV
	d	5.0	mV
	$\tilde{e}$	36.4	ms
	f	28.7(18.7)	mV
	g	3.7	mV
	h	43.1	ms
UNC2			
m_∞	$V_{0.5}$	-12.2 (-37.2)	mV
	k_a	4.0	mV
h_∞	$V_{0.5}$	-52.5 (-77.5)	mV
	k_i	5.6	mV
τ_m	a	1.5	ms
	b	-8.2 (-38.2)	mV
	c	9.1	mV
	d	15.4	mV
	$\tilde{e}$	0.1	ms
τ_h	a	83.8 (142.5)	ms
	b	52.9 (22.9)	mV
	c	-3.5	mV

	d	72.1 (122.6)	ms
	$\tilde{e}$	23.9 (-6.1)	mV
	f	-3.6	mV
CCA1			
m_∞	$V_{0.5}$	-43.32(-57.7)	mV
	k_a	7.6 (2.4)	mV
h_∞	$V_{0.5}$	-58.0 (-73.0)	mV
	k_i	7.0 (8.1)	mV
τ_m	a	40.0 (20)	ms
	b	-62.5 (-92.5)	mV
	c	-12.6 (21.1)	mV
	d	0.7 (0.4)	ms
τ_h	a	280 (22.4)	ms
	b	-60.7 (-75.7)	mV
	c	8.5 (9.4)	mV
	d	19.8 (1.6)	ms

Table B3: **List of voltage-gated calcium channels model parameters.**

Appendix C

Genetic Algorithms Essentials

Genetic algorithms (GA) are a class of optimization algorithms that draws inspiration from the natural evolution. The first idea to apply evolutionary principles to solve problems was proposed in 1940s, but the first application to optimization problems is dated back to 1960s when three different implementations have been developed independently: evolutionary programming by Owens and Walsh, genetic algorithm by Holland, and evolution strategies by Rechenberg and Schwefel [238].

Evolutionary algorithms are inspired to Darwinian theory of evolution in which the natural selection has a central role. The process of natural selection favours the individuals that most effectively compete for the available resources, in a process usually named "survival of the fittest". The idea to evaluate the phenotype of an individual on the basis of its capacity to adapt to the environmental conditions can be applied in a optimization routine by means of a series of operators that reproduce the mutations, crossover and recombination occurring in nature.

Fig. C4 describes the workflow of an evolutionary algorithm. The initial population is generated by an operator called "generator", that defines an initial set of individual to be evaluated by the fitness function. The fitness function evaluates the goodness of an individual with respect to the desired result. If none of the individuals satisfies the termination criteria the best candidates selected by the the "selection operator" undergoes to an evolutionary process performed by the crossover and mutation operators. In addition to crossover and mutations, some individuals could survive to the selection process and enter directly in the next generation. At the end of these operations the new population of individuals is evaluated. This process will continue until the termination criteria is met.

On the basis of the specific problem, different operators could be applied to perform selection, mutation and crossover. Moreover, for each problem the choice of a suitable fitness function is of critical importance. In this work, Genetic Algorithm are used as the main optimization strategy. In the following is reported the description of standard GA operators: 1-point crossover, bit-flip mutation, rank selection and generational replacement.

- *Generator.* New individuals are generated randomly between bounds specifically selected for each neuron.

- *Evaluator.* The evaluator establishes the goodness of a candidate on the basis of the fitness function evaluation. The evaluator is custom built and can work with different kinds of fitness functions to be chosen on the basis of the availab.le experimental data (see below)

- *Rank-based selector.* In the rank-based selection the population is sorted on the basis of the fitness and the selection probability for each individual is assigned on the basis of its rank in the population rather than of its fitness value. The rank of an individual indicates how many worse solutions are in the population [238].

APPENDIX C
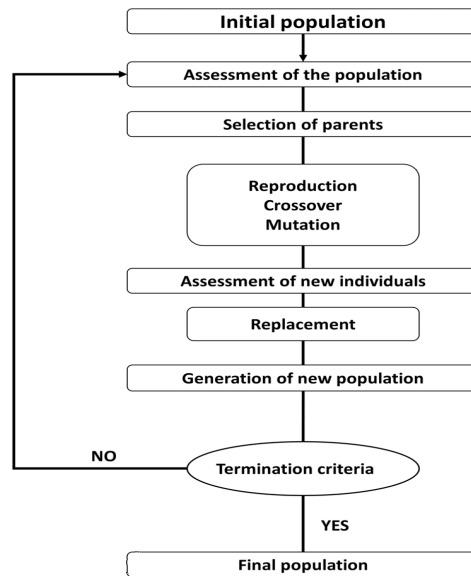
Figure C4: **Genetic algorithm operation scheme.** Scheme representing the optimization algorithm process.

- *1-point crossover.* In this form of crossover the chromosome (i.e., the individual) is broken in two pieces, and the offspring is generated by picking up alternative segments from the parents [238]. The basic scheme of operation of 1-point crossover in depicted in Fig. C5.
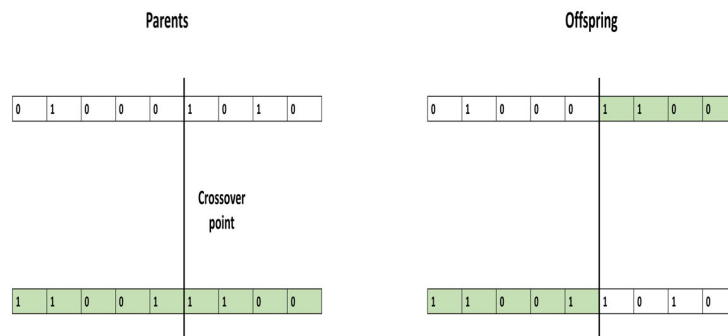
Figure C5: **1-point crossover.** The crossover point r is chosen randomly in the interval $[1, l-1]$, where l is the length of the chromosome. In this way the choice of $r = 0$ and $r = l$ are prevented

- *Bit-flip mutation.* In the bit flip mutation the binary representation fo the chro-

187

mosome undergoes to a mutation process in which each bit is allowed to flip with a small probability p. The number of flips is not fixed, but varies depending on p and on the length of the chromosome l. On average the numer of changed values is $l \cdot p$. The choice of p in most GA is made such that one gene per generation and one gene *per* offspring is mutated [238].

- *Trunkation replacement.* The replacer substitutes the entire population with the best individuals among the current population and the offspring. In this way the population size is preserved.

- *Average fitness terminator.* For each population both the best fitness and the average fitness of the population are calculated. If the difference between the two values is below the threshold tolerance the optimization is terminated.

In some cases the selection and replacement operators can be changed to match the specific characteristics of the problem, in particular the way in which the candidate is represented. In the case here presented, candidates are strings of real values, so that specific mutation and recombination operators are needed [238]. The list of used operators for each GA run is specified in the dedicated section. In the following, the working principles of the operators are described:

- *Guassian mutation* The Gaussian mutation is the analogous for real values representations of the creep mutation used in integer representation problems. The creep mutation operator performs the mutation by adding a small, positive or negative, value to each gene with a probability p. In the case of integer representation the value at each position is sampled randomly from a symmetric distribution centred in zero. In the case of Gaussian mutation the probability distribution from wich the values are picked is a Gaussian:

$$p(\Delta x_i) = \frac{1}{\sigma\sqrt{2\pi}} \cdot \exp\left[\frac{-(\Delta x_i - \zeta)^2}{2\sigma^2}\right] \tag{A69}$$

In Eq. A69 ζ represents the mean, which is assumed equal to zero ($\zeta = 0$), and σ the standard deviation. σ is the parameter that determines the extent to which the candidate is changed. Normally, it is set to 1, so that two thirds of the samples are picked within the interval $[-\sigma, \sigma]$, but leaving a non-zero probability of generating large changes of the parameters.

- *Blend crossover* The blend cross over (BLX) is a recombination operator suitable for real-values representations [238]. It allows to create an offspring in a region bigger than that defined by the parents. The additional available space is proportional to the distance between the parents (Fig. C6).

- *Truncation replacement.* In the truncation replacement the entire existing population is replaced by the best individual among the current population and the offspring, keeping the size of the population fixed.

APPENDIX C
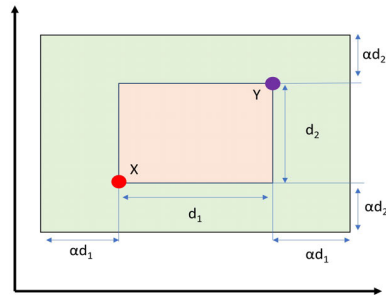
Figure C6: **Blend crossover** Given two parents X and Y with $X_i < Y_i$ in i-th position. The i-th values of the Z child span in the range $[X_i - \alpha \cdot d_i, X_i + \alpha \cdot d_i]$ whith $\alpha \in [0, 1]$ (green area), and is defined as $Z_i = (1 - \psi)X_i + \psi Y_i$, where $\psi = (1 - 2\alpha)w - \alpha$ with $w \in [0, 1]$ [238].

- *Diversity termination.* The diversity temination criterion is based on the calculation of the Euclidean distance between every pair of individuals of the population. Than the maximum of those distances is compared with the minimum diversity required.

Bibliography

[1] M. Usuyama, C. Ushida, and R. Shingai, "A model of the intracellular response of an olfactory neuron in *Caenorhabditis elegans* to odor stimulation," *PloS one*, vol. 7, no. 8, p. e42907, 2012.

[2] E. Maupas, "Modes et formes de reproduction des nematodes," *Archives de Zoologie Expérimentale et Générale*, vol. 8, pp. 463–624, 1900.

[3] T. *C.elegans* sequencing consortium, "Genome sequence of the nematode *C.elegans*: a platform for investigating biology," *Science*, vol. 282, pp. 2012–2017, 1998.

[4] P. Kuwabara and N. O'neil, "The use of functional genomics in *C. elegans* for studying human development and disease," *Journal of inherited metabolic disease*, vol. 24, no. 2, pp. 127–138, 2001.

[5] T. W. Harris, N. Chen, F. Cunningham, M. Tello-Ruiz, I. Antoshechkin, C. Bastiani, T. Bieri, D. Blasiar, K. Bradnam, J. Chan, *et al.*, "Wormbase: a multi-species resource for nematode biology and genomics," *Nucleic acids research*, vol. 32, no. suppl_1, pp. D411–D417, 2004.

[6] T. Kaletta and M. O. Hengartner, "Finding function in novel targets: *C. elegans* as a model organism," *Nature reviews Drug discovery*, vol. 5, no. 5, pp. 387–399, 2006.

[7] A. Corsi, B. Wightman, and M. Chalfie, "A transparent window into biology: a primer on *Caenorhabditis elegans* (june 18, 2015) wormbook, ed. the c. elegans research community, wormbook, doi/10.1895/wormbook. 1.177. 1," 2015.

[8] R. Baumeister, "The worm in us- *Caenorhabditis elegans* as a model of human disease," *TREND in Biotechnology*, vol. 20, pp. 147–148, 2002.

[9] G. B. Silverman, C. J. Luke, S. Bhatia, O. S. Long, A. C. Vetica, D. H. Perlmutter, and S. C. Pak, "Modeling molecular and cellular aspects of human disease using the nematode *Caenorhabditis elegans*," *Pediatr.Res.*, vol. 65, pp. 10–18, 2009.

[10] A. G. Alexander, V. Marfil, and C. Li, "Use of *Caenorhabditis elegans* as a model to study alzheimer's disease and other neurodegenerative diseases," *Frontiers in genetics*, vol. 5, p. 279, 2014.

[11] M. Carretero, G. M. Solis, and M. Petrascheck, "*C.elegans* as a model for drug discovery," *Current topics in medicinal chemistry*, vol. 17, pp. 1–10, 2017.

[12] J. G. White, E. Southgate, J. N. Thomson, and S. Brenner, "The structure of the nervous system of the nematode *Caenorhabditis elegans*," *Philosophical Transactions of the Royal Society of London. Series B, Biological*, vol. 314, pp. 1–340, 1986.

[13] S. H. Chalasani, N. Chronis, M. Tsunozaki, J. M. Gray, D. Ramot, M. B. Goodman, and C. I. Bargmann, "Dissecting a circuit for olfactory behaviour in *Caenorhabditis elegans*," *Nature*, vol. 450, no. 7166, pp. 63–70, 2007.

[14] M. Zhen and A. D. Samuel, "*C. elegans* locomotion: small circuits, complex functions," *Current opinion in neurobiology*, vol. 33, pp. 117–126, 2015.

[15] J. Larsch, S. W. Flavell, Q. Liu, A. Gordus, D. R. Albrecht, and C. I. Bargmann, "A circuit for gradient climbing in *C. elegans* chemotaxis," *Cell reports*, vol. 12, no. 11, pp. 1748–1760, 2015.

[16] A. Gordus, N. Pokala, S. Levy, S. W. Flavell, and C. I. Bargmann, "Feedback from network states generates variability in a probabilistic olfactory circuit," *Cell*, vol. 161, no. 2, pp. 215–227, 2015.

[17] S. G. Leinwand and S. H. Chalasani, "Neuropeptide signaling remodels chemosensory circuit composition in *Caenorhabditis elegans*," *Nature neuroscience*, vol. 16, no. 10, pp. 1461–1467, 2013.

[18] M. B. Goodman, D. H. Hall, L. Avery, and S. R. Lockery, "Active currents regulate sensitivity and dynamic range in *C. elegans* neurons," *Neuron*, vol. 20, no. 4, pp. 763–772, 1998.

[19] D. Ramot, B. MacInnis, and M. B. Goodman, "Bidirectional temperature-sensing by a single thermosensory neuron in *C.elegans*," *Nature Neuroscience*, vol. 11, pp. 908–915, 2008.

[20] J. E. Mellem, P. J. Brockie, D. M. Madsen, and A. Maricq, "Action potentials contribute to neuronal signaling in *C.elegans*," *Nat. Neuroscience*, vol. 11, pp. 865–867, 2008.

[21] Q. Liu, P. B. Kidd, M. Dobosiewicz, and C. I. Bargmann, "*C. elegans* AWA olfactory neurons fire calcium-mediated all-or-none action potentials," *Cell*, vol. 175, no. 1, pp. 57–70, 2018.

[22] T. Shindou, M. Ochi-Shindou, T. Murayama, E.-i. Saita, Y. Momohara, J. R. Wickens, and I. N. Maruyama, "Active propagation of dendritic electrical signals in *C. elegans*," *Scientific reports*, vol. 9, no. 1, pp. 1–12, 2019.

[23] P. Liu, B. Chen, and Z.-W. Wang, "SLO-2 potassium channel is an important regulator of neurotransmitter release in *Caenorhabditis elegans*," *Nature communications*, vol. 5, p. 5155, 2014.

[24] S. Faumont, T. Boulin, O. Hobert, and S. R. Lockery, "Developmental regulation of whole cell capacitance and membrane current in identified interneurons in *C. elegans*," *Journal of neurophysiology*, vol. 95, no. 6, pp. 3665–3673, 2006.

[25] M. Dobosiewicz, Q. Liu, and C. I. Bargmann, "Reliability of an interneuron response depends on an integrated sensory state," *Elife*, vol. 8, p. e50566, 2019.

[26] S. R. Wicks, C. J. Roehrig, and C. H. Rankin, "A dynamic network simulation of the nematode tap withdrawal circuit: predictions concerning synaptic function using behavioral criteria," *Journal of Neuroscience*, vol. 16, no. 12, pp. 4017–4031, 1996.

[27] E. J. Izquierdo, P. L. Williams, and R. D. Beer, "Information flow through a model of the *C. elegans* klinotaxis circuit," *PloS one*, vol. 10, no. 10, p. e0140397, 2015.

[28] E. J. Izquierdo and R. D. Beer, "Connecting a connectome to behavior: an ensemble of neuroanatomical models of *C. elegans* klinotaxis," *PLoS Comput Biol*, vol. 9, no. 2, p. e1002890, 2013.

[29] J. M. Kunert, J. L. Proctor, S. L. Brunton, and J. N. Kutz, "Spatiotemporal feedback and network structure drive and encode *Caenorhabditis elegans* locomotion," *PLoS computational biology*, vol. 13, no. 1, p. e1005303, 2017.

[30] J. M. Kunert-Graf, E. Shlizerman, A. Walker, and J. N. Kutz, "Multistability and long-timescale transients encoded by network structure in a model of *C. elegans* connectome dynamics," *Frontiers in computational neuroscience*, vol. 11, p. 53, 2017.

[31] J. Kunert, E. Shlizerman, and J. N. Kutz, "Low-dimensional functionality of complex network dynamics: Neurosensory integration in the *Caenorhabditis elegans* connectome," *Physical Review E*, vol. 89, no. 5, p. 052805, 2014.

[32] C. Fieseler, J. Kunert-Graf, and J. N. Kutz, "The control structure of the nematode *Caenorhabditis elegans*: Neuro-sensory integration and proprioceptive feedback," *Journal of biomechanics*, vol. 74, pp. 1–8, 2018.

[33] P. Gleeson, D. Lung, R. Grosu, R. Hasani, and S. D. Larson, "c302: a multiscale framework for modelling the nervous system of *Caenorhabditis elegans*," *Philosophical Transactions of the Royal Society B: Biological Sciences*, vol. 373, no. 1758, p. 20170379, 2018.

[34] J. Kim, W. Leahy, and E. Shlizerman, "Neural interactome: Interactive simulation of a neuronal system," *Frontiers in Computational Neuroscience*, vol. 13, p. 8, 2019.

[35] M. Kuramochi and M. Doi, "A computational model based on multi-regional calcium imaging represents the spatio-temporal dynamics in a caenorhabditis elegans sensory neuron," *PLoS One*, vol. 12, no. 1, p. e0168415, 2017.

[36] E. Mirzakhalili, B. I. Epureanu, and E. Gourgou, "A mathematical and computational model of the calcium dynamics in *Caenorhabditis elegans* ash sensory neuron," *PloS one*, vol. 13, no. 7, p. e0201302, 2018.

[37] M. Hammarlund, O. Hobert, D. M. Miller 3rd, and N. Sestan, "The CeNGEN project: the complete gene expression map of an entire nervous system," *Neuron*, vol. 99, no. 3, pp. 430–433, 2018.

[38] M. Nicoletti, A. Loppini, L. Chiodo, V. Folli, G. Ruocco, and S. Filippi, "Biophysical modeling of *C. elegans neurons*: Single ion currents and whole-cell dynamics of awcon and rmd," *PloS one*, vol. 14, no. 7, p. e0218738, 2019.

[39] M. Nicoletti, A. Loppini, L. Chiodo, V. Folli, G. Ruocco, and S. Filippi, "Mathematical modeling of the *Caenorhabditis elegans* RMD motor neurons," in *2020 11th Conference of the European Study Group on Cardiovascular Oscillations (ESGCO)*, pp. 1–2, IEEE, 2020.

[40] M. Nicoletti, A. Loppini, L. Chiodo, V. Folli, G. Ruocco, and S. Filippi, "AWC *C. elegans* neuron: a biological sensor model," in *2020 IEEE International Workshop on Metrology for Industry 4.0 & IoT*, pp. 329–333, IEEE, 2020.

[41] D. Caprini, S. Schwartz, E. Lanza, E. Milanetti, V. Lucente, G. Ferrarese, L. Chiodo, M. Nicoletti, and V. Folli, "Mechanosensitivity of the AWC^{ON} olfactory neuron in *C. elegans*," 2020, in preparation.

[42] D. Ventimiglia and C. I. Bargmann, "Diverse modes of synaptic signaling, regulation, and plasticity distinguish two classes of *C. elegans* glutamatergic neurons," *eLife*, vol. 6, no. e31234, 2017.

[43] N. T. Carnevale and M. L. Hines, *The NEURON book*. Cambridge University Press, 2006.

[44] K. Ashida, K. Hotta, and K. Oka, "The input-output relationship of aiy interneurons in *Caenorhabditis elegans* in noisy environment," *Iscience*, vol. 19, pp. 191–203, 2019.

[45] H. Shidara, J. Kobayashi, R. Tanamoto, K. Hotta, and K. Oka, "Odorant-induced membrane potential depolarization of aiy interneuron in *Caenorhabditis elegans*," *Neuroscience letters*, vol. 541, pp. 199–203, 2013.

[46] M.-A. Félix and C. Braendle, "The natural history of *Caenorhabditis elegans*," *Current Biology*, vol. 20, pp. R965–R969, 2010.

[47] L. Stevens, M. Felix, T. Beltran, C. Braendle, C. Caurcel, *et al.*, "Comparative genomics of 10 new *Caenorhabditis species*," *Evolution Letters*, vol. 3, pp. 217–236, 2019.

[48] J. E. Sulston and H. R. Horvitz, "Post-embryonic cell lineages of the nematode *Caenorhabditis elegans*," *Developmental biology*, vol. 56, no. 1, pp. 110–156, 1977.

[49] J. Kimble and D. Hirsh, "The postembryonic cell lineages of the hermaphrodite and male gonads in *Caenorhabditis elegans*," *Developmental biology*, vol. 70, no. 2, pp. 396–417, 1979.

[50] J. E. Sulston, E. Schierenberg, J. G. White, J. N. Thomson, *et al.*, "The embryonic cell lineage of the nematode *Caenorhabditis elegans*," *Developmental biology*, vol. 100, no. 1, pp. 64–119, 1983.

[51] E. Culetto and D. B. Sattelle, "A role for *Caenorhabditis elegans* in understanding the function and interactions of human disease genes," *Human molecular genetics*, vol. 9, no. 6, pp. 869–877, 2000.

[52] D. L. Riddle, T. Blumenthal, B. J. Meyer, and J. R. Priess, "Introduction to *C. elegans*," in *C. elegans II*, ch. 1, Cold Spring Harbor Laboratory Press, 1997.

[53] Z. Altun and D. Hall, "The handbook of *C. elegans* anatomy. introduction," 2015.

[54] D. L. Riddle, T. Blumenthal, B. J. Meyer, and J. R. Priess, "Sex determination and x chromosome dosage compensation," in *C. elegans II*, ch. 9, Cold Spring Harbor Laboratory Press, 1997.

[55] R. Lints and D. Hall, "Male introduction," *WormAtlas: Atlas of C. elegans Anatomy*, 2009.

[56] L. Byerly, R. Cassada, and R. Russell, "The life cycle of the nematode *Caenorhabditis elegans*: I. wild-type growth and reproduction," *Developmental biology*, vol. 51, no. 1, pp. 23–33, 1976.

[57] R. Lande, "Sexual dimorphism, sexual selection, and adaptation in polygenic characters," *Evolution*, pp. 292–305, 1980.

[58] Z. Altun and D. Hall, "Nervous system, general description," *WormAtlas*, vol. 10, pp. 103–116, 2011.

[59] R. Lints and D. Hall, "Male neuronal support cells, overview," 2009.

[60] S. J. Cook, T. A. Jarrell, C. A. Brittin, Y. Wang, A. E. Bloniarz, M. A. Yakovlev, K. C. Nguyen, L. T.-H. Tang, E. A. Bayer, J. S. Duerr, *et al.*, "Whole-animal connectomes of both *Caenorhabditis elegans* sexes," *Nature*, vol. 571, no. 7763, pp. 63–71, 2019.

[61] W. Zou, H. Cheng, S. Li, X. Yue, Y. Xue, S. Chen, and L. Kang, "Polymodal responses in *C. elegans* phasmid neurons rely on multiple intracellular and intercellular signaling pathways," *Scientific reports*, vol. 7, p. 42295, 2017.

[62] J. E. Mellem, P. J. Brockie, Y. Zheng, D. M. Madsen, and A. V. Maricq, "Decoding of polymodal sensory stimuli by postsynaptic glutamate receptors in *C. elegans*," *Neuron*, vol. 36, no. 5, pp. 933–944, 2002.

[63] O. Hobert, L. Glenwinkel, and J. White, "Revisiting neuronal cell type classification in *Caenorhabditis elegans*," *Current Biology*, vol. 26, pp. R1197–R1203, 2016.

[64] Z. Altun and D. . Hall, "Nervous system, neuronal support cells," *WormAtlas*, 2010.

[65] A. Albeg, C. J. Smith, M. Chatzigeorgiou, D. G. Feitelson, D. H. Hall, W. R. Schafer, D. M. Miller III, and M. Treinin, "C. elegans multi-dendritic sensory neurons: morphology and function," *Molecular and Cellular Neuroscience*, vol. 46, no. 1, pp. 308–317, 2011.

[66] M. B. Goodman and P. Sengupta, "How caenorhabditis elegans senses mechanical stress, temperature, and other physical stimuli," *Genetics*, vol. 212, no. 1, pp. 25–51, 2019.

[67] D. M. Tobin and C. I. Bargmann, "Invertebrate nociception: behaviors, neurons and molecules," *Journal of neurobiology*, vol. 61, no. 1, pp. 161–174, 2004.

[68] I. Sokolchik, T. Tanabe, P. F. Baldi, and J. Y. Sze, "Polymodal sensory function of the *Caenorhabditis elegans* OCR-2 channel arises from distinct intrinsic determinants within the protein and is selectively conserved in mammalian trpv proteins," *Journal of Neuroscience*, vol. 25, no. 4, pp. 1015–1023, 2005.

[69] T. Sassa, T. Murayama, and I. N. Maruyama, "Strongly alkaline ph avoidance mediated by ash sensory neurons in *C. elegans*," *Neuroscience letters*, vol. 555, pp. 248–252, 2013.

[70] D. A. Glauser, W. C. Chen, R. Agin, B. L. MacInnis, A. B. Hellman, P. A. Garrity, M.-W. Tan, and M. B. Goodman, "Heat avoidance is regulated by transient receptor potential (trp) channels and a neuropeptide signaling pathway in *Caenorhabditis elegans*," *Genetics*, vol. 188, no. 1, pp. 91–103, 2011.

[71] I. Mori, "Genetics of chemotaxis and thermotaxis in the nematode *Caenorhabditis elegans*," *Annual review of genetics*, vol. 33, no. 1, pp. 399–422, 1999.

[72] E. M. Hedgecock and R. L. Russell, "Normal and mutant thermotaxis in the nematode *Caenorhabditis elegans*," *Proceedings of the National Academy of Sciences*, vol. 72, no. 10, pp. 4061–4065, 1975.

APPENDIX C

[73] M. B. Goodman and P. Sengupta, "The extraordinary afd thermosensor of *C. elegans*," *Pflügers Archiv-European Journal of Physiology*, vol. 470, no. 5, pp. 839–849, 2018.

[74] C. V. Gabel, H. Gabel, D. Pavlichin, A. Kao, D. A. Clark, and A. D. Samuel, "Neural circuits mediate electrosensory behavior in *Caenorhabditis elegans*," *Journal of Neuroscience*, vol. 27, no. 28, pp. 7586–7596, 2007.

[75] S. D. Chrisman, C. B. Waite, A. G. Scoville, and L. Carnell, "*C. elegans* demonstrates distinct behaviors within a fixed and uniform electric field," *PloS one*, vol. 11, no. 3, p. e0151320, 2016.

[76] A. Vidal-Gadea, K. Ward, C. Beron, N. Ghorashian, S. Gokce, J. Russell, N. Truong, A. Parikh, O. Gadea, A. Ben-Yakar, *et al.*, "Magnetosensitive neurons mediate geomagnetic orientation in *Caenorhabditis elegans*," *Elife*, vol. 4, p. e07493, 2015.

[77] R. Ghosh, A. Mohammadi, L. Kruglyak, and W. S. Ryu, "Multiparameter behavioral profiling reveals distinct thermal response regimes in *Caenorhabditis elegans*," *BMC biology*, vol. 10, no. 1, p. 85, 2012.

[78] J. Liu, A. Ward, J. Gao, Y. Dong, N. Nishio, H. Inada, L. Kang, Y. Yu, D. Ma, T. Xu, *et al.*, "*C. elegans* phototransduction requires a g protein–dependent cgmp pathway and a taste receptor homolog," *Nature neuroscience*, vol. 13, no. 6, p. 715, 2010.

[79] M. A. Carrillo, M. L. Guillermin, S. Rengarajan, R. P. Okubo, and E. A. Hallem, "O_2-sensing neurons control co_2 response in *C. elegans*," *Journal of Neuroscience*, vol. 33, no. 23, pp. 9675–9683, 2013.

[80] A. J. Bretscher, E. Kodama-Namba, K. E. Busch, R. J. Murphy, Z. Soltesz, P. Laurent, and M. de Bono, "Temperature, oxygen, and salt-sensing neurons in *C. elegans* are carbon dioxide sensors that control avoidance behavior," *Neuron*, vol. 69, no. 6, pp. 1099–1113, 2011.

[81] C. Rogers, A. Persson, B. Cheung, and M. de Bono, "Behavioral motifs and neural pathways coordinating o2 responses and aggregation in *C. elegans*," *Current biology*, vol. 16, no. 7, pp. 649–659, 2006.

[82] B. H. Cheung, M. Cohen, C. Rogers, O. Albayram, and M. De Bono, "Experience-dependent modulation of *C. elegans* behavior by ambient oxygen," *Current Biology*, vol. 15, no. 10, pp. 905–917, 2005.

[83] C. I. Bargamann, "Chemosensation in *C. elegans*," *WormBook*, 2006.

[84] D. Biron, S. Wasserman, J. H. Thomas, A. D. Samuel, and P. Sengupta, "An olfactory neuron responds stochastically to temperature and modulates *Caenorhabditis*

197

elegans thermotactic behavior," *Proceedings of the National Academy of Sciences*, vol. 105, no. 31, pp. 11002–11007, 2008.

[85] J. Q. White and E. M. Jorgensen, "Sensation in a single neuron pair represses male behavior in hermaphrodites," *Neuron*, vol. 75, no. 4, pp. 593–600, 2012.

[86] P. D. Wes and C. Bargmann, "*C. elegans* odour discrimination requires asymmetric diversity in olfactory neurons," *Nature*, vol. 410, pp. 698–701, 2001.

[87] E. R. Troemel, A. Sagasti, and C. I. Bargmann, "Lateral signaling mediated by axon contact and calcium entry regulates asymmetric odorant receptor expression in *C. elegans*," *Cell*, vol. 99, no. 4, pp. 387–398, 1999.

[88] L. Frooninckx, L. Van Rompay, L. Temmerman, E. Van Sinay, I. Beets, T. Janssen, S. J. Husson, and L. Schoofs, "Neuropeptide gpcrs in *C. elegans*," *Frontiers in endocrinology*, vol. 3, p. 167, 2012.

[89] M. R. Koelle, "Neurotransmitter signaling through heterotrimeric g proteins: insights from studies in *C. elegans*," in *WormBook: The Online Review of C. elegans Biology [Internet]*, WormBook, 2018.

[90] B. Vidal, U. Aghayeva, H. Sun, C. Wang, L. Glenwinkel, E. A. Bayer, and O. Hobert, "An atlas of *Caenorhabditis elegans* chemoreceptor expression," *PLoS biology*, vol. 16, no. 1, p. e2004218, 2018.

[91] E. Itskovits, R. Ruach, and A. Zaslaver, "Concerted pulsatile and graded neural dynamics enables efficient chemotaxis in *C. elegans*," *Nature communications*, vol. 9, no. 1, pp. 1–11, 2018.

[92] J. M. Gray, J. J. Hill, and C. I. Bargmann, "A circuit for navigation in *Caenorhabditis elegans*," *Proceedings of the National Academy of Sciences*, vol. 102, no. 9, pp. 3184–3191, 2005.

[93] A. Kocabas, C.-H. Shen, Z. V. Guo, and S. Ramanathan, "Controlling interneuron activity in *Caenorhabditis elegans* to evoke chemotactic behaviour," *Nature*, vol. 490, no. 7419, pp. 273–277, 2012.

[94] S. H. Chalasani, S. Kato, D. R. Albrecht, T. Nakagawa, L. Abbott, and C. I. Bargmann, "Neuropeptide feedback modifies odor-evoked dynamics in *Caenorhabditis elegans* olfactory neurons," *Nature neuroscience*, vol. 13, no. 5, p. 615, 2010.

[95] I. Mori and Y. Ohshima, "Neural regulation of thermotaxis in *Caenorhabditis elegans*," *Nature*, vol. 376, no. 6538, pp. 344–348, 1995.

[96] E. L. Tsalik and O. Hobert, "Functional mapping of neurons that control locomotory behavior in *Caenorhabditis elegans*," *Journal of neurobiology*, vol. 56, no. 2, pp. 178–197, 2003.

APPENDIX C

[97] L. Shen, Y. Hu, T. Cai, X. Lin, and D. Wang, "Regulation of longevity by genes required for the functions of aiy interneuron in nematode *Caenorhabditis elegans*," *Mechanisms of ageing and development*, vol. 131, no. 11-12, pp. 732–738, 2010.

[98] Y.-C. Chen, H.-J. Chen, W.-C. Tseng, J.-M. Hsu, T.-T. Huang, C.-H. Chen, and C.-L. Pan, "A *C. elegans* thermosensory circuit regulates longevity through *crh-1*/creb-dependent *flp-6* neuropeptide signaling," *Developmental cell*, vol. 39, no. 2, pp. 209–223, 2016.

[99] B. J. Piggott, J. Liu, Z. Feng, S. A. Wescott, and X. S. Xu, "The neural circuits and synaptic mechanisms underlying motor initiation in *C. elegans*," *Cell*, vol. 147, no. 4, pp. 922–933, 2011.

[100] A. Gordus, N. Pokala, S. Levy, S. W. Flavell, and C. I. Bargmann, "Feedback from network states generates variability in a probabilistic olfactory circuit," *Cell*, vol. 161, no. 2, pp. 215–227, 2015.

[101] M. J. Alkema, M. Hunter-Ensor, N. Ringstad, and H. R. Horvitz, "Tyramine functions independently of octopamine in the *Caenorhabditis elegans* nervous system," *Neuron*, vol. 46, no. 2, pp. 247–260, 2005.

[102] J. K. Pirri, A. D. McPherson, J. L. Donnelly, M. M. Francis, and M. J. Alkema, "A tyramine-gated chloride channel coordinates distinct motor programs of a *Caenorhabditis elegans* escape response," *Neuron*, vol. 62, no. 4, pp. 526–538, 2009.

[103] O. Tolstenkov, P. Van der Auwera, W. S. Costa, O. Bazhanova, T. M. Gemeinhardt, A. C. Bergs, and A. Gottschalk, "Functionally asymmetric motor neurons contribute to coordinating locomotion of *Caenorhabditis elegans*," *Elife*, vol. 7, p. e34997, 2018.

[104] Q. Wen, S. Gao, and M. Zhen, "*Caenorhabditis elegans* excitatory ventral cord motor neurons derive rhythm for body undulation," *Philosophical Transactions of the Royal Society B: Biological Sciences*, vol. 373, no. 1758, p. 20170370, 2018.

[105] M. Zhen and A. D. Samuel, "*C. elegans* locomotion: small circuits, complex functions," *Current opinion in neurobiology*, vol. 33, pp. 117–126, 2015.

[106] Q. Wen, M. D. Po, E. Hulme, S. Chen, X. Liu, S. W. Kwok, M. Gershow, A. M. Leifer, V. Butler, C. Fang-Yen, *et al.*, "Proprioceptive coupling within motor neurons drives *C. elegans* forward locomotion," *Neuron*, vol. 76, no. 4, pp. 750–761, 2012.

[107] M. Chalfie, J. E. Sulston, J. G. White, E. Southgate, J. N. Thomson, and S. Brenner, "The neural circuit for touch sensitivity in *Caenorhabditis elegans*," *Journal of Neuroscience*, vol. 5, no. 4, pp. 956–964, 1985.

[108] I. A. Bany, M.-Q. Dong, and M. R. Koelle, "Genetic and cellular basis for acetylcholine inhibition of *Caenorhabditis elegans* egg-laying behavior," *Journal of Neuroscience*, vol. 23, no. 22, pp. 8060–8069, 2003.

[109] K. Schuske, A. A. Beg, and E. M. Jorgensen, "The gaba nervous system in *C. elegans*," *Trends in neurosciences*, vol. 27, no. 7, pp. 407–414, 2004.

[110] Z. Altun and D. Hall, "Muscle system, somatic muscle," *WormAtlas. Edited for the web by Laura A. Herndon. Last revision: May*, vol. 31, p. 2013, 2009.

[111] D. L. Riddle, T. Blumenthal, B. J. Meyer, and J. R. Priess, "Mechanosensory control of locomotion," 1997.

[112] A. C. Hart, S. Sims, and J. M. Kaplan, "Synaptic code for sensory modalities revealed by *C. elegans* glr-1 glutamate receptor," *Nature*, vol. 378, no. 6552, pp. 82–85, 1995.

[113] P. J. Brockie, D. M. Madsen, Y. Zheng, J. Mellem, and A. V. Maricq, "Differential expression of glutamate receptor subunits in the nervous system of *Caenorhabditis elegans* and their regulation by the homeodomain protein unc-42," *Journal of Neuroscience*, vol. 21, no. 5, pp. 1510–1522, 2001.

[114] N. Ohnishi, A. Kuhara, F. Nakamura, Y. Okochi, and I. Mori, "Bidirectional regulation of thermotaxis by glutamate transmissions in *Caenorhabditis elegans*," *The EMBO Journal*, vol. 30, no. 7, pp. 1376–1388, 2011.

[115] B. Alberts, A. Johson, J. Lewis, M. Raff, K. Roberts, P. Walter, D. Bray, and W. James D, *Molecular Biology of the Cell*. Garland Science, 2014.

[116] M. B. Jackson, *Molecular and cellular biophysics*. Cambridge University Press, 2006.

[117] E. R. Kandel, J. H. Schwartz, T. M. Jessell, D. of Biochemistry, M. B. T. Jessell, S. Siegelbaum, and A. Hudspeth, *Principles of neural science*. McGraw-hill New York, 2000.

[118] J.-B. Kim, "Channelopathies," *Korean journal of pediatrics*, vol. 57, no. 1, p. 1, 2014.

[119] D. Douguet and E. Honoré, "Mammalian mechanoelectrical transduction: Structure and function of force-gated ion channels," *Cell*, vol. 179, no. 2, pp. 340–354, 2019.

[120] X. Liang and J. Howard, "Structural biology: piezo senses tension through curvature," *Current Biology*, vol. 28, no. 8, pp. R357–R359, 2018.

[121] L. J. Drew and J. N. Wood, "Worm sensation!," *Molecular Pain*, vol. 1, pp. 1744–8069, 2005.

APPENDIX C

[122] M. B. Goodman, G. G. Ernstrom, D. S. Chelur, R. O'Hagan, C. A. Yao, and M. Chalfie, "MEC-2 regulates *C. elegans* deg/enac channels needed for mechanosensation," *Nature*, vol. 415, no. 6875, pp. 1039–1042, 2002.

[123] Y. Chen, S. Bharill, E. Y. Isacoff, and M. Chalfie, "Subunit composition of a DEG/ENaC mechanosensory channel of *Caenorhabditis elegans*," *Proceedings of the National Academy of Sciences*, vol. 112, no. 37, pp. 11690–11695, 2015.

[124] M. Huang, G. Gu, E. L. Ferguson, and M. Chalfie, "A stomatin-like protein necessary for mechanosensation in *C. elegans*," *Nature*, vol. 378, no. 6554, pp. 292–295, 1995.

[125] H. Du, G. Gu, C. M. William, and M. Chalfie, "Extracellular proteins needed for *C. elegans* mechanosensation," *Neuron*, vol. 16, no. 1, pp. 183–194, 1996.

[126] L. Emtage, G. Gu, E. Hartwieg, and M. Chalfie, "Extracellular proteins organize the mechanosensory channel complex in *C. elegans* touch receptor neurons," *Neuron*, vol. 44, no. 5, pp. 795–807, 2004.

[127] T. Fukushige, Z. K. Siddiqui, M. Chou, J. G. Culotti, C. B. Gogonea, S. S. Siddiqui, and M. Hamelin, "MEC-12, an alpha-tubulin required for touch sensitivity in *C. elegans*," *Journal of cell science*, vol. 112, no. 3, pp. 395–403, 1999.

[128] O. Hobert, "The neuronal genome of *Caenorhabditis elegans*," in *WormBook: The Online Review of C. elegans Biology [Internet]*, WormBook, 2018.

[129] J. J. Vowels and J. H. Thomas, "Multiple chemosensory defects in *daf-11* and *daf-21* mutants of *Caenorhabditis elegans*.," *Genetics*, vol. 138, no. 2, pp. 303–316, 1994.

[130] D. A. Birnby, E. M. Link, J. J. Vowels, H. Tian, P. L. Colacurcio, and J. H. Thomas, "A transmembrane guanylyl cyclase (DAF-11) and hsp90 (DAF-21) regulate a common set of chemosensory behaviors in *Caenorhabditis elegans*," *Genetics*, vol. 155, no. 1, pp. 85–104, 2000.

[131] H. Komatsu, I. Mori, J.-S. Rhee, N. Akaike, and Y. Ohshima, "Mutations in a cyclic nucleotide–gated channel lead to abnormal thermosensation and chemosensation in *C. elegans*," *Neuron*, vol. 17, no. 4, pp. 707–718, 1996.

[132] M. Wojtyniak, A. G. Brear, D. M. O'Halloran, and P. Sengupta, "Cell-and subunit-specific mechanisms of cng channel ciliary trafficking and localization in *C. elegans*," *Journal of cell science*, vol. 126, no. 19, pp. 4381–4395, 2013.

[133] K. Roayaie, J. G. Crump, A. Sagasti, and C. I. Bargmann, "The gα protein ODR-3 mediates olfactory and nociceptive function and controls cilium morphogenesis in *C. elegans* olfactory neurons," *Neuron*, vol. 20, no. 1, pp. 55–67, 1998.

[134] D. Noelle and C. I. Bargmann, "Olfaction and odor discrimination are mediated by the *C. elegans* guanylyl cyclase ODR-1," *Neuron*, vol. 25, no. 3, pp. 575–586, 2000.

[135] H. Komatsu, Y.-H. Jin, N. L'Etoile, I. Mori, C. I. Bargmann, N. Akaike, and Y. Ohshima, "Functional reconstitution of a heteromeric cyclic nucleotide-gated channel of caenorhabditis elegans in cultured cells," *Brain research*, vol. 821, no. 1, pp. 160–168, 1999.

[136] L. Salkoff, A. Butler, G. Fawcett, M. Kunkel, C. McArdle, G. Paz-y Mino, M. Nonet, N. Walton, Z.-w. Wang, A. Yuan, *et al.*, "Evolution tunes the excitability of individual neurons," *Neuroscience*, vol. 103, pp. 853–859, 2001.

[137] P. Liu, Q. Ge, B. Chen, L. Salkoff, M. I. Kotlikoff, and Z.-W. Wang, "Genetic dissection of ion currents underlying all-or-none action potentials in *C. elegans* body-wall muscle cells," *The Journal of Physiology*, vol. 589, pp. 101–117, 2011.

[138] G. L. Fawcett, C. M. Santi, A. Butler, T. Harris, M. Covarrubias, and L. Salkoff, "Mutant analysis of the Shal (kv4) voltage-gated fast transient k+ channel in *Caenorhabditis elegans*," *Journal of Biological Chemistry*, vol. 281, pp. 30725–30735, 2006.

[139] M. Jospin, V. Jacquemond, M.-C. Mariol, L. Ségalat, and B. Allard, "The L-type voltage-dependent Ca^{2+} channel EGL-19 controls body wall muscle function in *Caenorhabditis elegans*," *The Journal of cell biology*, vol. 159, pp. 337–348, 2002.

[140] B. B. Shtonda and L. Avery, "CCA-1, EGL-19 and EXP-2 currents shape action potentials in the *Caenorhabditis elegans* phatynx," *The Journal of Experimental Biology*, vol. 208, pp. 2177–2190, 2005.

[141] J. P. Adelman, C. T. Bond, M. Pessia, and J. Maylie, "Episodic ataxia results from voltage-dependent potassium channels with altered functions," *Neuron*, vol. 15, pp. 1449–1454, 1995.

[142] M. W. Davis, R. Fleischhauer, J. A. Dent, R. H. Joho, and L. Avery, "A mutation in the *C. elegans* EXP-2 potassium channel that alters feeding behavior," *Science*, vol. 286, no. 5449, pp. 2501–2504, 1999.

[143] D. B. Johnstone, A. Wei, A. Butler, L. Salkoff, and J. H. Thomas, "Behavioral defects in *C. elegans* egl-36 mutants result from potassium channels shifted in voltage-dependence of activation," *Neuron*, vol. 19, pp. 151–164, 1997.

[144] S.-Q. Cai and F. Sesti, "A new mode of regulation of N-type inactivation in a *Caenorhabditis elegans* voltage-gated potassium channel," *Journal of Biological Chemistry*, vol. 282, pp. 18597–18601, 2007.

APPENDIX C

[145] A. D. Wei, A. G. Butler, and L. B. Salkoff, "KCNQ-like potassium channels in *C. elegans*: Conserved properties and modulation," *Journal of Biological Chemistry*, 2005.

[146] D. Weinshenker, A. Wei, L. Salkoff, and J. H. Thomas, "Block of an ether-a-go-go-like K^+ channel by imipramine rescues *egl-2* excitation defects in *Caenorhabditis elegans*," *Journal of Neuroscience*, vol. 19, pp. 9831–9840, 1999.

[147] M. C. Sanguinetti, C. Jiang, M. E. Curran, and M. T. Keating, "A mechanistic link between an inherited and an acquird cardiac arrthytmia: HERG encodes the IKr potassium channel," *Cell*, vol. 81, no. 2, pp. 299–307, 1995.

[148] J. Ludwig, H. Terlau, F. Wunder, A. Brüggemann, L. Pardo, A. Marquardt, W. Stühmer, and O. Pongs, "Functional expression of a rat homologue of the voltage gated either á go-go potassium channel reveals differences in selectivity and activation kinetics between the *Drosophila* channel and its mammalian counterpart.," *The EMBO Journal*, vol. 13, pp. 4451–4458, 1994.

[149] L. Emtage, S. Zaman, O. Padovan-Merhar, H. Horvitz, C. Fang-Yen, and N. Ringstad, "IRK-1 potassium channels mediate peptidergic inhibition of *Caenorhabditis elegans* serotonin neurons via a g(o) signaling pathway," *J Neurosci*, vol. 32, no. 46, p. 16285–16295, 2012.

[150] J. Wolf, J. Moyer, M. Lazarewicz, D. Contreras, M. Benoit-Marand, P. O'Donnel, and F. LH, "NMDA/AMPA ratio impacts state transitions and entrainment to oscillations in a computational model of the nucleus accumbens medium spiny projection neuron," *The Journal of Neuroscience*, vol. 25, no. 40, pp. 9080–9095, 2005.

[151] H. Hayashi and H. M. Fishman, "Inward rectifier K^+ channel kinetic from analysis of the complex conductance of *Aplysia* neuronal membrane," *Bionphysical Journal*, vol. 53, pp. 747–757, 1998.

[152] Z.-W. Wang, O. Saifee, M. L. Nonet, and L. Salkoff, "SLO-1 potassium channels control quantal content of neurotransmitter release at the *C.elegans* neuromuscular junction," *Neuron*, vol. 32, pp. 867–881, 2001.

[153] Z. Zhang, Q. T. Tang, J. T. Alaimo, A. G. Davies, J. G. Bettinger, and D. E. Logothetis, "SLO-2 isoforms with unique Ca^{2+}-and voltage-dependence characteristics confer sensitivity to hypoxia in *C.elegans*," *Channels*, vol. 7, pp. 194–205, 2013.

[154] C. K. Chotoo, G. A. Silverman, D. C. Devor, and C. J. Luke, "A small conductance calcium-activated K^+ channels in *C.elegans*, KCNL-2, plays a role in regulation of the rate of egg-laying," *PloS ONE*, vol. 8, p. e75869, 2013.

[155] E. A. Mathews, E. Garcìa, C. M. Santi, G. P. Mullen, C. Thacker, D. G. Moerman, and T. P. Snutch, "Critical residues of the *Caenorhbdits elegans unc-2* voltage-gated calcium channel that affect behavioral and physiological properties," *The journal of Neuroscience*, vol. 23, pp. 6537–6545, 2003.

[156] L. Li, J. Bischofberger, and P. Jonas, "Differential gating and recruitment of P/Q-, N-, and R- Type Ca^{2+} channels in hippocampal mossy fiber boutons," *The Journal of Neuroscience*, vol. 27, no. 49, pp. 13420–13429, 2007.

[157] X. Huang, A. Senatore, and T. e. a. Dawson, "G-proteins modulate invertebrate synaptic calcium channel (LCa_v2) differently form the classical voltage-dependent regulation of mammalian $Ca_v2.1$ and $Ca_v2.2$ channels," *The Journal of Experimental Biology*, vol. 213, pp. 2094–2103, 2010.

[158] K. Jeong, S. Lee, H. Seo, Y. Oh, D. Jang, J. Choe, D. Kim, J.-H. Lee, and W. D. Jones, "Ca-α1T, a fly T-type Ca^{2+} channel, negatively modulates sleep," *Scientific Reports*, vol. 5, p. 17893, 2015.

[159] S. Gao, L. Xie, K. Taizo, M. D. Po, J. K. Pirri, S. Guan, M. Alkema, and M. Zhen, "The nca sodium leak channel is required for persistent motor circuit activity that sustains locomotion," *Nature Communications*, vol. 6, 2015.

[160] I. Topalidou, K. Cooper, L. Pereira, and M. Ailion, "Dopamine negatively modulates the nca ion channels in *C. elegans*," *PLoS genetics*, vol. 13, no. 10, p. e1007032, 2017.

[161] E. Yeh, N. Sharon, and M. e. a. Zhang, "A putative cation channel, NCA-1, and a novel protein, UNC-80, transmit neuronal activity in *C.elegans*," *PLoS Biology*, vol. 6, p. e55, 2008.

[162] L. Salkoff, A. Wei, B. Baban, A. Butler, G. Fawcett, G. Ferreira, and C. M. Santi, "Potassium channels in *C. elegans*," 2005.

[163] S. Gao and M. Zhen, "Action potentials drive body wall muscle contractions in *Caenorhabditis elegans*," *Proceedings of the National Academy of Sciences*, vol. 108, pp. 2557–2562, 2011.

[164] H. Hibino, A. Inanobe, K. Furutani, S. Murakami, I. Findlay, and Y. Kurachi, "Inwardly rectifying potassium channels: their structure, function, and physiological roles," *Physiological reviews*, vol. 90, no. 1, pp. 291–366, 2010.

[165] M. Nishida and R. MacKinnon, "Structural basis of inward rectification: cytoplasmic pore of the g protein-gated inward rectifier girk1 at 1.8 å resolution," *Cell*, vol. 111, no. 7, pp. 957–965, 2002.

[166] M. L. Olsen and H. Sontheimer, "Functional implications for Kir4.1 channels in glial biology: from K+ buffering to cell differentiation," *Journal of neurochemistry*, vol. 107, no. 3, pp. 589–601, 2008.

[167] P. A. Glazebrook, A. N. Ramirez, J. H. Schild, C.-C. Shieh, T. Doan, B. A. Wible, and D. L. Kunze, "Potassium channels Kv1.1, Kv1.2 and Kv1.6 influence excitability of rat visceral sensory neurons," *The Journal of physiology*, vol. 541, pp. 467–482, 2002.

[168] S. L. Smart, V. Lopantsev, C. Zhang, C. A. Robbins, H. Wang, S. Chiu, P. A. Schwartzkroin, A. Messing, and B. L. Tempel, "Deletion of the Kv1.1 potassium channel causes epilepsy in mice," *Neuron*, vol. 20, pp. 809–819, 1998.

[169] S. Zuberi, L. Eunson, A. Spauschus, R. De Silva, J. Tolmie, N. Wood, R. McWilliam, J. Stephenson, D. Kullmann, and M. Hanna, "A novel mutation in the human voltage-gated potassium channel gene (Kv1.1) associates with episodic ataxia type 1 and sometimes with partial epilepsy," *Brain*, vol. 122, pp. 817–825, 1999.

[170] E. Glasscock, N. Voigt, M. D. McCauley, Q. Sun, N. Li, D. Y. Chiang, X.-B. Zhou, C. E. Molina, D. Thomas, C. Schmidt, *et al.*, "Expression and function of Kv1.1 potassium channels in human atria from patients with atrial fibrillation," *Basic research in cardiology*, vol. 110, p. 47, 2015.

[171] R. Fleischhauer, M. W. Davis, I. Dzhura, A. Neely, L. Avery, and R. H. Joho, "Ultrafast inactivation causes inward rectification in a voltage-gated k+ channel from *Caenorhabditis elegans*," *Journal of Neuroscience*, vol. 20, no. 2, pp. 511–520, 2000.

[172] K. H. Park and F. Sesti, "An arrhythmia susceptibility gene in *Caenorhabditis elegans*," *Journal of Biological Chemistry*, vol. 282, no. 27, pp. 19799–19807, 2007.

[173] B. Rudy and C. J. McBain, "Kv3 channels: voltage-gated K+ channels designed for high-frequency repetitive firing," *Trends in neurosciences*, vol. 24, pp. 517–526, 2001.

[174] L. K. Kaczmarek and Y. Zhang, "Kv3 channels: enablers of rapid firing, neurotransmitter release, and neuronal endurance," *Physiological reviews*, vol. 97, pp. 1431–1468, 2017.

[175] D. A. Elkes, D. L. Cardozo, J. Madison, and J. M. Kaplan, "EGL-36 shaw channels regulate *C. elegans* egg-laying muscle activity," *Neuron*, vol. 19, pp. 165–174, 1997.

[176] H. H. Jerng, P. J. Pfaffinger, and M. Covarrubias, "Molecular physiology and modulation of somatodendritic a-type potassium channels," *Molecular and Cellular Neuroscience*, vol. 27, pp. 343–369, 2004.

[177] D. Brown and P. Adams, "Muscarinic suppression of a novel voltage-sensitive K+ current in a vertebrate neurone," *Nature*, vol. 283, p. 673, 1980.

[178] J. Schwarz, G. Glassmeier, E. Cooper, T.-C. Kao, H. Nodera, D. Tabuena, R. Kaji, and H. Bostock, "KCNQ channels mediate IKs, a slow K+ current regulating excitability in the rat node of ranvier," *The Journal of physiology*, vol. 573, pp. 17–34, 2006.

[179] D. A. Brown and G. M. Passmore, "Neural KCNQ (kv7) channels," *British journal of pharmacology*, vol. 156, pp. 1185–1195, 2009.

[180] W.-C. Tong, R. M. Tribe, R. Smith, and M. J. Taggart, "Computational modeling reveals key contributions of KCNQ and hERG currents to the malleability of uterine action potentials underpinning labor," *PloS one*, vol. 9, p. e114034, 2014.

[181] T. Jespersen, M. Grunnet, and S.-P. Olesen, "The KCNQ1 potassium channel: from gene to physiological function," *Physiology*, vol. 20, pp. 408–416, 2005.

[182] T. J. Jentsch, "Neuronal KCNQ potassium channels: physislogy and role in disease," *Nature Reviews Neuroscience*, vol. 1, p. 21, 2000.

[183] M. Okahata, A. D. Wei, A. Ohta, and A. Kuhara, "Cold acclimation via the KQT-2 potassium channel is modulated by oxygen in *Caenorhabditis elegans*," *Science advances*, vol. 5, no. 2, p. eaav3631, 2019.

[184] K. Nehrke, J. Denton, and W. Mowrey, "Intestinal ca2+ wave dynamics in freely moving *C. elegans* coordinate execution of a rhythmic motor program," *American Journal of Physiology-Cell Physiology*, vol. 294, no. 1, pp. C333–C344, 2008.

[185] C. K. Bauer and J. R. Schwarz, "Ether-à-go-go k+ channels: effective modulators of neuronal excitability," *The Journal of physiology*, vol. 596, pp. 769–783, 2018.

[186] M. C. Sanguinetti and M. Tristani-Firouzi, "herg potassium channels and cardiac arrhythmia," *Nature*, vol. 440, no. 7083, pp. 463–469, 2006.

[187] A. Becchetti, L. Munaron, and A. Arcangeli, "The role of ion channels and transporters in cell proliferation and cancer," *Frontiers in physiology*, vol. 4, p. 312, 2013.

[188] T. Sacco, A. Bruno, E. Wanke, and F. Tempia, "Functional roles of an ERG current isolated in cerebellar purkinje neurons," *Journal of neurophysiology*, vol. 90, pp. 1817–1828, 2003.

[189] B. Ganetzky, G. A. Robertson, G. F. Wilson, M. C. Trudeau, and S. A. Titus, "The eag family of k+ channels in *Drosophila* and mammals," *Annals of the New York Academy of Sciences*, vol. 868, pp. 356–369, 1999.

[190] F. Kortüm, V. Caputo, C. K. Bauer, L. Stella, A. Ciolfi, M. Alawi, G. Bocchinfuso, E. Flex, S. Paolacci, M. L. Dentici, *et al.*, "Mutations in KCNH1 and ATP6V1B2 cause zimmermann-laband syndrome," *Nature genetics*, vol. 47, no. 6, pp. 661–667, 2015.

APPENDIX C

[191] C. Simons, L. D. Rash, J. Crawford, L. Ma, B. Cristofori-Armstrong, D. Miller, K. Ru, G. J. Baillie, Y. Alanay, A. Jacquinet, *et al.*, "Mutations in the voltage-gated potassium channel gene KCNH1 cause temple-baraitser syndrome and epilepsy," *Nature genetics*, vol. 47, no. 1, p. 73, 2015.

[192] J. W. Warmke and B. Ganetzky, "A family of potassium channel genes related to eag in *Drosophila* and mammals.," *Proceedings of the National Academy of Sciences*, vol. 91, pp. 3438–3442, 1994.

[193] L. S. Mortensen, H. Schmidt, Z. Farsi, A. Barrantes-Freer, M. E. Rubio, R. Ufartes, J. Eilers, T. Sakaba, W. Stühmer, and L. A. Pardo, "Kv10. 1 opposes activity-dependent increase in ca2+ influx into the presynaptic terminal of the parallel fibre–purkinje cell synapse," *The Journal of physiology*, vol. 593, no. 1, pp. 181–196, 2015.

[194] A. E. Dubin, M. M. Liles, and G. L. Harris, "The K+ channel gene ether a go-go is required for the transduction of a subset of odorants in adult *Drosophila* melanogaster," *Journal of Neuroscience*, vol. 18, pp. 5603–5613, 1998.

[195] M. Pessia, I. Servettini, R. Panichi, L. Guasti, S. Grassi, A. Arcangeli, E. Wanke, and V. E. Pettorossi, "ERG voltage-gated k+ channels regulate excitability and discharge dynamics of the medial vestibular nucleus neurones," *The Journal of physiology*, vol. 586, no. 20, pp. 4877–4890, 2008.

[196] R. M. Hardman and I. D. Forsythe, "Ether-à-go-go-related gene k+ channels contribute to threshold excitability of mouse auditory brainstem neurons," *The Journal of physiology*, vol. 587, no. 11, pp. 2487–2497, 2009.

[197] W. Schledermann, I. Wulfsen, J. R. Schwarz, and C. K. Bauer, "Modulation of rat erg1, erg2, erg3 and HERG K+ currents by thyrotropin-releasing hormone in anterior pituitary cells via the native signal cascade," *The Journal of physiology*, vol. 532, no. 1, pp. 143–163, 2001.

[198] L. R. Garcia and P. W. Sternberg, "*Caenorhabditis elegans* UNC-103 ERG-like potassium channel regulates contractile behaviors of sex muscles in males before and during mating," *Journal of Neuroscience*, vol. 23, no. 7, pp. 2696–2705, 2003.

[199] D. J. Reiner, E. M. Newton, H. Tian, and J. H. Thomas, "Diverse behavioural defects caused by mutations in *Caenorhabditis elegans unc-43* CaM kinase II," *Nature*, vol. 402, no. 6758, pp. 199–203, 1999.

[200] P. Rojas, J. Garst-Orozco, B. Baban, J. A. de Santiago-Castillo, M. Covarrubias, and L. Salkoff, "Cumulative activation of voltage-dependent KVS-1 potassium channels," *Journal of Neuroscience*, vol. 28, pp. 757–765, 2008.

[201] L. Bianchi, S.-M. Kwok, M. Driscoll, and F. Sesti, "A potassium channel-MiRP complex controls neurosensory function in *Caenorhabditis elegans*," *Journal of Biological Chemistry*, vol. 278, pp. 12415–12424, 2003.

[202] P. N'Gouemo, "bk_{Ca} channel dysfunction in neurological diseases," *Frontiers in Physiology*, vol. 5, 2014.

[203] G. Raffaeli, G. Saviane, M. Mohajerani, P. Pedarzani, and E. Cherubini, "BK potassium channel control transmitter release at CA3-CA3 synapses in the rat hippocampus," *Journal of Physiology*, vol. 557, pp. 147–157, 2004.

[204] B. Fakler and J. P. Adelman, "Control of k_{Ca} channels by calcium nano/microdomains," *Neuron*, vol. 59, pp. 873–881, 2008.

[205] A. Alqadah, Y. W. Hsieh, and J. e. a. Schumacher, "SLO BK potassium channels couple gap junctions to inhibition of calcium signaling in olfactory neurons diversification," *PLoS Genetics*, vol. 12, p. e1005654, 2016.

[206] A. Yuan, M. Dourado, A. Butler, N. Walton, A. Wei, and L. Salkoff, "SLO-2,a K^+ channel with an unusual Cl- dependence," *Nature Neuroscience*, vol. 3, pp. 771–779, 2000.

[207] J. P. Adelman, J. Maylie, and P. Sah, "Small-conductance ca^{2+}-activated k^+ channels: Form and function," *Annu. Rev. Physiol*, vol. 74, pp. 245–269, 2012.

[208] T. J. B. Simons, "Calcium and neural function," *Neurosurg. Rev*, vol. 11, pp. 119–129, 1988.

[209] W. A. Catterall, "Voltage-gated calcium channels," *Cold Spring Harbor perspectives in biology*, vol. 3, no. 8, p. a003947, 2011.

[210] S. R. Lockery and M. B. Goodman, "The quest for action potentials in *C.elegans* hits a plateau," *Nature Neuroscience*, vol. 12, pp. 377–378, 2009.

[211] M. Simon, J. F. Perrier, and J. Hounsgaard, "Subcellular ditribution of l-type ca2+ channels responsible for plateau potentials in motoneurons from the lumbar spinal cord of the turtle," *European Journal of Neuroscience*, vol. 18, pp. 258–266, 2003.

[212] V. Lainé, C. Frøkjær-Jensen, H. Couchoux, and M. Jospin, "The α1 subunit egl-19, the $\alpha2/\delta$ subunit unc-36, and the β subunit ccb-1 underlie voltage-dependent calcium currents in *Caenorhabditis elegans* striated muscle," *Journal of Biological Chemistry*, vol. 286, no. 42, pp. 36180–36187, 2011.

[213] T. e. a. Tsunemi, "Novel Cav2.1 splice variants isolated from purkinje cells do not generate P-type Ca2+ current," *The Journal of Biological Chemistry*, vol. 277, pp. 7214–7221, 2002.

[214] Y. Saheki and C. Bargmann, "Presynaptic CaV2 calcium channel traffic requires CALF-1 and the alpha2-delta subunit UNC-36," *Nature Neuroscience*, vol. 12, pp. 1257–1265, 2009.

APPENDIX C

[215] J. Arikkath and K. P. Campbell, "Auxiliary subunits: essential components of the voltage-gated calcium channel complex," *Current Opinion in Neurobiology*, vol. 13, pp. 298–307, 2003.

[216] S. L. Bauer Huang, Y. Saheki, M. K. VanHoven, I. Torayama, T. Ishihara, I. Katsura, A. Van der Linden, P. Sengupta, and C. I. Bargamnn, "Left-right olfactory asymmetry result from antagonistic functions of voltage-activated calcium channels and the raw repeat protein OLRN-1 in *C.elegans*," *Neural Development*, vol. 2, 2007.

[217] A. Senatore, B. B. Zhorov, and J. D. Spafford, "Ca_v3 T-type calcium channels," *WIREs Membr Transp Signal*, vol. 1, pp. 467–491, 2012.

[218] C. L. Smith, S. Abdallah, Y. Y. Wong, P. Le, A. N. Harracksingh, L. Artinian, A. N. Tamvacakis, V. Rehder, T. S. Reese, and A. Senatore, "Evolutionary insights into T-type ca^{2+} channel structure, function, and ion selectivity from *Trichoplax adhaerens* homologue," *The Journal of General Physiology*, vol. 149, pp. 483–510, 2017.

[219] S. M. Cain and T. P. Snutch, "Contributions of t-type calcium channels isoforms to neuronal firing," *Channels*, vol. 4, pp. 475–482, 2010.

[220] V. Crunelli, T. I. Thóth, D. W. Cope, K. Blethyn, and S. W. Hughes, "The 'window' T-type calcium current in brain dynamics of different behavioral states," *J Physiol*, vol. 562, pp. 121–129, 2005.

[221] K. A. Steger, B. B. Shtonda, C. Thacker, T. P. Snutch, and L. Avery, "The *C.elegans* T-type calcium channels CCA-1 boosts neuromuscular transmission," *The Journal of Experimental Biology*, vol. 208, pp. 2191–2203, 2005.

[222] K. E. Zang, E. Ho, and N. Ringstad, "Inhibitory peptidergic modulations of *C.elegans* serotonin neurons is gated by t-type calcium channels," *eLife*, vol. 6, p. e22771, 2017.

[223] M. Cochet-Bissuel, P. Lory, and A. Monteil, "The sodium leak channel, NALCN, in helath and disease," *Frontier in Cellular Neuroscience*, vol. 8, 2014.

[224] M. Jospin, W. S, D. Joshi, S. Young, K. Hamming, C. Thacker, T. Snutch, E. Jorgensen, and K. Schuske1, "UNC-80 and the NCA ion channels contribute to endocytosis defects in synaptojanin mutants," *Current Biology*, vol. 17, pp. 1595–1600, 2017.

[225] B. Lu, Q. Zhang, H. Wang, Y. Wang, M. Nakayama, and D. Ren, "Extracellular calcium controls background current and neuronal excitability via an UNC79-UNC80-NALCN cation channel complex," *Neuron*, vol. 68, pp. 488–499, 2010.

[226] I. Topalidou, P.-A. Chen, K. Copper, S. Watanabe, E. M. Jorgensen, and M. Ailion, "The NCA-1 and NCA-2 ion channels function downstream of gq and rho to regulate locomotion in *Caenorhabditis elegans*," *Genetics*, vol. 206, pp. 265–282, 2017.

[227] R. Davis and A. Stretton, "Passive membrane properties of motorneurons and their role in long-distance signaling in the nematode ascaris," *Journal of Neuroscience*, vol. 9, no. 2, pp. 403–414, 1989.

[228] A. L. Hogkin and A. F. Huxley, "A quantitative description of membrane current and its application to conduction and excitation nerve," *Journal of Physiology*, vol. 117, pp. 500–544, 1952.

[229] A. Molleman, *Patch clamping: an introductory guide to patch clamp electrophysiology*. John Wiley & Sons, 2003.

[230] X.-M. Xia, B. Fakler, A. Rivard, G. Wayman, T. Johnson-Pais, J. Keen, T. Ishii, B. Hirschberg, C. Bond, S. Lutsenko, *et al.*, "Mechanism of calcium gating in small-conductance calcium-activated potassium channels," *Nature*, vol. 395, no. 6701, p. 503, 1998.

[231] T. Griffith, K. Tsaneva-Atasanova, and J. Mellor, "Control of ca^{2+} influx and calmodulin activation by sk-channels in dendritic spines," *PloS Computational Biology*, vol. 12, no. 5, p. e1004949, 2019.

[232] A. Sherman, R. J, and K. J, "Emergence of organized bursting in clusters of pancreatic β-cells by channel sharing," *Biophysical Journal*, vol. 54, pp. 411–425, 1988.

[233] F. Montefusco, A. Tagliavini, M. Ferrante, and M. G. Pedersen, "Concise whole-cell modeling if bk_{Ca}-cav activity controlled by local coupling and stoichiometry," *Biophysical Journal*, vol. 112, pp. 2387–2396, 2017.

[234] G. D. Smith, "Modeling local and global calcium signals using reaction-diffusion equations," pp. 49–85, 2000.

[235] D. H. Cox, "Modeling Ca^{2+} Channel/BK_{Ca} channels complex at the single-complex level," *Biophysical Journal*, vol. 107, pp. 2797–2814, 2014.

[236] M. Riz, M. Braun, and M. G. Pedersen, "Mathematical modeling of heterogeneous electrophysiological responses in human β-cells," *PloS Computational Biology*, vol. 10, p. e1003389, 2014.

[237] G. Dupont, M. Falcke, V. Kirk, and J. Sneyd, *Models of calcium signalling*, vol. 43. Springer, 2016.

[238] A. E. Eiben and J. E. Smith, *Introduction to evolutionary computing*. Springer, 2015.

[239] S. Attaway, *Matlab: a practical introduction to programming and problem solving*. Butterworth-Heinemann, 2013.

[240] B. Ermentrout, *Simulating, analyzing, and animating dynamical systems: a guide to XPPAUT for researchers and students*. SIAM, 2002.

[241] M. Hines, A. P. Davison, and E. Muller, "Neuron and python," *Frontiers in neuroinformatics*, vol. 3, p. 1, 2009.

[242] F. Perez, B. E. Granger, and J. D. Hunter, "Python: an ecosystem for scientific computing," *Computing in Science & Engineering*, vol. 13, no. 2, pp. 13–21, 2010.

[243] A. Tonda, "Inspyred: Bio-inspired algorithms in python," *Genetic Programming and Evolvable Machines*, pp. 1–4, 2019.

[244] W. Press, S. Teukolsky, W. Vetterling, and B. Flannery, "Numerical recipes in c (new york)," 1992.

[245] J. Larsch, D. Ventimiglia, C. I. Bargmann, and D. R. Albrecht, "High-throughput imaging of neuronal activity in *Caenorhabditis elegans*," *Proceedings of the National Academy of Sciences*, vol. 110, no. 45, pp. E4266–E4273, 2013.

[246] B. Sakmann and E. Neher, "Single channel currents recorded from membrane of denervated frog muscle fibers," *Nature*, vol. 260, no. 7, 1976.

[247] S. Speese, M. Petrie, K. Schuske, M. Ailion, K. Ann, K. Iwasaki, E. M. Jorgensen, and T. F. Martin, "UNC-31 (CAPS) is required for dense-core vesicle but not synaptic vesicle exocytosis in *Caenorhabditis elegans*," *Journal of Neuroscience*, vol. 27, no. 23, pp. 6150–6162, 2007.

[248] J. E. Richmond, W. S. Davis, and E. M. Jorgensen, "UNC-13 is required for synaptic vesicle fusion in *C. elegans*," *Nature neuroscience*, vol. 2, no. 11, pp. 959–964, 1999.

[249] H. A. Colbert, T. L. Smith, and C. I. Bargmann, "Osm-9, a novel protein with structural similarity to channels, is required for olfaction, mechanosensation, and olfactory adaptation in *Caenorhabditis elegans*," *Journal of Neuroscience*, vol. 17, no. 21, pp. 8259–8269, 1997.

[250] H. Zhang, X. Yue, H. Cheng, X. Zhang, Y. Cai, W. Zou, G. Huang, L. Cheng, F. Ye, and L. Kang, "OSM-9 and an amiloride-sensitive channel, but not PKD-2, are involved in mechanosensation in *C. elegans* male ray neurons," *Scientific reports*, vol. 8, no. 1, pp. 1–8, 2018.

[251] D. M. Tobin, D. M. Madsen, A. Kahn-Kirby, E. L. Peckol, G. Moulder, R. Barstead, A. V. Maricq, and C. I. Bargmann, "Combinatorial expression of trpv channel proteins defines their sensory functions and subcellular localization in *C. elegans* neurons," *Neuron*, vol. 35, no. 2, pp. 307–318, 2002.

[252] H. Komatsu, I. Mori, J.-S. Rhee, N. Akaike, and Y. Ohshima, "Mutations in a cyclic nucleotide–gated channel lead to abnormal thermosensation and chemosensation in *C. elegans*," *Neuron*, vol. 17, no. 4, pp. 707–718, 1996.

[253] P. S. Spector, M. E. Curran, A. Zou, M. T. Keating, and M. C. Sanguinetti, "Fast inactivation causes rectification of the ikr channel.," *The Journal of general physiology*, vol. 107, no. 5, pp. 611–619, 1996.

[254] M. C. Trudeau, J. W. Warmke, B. Ganetzky, and G. A. Robertson, "Herg, a human inward rectifier in the voltage-gated potassium channel family," *Science*, vol. 269, no. 5220, pp. 92–95, 1995.

[255] S. Zhang, S. J. Kehl, and D. Fedida, "Modulation of human ether-à-go-go-related K$^+$ (HERG) channel inactivation by Cs$^+$ and K$^+$," *The Journal of physiology*, vol. 548, no. 3, pp. 691–702, 2003.

[256] K. H. Oh and H. Kim, "BK channel clustering is required for normal behavioral alcohol sensitivity in *C. elegans*," *Scientific reports*, vol. 9, no. 1, pp. 1–11, 2019.

[257] K. H. Oh, L. S. Abraham, C. Gegg, and C. e. a. Silvestri, "Presynaptic BK channel localization is dependent on the hierarchicalorganization of alpha-catulin and dystrobrevin and fine-tuned by cav2 calcium channels," *BMC Neuroscience*, vol. 16, 2015.

[258] L. Sun, J.-S. Fan, J. W. Clark, and P. T. Palade, "A model of the L-type Ca2+ channel in rat ventricular myocytes: ion selectivity and inactivation mechanisms," *The Journal of physiology*, vol. 529, pp. 139–158, 2000.

[259] G. Harris, Y. Shen, H. Ha, A. Donato, S. Wallis, X. Zhang, and Y. Zhang, "Dissecting the signaling mechanisms underlying recognition and preference of food odors," *Journal of Neuroscience*, vol. 34, no. 28, pp. 9389–9403, 2014.

[260] J. Q. White and E. M. Jorgensen, "Sensation in a single neuron pair represses male behavior in hermaphrodites," *Neuron*, vol. 75, no. 4, pp. 593–600, 2012.

[261] L. Bianchi and M. Driscoll, "Heterologous expression of *C. elegans* ion channels in xenopus oocytes," in *WormBook: The Online Review of C. elegans Biology [Internet]*, WormBook, 2006.

[262] T. W. Harris, I. Antoshechkin, T. Bieri, D. Blasiar, J. Chan, W. J. Chen, N. De La Cruz, P. Davis, M. Duesbury, R. Fang, *et al.*, "Wormbase: a comprehensive resource for nematode research," *Nucleic acids research*, vol. 38, no. suppl_1, pp. D463–D467, 2010.

[263] Y. Fan, W. Zou, J. Liu, U. Al-Sheikh, H. Cheng, D. Duan, D. Chen, S. Liu, L. Chen, J. Xu, *et al.*, "Polymodal functionality of c. elegans oll neurons in mechanosensation and thermosensation," *Neuroscience Bulletin*, pp. 1–12, 2021.

[264] S. L. Geffeney and M. B. Goodman, "How we feel: ion channel partnerships that detect mechanical inputs and give rise to touch and pain perception," *Neuron*, vol. 74, no. 4, pp. 609–619, 2012.

[265] Y.-Q. Tang, S. A. Lee, M. Rahman, and S. A., "Ankyrin is an intracellular tether for tmc mechanotransduction channels," *Neuron*, vol. 107, no. 1, pp. 112 – 125.e10, 2020.

[266] H. A. Colbert, T. L. Smith, and C. I. Bargmann, "OSM-9, a novel protein with structural similarity to channels, is required for olfaction, mechanosensation, and olfactory adaptation incaenorhabditis elegans," *Journal of Neuroscience*, vol. 17, no. 21, pp. 8259–8269, 1997.

[267] D. M. O'Halloran, S. Altshuler-Keylin, J. I. Lee, and D. Noelle, "Regulators of AWC-mediated olfactory plasticity in *Caenorhabditis elegans*," *PLoS Genet*, vol. 5, no. 12, p. e1000761, 2009.

[268] M. B. Goodman and E. M. Schwarz, "Transducing touch in *Caenorhabditis elegans*," *Annual review of physiology*, vol. 65, no. 1, pp. 429–452, 2003.

[269] A. Upadhyay, A. Pisupati, T. Jegla, M. Crook, K. J. Mickolajczyk, M. Shorey, L. E. Rohan, K. A. Billings, M. M. Rolls, W. O. Hancock, *et al.*, "Nicotinamide is an endogenous agonist for a *C. elegans* trpv osm-9 and ocr-4 channel," *Nature communications*, vol. 7, no. 1, pp. 1–11, 2016.

[270] D. M. Tobin, D. M. Madsen, A. Kahn-Kirby, E. L. Peckol, G. Moulder, R. Barstead, A. V. Maricq, and C. I. Bargmann, "Combinatorial expression of trpv channel proteins defines their sensory functions and subcellular localization in *C. elegans neurons*," *Neuron*, vol. 35, no. 2, pp. 307–318, 2002.

[271] J. M. Kaplan and H. R. HoRVITZ, "A dual mechanosensory and chemosensory neuron in *Caenorhabditis elegans*.," *Proceedings of the National Academy of Sciences*, vol. 90, no. 6, pp. 2227–2231, 1993.

[272] S. Erdogmus, U. Storch, L. Danner, J. Becker, M. Winter, N. Ziegler, A. Wirth, S. Offermanns, C. Hoffmann, T. Gudermann, *et al.*, "Helix 8 is the essential structural motif of mechanosensitive GPCRs," *Nature communications*, vol. 10, no. 1, pp. 1–15, 2019.

[273] M. Mederos y Schnitzler, U. Storch, and T. Gudermann, "Mechanosensitive Gq/11 Protein-Coupled receptors mediate myogenic vasoconstriction," *Microcirculation*, vol. 23, no. 8, pp. 621–625, 2016.

[274] U. Storch, M. M. y. Schnitzler, and T. Gudermann, "G protein-mediated stretch reception," *American Journal of Physiology-Heart and Circulatory Physiology*, vol. 302, no. 6, pp. H1241–H1249, 2012.

[275] X. Chen, Z. Xia, and D. R. Storm, "Stimulation of electro-olfactogram responses in the main olfactory epithelia by airflow depends on the type 3 adenylyl cyclase," *Journal of Neuroscience*, vol. 32, no. 45, pp. 15769–15778, 2012.

[276] T. Connelly, Y. Yu, X. Grosmaitre, J. Wang, L. C. Santarelli, A. Savigner, X. Qiao, Z. Wang, D. R. Storm, and M. Ma, "G protein-coupled odorant receptors underlie mechanosensitivity in mammalian olfactory sensory neurons," *Proceedings of the National Academy of Sciences*, vol. 112, no. 2, pp. 590–595, 2015.

[277] X. Grosmaitre, L. C. Santarelli, J. Tan, M. Luo, and M. Ma, "Dual functions of mammalian olfactory sensory neurons as odor detectors and mechanical sensors," *Nature neuroscience*, vol. 10, no. 3, pp. 348–354, 2007.

[278] E. Milanetti, G. Gosti, L. De Flaviis, P. P. Olimpieri, S. Schwartz, D. Caprini, G. Ruocco, and V. Folli, "Investigation of the binding between olfactory receptors and odorant molecules in *C. elegans* organism," *Biophysical chemistry*, vol. 255, p. 106264, 2019.

[279] A. B. Hellman and K. Shen, "Sensory transduction channel subunits, *tax-4* and *tax-2*, modify presynaptic molecular architecture in *C. elegans*," *PLoS One*, vol. 6, no. 9, p. e24562, 2011.

[280] C. M. Coburn, I. Mori, Y. Ohshima, and C. I. Bargmann, "A cyclic nucleotide-gated channel inhibits sensory axon outgrowth in larval and adult *Caenorhabditis elegans*: a distinct pathway for maintenance of sensory axon structure," *Development*, vol. 125, no. 2, pp. 249–258, 1998.

[281] D. S. Walker and W. R. Schafer, "Distinct roles for innexin gap junctions and hemichannels in mechanosensation," *Elife*, vol. 9, p. e50597, 2020.

[282] G. L. Lyford, P. R. Strege, A. Shepard, Y. Ou, L. Ermilov, S. M. Miller, S. J. Gibbons, J. L. Rae, J. H. Szurszewski, and G. Farrugia, "$\alpha 1c$ (CaV1. 2) L-type calcium channel mediates mechanosensitive calcium regulation," *American Journal of Physiology-Cell Physiology*, vol. 283, no. 3, pp. C1001–C1008, 2002.

[283] J. Hao, F. Padilla, M. Dandonneau, C. Lavebratt, F. Lesage, J. Noël, and P. Delmas, "Kv1.1 channels act as mechanical brake in the senses of touch and pain," *Neuron*, vol. 77, no. 5, pp. 899–914, 2013.

[284] C. E. Morris, E. A. Prikryl, and B. Joós, "Mechanosensitive gating of Kv channels," *PLoS One*, vol. 10, no. 2, p. e0118335, 2015.

[285] J. Gullingsrud and K. Schulten, "Lipid bilayer pressure profiles and mechanosensitive channel gating," *Biophysical journal*, vol. 86, no. 6, pp. 3496–3509, 2004.

[286] A. Kuhara, M. Okumura, T. Kimata, Y. Tanizawa, R. Takano, K. D. Kimura, H. Inada, K. Matsumoto, and I. Mori, "Temperature sensing by an olfactory neuron

BIBLIOGRAPHY

in a circuit controlling behavior of *C. elegans*," *Science*, vol. 320, no. 5877, pp. 803–807, 2008.

[287] Z. V. Guo, A. C. Hart, and S. Ramanathan, "Optical interrogation of neural circuits in *Caenorhabditis elegans*," *Nature methods*, vol. 6, no. 12, pp. 891–896, 2009.

[288] K. S. Kindt, V. Viswanath, L. Macpherson, K. Quast, H. Hu, A. Patapoutian, and W. R. Schafer, "*Caenorhabditis elegans* trpa-1 functions in mechanosensation," *Nature neuroscience*, vol. 10, no. 5, pp. 568–577, 2007.

[289] V. Lainé, J. R. Ségor, H. Zhan, J.-L. Bessereau, and M. Jospin, "Hyperactivation of l-type voltage-gated ca2+ channels in caenorhabditis elegans striated muscle can result from point mutations in the is6 or the iiis4 segment of the $\alpha 1$ subunit," *Journal of Experimental Biology*, vol. 217, no. 21, pp. 3805–3814, 2014.

[290] C. Schüler, E. Fischer, L. Shaltiel, W. S. Costa, and A. Gottschalk, "Arrhythmogenic effects of mutated l-type ca 2+-channels on an optogenetically paced muscular pump in caenorhabditis elegans," *Scientific reports*, vol. 5, no. 1, pp. 1–16, 2015.

[291] Y. Gu, D. Servello, Z. Han, R. R. Lalchandani, J. B. Ding, K. Huang, and C. Gu, "Balanced activity between kv3 and nav channels determines fast-spiking in mammalian central neurons," *Iscience*, vol. 9, pp. 120–137, 2018.

[292] Y. Loewenstein, S. Mahon, P. Chadderton, K. Kitamura, H. Sompolinsky, Y. Yarom, and M. Häusser, "Bistability of cerebellar purkinje cells modulated by sensory stimulation," *Nature neuroscience*, vol. 8, no. 2, pp. 202–211, 2005.

[293] P. Fuentealba, I. Timofeev, M. Bazhenov, T. J. Sejnowski, and M. Steriade, "Membrane bistability in thalamic reticular neurons during spindle oscillations," *Journal of neurophysiology*, vol. 93, no. 1, pp. 294–304, 2005.

[294] L. Horoszok, V. Raymond, D. B. Sattelle, and A. J. Wolstenholme, "GLC-3: a novel fipronil and bidn-sensitive, but picrotoxinin-insensitive, L-glutamate-gated chloride channel subunit from *Caenorhabditis elegans*," *British journal of pharmacology*, vol. 132, no. 6, pp. 1247–1254, 2001.

[295] J. Larsch, D. Ventimiglia, C. I. Bargmann, and D. R. Albrecht, "High-throughput imaging of neuronal activity in *Caenorhabditis elegans*," *Proceedings of the National Academy of Sciences*, vol. 110, no. 45, pp. E4266–E4273, 2013.

[296] I. Kotera, N. A. Tran, D. Fu, J. H. Kim, J. B. Rodgers, and W. S. Ryu, "Panneuronal screening in *Caenorhabditis elegans* reveals asymmetric dynamics of AWC neurons is critical for thermal avoidance behavior," *Elife*, vol. 5, p. e19021, 2016.